

Springer Theses

Recognizing Outstanding Ph.D. Research

Daniel Schauries

Ion Tracks in Apatite and Quartz

And Their Behaviour with
Temperature and Pressure

 Springer

Springer Theses

Recognizing Outstanding Ph.D. Research

Aims and Scope

The series “Springer Theses” brings together a selection of the very best Ph.D. theses from around the world and across the physical sciences. Nominated and endorsed by two recognized specialists, each published volume has been selected for its scientific excellence and the high impact of its contents for the pertinent field of research. For greater accessibility to non-specialists, the published versions include an extended introduction, as well as a foreword by the student’s supervisor explaining the special relevance of the work for the field. As a whole, the series will provide a valuable resource both for newcomers to the research fields described, and for other scientists seeking detailed background information on special questions. Finally, it provides an accredited documentation of the valuable contributions made by today’s younger generation of scientists.

Theses are accepted into the series by invited nomination only and must fulfill all of the following criteria

- They must be written in good English.
- The topic should fall within the confines of Chemistry, Physics, Earth Sciences, Engineering and related interdisciplinary fields such as Materials, Nanoscience, Chemical Engineering, Complex Systems and Biophysics.
- The work reported in the thesis must represent a significant scientific advance.
- If the thesis includes previously published material, permission to reproduce this must be gained from the respective copyright holder.
- They must have been examined and passed during the 12 months prior to nomination.
- Each thesis should include a foreword by the supervisor outlining the significance of its content.
- The theses should have a clearly defined structure including an introduction accessible to scientists not expert in that particular field.

More information about this series at <http://www.springer.com/series/8790>

Daniel Schauries

Ion Tracks in Apatite and Quartz

And Their Behaviour with Temperature
and Pressure

Doctoral Thesis accepted by
the Australian National University, Acton, Australia

Author

Dr. Daniel Schauries
Department of Electronic Materials
Engineering
The Australian National University
Acton, ACT, Australia

Supervisor

Prof. Patrick Kluth
The Australian National University
Acton, ACT, Australia

ISSN 2190-5053

Springer Theses

ISBN 978-3-319-96282-5

<https://doi.org/10.1007/978-3-319-96283-2>

ISSN 2190-5061 (electronic)

ISBN 978-3-319-96283-2 (eBook)

Library of Congress Control Number: 2018948832

© Springer International Publishing AG, part of Springer Nature 2018

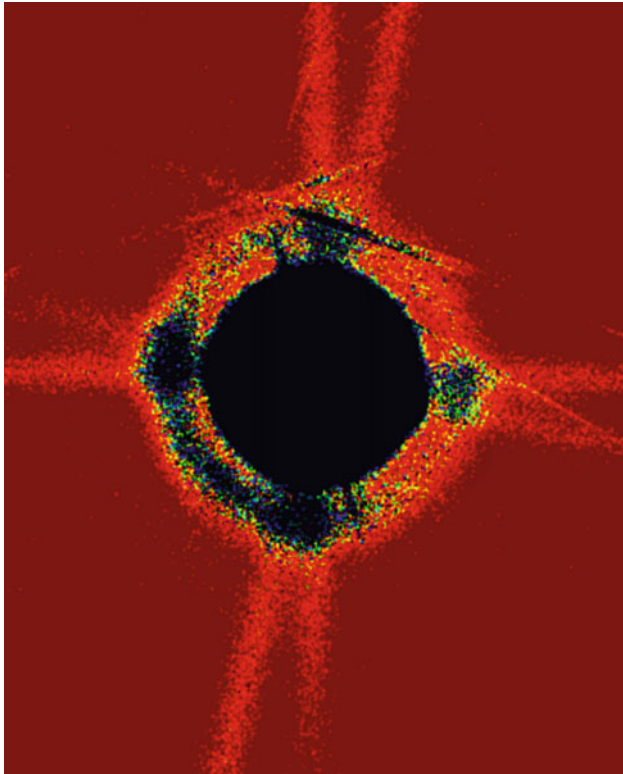
This work is subject to copyright. All rights are reserved by the Publisher, whether the whole or part of the material is concerned, specifically the rights of translation, reprinting, reuse of illustrations, recitation, broadcasting, reproduction on microfilms or in any other physical way, and transmission or information storage and retrieval, electronic adaptation, computer software, or by similar or dissimilar methodology now known or hereafter developed.

The use of general descriptive names, registered names, trademarks, service marks, etc. in this publication does not imply, even in the absence of a specific statement, that such names are exempt from the relevant protective laws and regulations and therefore free for general use.

The publisher, the authors, and the editors are safe to assume that the advice and information in this book are believed to be true and accurate at the date of publication. Neither the publisher nor the authors or the editors give a warranty, express or implied, with respect to the material contained herein or for any errors or omissions that may have been made. The publisher remains neutral with regard to jurisdictional claims in published maps and institutional affiliations.

Printed on acid-free paper

This Springer imprint is published by the registered company Springer Nature Switzerland AG
The registered company address is: Gewerbestrasse 11, 6330 Cham, Switzerland



Scattering pattern of ion tracks in apatite within a diamond anvil high-pressure cell, imaged with small-angle X-ray scattering

To my parents

Supervisor's Foreword

The interaction of high-energetic heavy particles such as ions or molecules with solids has many applications in a variety of different areas, including geology, nuclear physics, nanotechnology, and medical science. Such particles occur naturally as cosmic radiation or from the decay of radioactive elements such as uranium and thorium. With the advent of large particle accelerators around 1980, high-energy particles were accessible to laboratories and utilised for the fabrication of new nanostructures, the study of radiation resistance of materials and treating tumours by hadron therapy, among others. An early application of the modification resulting from high-energy particle–solid interactions is their use in geo- and thermochronology. Natural impurities of uranium that occur in minerals undergo fission related to well-understood decay laws. The high-energy fission fragments released during that process create long damage tracks, so-called *fission tracks* in the mineral that are highly susceptible to chemical etching. The number and size distribution of etched tracks can be related to the age and thermal history of the mineral, the latter resulting from shrinkage of the track damage when exposed to elevated temperatures. Etched fission tracks are used for determining the age and thermal history of Earth's crust and taken together with other techniques, to infer rates of tectonic uplift and landscape evolution. The technique utilises empirical models that are calibrated against standard minerals from areas with well-known geological history. The etching, however, erases the damage structure such that information on the actual radiation damage in the crystal is lost. Little is known about the primary, latent damage track, and how its morphology depends on geological parameters such as pressure, temperature, and mineral composition. It is this missing information that is required in order to fully interpret and explain the details of fission-track dating and interpretation of etched track distributions. The quantitative analysis of un-etched track distributions with the required precision, however, is very challenging due to the small size and high aspect ratio of the damaged regions and technical challenges of monitoring tracks in high-temperature and high-pressure environments.

In his Ph.D. work, Daniel Schauries addressed this problem by using synchrotron-based small-angle scattering to study the morphology of ion tracks in minerals and how the formation and annealing depend on important geological parameters such as temperature, pressure, and crystal orientation. This included the implementation of innovative in situ measurements under high-pressure and high-temperature conditions that ultimately lead to resolving open controversies in the relevant literature. His studies are not only important for fission-track geo- and thermochronology but significantly contribute to a better understanding of the process of ion track formation which is extremely complex and despite its discovery more than 50 years ago still far from being fully understood. Liaising with world leaders in molecular dynamics simulation of radiation effects in materials, he has made a seminal contribution to the field with his work. The implementation of the novel analytical in situ techniques opens up new opportunities for studying materials under extreme conditions that are useful far beyond the topic of his investigations. Daniel's thesis gives a thorough introduction into the field of ion track physics with a focus on geological applications and describes in detail the small-angle scattering technique. I trust it will be interesting for scientists from many areas with an interest in radiation effects and useful for researchers using the small-angle scattering technique. I am delighted that Springer is publishing this outstanding thesis.

Canberra, Australia
June, 2018

Patrick Kluth

Abstract

Interaction between high-energetic particles and matter typically leads to structural damage of the irradiated material. Swift heavy ions predominantly interact with a solid by exciting its electrons. The energy transfer from the electrons to the atoms can lead to the formation of so-called ion tracks. These represent damage regions of cylindrical shape, which surround the entire length of the ion trajectory with a radial size of several nanometres. In materials science, ion tracks are utilised for a wide range of applications, from the detection of radiation to the fabrication of nano-pore filters or nano-electronic devices.

In geology, similar tracks occur naturally in minerals from the spontaneous fission of radioactive impurities. These fission tracks can partially anneal and shrink in length when exposed to elevated temperatures. In this way, the thermal history of a rock can be determined. Fission tracks within rocks from thousands of metres below the Earth's surface have inevitably experienced high pressures of several thousand atmospheres. However, pressure is generally not taken into account when investigating fission tracks.

The present work shows a detailed investigation of ion tracks in apatite and quartz, specifically a characterisation of their structure, formation, and thermal stability under ambient and high-pressure conditions. All tracks were created under controlled conditions by irradiation with ions of energies between 100 MeV and 37.2 GeV in Canberra, Australia, and Darmstadt, Germany. The tracks were subsequently characterised at the Australian Synchrotron in Melbourne through small-angle X-ray scattering (SAXS).

Combining the ability to create tracks under well-controlled conditions with SAXS characterisation, track formation in high-pressure and high-temperature environments was studied. The size of the track radii showed a positive correlation with temperature and pressure. In situ SAXS was used to monitor the size of the ion tracks during thermal annealing. For tracks in quartz, an anisotropic annealing behaviour was found, depending on the direction of the tracks within the crystal lattice. To study thermal track annealing at high pressures, apatite samples were annealed in heatable diamond anvil cells. An increase in annealing rate was demonstrated and attributed to the high-pressure environment.

The effects of pressure on track annealing were demonstrated to be negligible when extrapolated to geological values. Thus, the present results confirm the validity of current fission-track annealing models. Moreover, the present findings contribute to the field of radiation materials under extreme conditions and the theoretical modelling of such effects.

Preface

First, I would like to take this opportunity to thank my Ph.D. supervisor Patrick Kluth for his enormous support over the last four years and the large amount of freedom I have received under his supervision.

Further gratitude goes to the late Mark Ridgway, James Sullivan, Andrew Barry, and Matias Rodriguez for serving on my panel of advisors and Maik Lang for generously hosting me as a visiting researcher at the University of Tennessee for the summer of 2014.

I would also like to thank Helen and Bob Crompton for the generous support through their travel grant and all other funding sources that have allowed me to travel more than 160,000 miles during the course of my Ph.D. as well as Department Administrator Julie Arnold for managing all these flight bookings and travel reimbursements.

This Ph.D. thesis was conducted in close collaboration with several other research groups from three different continents; I would like to thank:

- The team around Christina Trautmann at GSI in Germany, in particular Daniel Severin and Markus Bender for performing the ion irradiations with high energies.
- The research group of Kai Nordlund at the University of Helsinki in Finland, in particular Flyura Djurabekova, Aleksii Leino, and Olli Pakarinen for their molecular dynamics simulations.
- The research group around Rod Ewing at Stanford University in Palo Alto and University of Michigan in Ann Arbor, which includes Maik Lang, Weixing Li, Fujian Zhang, Cameron Tracy, Sulgi Park, and Raul Palomares for their TEM measurements and help with the DACs.
- The staff at the SAXS/WAXS beamline at the Australian Synchrotron in Melbourne, including Nigel Kirby, Adrian Hawley, and Stephen Mudie for all their assistance during the days and nights of our SAXS measurements.

Similar thanks go to my colleagues Boshra Afra, Pablo Ernesto Mota-Santiago, Thomas Bierschenk, Allina Nadzri, and Andrea Hadley. For proofreading, I would like to thank Patrick, Andrea, and Jonathan Fu. Finally, I would address a special “Dankeschön” to my family, Roland and Magdalena Schauries, for their limitless support.

Canberra, Australia
2018

Daniel Schauries

Contents

1 Introduction	1
1.1 Motivation for This Work	4
1.2 Fission Tracks in Apatite	5
1.2.1 Apatite Minerals	6
1.2.2 Fission Track Analysis	7
1.2.3 Lab-Based Fission Track Annealing	11
1.3 Ion Tracks in Quartz	13
1.3.1 Natural and Synthetic Quartz	13
1.3.2 Applications of Ion Tracks in Quartz	14
References	16
2 Physical Background of Ion Tracks	21
2.1 Interaction of Ions with Matter	21
2.2 Formation of Ion Tracks	23
2.2.1 Ion Track Morphology in Crystals	23
2.2.2 Ion Tracks in Other Materials	25
2.2.3 Modelling of Ion Tracks	26
References	29
3 X-Ray Characterisation Techniques	33
3.1 Interaction of X-Rays with Matter	34
3.1.1 X-Ray Absorption	34
3.1.2 X-Ray Scattering Processes	35
3.2 X-Ray Diffraction (XRD)	36
3.3 Small Angle X-Ray Scattering (SAXS)	37
3.3.1 Scattering Patterns of Cylindrical Objects	41
3.3.2 Intersection Between the Ewald Sphere and Ion Tracks	45
3.3.3 Experimental SAXS Detector Images	46
References	51

4	Experimental Methods	53
4.1	Sample Preparation Techniques	54
4.2	High-Pressure Diamond Anvil Cells	55
4.3	Swift Heavy Ion Irradiation	60
4.3.1	ANU Heavy Ion Accelerator Facility	60
4.3.2	GSI UNILAC	62
4.3.3	GSI SIS 18	63
4.4	Synchrotron-Based Small Angle X-Ray Scattering	65
4.4.1	The Australian Synchrotron	65
4.4.2	The SAXS/WAXS Beamline	68
4.5	Neutron Sources	74
4.5.1	Open Pool Australian Lightwater (OPAL) at ANSTO	74
4.5.2	Spallation Neutron Source (SNS) at ORNL	75
	References	77
5	Ion Track Formation Under Ambient Conditions	79
5.1	Track Characterisation with SAXS and SANS	79
5.2	Effects of Ion Irradiation Parameters on Tracks	83
5.2.1	Ion Fluence Effects	83
5.2.2	Ion Energy and Energy Loss	85
5.3	Effects of the Crystallographic Direction on Tracks	86
5.3.1	Quartz	87
5.3.2	Apatite	88
5.4	The Shape of Ion Tracks in Apatite	89
5.5	The Cross-Section of Ion Tracks in Quartz	92
5.6	Summary	94
	References	94
6	Track Formation Under Temperature and Pressure	97
6.1	Temperature-Dependence of Ion Track Formation	97
6.1.1	Apatite	98
6.1.2	Quartz	101
6.1.3	Simulations and Discussion	101
6.2	Ion Irradiation Under Pressure	104
6.2.1	Track Formation in Quartz Within Diamond Anvil Cells	105
6.2.2	Thermal Spike Calculations for Elevated Pressure	109
6.2.3	Molecular Dynamics Simulations	111
6.3	Summary	111
	References	112

7 Thermal Annealing of Ion Tracks	115
7.1 Ion Tracks in Quartz	117
7.1.1 Isochronal Annealing	117
7.1.2 Isothermal Annealing	123
7.2 Ion Tracks in Apatite and the Effects of Pressure	127
7.2.1 Isothermal Annealing Under Ambient Pressure	128
7.2.2 Thermal Stability of Ion Tracks Formed at Elevated Temperatures	133
7.2.3 Effect of Pressure on Non-irradiated Apatite and Pre-existing Tracks	134
7.2.4 In situ Annealing Using Diamond Anvil Cells	136
7.2.5 Discussion and Extrapolation to Geologically Relevant Pressures	140
7.3 Summary	142
References	143
8 Summary and Outlook	147
8.1 Future Directions	148
8.1.1 Effects of Pressure on the Recrystallisation of Tracks	148
8.1.2 Generalisation of the Effects of Pressure During Track Formation	149
8.1.3 Small Angle Neutron Scattering	149
8.1.4 SAXS Modelling of Tracks with Non-uniform Depth Profiles	150
8.1.5 Simulations of Track Recrystallisation	150
Curriculum Vitae	151

Chapter 1

Introduction



In the late 1950s, Young reported the discovery of continuous damage tracks in the insulator lithium fluoride (LiF) [1]. The origin of these tracks was correctly attributed to damage produced by naturally occurring nuclear fission fragments from the decay of radioactive impurities. Consequently, they are referred to as fission tracks in modern literature.¹ They occur as a result of spontaneous fission, where radioactive isotopes such as ^{238}U break into two lighter nuclei, releasing a combined kinetic energy of around a 170 MeV [4]. This energy dissipates into the crystal lattice as the fission fragments penetrate through the crystalline material, leaving the observed trail of damage behind. The track typically resembles a cylindrical damage region a few nanometres in diameter. It is often of amorphous character within a crystalline host matrix. The large amount of energy results in these tracks reaching relatively long lengths, with fission tracks typically reaching lengths of approximately 15 μm . Although initially discovered as a result of spontaneous nuclear fission, similar tracks can be produced by exposing the material to an external radiation source [5].

Young [1], Price and Walker [2], and Fleischer [6] have pioneered the visualisation of fission tracks through chemical etching. The damage shows a higher susceptibility when exposed to an acid or base than the undamaged material such that the initial damage structure is quickly removed. As a result, the track becomes hollow and exhibits a significantly larger surface area. Along this surface the etchant greatly increases the diameter, enlarging the track width from nanometres to micrometres. This allows an easier and faster characterisation of their length as they can already be imaged with optical microscopes techniques [1, 2, 4]. Figure 1.1 (shows an example of) such optically imaged etched tracks in apatite. The drawback of the chemical treatment is the removal of the underlying damage structure. The study of the track structure is thus limited to empirical interpretation of the etch pits which depends critically on the etching process. Nevertheless, for thermochronology—the investigation of the thermal history of the mineral and its surrounding environment—track etching is the current standard technique to study the number and length distributions.

¹Historically ion tracks were called “charged particle tracks” [2, 3].

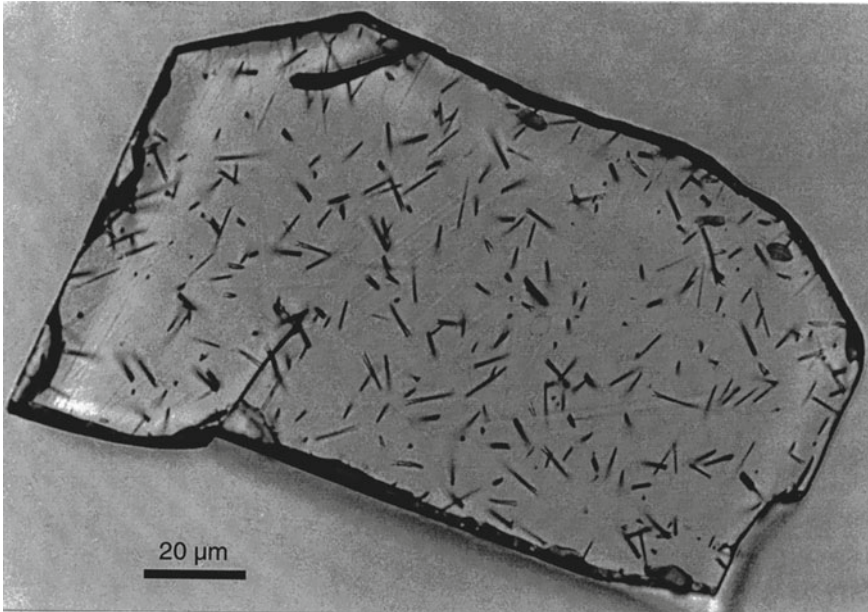


Fig. 1.1 Natural etched fission tracks in an apatite grain, imaged by optical microscopy. The tracks appear as dark, high-contrast features and show their characteristic appearance as randomly oriented, straight-line etch channels. [Image Courtesy: A. Gleadow [7]]

The mineral apatite commonly contains impurities of U and Th of sufficiently high density, allowing to correlate the amount of fission tracks with the length of the period of radioactive decays. This information can be used for the purpose of dating the mineral, by determining the concentration of the impurity and number of the tracks. One issue, however, is that this method requires the tracks to be stable over long periods of time. It has been shown that the exposure to elevated temperatures leads to shrinking of the track sizes by recrystallisation of the amorphous region until the track damage vanishes entirely. Therefore, dating through fission tracks typically shows ages that are underestimated [4, 8]. This reduced fission track age and the track shrinkage, however, can be used to understand the thermal history of the rock and its originating region [8]. To obtain this information, the distribution of etched track lengths is investigated. It can even be used to distinguish multiple heating events, as long as the temperature of each heating event has been below the temperature for track recrystallisation over geological time scales (closure temperature). The thermal history is well suited to investigate tectonic movements and climate-driven surface interactions occurring within the top few kilometres (<5 km) of the Earth's crust. These are critical to understand landscape evolution, climate, and the deposition of natural resources [8]. In particular for the exploration of petroleum deposits, fission track thermochronology allows a direct estimate of the cooling time of a section to understand the timing of oil generation [9].

Temperature has been early on identified as the primary parameter for the shrinkage of fission track lengths [4, 10]. The rate of shrinkage can be influenced by mineral composition [11] and track orientation with respect to crystalline axis [12, 13]. The temperature during track formation is currently not considered to have a measurable influence on their size, structure or annealing behaviour. The external pressure has also been subject to a small number of investigations, historically attributing no measurable influence on track annealing [10, 14, 15]. Recently, however, some investigations have claimed a noticeable influence of pressure on track shrinkage, with reports of a reduced rate of track annealing [16], and conversely, an increased rate [17]. These findings have led to a controversial discussion about the neglect of pressure in previous studies [18, 19].

These tracks are not just relevant for geological studies. Another early motivation for their investigation was the degradation of materials in nuclear environments from radiation [20]. The emergence of ion accelerators has allowed to create so-called ion tracks by irradiating a wide range of materials with swift heavy ions with energies in the range of MeV to GeV. This has led to a focus on other types of target materials, with ion tracks in organic polymers showing numerous commercial applications. Upon chemical etching, tracks in polymers leave nano-sized hollow cylinders behind that can stretch throughout the entire thickness of the polymer. These channels can be used for nano-sized membranes and filters or as a template for the fabrication of nanowire networks [21]. Additional applications of un-etched tracks use their reduced density to fabricate ion-selective membranes [22, 23]. In dielectric materials, the changes in density and optical properties from ion tracks are used to produce optical waveguides [24]. In addition to insulators, ion track formation has also been studied in amorphous semiconductors [25, 26] and in some metals [27, 28].

Microscopy is the most common tool to study small objects. It magnifies them in real-space, allowing a characterisation of shapes and sizes based only on a few specimens. The current fission track analysis methodologies use chemically-etched tracks that can be visualised with an optical microscope. This technique however, is limited by the wavelength of visible light and only allows us to study structures down to $\sim 30 \mu\text{m}$, which is more than three magnitudes above the size of unetched tracks. Electrons, on the other hand, can resolve structures of sub-nanometre dimensions. This makes transmission electron microscopy (TEM) a suitable technique for the purpose of systematically studying unetched fission tracks. The downsides of transmission electron microscopy are the laborious sample preparation and the electron annealing of tracks, as well as the limited viewing area and the related difficulties in imaging tracks along the entire length [5, 29]. An additional issue is the limitation of the sample environment when using TEM, as in situ characterisation in the presence of high and low temperatures and elevated pressures is very limited.

Small angle X-ray scattering (SAXS) is well suited to characterise nano-sized objects. SAXS averages over its beam spot size with a diameter of hundreds of micrometres, which typically contains over millions of tracks. When generated by an ion accelerator the tracks comprise almost identical, well aligned objects. Thus the measurement of a large number of tracks can be interpreted as the individual track

structure, averaging out fluctuations on an atomic scale. Since the first measurements of SAXS on ion tracks were carried out in the mineral mica in 1970 [30] and 1977 [31], the arrival of powerful X-ray sources has allowed to measure ion tracks with unprecedented precision. In particular, synchrotron-based SAXS has been used as a technique to characterise the track radius with uncertainties of less than a tenth of a nanometre [26, 32, 33]. It also allows estimating the relative density of the tracks, even when differing less than 1% from the undamaged material [34]. SAXS is well suited for in situ characterisation, using sample environments capable of generating elevated temperatures during measurement. Even high pressure during the characterisation can be achieved by using (heatable) diamond anvil cells with X-ray transparent diamonds.

1.1 Motivation for This Work

The principal questions in the present work address the formation and stability of tracks in high pressure and high temperature environments. It also investigates the influence of the track orientation in a crystalline material on the track size and annealing behaviour. The research on the effects of temperature on tracks during formation was fuelled by the current lack of clear experimental and theoretical evidence for temperature-related influences. The simultaneous exposure of ion tracks in apatite to pressure and temperature was triggered by the current discussion about the effects of pressure on track recrystallisation in the context of fission track thermochronology [16–19] and to expand the knowledge about the fundamental processes which occur when pressure is applied to ion tracks during and after their formation. This is of great interest to test the validity of current models used to describe track formation, as well as for applications of radiation processing in extreme environments.

The ion tracks discussed within this work were of comparable structure and diameter as fission tracks. To produce these tracks under controlled conditions, apatite and quartz crystals were subjected to ion irradiation at a range of different ion accelerators. In particular, the accelerators at GSI in Darmstadt, Germany allow an investigation in a large range of parameters such as high and low temperatures and extreme pressure environments.

The primary characterisation technique in this work was SAXS, due to its high precision of measuring potentially small effects and its ability to study ion tracks in situ, monitoring the track size during thermal annealing. In particular, it allows in situ measurements during the simultaneous exposure of ion tracks to high pressure and elevated temperatures. As SAXS allows a non-intrusive characterisation and does not require any prior modification of the tracks, the technique assesses the primary track damage without chemical etching.

This thesis is structured as follows:

In the remainder of **Chapter 1** the basics of fission track thermochronology on apatite and application of ion tracks in quartz are discussed.

Chapter 2 describes the physical fundamentals of ion irradiation and ion tracks and common models to explain track formation.

Chapter 3 describes X-ray diffraction and scattering techniques, in particular the theoretical background on the characterisation of ion tracks with SAXS.

Chapter 4 describes the experimental set-up, including the use of diamond anvil cells for high pressure experiments, ion irradiation on different ion accelerators, and the SAXS/WAXS beamline at the Australian Synchrotron.

Chapter 5 discusses general relationships between ion tracks and the formation condition, i.e. crystalline orientation, different ion types, energies, and fluences as well as longitudinal and radial shape of ion tracks.

Chapter 6 discusses results on the influence of external parameters during the formation of ion tracks, primarily elevated temperatures and pressures. These measurements are compared with theoretical simulations.

Chapter 7 discusses results on the recrystallisation of ion tracks as a result of thermal annealing. The effects of temperature are shown under ambient pressures, as well as under high pressures to mimic geological conditions.

Finally, **Chapter 8** quickly summarises all results and goes an outlook onto future research directions.

1.2 Fission Tracks in Apatite

Fission tracks are formed by the energy loss from high energetic fission fragments, that result from the spontaneous decay of naturally occurring radioactive impurities. For the heavy ^{238}U nuclide for example, the nuclear decay split the isotope into two fragments that possess a combined energy of around 170 MeV, shared approximately equally between both nuclei [4]. This energy is sufficiently high for the fission fragments to penetrate through the crystalline structure of their host material, deposit their energy to the host material's electrons and, subsequently, form so-called fission tracks along their trajectories. The resulting tracks are approximately 16 μm long, while their track radius is typically only around 5 nm [4, 11]. Figure 1.2 shows an TEM image of ion tracks in apatite in their latent (un-etched) state. Due to their large aspect ratio, only a short section is visible.

Apatite has evolved into one of the most commonly used materials for the investigation of fission tracks to assess the thermal history of rocks. This is a consequence of its common occurrence, as well as its high sensitivity to thermal annealing and with partial annealing within a temperature range between 80 and 110 $^{\circ}\text{C}$. It therefore provides a powerful tool to reconstruct the low temperature thermochronology associated with depth levels relevant for continental drift and oil exploration (i.e. <5 km) [4, 8].

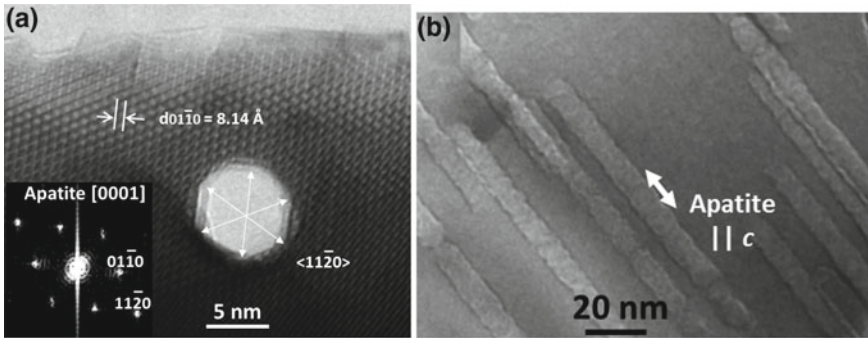


Fig. 1.2 TEM image of latent ion tracks along their cross-section (a) and along a short section of their length (b) The tracks were created by irradiation with swift heavy ions. [Image Courtesy: W. Li [35]]

1.2.1 Apatite Minerals

The mineral apatite, stoichiometric formula $\text{Ca}_{10}(\text{PO}_4)_6\text{A}_2$, is commonly found in a wide range of different rocks. It typically occurs with grain sizes between 75 and 170 μm [36], but also exists in the form of large single crystals, several millimetres to centimetres in size, as used in the present work. The symbol **A** typically represents a combination of halide- and/or hydroxy- ions, mainly, but not limited to F^- , Cl^- and OH^- . Their ratio to each other differs depending on the geographic origin and type of rock it originates from. Apatite is commonly found in igneous rocks (i.e. F-apatite), but also in sedimentary rocks as carbonate (CO_3^{2-}) apatite. Samples of apatite from the Cerro de Mercado mine in Durango, Mexico were used for the majority of the present work. The value of **A** for apatite minerals from this region is dominated by a high F concentration with 4.7 wt% F and negligible Cl concentration, giving the crystal a distinct yellow colour. Durango F-apatite has emerged as a reference standard for applications of ion tracks in fission track dating due to its composition and well-known history [37]. An additional sample investigated in this work was from Dashkesan (Azerbaijan) with a concentration of 3.5 wt% F and 0.5 wt% Cl.

Apatite crystallises in a hexagonal dipyramidal structure (P6/m) at ambient temperature [39], although apatite with significant amounts of hydroxyl or chlorine ions can also exhibit a monoclinic structure, as a result of the disorder of OH^- and Cl^- ions along the *c*-axis [38, 40]. The densities are nearly independent of the exact composition, but the lattice parameters *a* and *c* change slightly with composition. The lattice parameters for the three pure cases are shown in Table 1.1. No change in crystallographic phase occurs [41] for the temperatures employed during the experiments in this work (below 400 °C). Apatite also remains within the same crystallographic phase up to pressures of a least 10 GPa at ambient temperatures (compare experiments in Sect. 7.2.3).

Table 1.1 List of lattice constants (a and c) and other physical properties of different apatite compositions. The lattice constants were compiled by Wu et al. [38]

Composition	Crystallographic structure	a [Å]	c [Å]	Colour	ρ [g/cm ³]
Ca ₅ (PO ₄) ₃ F	Hexagonal	9.363	6.878	Yellow	3.18
Ca ₅ (PO ₄) ₃ Cl	Hexagonal / monoclinic	9.52	6.85	Grey-white	3.17
Ca ₅ (PO ₄) ₃ OH	Hexagonal / monoclinic	9.417	6.875	White	3.16

1.2.2 Fission Track Analysis

Fission Track Age Dating

The most commonly employed technique to obtain fission track ages is the external detector method [42]. This first requires extraction of the apatite grains from the rock. They are then polished to prepare them for chemical etching, where the fission tracks are exposed to concentrated nitric acid (HNO₃) for a short duration (approximately 20 s at 20 °C). This dissolves their primary damage structure and enlarges the tracks significantly, such that they can be visualised and counted using an optical microscope to calculate the spontaneous fission track density ρ_S .

The fission track density then needs to be normalised to the amount of ²³⁸U that was initially present. The most commonly employed method to determine this value is thermal ionisation mass spectroscopy (TIMS). Instead of measuring the amount of ²³⁸U directly, it determines the concentration of ²³⁵U, as this isotope rarely undergoes spontaneous fission. By using the ratio between these two isotopes [43] of $\eta = 137.9$, the initial content of ²³⁸U can be estimated. For this purpose, the sample is irradiated with neutrons from a nuclear reactor to induce the fission process (compare Sect. 4.5.1). In order to register the induced fission decay events, a thin layer of mica is placed onto the polished surface of the apatite crystal. In the same manner as for the apatite crystal, chemical etching and optical microscopy is used to determine the density ρ_i of induced fission tracks. The fission track age can then be calculated by substituting the neutron fluence F , cross-section σ as well as λ_α and λ_f as the decay constant of the α -decay² and spontaneous fission, respectively:

$$\text{FT age} = \lambda_\alpha^{-1} \ln \left(1 + \frac{\lambda_\alpha F \sigma}{\lambda_f \eta} \frac{2\rho_S}{\rho_i} \zeta \right) \quad (1.1)$$

The procedure factor ζ is a dimensionless parameter, specific to each individual analyst, taking a range of aspects such as etching characteristics into account. The

²This term is critical to distinguish between the amount of ²³⁸U that has disintegrated from fission-induced decay and the — much more likely occurring — α -decay.

factor of 2 takes the different geometries of track etching between the apatite sample (internal surface) and mica detector (external surface) into account [4].

Alternative methods have been discussed to simplify the measurements of the isotope concentration, i.e. laser ablation mass spectrometry [44], or more recently, the use of secondary ion mass spectrometry (SIMS) [45, 46]. These methods do not require access to a large-scale neutron source and are therefore more suited for a commercial application.

In principle, the number of fission tracks, together with the amount of radioactive impurities, can also be used for regular dating purposes. The typically low density of tracks and the resulting large uncertainties, however, make this method less favourable to other dating techniques [4] and its key advantage is clearly in thermochronology.

Fission Track Analysis for Thermochronology

As all tracks result from decay events of similar energy (170 MeV), their lengths are nearly identical upon formation. Once exposed to elevated temperatures above approximately 80°C over timescales in excess of several million years, the tracks start to partially anneal and recrystallise, resulting in a shortening of their length.³ The so-called closure temperature T_C is defined as the minimum temperature a geochronological system has experienced such that no measurable amount of fission tracks can be visualised anymore [47]. For apatite, this temperature is typically between 110 and 150°C, as all fission tracks would have fully annealed above T_C over geological timescales. Consequently, when a sample containing fission tracks is exposed to T_C , this leads to a reset of the fission track clock. Therefore the obtained fission track “age” is not identical to the actual age of the material. Rather, it represents the period of elapsed time since the last cooling event where temperatures stayed below T_C . In thermochronology, these cooling ages are dated. Using fission tracks, the amount of tracks within the crystal can be attributed to the most recent point in time where the rock was exposed to temperatures above its T_C value.

The thermal history of apatite can also be determined by studying the distribution of the shortened track lengths as a result of thermal annealing. The shortening of tracks occurs when the rock has been exposed to temperatures below T_C , but sufficiently large to partially anneal them. This temperature region is called partial annealing zone (PAZ) and ranges between 80 and 110°C for F-apatite. Instead of just obtaining a single fission track age, the length distribution gives an account of several periods of cooling and heating. Figure 1.3 shows histograms for the five main types of typical etched fission track length distributions [48–50]:

- (a) Tracks form a narrow, symmetrical distribution around 16 μm, the typical track length for the kinetic energy of the uranium decay (e.g. freshly induced tracks).
- (b) Tracks were rapidly cooled down and have not experienced any reheating since. The brief exposure to elevated temperatures during the cooling process resulting in limited amount of tracks to shorten (e.g. undisturbed volcanic-type).

³Thermal annealing also leads to shrinkage of the track radius, but as fission track analysis typically focuses on the track length, this has not been widely studied for naturally occurring fission tracks.

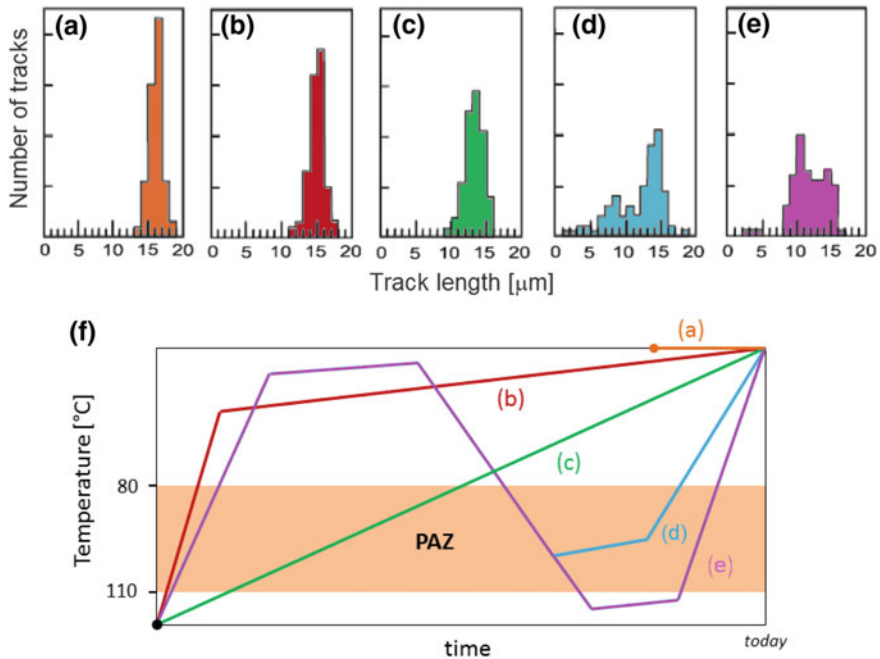


Fig. 1.3 A comparison of fission track length distributions in apatite for different geological events: **a** freshly induced tracks, **b** volcanic origin without disturbance, **c** basement type without disturbance, **d** bimodal distribution with disturbance, and **e** mixed distribution as a result of reheating. **f** Schematic temperature-time curves for the different fission track length distributions with different histories throughout the partial annealing zone (PAZ). [after Gleadow et al. [48]]

- (c) A distribution resulting from a cooling process without reheating. As the cooling process, however, has occurred over a significantly longer timescale, a larger shift to shorter track lengths is observed (e.g. undisturbed basement-type)
- (d) A bimodal distribution also underwent another reheating process, leading to a shortening of all tracks predating this event (left peak) and a distinct distribution of more recently formed tracks (right peak). This shape is only observed if the reheating event did not exceed the materials closure temperature T_C .
- (e) A mixed track distribution occurs when the rock has been reheated post T_C after its cooling process. The distribution is characterised by a very broad peak.

Alternative Methods for Thermochronology

The thermal history can also be studied on etched fission tracks by using the etch pit areal density at an artificially polished internal surface [4]. However, as the present work focuses entirely on non-etched tracks, only track shrinkage is discussed.

A method that uses nuclear isotopes to estimate the thermal history without studying fission tracks is called (U-Th-Sm)/He thermochronology. Instead of using the effects of the energy release from radioactive decays, this methods uses the amount of ^4He gas atoms trapped within isolated bubbles in crack-free apatite grains. These

gas atoms occur as the decay products of the α -decay of either $^{238}\text{U}/^{235}\text{U}$, ^{232}Th , ^{147}Sm , or their α -emitting daughter isotopes. As the amount of radioactive isotopes can be measured accurately, the amount of He trapped within the mineral should normally relate to the age of the rock. The amounts typically discovered, however, are lower than one would expect, resulting in ages that are too young. The reason for this discrepancy can be found in a loss of helium gas over time, preventing this technique to be used for accurate dating. Similar to fission track dating, the concentration in helium can be utilised to estimate the thermal history of the apatite crystal and the whole rock, as the volume diffusion of helium out of the mineral is temperature-dependent [51]. In direct comparison to fission track analysis, the (U-Th-Sm)/He technique is more sensitive to lower temperatures with a partial retention zone starting at 40°C and a closure temperature around $70 \pm 7^\circ\text{C}$ [8].

To-date, apatite fission track analysis and apatite (U-Th-Sm)/He analysis, are among the most used thermochronology methods due to their high sensitivity to low temperatures between 40 and 130°C over geological timescales around 10–100 million years (Ma) [48, 52, 53]. This makes them ideal to investigate geological events taking place within a few kilometres depth within the Earth's crust such as tectonic drift and uplift rates. These processes govern the formation of natural resources and are therefore of particular interest for commercial applications, e.g. evaluating conditions necessary for oil formation [8].

Influence of Apatite Composition and Crystallographic Direction

The influence of the exact type and composition of apatite has been extensively studied in the context of fission track annealing. Gleadow and Duddy and Green et al. have shown that depending on the ratio of the halide concentration (F : OH : Cl), the annealing rate can differ significantly when exposed to similar temperature conditions [11, 42, 54]. Their investigation of samples from different locations shows that F-rich apatite (e.g. from Durango, Mexico) starts to anneal around 80°C and the tracks are completely annealed on geological timescales at temperatures exceeding 110°C. In contrast, for chlorine-rich apatites the partial annealing zone does not start until 110°C and they do not fully anneal until exposed to a significantly higher temperature of approximately 150°C [40]. This demonstrates the importance of using a mineral of standard composition such as Durango apatite for principal studies of fission track annealing [37].

Another influential factor for ion track annealing in apatite is the direction of the fission track with respect to the crystal axes. It has been widely established that track annealing leads to a slower length reduction for tracks aligned in direction of the *c*-axis, compared to those under large angles or perpendicular [11–13, 55–57]. In this work, all apatite samples used for thermal annealing were cut such that the surface normal was either parallel or perpendicular to the *c*-axis. This allows a better comparison of experiments at different temperatures and pressures with each other.

To study thermochronology for higher closure temperatures, fission tracks can also be analysed in zircon (ZrSiO_4) and sphene (CaTiSiO_5). In these two minerals, fission tracks possess closure temperatures around 230–300°C and $\sim 300^\circ\text{C}$, respectively [4].

1.2.3 Lab-Based Fission Track Annealing

When interpreting the thermal history from a length distribution of fission tracks in a natural sample, an algorithm is required that models the length distribution to each temperature event (e.g. HeFTy [58]). Such an algorithm requires an accurate database with fission track data from areas of well-known thermal history as well as complementary results from lab-based annealing experiments extrapolated to geological timescales [11, 52, 57, 59–61].

In order to assess the effects of the temperature T over long periods of time, annealing experiments are performed on short timescale in the laboratory under controlled conditions, with detailed knowledge of annealing time, temperature, and orientation of the tracks within the crystal [8, 53, 54, 60–62]. The annealing is carried out at higher temperatures than T_c to accelerate the annealing and the findings are subsequently extrapolated to geological temperatures and times. Artificial fission tracks can be introduced by a variety of external methods, such as induced fission of natural uranium or bombardment with swift heavy ions. It is important to use *freshly* induced ion tracks without a history of pre-annealing. Only this ensures that all tracks of similar sizes can be compared with natural tracks that have annealed for a range of different periods of time [18].

Figure 1.4a shows annealing curves where tracks were annealed between 20 min and 30 days, at a variety of temperatures until they fully disappeared. The tracks were chemically etched and subsequently characterised by optical microscopy [54]. One can observe only small track shrinkage at low temperatures, although it requires 30 days for the tracks to fully disappear at 275 °C. At higher temperatures track length decreases rapidly and at 400 °C, an annealing duration of just 20 min is sufficient for all observable tracks to vanish.

The physical origin for the fading of tracks is typically attributed to the diffusion of displaced atoms back to their lattice position within the crystalline structure. Therefore the temperature dependence of annealing is characterised by a Boltzmann distribution of the diffusion rate $D(T)$:

$$D(T) = D_0 \exp\left(-\frac{E_a}{k_B T}\right) \quad (1.2)$$

with k_B as the Boltzmann constant and D_0 as the pre-exponential constant as described by Fick's first law of diffusion. The activation energy E_a can be considered as the energy barrier to overcome to trigger the track recrystallisation.

To model the annealing behaviour of tracks, a suitable characterisation parameter $r(t, T)$ is chosen. This can be the track length, or another property such as track radius, number density or combination thereof. A transform function $g(r)$ is defined as $g(r) = \ln(1 - r/r_0)$ with $r(t, T)/r_0$ as the normalised characterisation parameter with respect to its initial (pre-annealing) value. The simplest model to extrapolate and interpolate the exponential dependence on the inverse temperature, the parallel Arrhenius model, uses the exponential dependence from Eq. (1.2). The corresponding

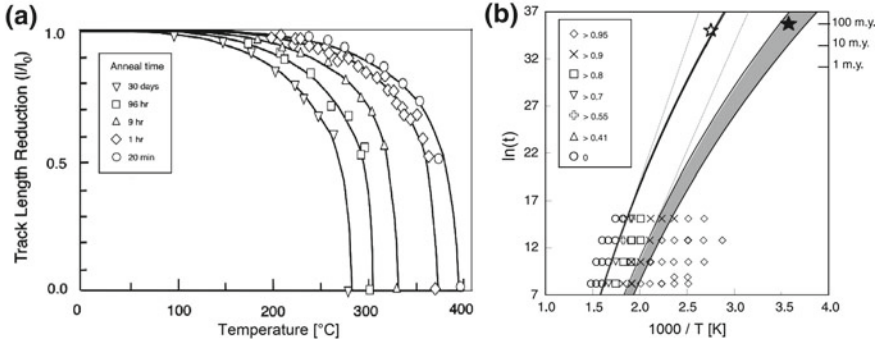


Fig. 1.4 **a** Normalised track lengths from lab-based thermal annealing experiments. The values were obtained from chemically etched tracks (after data from Green et al. [54], fanning model fits by Laslett et al. [59]). **b** Arrhenius diagram showing two models—fanning Arrhenius (dashed) and fanning curvilinear (solid lines)—for the extrapolation of such data to geological timescales of high temperature (open star) and ambient temperature (solid star) events (after Ketcham et al. [61])

$g(r)$ function is [63]:

$$g(r) = C_0 + C_1 \left[\frac{1}{T} \right] + C_2 \cdot \ln(t) \quad (1.3)$$

with the constants C_0 (offset), C_1 (slope) and C_2 . The application of this model to fission track annealing data from laboratory and geological timescales, has led to a range of non-satisfactory results once annealing times exceed several days [63]. Hence, Laslett et al. suggested the fanning linear Arrhenius model with an additional constant C_3 for a better description of the annealing data [59]:

$$g(r) = C_0 + C_1 \frac{\ln(t) - C_2}{1/T - C_3} \quad (1.4)$$

Figure 1.4b shows a range of annealing times t [in sec] required to observe a relative reduction in the average track lengths. The values are displayed as a function of reciprocal temperature in an Arrhenius diagram. Each point corresponds to the duration that was required at a given temperature to reduce the relative track length to a value of: 0 (circles), >0.41 (triangles up), >0.55 (crosses), >0.7 (triangles down), >0.8 (squares), >0.9 (\times), and >0.95 (diamonds).

The laboratory-based annealing data, where t is below 30 days, can be interpolated using the fanning linear Arrhenius model (dotted lines) from Eq. (1.4). Thus for short timescales the reduction in track lengths follows Eq. (1.3).

The region marked with the open star represents actual measurements on samples from boreholes that correspond to a total disappearance of all fission tracks. The other region, marked with a solid star, corresponds to annealing times of tracks from sea-floor sediments that have not been exposed to elevated temperatures. Despite the

fits showing a good agreement within the timescales of the laboratory experiments, when extrapolated to geological timescales, their lack of agreement is evident.

Therefore, in order to extrapolate lab-results over 9 orders of magnitude, from a few weeks to tens of millions of years, an more appropriate model is required. The improved fanning curvilinear model was suggested [60–62]:

$$g(r) = C_0 + C_1 \frac{\ln(t) - C_2}{\ln(1/T) - C_3} \quad (1.5)$$

Figure 1.4b shows how the fanning curvilinear model (solid lines) connects the borehole measurements significantly better with the lab-based data due to its curvature on long timescales. Hence, this model is routinely used to extrapolate lab-based annealing experiments to geological timescales.

However, for the very short annealing times in the present work (<1 h), the data can be satisfactorily fitted with the simplest of these models, the parallel Arrhenius relation as in Eq. (1.3). For practical purposes, C_1 is the activation energy E_a/k_b and $C_2 = n$, establishing a reciprocal relationship between diffusion coefficient and time $D \sim t^{-n}$ with $n > 0$ as a dimensionless number, depending on the ion type and irradiated material [64]. This leads to the formula used for all interpolations of track annealing data in the present work as further discussed in Chap. 7:

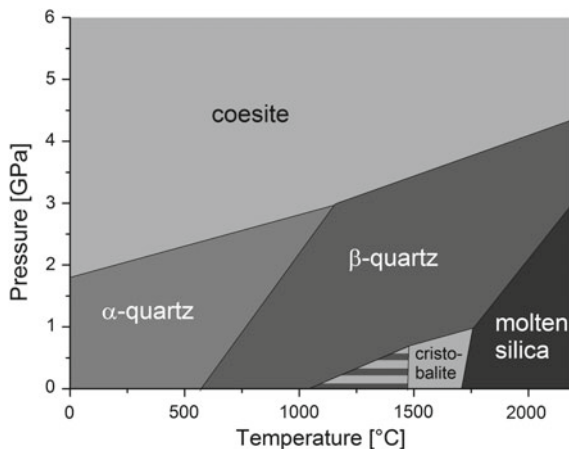
$$\ln(1 - r/r_0) = \text{const.} + E_a \left(\frac{1}{k_b T} \right) + n \ln(t) \quad (1.6)$$

1.3 Ion Tracks in Quartz

1.3.1 Natural and Synthetic Quartz

Quartz is the ambient-pressure polymorph of crystalline silicon dioxide (c – SiO₂). It occurs naturally as single crystals of all sizes and can also easily be synthetically grown as large crystals. As all annealing experiments in this work were carried out with synthetic quartz, a phase diagram of this quartz type is shown in Fig. 1.5 to discuss the high temperature and pressure behaviour of quartz. For temperatures below 573 °C, quartz crystallises in its standard α -quartz structure, while above 573 °C a reversible phase transition to β -quartz occurs. The crystalline structure of α -quartz is trigonal with a density of 2.65 g/cm³. For β -quartz the SiO₄ tetrahedra exhibit a small twist causing the crystal to exhibit hexagonal symmetry. The phase transformation leads to a reduction in density to 2.53 g/cm³. However, it does not break up any chemical bonds and the tetrahedra display no distortion [65]. At 1050 °C synthetic quartz shows another phase transition and turns into β -Cristobalite, although these temperatures were not reached in the present work. Additionally, above 1705 °C quartz starts to melt (all temperatures are stated for 1 bar). The high-pressure modi-

Fig. 1.5 Pressure-temperature phase diagram of synthetic quartz / SiO_2 . The striped area within cristobalite can transform into tridymite between 840°C and 1470°C for natural quartz, while it remains cristobalite for synthetic quartz [diagram drawn with values from Ref. [65]]



fications such as coesite (for pressures above 2–4 GPa) and stishovite (for pressures above 8–10 GPa) can be obtained by exposing α -quartz to the respective pressures for a sufficiently long amount of time. For low-temperatures as for the high pressure experiments in the present work, this process is far too slow to play any role, but once heated above 500°C a metastable transformation⁴ into the high-pressure polymorph commonly occurs within a few hours [66].

Natural quartz has a structure very comparable to that of synthetic quartz. While the former grows naturally over large timescales, synthetic quartz is most commonly grown under high temperature and heat in an autoclave from a smaller seed crystal. In addition, natural quartz typically has a larger amount of impurities that can lead to a larger range of thermodynamic phases, such as a tridymite [67, 68].

1.3.2 Applications of Ion Tracks in Quartz

Crystalline and amorphous SiO_2 show ion track formation when exposed to an external source of swift heavy ions above the track formation threshold of ~ 2 keV/nm [69]. Consequently natural quartz itself would be an ideal candidate for fission track dating due to its abundant presence in a large variety of rocks. However, quartz only has limited applications as a track detector for fission track dating, as the concentration of nuclear isotopes is typically very low ($\ll 0.1 \mu\text{g/g U}$), generating insufficiently low track densities [4]. A notable exception is quartz with U-rich clusters near uranium deposits that can indeed be used for dating purposes. One example are quartz crystals from the Oklo uranium deposit in Gabon with 0.2% U concentration [70]. These

⁴A metastable mineral remains within its high-pressure or high-temperature phase after reaching ambient conditions, creating a temporary equilibrium. Once exposed to a disturbance acting as a catalyst, e.g. erosion, their ambient phase occurs again.

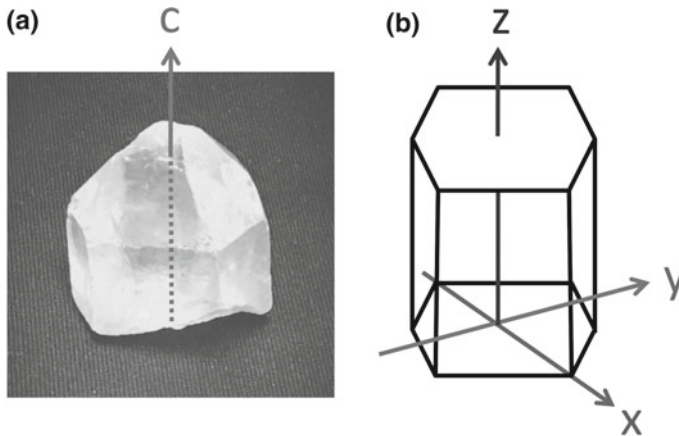


Fig. 1.6 **a** Photographic image of a natural quartz single-crystal with c -axis clearly visible. **b** Schematic image of a hexagonal lattice with x -cut and y -cut ($\perp c$ -axis) and z -cut ($\parallel c$ -axis) shown

quartz samples possess very *high* track densities instead ($\sim 10^8 - 10^9 \text{ cm}^{-2}$) and thus cannot be subjected to the classical approach of chemical etching to the micrometre-scale and subsequent visualisation with optical microscopy. This workflow would enlarge all tracks to the point that adjacent tracks overlap with each other. Consequently, the majority of the framework material would dissolve, making it impossible to observe individual tracks. The issue is solved by imaging the tracks with a transmission or scanning electron microscope (TEM / SEM) instead, which can already detect lightly etched tracks with a minimal increase in diameter.

Apart from fission track analysis, tracks in natural and synthetic quartz have a range of other applications. In contrast to other minerals and crystals, tracks in quartz exhibit a high closure temperature ($800^\circ\text{C}+$), making it an ideal track detector for extreme environments [71, 72]. In micro-electronics, where quartz is used for a variety of applications, low-energy ion implantation and swift heavy ion irradiation is used to modify structural properties. Prominent examples are nano-sized optical waveguides, that can be fabricated by ion track technology. They trap optical modes by using the change in refractive index between the ion track and undamaged area [24, 73].

Quartz crystals used in microelectronics show different properties, depending on their crystallographic cut. Commonly used directions are along the x -, y - and z -directions of the main axes of quartz. Figure 1.6 shows a picture of a natural quartz single-crystal (a) and a schematic representation of the hexagonal lattice of quartz (b). The photograph clearly shows its growth-direction (c -axis) and its hexagonal plane perpendicular to the c -axis. The schematic shows the c -axis under its technical term (z -cut direction). The two in-plane directions $\perp c$ -axis are commonly referred to as x -cut (with a normal vector not along any of the six hexagonal planes) and y -cut (with normal vector parallel to one pair of hexagonal planes).

Finally, the simple and well-understood structure of quartz allows the conduction of molecular dynamics simulations [74] and thermal spike calculations on the ion track formation process [75, 76]. This can improve the general understanding of the fundamental properties of ion track formation and stability that apply to many other materials.

References

1. D.A. Young, Etching of radiation damage in lithium fluoride. *Nature* **182**, 375–377 (1958)
2. P.B. Price, R.M. Walker, Chemical etching of charged-particle tracks in solids. *J. Appl. Phys.* **33**(12), 3407–3412 (1962)
3. R.L. Fleischer, P.B. Price, R.M. Walker, Ion explosion spike mechanism for formation of charged-particle tracks in solids. *J. Appl. Phys.* **36**(11), 3645–3652 (1965)
4. G.A. Wagner, P. Van den Haute, *Fission-Track Dating* (Kluwer Academic Publishers, Dordrecht, 1992)
5. E.C.H. Silk, R.S. Barnes, Examination of fission fragment tracks with an electron microscope. *Philos. Mag.* **4**(44), 970–972 (1959)
6. R.L. Fleischer, P.B. Price, R.M. Walker, Method of forming fine holes of near atomic dimensions. *Rev. Sci. Instrum.* **34**(5), 510–512 (1963)
7. A.J.W. Gleadow, D.X. Belton, B.P. Kohn, R.W. Brown, Fission track dating of phosphate minerals and the thermochronology of apatite. *Rev. Mineral. Geochem.* **48**(1), 579 (2002)
8. F. Lisker, B. Ventura, U.A. Glasmacher, Apatite thermochronology in modern geology. *Geol. Soc. Lond. Spec. Publ.* **324**(1), 1–23 (2009)
9. R.J. Bray, P.F. Green, I.R. Duddy, Thermal history reconstruction using apatite fission track analysis and vitrinite reflectance: a case study from the UK East Midlands and Southern North Sea. *Geol. Soc. Lond. Spec. Publ.* **67**(1), 3–25 (1992)
10. R.L. Fleischer, P.B. Price, R.M. Walker, Effects of temperature, pressure, and ionization of the formation and stability of fission tracks in minerals and glasses. *J. Geophys. Res.* **70**(6), 1497–1502 (1965)
11. P.F. Green, I.R. Duddy, A.J.W. Gleadow, P.R. Tingate, G.M. Laslett, Thermal annealing of fission tracks in apatite: 1. A qualitative description. *Chem. Geol. Isot. Geosci. Sect.* **59**, 237–253 (1986). Calibration of the Phanerozoic Time Scale
12. R.A. Donelick, Crystallographic orientation dependence of mean etchable fission track length in apatite; an empirical model and experimental observations. *Am. Mineral.* **76**(1–2), 83–91 (1991)
13. R.A. Donelick, R.A. Ketcham, W.D. Carlson, Variability of apatite fission-track annealing kinetics; II, crystallographic orientation effects. *Am. Mineral.* **84**(9), 1224–1234 (1999)
14. C.W. Naeser, H. Faul, Fission track annealing in apatite and sphene. *J. Geophys. Res.* **74**(2), 705–710 (1969)
15. R.L. Fleischer, R.T. Woods, H.R. Hart, P.B. Price, N.M. Short, Effect of shock on fission track dating of apatite and sphene crystals from the Hardhat and Sedan underground nuclear explosions. *J. Geophys. Res.* **79**(2), 339–342 (1974)
16. A.S. Wendt, O. Vidal, L.T. Chadderton, Experimental evidence for the pressure dependence of fission track annealing in apatite. *Earth Planet. Sci. Lett.* **201**, 593–607 (2002)
17. J.S. Schmidt, M.L.M.V. Lelarge, R.V. Conceicao, N.M. Balzaretta, Experimental evidence regarding the pressure dependence of fission track annealing in apatite. *Earth Planet. Sci. Lett.* **390**, 1–7 (2014)
18. B.P. Kohn, D.X. Belton, R.W. Brown, A.J.W. Gleadow, P.F. Green, J.F. Lovering, Comment on: Experimental evidence for the pressure dependence of fission track annealing in apatite by A.S. Wendt, et al., *Earth Planet. Sci. Lett.* **201** (2002) 593. *Earth Planet. Sci. Lett.* **215**, 299–306 (2003)

19. O. Vidal, A.S. Wendt, L.T. Chadderton, Further discussion on the pressure dependence of fission track annealing in apatite: reply to the critical comment of Kohn. *Earth Planet. Sci. Lett.* **215**(1–2), 307–316 (2003)
20. F. Seitz, J.S. Koehler, *Solid State Physics Vol. 2*, vol. 2 (Academic Press, New York, 1956)
21. M.F.P. Wagner, F. Völklein, H. Reith, Ch. Trautmann, MD.E. Toimil-Molares, Fabrication and thermoelectrical characterization of three-dimensional nanowire networks. *Phys. Status Solidi (a)* **213**(3), 610–619 (2016)
22. D. Fink, M. Behar, *Fundamentals of Ion-Irradiated Polymers* (Springer, Berlin, 2004)
23. Q. Wen, D. Yan, F. Liu, M. Wang, Y. Ling, P. Wang, P. Kluth, D. Schauries, Ch. Trautmann, P. Apel, W. Guo, G. Xiao, J. Liu, J. Xue, Y. Wang. Highly selective ionic transport through subnanometer pores in polymer films. *Adv. Funct. Mater.*, in print (2016)
24. J. Olivares, A. Garcia-Navarro, A. Mendez, F. Agullo-Lopez, G. Garcia, A. Garcia-Cabanes, M. Carrascosa, Novel optical waveguides by in-depth controlled electronic damage with swift ions. *Nucl. Instrum. Methods Phys. Res., Sect. B* **257**, 765–770 (2007)
25. G. Szenes, Z.E. Horváth, B. Pécz, F. Pászti, L. Tóth, Tracks induced by swift heavy ions in semiconductors. *Phys. Rev. B* **65**, 045206 (2002)
26. P. Kluth, C.S. Schnohr, O.H. Pakarinen, F. Djurabekova, D.J. Sprouster, R. Giuliani, M.C. Ridgway, A.P. Byrne, C. Trautmann, D.J. Cookson, K. Nordlund, M. Toulemonde, Fine structure in swift heavy ion tracks in amorphous SiO₂. *Phys. Rev. Lett.* **101**, 175503–175506 (2008)
27. J.A. Brinkman, On the nature of radiation damage in metals. *J. Appl. Phys.* **25**, 961–970 (1954)
28. F.F. Komarov, Defect and track formation in solids irradiated by superhigh-energy ions. *Phys. Usp.* **46**(12), 1253–1282 (2003)
29. T.A. Paul, P.G. Fitzgerald, Transmission electron microscopic investigation of fission tracks in fluorapatite. *Am. Mineral.* **77**, 336–344 (1992)
30. M. Lambert, A.M. Levelut, M. Maurette, H. Heckman, Etude par diffusion des rayons X aux petits angles de mica muscovite irradiée par des ions d'argon. *Radiat. Eff.* **3**(2), 155–160 (1970)
31. E. Dartyge, J.P. Duraud, Y. Langevin, Thermal annealing of iron tracks in muscovite, labradorite and olivine. *Radiat. Eff.* **34**(1–3), 77–79 (1977)
32. D. Albrecht, P. Armbruster, R. Spohr, M. Roth, K. Schaupt, H. Stuhmann, Small angle scattering from oriented latent nuclear tracks. *Nucl. Instrum. Methods Phys. Res. Sect. B* **2**, 702–705 (1984)
33. P. Kluth, C.S. Schnohr, D.J. Sprouster, A.P. Byrne, D.J. Cookson, M.C. Ridgway, Measurement of latent tracks in amorphous SiO₂ using small angle X-ray scattering. *Nucl. Instrum. Meth. Phys. Res. B* **266**, 2994–2997 (2008)
34. B. Afra, M.D. Rodriguez, C. Trautmann, O.H. Pakarinen, F. Djurabekova, K. Nordlund, T. Bierschenk, R. Giuliani, M.C. Ridgway, G. Rizza, N. Kirby, M. Toulemonde, P. Kluth, Saxs investigations of the morphology of swift heavy ion tracks in alpha-quartz. *J. Phys. Condens. Matter* **25**(4), 045006 (2013)
35. W. Li, P. Kluth, D. Schauries, M.D. Rodriguez, M. Lang, F. Zhang, M. Zdorovets, Ch. Trautmann, R.C. Ewing, Effect of orientation on ion track formation in apatite and zircon. *Am. Mineral.* **99**(5–6), 1127–1132 (2014)
36. T.A. Ehlers, K.A. Farley, Apatite (U-Th)/He thermochronometry: methods and applications to problems in tectonic and surface processes. *Earth Planet. Sci. Lett.* **206**(1–2), 1–14 (2003)
37. F.W. McDowell, W.C. McIntosh, K.A. Farley, A precise 40Ar-39Ar reference age for the Durango apatite (U-Th)/He and fission-track dating standard. *Chem. Geol.* **214**, 249–263 (2005)
38. P. Wu, Y.Z. Zeng, C.M. Wang, Prediction of apatite lattice constants from their constituent elemental radii and artificial intelligence methods. *Biomaterials* **25**(6), 1123–1130 (2004)
39. E.R. Kreidler, F.A. Hummel, The crystal chemistry of apatite: structure fields of fluor- and chlorapatite. *Am. Mineral.* **55**, 170 (1970)
40. J. Barbarand, A. Carter, I. Wood, T. Hurford, Compositional and structural control of fission-track annealing in apatite. *Chem. Geol.* **198**, 107–137 (2003)
41. N.G. Chernorukov, A.V. Knyazev, E.N. Bulanov, Phase transitions and thermal expansion of apatite-structured compounds. *Inorg. Mater.* **47**(2), 172–177 (2011)

42. A.J.W. Gleadow, I.R. Duddy, A natural long-term track annealing experiment for apatite. *Nucl. Tracks* **5**, 169–174 (1981)
43. S. Weyer, A.D. Anbar, A. Gerdes, G.W. Gordon, T.J. Algeo, E.A. Boyle, Natural fractionation of $^{238}\text{U}/^{235}\text{U}$. *Geochim. Cosmochim. Acta* **72**(2), 345–359 (2008)
44. N. Hasebe, J. Barbarand, K. Jarvis, A. Carter, A.J. Hurford, Apatite fission-track chronometry using laser ablation ICP-MS. *Chem. Geol.* **207**(3–4), 135–145 (2004)
45. C.G. Lee, K. Iguchi, J. Inagawa, D. Suzuki, F. Esaka, M. Magara, S. Sakurai, K. Watanabe, S. Usuda, Development in fission track-thermal ionization mass spectrometry for particle analysis of safeguards environmental samples. *J. Radioanal. Nucl. Chem.* **272**(2), 299–302 (2007)
46. F. Esaka, C.-G. Lee, M. Magara, T. Kimura, Fission track-secondary ion mass spectrometry as a tool for detecting the isotopic signature of individual uranium containing particles. *Anal. Chim. Acta* **721**, 122–128 (2012)
47. M.H. Dodson, Closure temperature in cooling geochronological and petrological systems. *Contrib. Miner. Petrol.* **40**(3), 259–274 (1973)
48. A.J.W. Gleadow, I.R. Duddy, P.F. Green, J.F. Lovering, Confined fission track lengths in apatite: a diagnostic tool for thermal history analysis. *Contrib. Mineral. Petrol.* **94**(4), 405–415 (1986)
49. J. De Grave, Apatite fission-track thermochronology of the Altai Mountains (South Siberia, Russia) and the Tien Shan Mountains (Kyrgyzstan): relevance to Meso-Cenozoic tectonics and denudation in Central Asia. Ph.D. thesis, Ghent University, Belgium (2003)
50. G. Lynn, Macrogeomorphology and Erosional History of the Post-Orogenic Pyrenean Mountain Belt. Ph.D. thesis, The University of Edinburgh, Edinburgh (2005)
51. P.K. Zeitler, A.L. Herczeg, I. McDougall, M. Honda, U-Th-He dating of apatite: a potential thermochronometer. *Geochim. Cosmochim. Acta* **51**(10), 2865–2868 (1987)
52. P.F. Green, I.R. Duddy, A.J.W. Gleadow, J.F. Lovering, Apatite fission-track analysis as a paleotemperature indicator for hydrocarbon exploration, in *Thermal History of Sedimentary Basins*, ed. by Nancy D. Naeser, Thane H. McCulloh (Springer, New York, 1989), pp. 181–195
53. P.F. Green, I.R. Duddy, Some comments on paleotemperature estimation from apatite fission track analysis. *J. Pet. Geol.* **12**(1), 111–114 (1989)
54. P.F. Green, Comparison of zeta calibration baselines for fission-track dating of apatite, zircon and sphene. *Chem. Geol. Isot. Geosci. Sect.* **58**(1), 1–22 (1985)
55. P.F. Green, S.A. Durrani, Annealing studies of tracks in crystals. *Nucl. Track Detect.* **1**(1), 33–39 (1977)
56. R.A. Donelick, M.K. Roden, J.D. Mooers, B.S. Carpenter, D.S. Miller, Etchable length reduction of induced fission tracks in apatite at room temperature: crystallographic orientation effects and initial mean lengths. *Int. J. Radiat. Appl. Instrum. Part D. Nucl. Tracks Radiat. Meas.* **17**(3), 261–265 (1990)
57. J. Barbarand, T. Hurford, A. Carter, Variation in apatite fission-track length measurement: implications for thermal history modelling. *Chem. Geol.* **198**, 00423 (2003)
58. P. Vermeesch, Y. Tian, Thermal history modelling: HeFTy versus QTQt. *Earth-Sci. Rev.* **139**, 279–290 (2014)
59. G.M. Laslett, P.F. Green, I.R. Duddy, A.J.W. Gleadow, Thermal annealing of fission tracks in apatite. a quantitative analysis. *Chem. Geol. Isot. Geosci. Sect.* **65**(1), 1–13 (1987)
60. K. Crowley, M. Cameron, R.L. Schaefer, Experimental studies of annealing of etched fission tracks in fluorapatite. *Geochim. Cosmochim. Acta* **55**(5), 1449–1465 (1991)
61. R.A. Ketcham, R.A. Donelick, W.D. Carlson, Variability of apatite fission-track annealing kinetics; III, extrapolation to geological time scales. *Am. Mineral.* **84**(9), 1235–1255 (1999)
62. R.A. Ketcham, A. Carter, R.A. Donelick, J. Barbarand, A.J. Hurford, Improved modeling of fission-track annealing in apatite. *Am. Mineral.* **92**(5–6), 799–810 (2007)
63. P.F. Green, I.R. Duddy, A.J.W. Gleadow, P.R. Tingate, G.M. Laslett, Fission-track annealing in apatite: track length measurements and the form of the Arrhenius plot. *Nuclear Tracks and Radiation Measurements* (1982) **10**(3), 323–328 (1985)
64. H.S. Virk, Single-activation-energy model of radiation damage in solid-state nuclear-track detectors. *Curr. Sci.* **61**, 386–390 (1991)
65. Website quartz (<http://www.quartzpage.de/>)

66. L. Coes, A new dense crystalline silica. *Science* **118**(3057), 131–132 (1953)
67. P.J. Heaney, Structure and chemistry of the low-pressure silica polymorphs. *Rev. Mineral.* **29**, 1–40 (1994)
68. S.B. Holmquist, Conversion of quartz to tridymite. *J. Am. Ceram. Soc.* **44**(2), 82–86 (1961)
69. S. Klaumünzer, Ion tracks in quartz and vitreous silica. *Nucl. Instrum. Meth. Phys. Res. B* **225**, 136–153 (2004)
70. E.F. Weiland, K.R. Ludwig, Ch. W. Naeser, E.C. Simmons, Fission-track dating applied to uranium mineralization. Technical report 80-380, USGS Numbered Series (1980)
71. R.L. Fleischer, P.B. Price, R.M. Walker, *Charged particle tracks: tool for geochronology and meteorite studies in Radiometric Dating for Geologists*. Wiley Interscience (1968)
72. H.A. Khan, The usefulness of mica and quartz track detectors at high environmental temperatures. *Nucl. Instrum. Methods* **114**(1), 61–63 (1974)
73. J. Manzano-Santamaria, J. Olivares, A. Rivera, F. Agullo-Lopez, Electronic damage in quartz (c-SiO₂) by MeV ion irradiations: potentiality for optical waveguiding applications. *Nucl. Instrum. Meth. Phys. Res. B* **272**, 271–274 (2012)
74. A.A. Leino, S.L. Daraszewicz, O.H. Pakarinen, K. Nordlund, F. Djurabekova, Atomistic two-temperature modelling of ion track formation in silicon dioxide. *Europhys. Lett.* **110**(1), 16004 (2015)
75. A. Meftah, F. Brisard, J.M. Costantini, E. Dooryhee, M. Hage-Ali, M. Hervieu, J.P. Stoquert, F. Studer, M. Toulemonde, Track formation in SiO₂ quartz and the thermal-spike mechanism. *Phys. Rev. B* **49**, 12457–12463 (1994)
76. S. Klaumünzer, Thermal-spike model for ion track physics: a critical examination. *Mathematisk-Fysiske Meddelelser* **52**, 293 (2006)

Chapter 2

Physical Background of Ion Tracks



2.1 Interaction of Ions with Matter

When energetic ions pass through solids, they dissipate their energy into the target. The resulting energy loss can be divided into two main regimes. The first is nuclear energy loss, which displaces atoms by elastic collisions between the ion and the nuclei. This process typically dominates for heavy ions with kinetic energies around and below 1 MeV. The second type of interaction, the electronic energy loss, occurs mainly between the ions and the electrons of the target and is the primary type of energy loss for ion energies above 10 MeV (so-called swift heavy ions). Additional energy losses can result from repulsive decay of excited states, track potential, and exciting of vibrational states in molecular solids. Radiation emitted from the particle and nuclear reactions can also dissipate energy, although this is only relevant at energies higher than those within the present work.¹

The characteristic parameter describing ion-solid interaction is the energy loss dE/dx or stopping power $S = -dE/dx$ (for ions of energy E moving along a direction x). The total stopping power can be split into its nuclear and electronic interaction components, S_n and S_e , respectively:

$$S = S_n + S_e = - \left[\frac{dE}{dx} \right]_n - \left[\frac{dE}{dx} \right]_e \quad (2.1)$$

The path of an ion, while penetrating a solid, can be simulated with the SRIM-2008 package [2]. It was initially developed by J. Ziegler to calculate the effects of ion implantation in silicon. It can be used to calculate the energy loss of any ion when interacting with the target's electrons and nuclei. For nuclear energy losses, the code actively simulates $[dE/dx]_n$ using binary collisions [3]. For electronic energy losses, however, SRIM only extrapolates tabulated experimental data to calculate the

¹i.e. Collision of 20 TeV Au ions at the Brookhaven National Laboratory in Upton, New York [1].

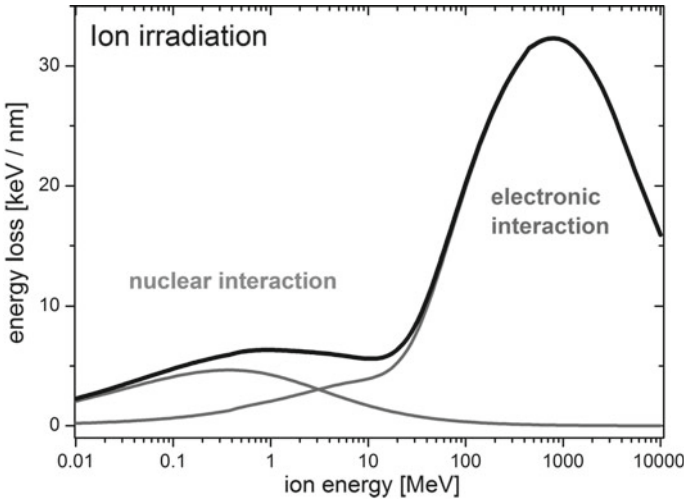


Fig. 2.1 Energy loss of Au ions over a wide range of energies. The combined energy loss (black line) is divided into nuclear energy loss (left peak) and electronic energy loss (right peak), which dominate for low and high energies, respectively [all values calculated with SRIM-2008 [2] for Au ions in apatite]

corresponding $[dE/dx]_e$ values. Nevertheless, the SRIM software has emerged as a standard tool to estimate energy losses in ion-matter interactions.

Figure 2.1 shows an example of energy losses for Au ions of different energies in the mineral apatite (density 3.2 g/cm^3). The nuclear energy loss (left peak) with a maximum around 1 MeV and the electronic energy loss (right peak) with a maximum around 0.4 MeV. The energy corresponding to the maximum energy loss is called the Bragg peak.² For ions with energies higher than this point, less energy is dissipated into the lattice, which typically leads to less damage within the target material. It is evident that at the Bragg peak the electronic energy loss generally supersedes the nuclear energy loss.

Figure 2.2a shows SRIM-calculations of the trajectories of a large number of Au ions (1000+), each penetrating apatite with an initial energy of 2.2 GeV. The first axis describes their path along the initial ion direction, while the second axis shows potential vertical displacement. A mostly straight trajectory is evident with the ions coming to a complete stop at approximately $85 \mu\text{m}$. A single outlier with larger negative vertical displacement can be observed, but is not of statistical relevance for the purpose of ion range calculation.

Using the same horizontal axis, Fig. 2.2b shows the energy loss dE/dx of the ions as they penetrate through the material. Its value is almost constant for approximately the first $70 \mu\text{m}$. This corresponds to ions with energies below 2.2 GeV and 200 MeV

²The concept of the Bragg-peak of ion irradiation should not be mistaken with the theory of diffraction, where such peaks occur for interfering waves when satisfying the Bragg reflection condition. In the present work, such Bragg peaks are discussed in the context of X-ray diffraction in Sect. 3.2.

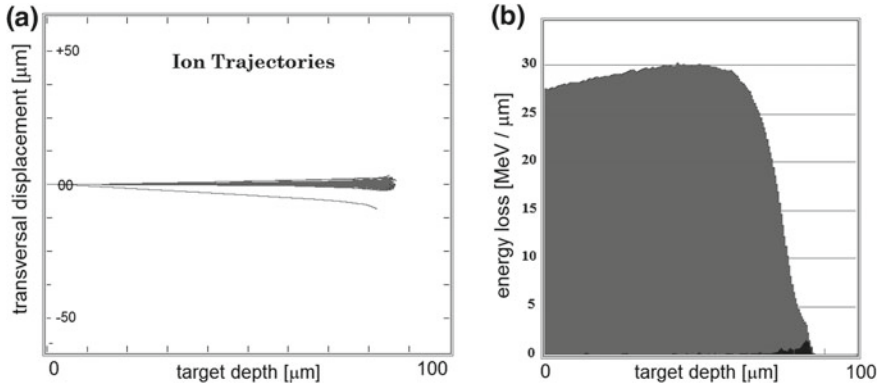


Fig. 2.2 **a** Ion trajectories along the ion penetration depth. **b** Energy loss of ions to the electrons (grey) and to the nuclei (black) of the irradiation target as a function of target depth [all values calculated with SRIM-2008 for 2.2 GeV Au ions in apatite]

or equivalently between 100 and 10% of their initial energy. Only when the ions possess energies below this value, their electronic energy loss decreases rapidly. In addition, nuclear interactions (black curve) come into place as well for the low energies towards the end of the ion trajectory.

2.2 Formation of Ion Tracks

2.2.1 Ion Track Morphology in Crystals

Ion tracks result from the coupling of electronic energy into the atomic system, hence they predominately occur for ion energies in the electronic stopping regime.³ The ion-electron interaction results in an electron-electron cascade, sharing the deposited energy until a fraction of it is transferred to the atomic lattice via electron-phonon coupling. This deposition of a large amount of energy leads to a radial region surrounding the ion trajectory, in which the solid starts to melt, breaking atomic bonds as a consequence. This localised phase transformation is only temporary, as the lattice starts to cool down and quenches rapidly.

For energy losses above a material-specific threshold of a few keV/nm (e.g. 5 keV/nm in apatite [5] or 2–4 keV/nm in quartz [6, 7]) the resulting lattice displacement damage is severe enough to form a continuous damage track in the host material, termed ion track. It consists of a large number of defects as a response of the atomic system to the energy deposited. The radial extent of ion tracks is determined

³The exact processes of the nature of electronic and nuclear stopping power and possible synergy effects are a topic of recent discussion [4].

by the range of the damage perpendicular to the ion trajectory and is typically only a few nanometres wide. For example, the cylindrical ion tracks in apatite in this thesis only have a diameter of approximately 10 nm. The length of an ion track is primarily dependent on the electronic energy loss of the ion within the target material. It can be estimated as the distance from the target surface to the depth where the energy loss drops below the threshold for track formation. For some materials or for ion energies below the ion track formation threshold, the swift heavy ions create a range of discontinuous defects along their trajectories.

A major issue with experimental characterisation of ion track radii in crystals is the sensitivity of different measurement techniques to different aspects of the track damage. For ion tracks in quartz it was shown that small angle X-ray scattering (SAXS) and Rutherford backscattering (RBS) can yield track radii that differ from each other by up to a factor of two [8]. This is a result of the latter technique also taking into account the defective halo consisting of point defects located beyond the track boundary [9]. While RBS measurements can detect these point defects by dechanneling and therefore shows large damage cross-sections, SAXS is unable to register these as they do not exhibit a major change in density. As a result this typically leads to apparent discrepancies when comparing the radial size of tracks between different measurement techniques, as they both probe very different aspects of the track structure [8].

The Velocity Effect

When an ion track is formed, its damage cross section depends on the ion energy loss dE/dx as well as the radial energy density $e(r)$ for bond breaking. Only when the latter exceeds its critical value $e(r = R) = e_c$, the damage is sufficiently large enough to form an ion track with radius R . Ions with higher energy (or equivalently, higher velocity) exhibit a radial energy density that is spread out wider but in turn weaker than for ions of lower energies [10, 11].

In the context of this work, ions of identical energy losses but different energies still differ in their radial energy density $e(r)$ profile. Figure 2.1 shows an example where the energy loss for two very different energies, 200 MeV and 2.2 GeV, is 25 keV/nm for both. However, the ions with 200 MeV exhibit a more localised energy transfer.

This can have significant effects on the damage created as the ion passes through the solid. For ion tracks, as they are only formed above a certain threshold of energy loss, lower ion energies produce a larger volume where the radial dE/dx reaches this threshold, thus generally yielding larger ion tracks. On the other hand, ions of higher energies deposit their energy over a larger total volume, but a smaller region has a sufficiently high dE/dx to form ion tracks. Consequently, the radial size of ion tracks does not only purely depend on the energy loss, but also the radial energy density distribution, which in turn depends on the ion energy. This has been observed in different experimental studies [9, 12] as well as been investigated from a theoretical point of view. In particular Monte Carlo simulations were used to estimate the radial energy distribution of ions and have led to the present model description [7].

2.2.2 *Ion Tracks in Other Materials*

This work only focuses on amorphous ion tracks within single-crystalline materials. Thus the ion track consists of a secondary, amorphous phase of reduced density, embedded within their host matrix [8, 13]. The reduction in density can lead to an overdense shell surrounding the track that can often exceed the primary core track in size. In the present work, no such structure was identified. This can be explained by assuming the reduction in density of the tracks leads to an overall expansion of the material, which is also putting large strain onto the host matrix. In addition, ion tracks can often result in a characteristic swelling on the surface of the material and the formation of hillocks [14, 15].

In principle, the reduction in density can also result in a reduction of the overall number of atoms, e.g. formation of gaseous residue that leaves the material permanently [16]. Since the ion track damages in the present work appear to be fully reversible (compare thermal annealing in Chap. 7), it is assumed that this process does not occur.

Ion tracks are not limited to crystals and can also be observed in a range of other solids, including amorphous materials, organic polymers, and even metals [17, 18]. A brief overview on tracks in amorphous and organic materials is discussed in the remainder of this subsection:

Ion Tracks in Amorphous Materials

In non-crystalline materials ion tracks can also be observed upon exposure to swift heavy ion radiation [6]. Similar to crystals, the tracks in amorphous materials typically consist of a small core region with significantly different density than the initial density of the target material. This core is typically surrounded by a larger shell-shaped region with only a small density mismatch. As a result of the swift heavy ion irradiation, the material also undergoes a shrinkage along the direction of the ion impact. This effect is called ion hammering and is large enough to lead to changes on a macroscopic scale [6].

In order to image the individual tracks, microscopy techniques do not provide the required resolution without prior etching of the tracks. For most amorphous materials, transmission electron microscopy does not allow the imaging of tracks. An exception is a recent investigation using high-angle annular dark field scanning transmission electron microscopy on tracks in a-SiN [19]. It was carried out on ion tracks that provided sufficient contrast, as a result of the high density differences between core, shell and surrounding amorphous material.

Measurements using SAXS, however, are highly sensitive to even small changes in density. A recent study employed synchrotron-based SAXS to characterised the size and density difference of ion tracks in amorphous silica (a-SiO₂) [20]. It shows ion tracks with an underdense core and a slightly overdense shell. Subsequent investigations on the materials amorphous silicon (a-Si) [21] and amorphous germanium (a-Ge) [22] also showed a core-shell track when characterised by SAXS.

Ion Tracks in Organic Materials

The formation of ion tracks is not limited to inorganic materials. In fact, from early on, ion tracks have been studied in organic polymers as well. One example is the investigation by Comstock et al. in 1971, which has studied the ion tracks formed by cosmic rays in the polycarbonate helmets worn by the astronauts of the Apollo Lunar Missions [23]. Using similar etching techniques as established for fission tracks in minerals, they could observe the cosmic radiation-induced ion tracks and estimate the radiation exposure on the astronauts.

Ion tracks in polymers are typically created from the destruction of links and bonds between the polymer chains, resulting in a lower density of the track in comparison to its surrounding region. During that process the structure and composition of the irradiated polymer matrix is permanently altered and chemical reactions form gaseous molecules [16]. A range of models have been suggested to describe the ion track profile in several polymers. One of the most successful candidates is a core-shell model with a highly underdense core and an only slightly underdense shell of comparable radii [24]. In addition, polymers often display a semi-crystalline structure, alternating between crystalline and non-crystalline (disordered) zones. As the energy loss of ions differs between these two zones, their radial size may also change [25].

Today, the irradiation of polymers and subsequent etching is one of the largest commercial applications of ion track technology. Available products include polymer membranes with nano-sized etched ion tracks, so-called nano-pore membranes, provided by companies such as Trackpore Technology.⁴ Another application are nanowires incorporated within polymers [26]. For this application, polymer foils are irradiated with swift heavy ions and subsequently etched to produce hollow templates. A metallic layer substrate is deposited on one side of the polymer and metallic nanowires are grown in the channels via electrodeposition. Finally, the entire polymer membrane is dissolved, leaving freestanding nanowires on the substrate. Additional potential applications include the growth of nano-sized microelectronic devices, diodes and sensors in ion etched track polymers [27].

2.2.3 Modelling of Ion Tracks

Thermal-Spike Model

When the formation of ion tracks was first investigated after their discovery, it was suggested that the primary damage results from immediate atom displacements in collision cascades [28]. This approach, however, disregards any effects of the ion-electron interaction. Initially developed to explain and model the interaction between photons from a laser source and solids, the inelastic thermal spike model (ITS) has demonstrated great success in the field of swift heavy ion irradiation.

⁴www.trackpore.com.

The iTS model was introduced around 1960 and allows us to take the effects of photon-electron interaction into account via the incorporation of the heat exchange between the electron and the ionic sub-system [7, 9, 29–32]. Both sub-systems are coupled by electron-phonon interactions allowing energy exchange via diffusion. The model is named after the very short, 10^{-10} s lasting thermal spike, which thermalises the electronic system from the ion energy transfer by electron-electron scattering. This excites the electrons to high temperatures, allowing them to be treated as a free electron gas. The coupling between the two systems is described by a modified version of the classical heat equations within cylindrical geometry:

$$C_e(T_e) \frac{\partial T_e}{\partial t} = \frac{1}{r} \frac{\partial}{\partial r} \left[r K_e(T_e) \frac{\partial T_e}{\partial r} \right] - g(T_e - T_a) + A(r, t) \quad (2.2)$$

$$C_a(T_a) \frac{\partial T_a}{\partial t} = \frac{1}{r} \frac{\partial}{\partial r} \left[r K_a(T_a) \frac{\partial T_a}{\partial r} \right] + g(T_e - T_a) \quad (2.3)$$

with T , C and K representing the temperature, specific heat and thermal conductivity of the electronic (e) and atomic (a) systems. For most materials, the values for the lattice are available through tabulated experimental or calculated values. The values for the electronic sub-system are taken from the electron-phonon coupling with the coupling constant g being treated as an empirically chosen free parameter or calculated to give the best agreement to experimental track radii. The energy deposition of the projectile to the electronic sub-system is implemented by the term $A(r, t)$ as the energy density deposited at a radius r at time t [10]. The integration of $A(r, t)$ over time and space gives the energy loss dE/dx . The model allows calculating the radial temperature profile in the material as a function of time. The track radius is assumed to be the radius where the melting temperature is exceeded.

The thermal spike model was first used to explain track formation in metals by Brinkman [17] and Seitz and Koehler [33]. Subsequently it was also used to explain tracks in insulators by Chadderton [34]. The model still possesses some significant downsides due to its simplifications and has lately received a range of criticisms (e.g. Klaumünzer [30], Szenes [35]). One of the key issues is the lack of variation in space and time that is assumed for C and K . In particular when the model is applied to insulators, as in the present work, it does not consider any change of these parameters in proximity to the trajectory of the swift heavy ion [30]. Despite these limitations it has provided good agreement when the calculations were fitted to the experimental values, as summarised by Toulemonde [7].

Coulomb Explosion Model

The Coulomb explosion model (or ion explosion model) is an alternative approach to explain ion track formation, first suggested in 1965 by Fleischer et al. [36, 37]. It considers the removal of electrons along the ion trajectory as the primary cause of ion track formation. As a result of the electron stripping, a narrow cylindrical region of positively charged ions emerges with reduced electron concentration, respectively an increased hole concentration. These ions are electrostatically unstable and con-

sequently forced from their initial lattice positions into interstitial sites, leading to a reduction in density of the region along the ion path, forming the ion track.

Within the framework of this model, ion tracks are created when the repulsive forces of the electron-stripped ions exceed the attractive bonding forces of the lattice. The model requires the electron-depleted region to stay positively charged for long enough for at least the timescale of the atomic motion ($\sim 10^{-13}$ s). Hence, the electron mobility of the atoms from the outside region and the holes from inside the charge region are required to be slow. Otherwise the gradient in the concentration of electrons and holes, leads to diffusion that destroys this charge inhomogeneity. The former is typically fulfilled for insulators and semiconductors, but not metals.

The Coulomb explosion model has successfully explained aspects of how track formation occurs in insulators. Its assumptions, however, contradict the experimental evidence for ion tracks in many semiconductors (e.g. amorphous silicon and germanium) and metals, where the thermal spike model has succeeded [29, 36].

Molecular Dynamics

The most realistic approach to estimate ion-irradiation induced defects on an atomic level are Molecular Dynamics (MD) calculations. This technique was initially developed to simulate atomic vibrations in molecules — hence the name [38] — but is now commonly applied to systems of solids due to the evolution of supercomputers and their computational power available today. The key idea is predicting the movement of each single atom over time by calculating the resulting forces. The time parameter becomes a discrete value in the order of femto-seconds and is increased iteratively.

The most critical part of MD simulations is the choice of the appropriate interaction potential of the atoms in the material; these are typically calculated using ab-initio software packages. The potential is obtained by formulating the Schrödinger equation for the interaction between each of the particles and solving it using numerical methods. As the full Schrödinger equation for electrons and nuclei is impossible to solve, the Born-Oppenheimer approximation is used. It separates the Schrödinger equation in two independent equations: one for the nuclei and one for the electrons. The equation for nuclei can be solved within the classical limit, where the Schrödinger equation is turned into Newton's equation of motion.

To calculate the interaction of swift heavy ions and matter, and thus the formation of ion tracks, the lattice atoms are placed in a cell with a side length of tens of nanometres with periodic boundary conditions. This size corresponds to a few million atoms and is limited by computational constraints. The pre-calculated expression for the potential is then used as input in classical MD simulations.⁵ For all calculations shown in the present work, the PARCAS [39] code was used to represent the ground state and implement electronic stopping and a variable time step into the calculations. Furthermore, boundary conditions such as temperature and pressure can be taken into account by the calculations. Here, the MD simulations use the Berendsen model approximation to take into account the influence of temperature and pressure [40].

⁵MD calculations are also possible by solving the Schrödinger equations directly while calculating the atom trajectories as so-called ab initio MD. However, this technique is computationally expensive and, therefore, limited to small systems and short time scales.

For all MD simulations in the present work the Two-Temperature (2T-MD) model was used to implement the electronic energy loss through the evolution of the atomic lattice temperature from the inelastic thermal spike model [41]. Within a time-scale of only 100 fs, most of the energy of the excited electrons is transferred into the lattice.

While the present work uses MD simulations of ion tracks during their formation stage in Chaps. 5 and 6, their short timescales accessible (~ 100 ps) limit the calculation of effects like long-term relaxation. Thus the recrystallisation from thermal annealing, which is demonstrated in Chap. 7, is clearly beyond the scope of MD simulations.

References

1. S. Ozaki, T. Roser, Relativistic heavy ion collider, its construction and upgrade. *Prog. Theor. Exp. Phys.* **03A102**, 1–11 (2015)
2. J.F. Ziegler, J.P. Biersack, U. Littmark, *The Stopping and Range of Ions in Matter* (Pergamon, New York, 1985)
3. J.F. Ziegler, M.D. Ziegler, J.P. Biersack, SRIM - the stopping and range of ions in matter. *Nucl. Instrum. Methods Phys. Res. Sect. B: Beam Interact. with Mater. At.* **268**(11–12), 1818–1823 (2010). 19th International Conference on Ion Beam Analysis
4. W.J. Weber, E. Zarkadoula, O.H. Pakarinen, R. Sachan, M.F. Chisholm, P. Liu, H. Xue, K. Jin, Y. Zhang, Synergy of elastic and inelastic energy loss on ion track formation in SrTiO₃. *Sci. Rep.* **5**(7726 EP), 01 (2015)
5. R. Tisserand, M. Rebetez, M. Grivet, S. Bouffard, A. Benyagoub, F. Levesque, J. Carpena, Comparative amorphization quantification of two apatitic materials irradiated with heavy ions using XRD and RBS results. *Nucl. Instrum. Method Phys. Res. B* **215**, 129–136 (2004)
6. S. Klaumünzer, Ion tracks in quartz and vitreous silica. *Nucl. Instrum. Method Phys. Res. B* **225**, 136–153 (2004)
7. M. Toulemonde, W. Assmann, C. Dufour, A. Meftah, F. Studer, C. Trautmann, Experimental phenomena and thermal spike model description of ion tracks in amorphisable inorganic insulators. *Mat. Fys. Medd.* **52**, 263–292 (2006)
8. B. Afra, M.D. Rodriguez, C. Trautmann, O.H. Pakarinen, F. Djurabekova, K. Nordlund, T. Bierschenk, R. Giuliani, M.C. Ridgway, G. Rizza, N. Kirby, M. Toulemonde, P. Kluth, Saxs investigations of the morphology of swift heavy ion tracks in alpha-quartz. *J. Phys. Condens. Matter* **25**(4), 045006 (2013)
9. A. Meftah, F. Brisard, J.M. Costantini, E. Dooryhee, M. Hage-Ali, M. Hervieu, J.P. Stoquert, F. Studer, M. Toulemonde, Track formation in SiO₂ quartz and the thermal-spike mechanism. *Phys. Rev. B* **49**, 12457–12463 (1994)
10. M.P.R. Waligorski, R.N. Hamm, R. Katz, The radial distribution of dose around the path of a heavy ion in liquid water. *Nucl. Tracks Radiat. Meas.* **11**, 309–319 (1986)
11. R.M. Papaléo, A. Hallén, B.U.R. Sundqvist, L. Farenzena, R.P. Livi, M.A. de Araujo, R.E. Johnson, Chemical damage in poly(phenylene sulphide) from fast ions: dependence on the primary-ion stopping power. *Phys. Rev. B* **53**, 2303–2313 (1996)
12. D. Schauries, B. Afra, T. Bierschenk, M. Lang, M.D. Rodriguez, C. Trautmann, W. Li, R.C. Ewing, P. Kluth, The shape of ion tracks in natural apatite. *Nucl. Instrum. Method Phys. Res. B* **326**, 117–120 (2014). 17th International Conference on Radiation Effects in Insulators (REI)
13. B. Afra, M. Lang, M.D. Rodriguez, J. Zhang, R. Giuliani, N. Kirby, R.C. Ewing, C. Trautmann, M. Toulemonde, P. Kluth, Annealing kinetics of latent particle tracks in Durango apatite. *Phys. Rev. B* **83**, 064116 (2011)

14. Ch. Trautmann, M. Boccanfuso, A. Benyagoub, S. Klaumünzer, K. Schwartz, M. Toulemonde, Swelling of insulators induced by swift heavy ions. Nucl. Instrum. Methods Phys. Res. Sect. B: Beam Interact. with Mater. At. **191**, 144–148 (2002)
15. Y.-J. Ma, P. Mota Santiago, M.D. Rodriguez, F. Kremer, D. Schauries, B. Afra, T. Bierschenk, D.J. Llewellyn, F. Lu, M.C. Ridgway, P. Kluth, Orientation dependence of swift heavy ion track formation in potassium titanyl phosphate **31**, 2329–2336 (2016)
16. D. Severin, E. Balanzat, W. Ensinger, Ch. Trautmann, Outgassing and degradation of polyimide induced by swift heavy ion irradiation at cryogenic temperature. J. Appl. Phys. **108**(2), 024901 (2010)
17. J.A. Brinkman, On the nature of radiation damage in metals. J. Appl. Phys. **25**, 961–970 (1954)
18. F.F. Komarov, Defect and track formation in solids irradiated by superhigh-energy ions. Phys. Uspekhi **46**(12), 1253–1282 (2003)
19. T. Kitayama, Y. Morita, K. Nakajima, K. Narumi, Y. Saitoh, M. Matsuda, M. Sataka, M. Tsujimoto, S. Isoda, M. Toulemonde, K. Kimura, Formation of ion tracks in amorphous silicon nitride films with MeV C60 ions. Nucl. Instrum. Methods Phys. Res. Sect. B: Beam Interact. with Mater. At. **356–357**, 22–27 (2015)
20. P. Kluth, C.S. Schnohr, O.H. Pakarinen, F. Djurabekova, D.J. Sprouster, R. Giuliani, M.C. Ridgway, A.P. Byrne, C. Trautmann, D.J. Cookson, K. Nordlund, M. Toulemonde, Fine structure in swift heavy ion tracks in amorphous SiO₂. Phys. Rev. Lett. **101**, 175503–175506 (2008)
21. T. Bierschenk, R. Giuliani, B. Afra, M.D. Rodriguez, D. Schauries, S. Mudie, O.H. Pakarinen, F. Djurabekova, K. Nordlund, O. Osmani, N. Medvedev, B. Rethfeld, M.C. Ridgway, P. Kluth, Latent ion tracks in amorphous silicon. Phys. Rev. B **88**, 174111 (2013)
22. M.C. Ridgway, T. Bierschenk, R. Giuliani, B. Afra, M.D. Rodriguez, L.L. Araujo, A.P. Byrne, N. Kirby, O.H. Pakarinen, F. Djurabekova, K. Nordlund, M. Schlegelberger, O. Osmani, N. Medvedev, B. Rethfeld, P. Kluth, Tracks and voids in amorphous Ge induced by swift heavy-ion irradiation. Phys. Rev. Lett. **110**, 245502 (2013)
23. G.M. Comstock, R.L. Fleischer, W.R. Giard, H.R. Hart, G.E. Nichols, P.B. Price, Cosmic-ray tracks in plastics: the apollo helmet dosimetry experiment. Science **172**(3979), 154–157 (1971)
24. S. Abu Saleh, Y. Eyal, Porous tracks along wakes of swift uranium ions in polyimide. Appl. Phys. Lett. **85**(13), 2529–2531 (2004)
25. R. Spohr, Ion tracks for micro- and nanofabrication - from single channels to superhydrophobic surfaces. Ph.D. thesis, Uppsala Universitet, 2009
26. H. Reith, F. Völklein, M.C. Schmitt, D. Huzel, Nanowires - Implementations and Applications (InTech, 2011)
27. D. Fink, M. Behar, *Fundamentals of Ion-Irradiated Polymers* (Springer, Berlin, 2004)
28. P.B. Price, R.M. Walker, Chemical etching of charged-particle tracks in solids. J. Appl. Phys. **33**(12), 3407–3412 (1962)
29. M. Toulemonde, E. Paumier, C. Dufour, Thermal spike model in the electronic stopping power regime. Radiat. Eff. Defects Solids **126**(1–4), 201–206 (1993)
30. S. Klaumünzer, Thermal-spike model for ion track physics: a critical examination. Math. Fys. Medd. **52**, 293 (2006)
31. I.M. Lifshits, M.I. Kaganov, L.V. Tanatarov, On the theory of radiation-induced changes in metals. J. Nucl. Energy Part A. React. Sci. **12**(1), 69–78 (1960)
32. G. Bonfiglioli, A. Ferro, A. Mojoni, Electron microscope investigation on the nature of tracks of fission products in mica. J. Appl. Phys. **32**(12), 2499–2503 (1961)
33. F. Seitz, J.S. Koehler, *Solid State Physics*, vol. 2 (Academic Press, New York, 1956)
34. L.T. Chadderton, H.M. Montagu-Pollock, Fission fragment damage to crystal lattices: heat-sensitive crystals. Proc. R. Soc. A **274**(1357), 239–252 (1963)
35. G. Szenes, Comparison of two thermal spike models for ion-solid interaction. Nucl. Instrum. Methods Phys. Res. Sect. B: Beam Interact. with Mater. At. **269**(2), 174–179 (2011)
36. R.L. Fleischer, P.B. Price, R.M. Walker, Ion explosion spike mechanism for formation of charged-particle tracks in solids. J. Appl. Phys. **36**(11), 3645–3652 (1965)
37. E.M. Bringa, R.E. Johnson, Coulomb explosion and thermal spikes. Phys. Rev. Lett. **88**, 165501 (2002)

38. B.J. Alder, T.E. Wainwright, Phase transition for a hard sphere system. *J. Chem. Phys.* **27**(5), 1208–1209 (1957)
39. K. Nordlund, M. Ghaly, R.S. Averback, M. Caturla, T. Diaz de la Rubia, J. Tarus, Defect production in collision cascades in elemental semiconductors and FCC metals. *Phys. Rev. B* **57**, 7556–7570 (1998)
40. H.J.C. Berendsen, J.P.M. Postma, W.F. van Gunsteren, A. DiNola, J.R. Haak, Molecular dynamics with coupling to an external bath. *J. Chem. Phys.* **81**(8), 3684–3690 (1984)
41. A.A. Leino, S.L. Daraszewicz, O.H. Pakarinen, K. Nordlund, F. Djurabekova, Atomistic two-temperature modelling of ion track formation in silicon dioxide. *Europhys. Lett.* **110**(1), 16004 (2015)

Chapter 3

X-Ray Characterisation Techniques



The present chapter discusses the theory of X-rays characterisation methods in material science, based on the interaction of X-rays with matter through absorption and scattering. In particular, the theoretical aspects of X-ray diffraction and scattering are introduced and the concepts of small angle X-ray scattering (SAXS) are explained. As the main characterisation technique used in this work, focus is set on the application of this technique on cylindrical ion tracks and the analysis of the SAXS patterns to extract their size and density profile.

X-rays were originally discovered and named by W. Röntgen in 1895 [1]. They are defined as the part of the electromagnetic spectrum with energies between a several keV and several hundred keV, with respective wavelengths between 1 and 0.001 nm. X-rays come from two different processes:

The emission of photons from the transitions of electrons between atomic states in heavy elements can result in X-rays. An atom that is bombarded with heavy-energy particles, can eject an electron from an inner shell, producing a temporary electronic vacancy. This core hole is quickly filled with an electron from a higher, more energetic state. The reduction in the energy that electron underwent results in the emission of an X-ray photon. Its energy is well-defined by the energy difference between the initial and final state of the electron. Thus, these X-rays are referred to as characteristic X-rays, i.e. Cu K_{α} -line from the first K-shell transition [2, 3].

The second source of X-rays is the acceleration or deceleration of charge particles. From Maxwell's equations, an expression can be derived for the radiation that is produced by charged particles (i.e. electrons) experiencing a change in velocity \mathbf{v} . In its relativistic form, the Larmor formula states the total power P_{ph} of the emitted radiation as [2, 3]:

$$P_{ph} = \frac{2e^2\gamma^6}{3c^3} \left[\left(\frac{d\mathbf{v}}{dt} \right)^2 - \left(\mathbf{v} \times \frac{d\mathbf{v}}{dt} \right)^2 \right] \quad (3.1)$$

with $\gamma = (1 - v^2/c^2)^{-1/2}$ as the relativistic Lorentz factor. X-ray radiation originating from this method is typically generated by deceleration of electrons, thus it is often referred to as Bremsstrahlung. In a synchrotron facility, a large number of electrons ($\sim 10^{18} \text{ s}^{-1}$) is sent on a curved trajectory at relativistic velocities for the sole purpose of producing X-rays. Photons of a single energy can then be extracted from the continuous spectrum using double crystal reflection monochromators. The obtained X-rays still supersede any lab-based instrument in their brightness as a result of the large number of photons generated. The technical details about the operation of a synchrotron are explained in Sect. 4.4.

3.1 Interaction of X-Rays with Matter

When an X-ray beam penetrates and interacts with solids, it undergoes a range of competing processes, which depend on the absorption and scattering properties of the target material.

3.1.1 X-Ray Absorption

The most prominent aspect of X-rays is their ability to penetrate solids with different attenuation rates, predominately depending on the target density. Absorption is a result of the reduction of the initial X-ray intensity I_0 to the transmitted intensity $I(x)$ by the Lambert-Beer law [4, 5]:

$$I(x) = I_0 \exp(-\mu x) \quad (3.2)$$

for X-rays travelling along a distance x within a material with the energy-specific X-ray absorption coefficient $\mu = \mu(E)$. For X-rays, absorption can be easily estimated by measuring the intensity of transmitted photons and comparing it with the initial intensity, as long as other processes (i.e. reflection) are negligible. An example of characterising matter with inhomogeneous X-ray absorption properties is that of medical X-ray imaging. Here, the attenuated X-ray intensities are visualised by the transmitted X-ray photons. A detector screen is used to register these after they have penetrated the entire thickness of the sample.

Figure 3.1 shows such a two-dimensional image for the density profile of a human hand. The attenuation is proportional to the density of each type of matter it penetrates, hence a projection of the density and thickness of the imaged object onto a 2D detector is created.¹ In this case, the image clearly distinguishes between low-attenuating

¹Absorption imaging can be extended from 2D to 3D by means of X-ray computer tomography (CT). This technique utilises a controlled movement of the imaged specimen or, alternatively, of the X-ray source and detector (i.e. medical CT), to vary the X-ray trajectory through the sample.



Fig. 3.1 Transmission image from X-rays penetrating through a human hand after surgery. The density is represented by the greyscale value: White regions represent high absorption (metallic screws), grey regions intermediate absorption (bones), and dark regions low absorption (tissue)

tissue (dark grey), partially absorbing bone (grey), and high-attenuating metallic screws (white).

3.1.2 X-Ray Scattering Processes

For X-rays, the process of absorption competes with scattering effects. X-ray photons scatter predominately with the electrons of their target atoms and any scattering between photons and atomic nuclei is negligible. Depending on the type of collision, the scattering is classified either as elastic or inelastic.

Elastic Scattering

Elastic scattering events (without change in photon energy) preserve structural information of the scatterer. For the scattering of photons with frequency ω in a particular angle 2θ , the scattering intensity $I(\omega)$ can be written as [2]:

$$I(\omega) \propto \frac{1}{2}[1 + \cos(2\theta)] \cdot \frac{\omega^4}{(\omega_0^2 - \omega^2)^2} \quad (3.3)$$

The large stack of 2D-projections is then used to calculate a full 3D model of the specimen that contains the attenuation value for each feature within the sample.

Here, the electron oscillator frequency ω_0 , corresponds to the bonding strength of the electrons and is within the ultraviolet part of the spectrum.

X-rays predominantly undergo Thomson scattering, which is the high-energy limit of Eq. (3.3). It can be calculated by assuming $\omega \gg \omega_0$ and simplifies the scattering intensity to a frequency-independent quantity, $I = \frac{1}{2}[1 + \cos(2\theta)]$. Rayleigh scattering, on the other hand, is defined for scattering of photons with wavelengths significantly above the sizes of the scattered particles. Thus Rayleigh scattering has no relevance for X-rays due to their sub-nanometre wavelength and is only of importance for photons of lower energy (i.e. visible light), hence, the conditions $\omega \ll \omega_0$ applies. The scattering intensity consequently shows a frequency dependence of $I(\omega) \propto \omega^4$.

Inelastic Scattering

X-rays of sufficiently high energy also undergo inelastic Compton scattering (with a change in photonic energy). When an incident photon is absorbed by the electrons from the outer atomic shell, the wavelength of the re-emitted photon has changed, which leads to a disappearance of coherence. This eliminates any potential for interference and retrieval of structural information. In scattering experiments, Compton scattering contributes to the background radiation, although it is virtually non-existent for small angles as used in the present work [6].

3.2 X-Ray Diffraction (XRD)

The word *diffraction* usually refers to interaction of X-rays with ordered structures, while *scattering* refers to any transfer of momentum. X-ray diffraction (XRD) is an experimental technique that uses Thomson scattering to characterise Angstrom-sized dimensions in ordered systems, such as spacings of atomic planes in (semi)crystalline materials. Although the concept is explained for crystalline samples, the principle can also be applied to crushed powder (X-ray powder diffraction) as applied in Chap. 7 of this thesis.

Diffraction in Real Space

Figure 3.2a shows a schematic illustration of the diffraction of X-rays on a periodic, non-cubic lattice with lattice constants a and c . Typical values for lattice constants are between 0.2 and 1.0 nm. The incident X-rays with wavevector \mathbf{k}_i , wavelength λ and wavenumber $|\mathbf{k}_i| = 2\pi/\lambda$ are diffracted by interacting with the electrons of each lattice atom. This results in a change in momentum by the scattering angle 2θ to the scattered wavevector \mathbf{k}_0 . The difference in the optical path length is $2 \times d \sin \theta$. Here, the lattice spacing distance d is the separation between each diffraction plane. For values of multiple wavelengths ($n\lambda$ with a positive integer n) constructive interference is observed after Bragg's law (after W. L. Bragg and W. C. Bragg [7]):

$$n\lambda = 2d \sin \theta \quad (3.4)$$

For X-ray energies typically used for XRD in the range of tens of keV, the scattering angle 2θ varies between 10 and 90°. The lower angles correspond to the first order reflection ($n = 1$), while higher angles denote higher order peaks of the same lattice planes ($n > 1$).

Diffraction in Reciprocal Space

The theory of X-ray diffraction on periodic lattices is commonly explained using the reciprocal space representation of the crystal lattice. The reciprocal space is mathematically connected with the real space through a Fourier transform. While points in real space are defined by their three position vectors $\mathbf{r}_a, \mathbf{r}_b, \mathbf{r}_c$ with the unit [length], the reciprocal space is defined by three momentum vectors $\mathbf{k}_a, \mathbf{k}_b,$ and \mathbf{k}_c with unit [length⁻¹]. Therefore reciprocal space is often referred to as \mathbf{k} -space or momentum space.

Figure 3.2b demonstrates X-ray scattering on a crystal lattice in reciprocal space. Each Bragg condition results from Eq. (3.4) and is marked with a point in the reciprocal lattice space (green circles). For an incident X-ray wave \mathbf{k}_i of constant wavelength, its momentum can be shown by the surface of the so-called “Ewald sphere” with a radius of the magnitude of $|\mathbf{k}_i| = 2\pi/\lambda$. For elastic scattering, the magnitudes of the incident and scattered waves have to be identical, thus $|\mathbf{k}_i| = |\mathbf{k}_0|$. The range of possible scattering planes can be represented by the intersections of the Ewald sphere with the reciprocal lattice. A detector measuring the scattered X-rays shows a peak at the angle 2θ satisfying Eq. (3.4) for each atom of the reciprocal lattice that intersects with the Ewald sphere. The change in the X-ray momentum can be described by the scattering vector \mathbf{q} :

$$\mathbf{q} = \mathbf{k}_i - \mathbf{k}_0 \quad \text{with} \quad |\mathbf{q}| = 4\pi \sin \theta / \lambda \quad (3.5)$$

The present work primarily characterises structures in the nanometre regime, which is 1-2 orders of magnitude above typical lattice constants. Bragg’s law from Eq. (3.4) implies that for larger values of d , the X-rays scatter under small angles of 2θ . These structures can be investigated by using small angle X-ray scattering. The upcoming section discusses this technique in detail and shows the relevant calculations for a scattering amplitude with cylindrical geometry that represent ion tracks.

3.3 Small Angle X-Ray Scattering (SAXS)

Small angle X-ray scattering (SAXS) is an experimental technique using similar physical principles as diffraction. The main difference is in the investigated target: while XRD experiments are generally conducted on Angstrom-sized features with periodically order and large repetitions (e.g. crystal lattices), SAXS investigates nano-sized objects, that differ in their electronic density from their surrounding medium. The primary application of SAXS is to characterise the sizes, shapes and spatial arrangement of objects in a wide range of fields including biology, chemistry, material

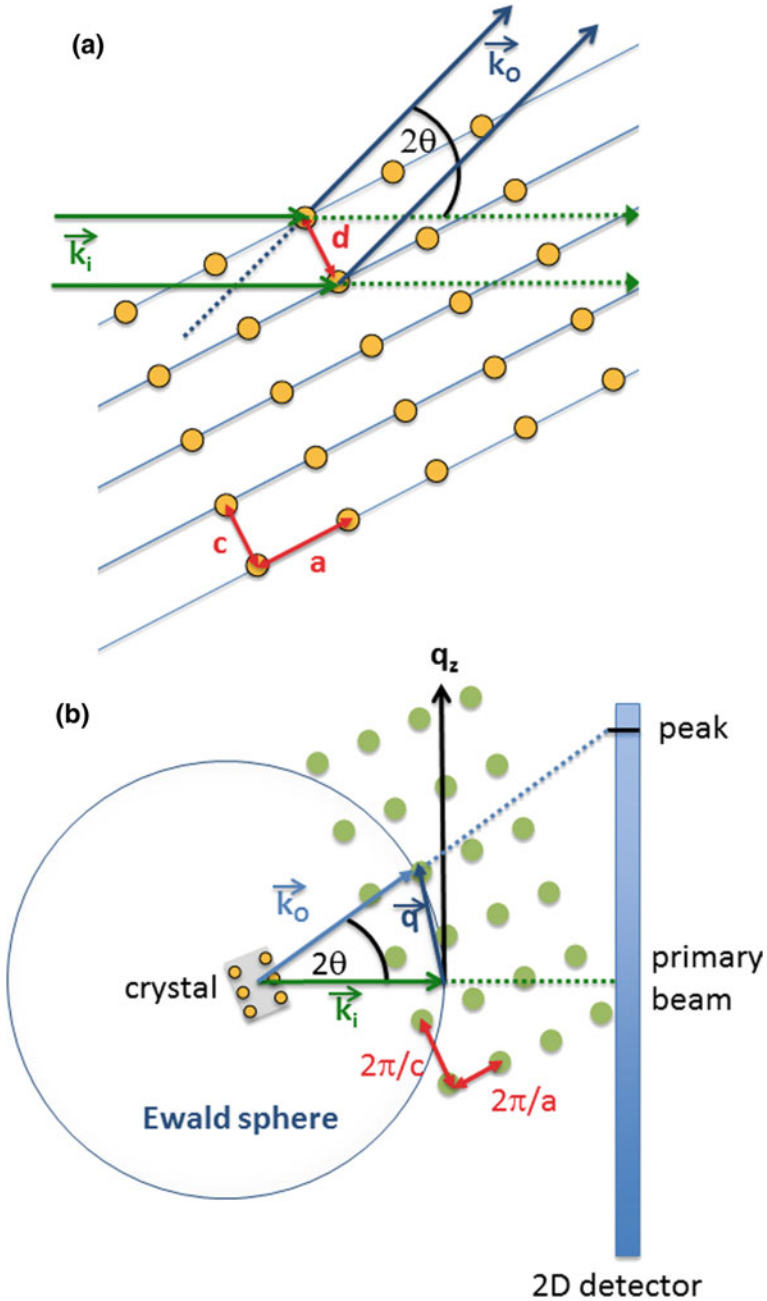


Fig. 3.2 **a** Schematic illustration of XRD in real space on a periodic lattice with lattice constants a and c . The incident wave \vec{k}_i (green) and scattered wave \vec{k}_o (blue) differ in direction by the scattering angle 2θ . **b** Schematic illustration of XRD in reciprocal space with the intersection of the Ewald sphere with the reciprocal lattice. The visible peaks shown on the detector screen are the intersection points between the Ewald sphere and the reciprocal lattice with lattice constants $2\pi/a$ and $2\pi/c$

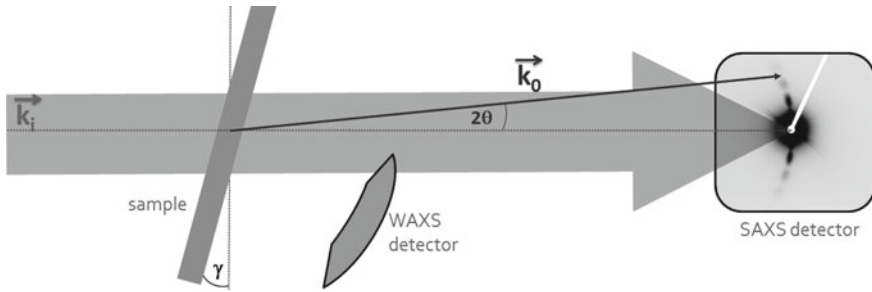


Fig. 3.3 Schematic showing a typical set-up for transmission SAXS. The incident X-ray beam with wavevector \mathbf{k}_i hits the sample under an angle γ . For an arbitrary scattered photon, the scattering angle 2θ and new wavevector \mathbf{k}_0 are shown. All photons scattered under small angles are collected by the SAXS detector. The unscattered part of the beam at the centre of the detector is blocked out (white circle). An optional WAXS detector can be used to register photons scattered at higher angles

science and physics. Small angle scattering can also be performed using neutrons, which is referred to as small angle neutron scattering (SANS). As the scattering experiments presented in this work are mainly carried out using X-rays, this section focuses on explaining small angle scattering in the context of X-rays, although most concepts can be easily transferred to SANS as well [8]. The theory of SAXS is discussed in textbooks by Glatter and Kratky [6], Feigin and Svergun [9], and Guinier and Fournet [10] or — more recently — Brumberger [11]. The application of SAXS to cylindrical objects has been discussed by Engel et al. [12] and specifically to ion tracks by Eyal et al. [13] and Kluth et al. [14].

Figure 3.3 shows a schematic of a SAXS measurements as performed in the present work on a thin sample in transmission geometry. The incident X-ray beam with wavevector \mathbf{k}_i hits the sample under an angle γ and the majority of the transmitted X-ray photons experience no change in the direction of their wavevector. However, some photons undergo scattering and show a change in momentum to \mathbf{k}_0 by an angle 2θ , comparable to XRD as discussed in Sect. 3.2.

The fluctuations in electronic density within the target lead to differences in the number of photons scattered from different regions within the sample. A two-dimensional detector plane (SAXS detector) collects the X-rays deflected under angles below $\sim 10^\circ$, hence the name small angle X-ray scattering. A beam-stop is used to protect the detector from the high intensity beam of the transmitted X-rays. It also introduces an experimental lower limit for angles measured by SAXS. Typically angles between 0.1 and 10° are resolved, which correspond to structures sizes between 1 and 100 nm. To probe dimensions smaller than 1 nm, such as the sizes of typical lattice constants, measurement under larger angles are required. This technique is referred to as wide angle X-ray scattering (WAXS). A WAXS detector can also be positioned behind the sample to capture those photons which are scattered under larger angles than detectable by the SAXS detector. The WAXS can then give

information about the crystal structure of the sample and is essentially the same technique as XRD.

The total scattering amplitude $F(\mathbf{q})$ for an ensemble of n scatterers with individual scattering amplitudes $f_1(\theta)$, $f_2(\theta)$, \dots , $f_n(\theta)$ and real space vectors \mathbf{r}_1 , \mathbf{r}_2 , \dots , \mathbf{r}_n (each to the location of each scatterer j relative to an arbitrary origin $\mathbf{r} = 0$) is defined as [11]:

$$F(\mathbf{q}) = \sum_{j=1}^n f_j(\theta) \exp(i\mathbf{q} \cdot \mathbf{r}_j) \quad (3.6)$$

In general, f_j is dependent on 2θ , although it can be assumed to be constant for small angles, i.e. $\cos(\theta \rightarrow 0) = 1$. For a large number n of scatterers and an infinitesimal $d\mathbf{r}$, the scattering amplitudes can be represented by the scattering length density (SLD) function, such that $\beta(\mathbf{r}) d\mathbf{r} = f(\theta)$. This replaces the sum with a volume integral:

$$F(\mathbf{q}) = \int \beta(\mathbf{r}) \exp(i\mathbf{q} \cdot \mathbf{r}) d\mathbf{r} \quad (3.7)$$

If Eq.(3.7) is applied on an ensemble of scatterers with $\beta(\mathbf{r})$ embedded within a homogeneous matrix with $\beta_0 = \text{const.}$, only the difference in SLD is observed, thus $\Delta\beta(\mathbf{r}) = \beta(\mathbf{r}) - \beta_0$. The scattering amplitude $F(\mathbf{q})$ then assumes the form:

$$F(\mathbf{q}) = \int \Delta\beta(\mathbf{r}) \exp(i\mathbf{q} \cdot \mathbf{r}) d\mathbf{r} \quad (3.8)$$

The total SLD β is correlated with the SLD of each individual scatterer β_j via [11]:

$$\beta(\mathbf{r}) = \sum_{j=1}^n \beta_j(\mathbf{r} - \mathbf{r}_j)$$

This allows to derive the proportional correlation between SLD and the electronic charge distribution, $\rho_e(\mathbf{r}) \propto \beta(\mathbf{r})$, and finally the scattering amplitude of the ensemble is:

$$F(\mathbf{q}) = \int \rho_e(\mathbf{r}) \exp(i\mathbf{q} \cdot \mathbf{r}) d\mathbf{r} \quad (3.9)$$

The total scattering intensity $I(\mathbf{q})$ of an ensemble of objects can be calculated by taking the sum of the interaction between all scatterers and separated into two factors:

1. The scattering amplitude $F(\mathbf{q})$, describing the scattering from the objects.
2. The structure factor $S(\mathbf{q})$, describing the inter-particle scattering.

For an ensemble of n identical scatterers the scattering intensity is²:

²In general, the expression for the scattering intensity from a system of n scatterers is defined as $I(\mathbf{q}) = n [\langle F(\mathbf{q}) \rangle^2 S(\mathbf{q}) + \langle F^2(\mathbf{q}) \rangle - \langle F(\mathbf{q}) \rangle^2]$. The difference, the so-called Laue scattering term, cancels out for scattering systems independent of time as in the present work.

$$I(\mathbf{q}) = n \cdot F(\mathbf{q})^2 S(\mathbf{q}) \quad (3.10)$$

For sufficiently diluted particles with negligible neighbour-neighbour-interaction, such as the ion tracks in the present work, the structure factor $S(\mathbf{q}) \rightarrow 1$, which simplifies:

$$I(\mathbf{q}) = n \cdot F(\mathbf{q})^2 \quad (3.11)$$

For complex scatterers, $F(\mathbf{q})$ may not possess an analytical solution and calculations with numerical methods are necessary. However, for many scattering objects, such as spheres or cylinders with simple radial densities, an analytical form can often be derived.

3.3.1 Scattering Patterns of Cylindrical Objects

Ion Track Models

For most ion tracks of cylindrical geometry, the measured SAXS patterns can be approximated using analytical models. Such models make the assumption that the ion track consists of a cylinder that is embedded into a host matrix and differs from the matrix with its electronic density. Figure 3.4 shows radial electronic density profiles $\rho_e(r)$ for two different cylindrical models which can be used for the fitting of ion track SAXS patterns:

- (a) The hard cylinder model assumes a simple cylinder with radius R and length L . The parameter $\Delta\rho_e = \rho_e - \rho_{e0}$ represents the difference in electronic density between the scatterer with electronic density ρ_e and its surrounding host matrix with electronic density ρ_{e0} . For amorphous tracks within a crystalline matrix, as for the ion tracks in the present work, $\Delta\rho_e$ is only a few percent (or less) different from the electronic density ρ_{e0} of the host matrix it is embedded in. This model is used for the description of all ion tracks in the present work [15, 16].
- (b) The core-shell cylinder model uses two concentric cylinders with inner radius R_1 , outer radius R_2 , and length L . The volume of the two regions show both different electronic densities (ρ_{e1} and ρ_{e2} , respectively) compared to ρ_{e0} of the undamaged material. This model allows us to describe ion tracks with an underdense core and overdense shell. It was not used in the present work, but was successfully used to describe ion tracks in amorphous materials [14, 17].

Scattering Amplitudes

The scattering amplitude³ $F(\mathbf{q})$ can be derived by computing the volume integral over $\rho_e(\mathbf{r}) \cdot \exp(i\mathbf{q} \cdot \mathbf{r})$ in Eq. (3.9) [12]. To resemble the geometry of the ion tracks, cylindrical coordinates are used for \mathbf{r} and \mathbf{q} .

³All equations in this section can also be defined with the scattering amplitude replaced by the form factor. However, as the form factor is dimensionless this requires additional constants.

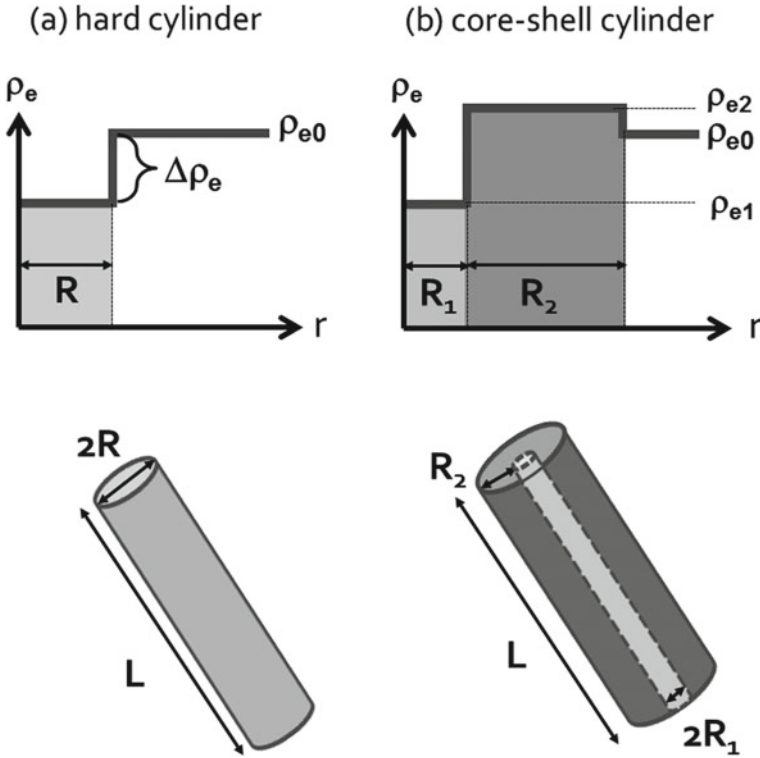


Fig. 3.4 Radial electron density profiles $\rho_e(r)$ modelling the ion track as **a** hard cylinder and **b** core-shell cylinder

$$\mathbf{r} = \begin{pmatrix} r \cdot \cos \varphi \\ r \cdot \sin \varphi \\ z \end{pmatrix} \quad \text{and} \quad \mathbf{q} = \begin{pmatrix} q_r \cdot \cos \phi \\ q_r \cdot \sin \phi \\ q_z \end{pmatrix} \quad (3.12)$$

This simplifies the argument of the exponential function to $\mathbf{q} \cdot \mathbf{r} = q_r r \cos \varphi \cos \phi + q_r r \sin \varphi \sin \phi + q_z z = q_r r \cos(\varphi - \phi) + q_z z$. The cylindrical symmetry allows us to assume a radial electronic density distribution, thus $\rho_e(r, \varphi, z) = \rho_e(r, z)$. Using $d\mathbf{r} = r \cdot dr d\varphi dz$, the integral from Eq. (3.9) is then rewritten as:

$$F(\mathbf{q}) = \int_{-\infty}^{\infty} \int_{-\pi}^{\pi} \int_0^{\infty} \rho_e(r, z) \exp(i [q_r r \cos(\varphi - \phi) + q_z z]) r dr d\varphi dz \quad (3.13)$$

The argument of the cosine can be substituted as $\psi = \varphi - \phi$. The cylindrical symmetry allows similar limits for the polar integration, such that:

$$F(\mathbf{q}) = \int_{-\infty}^{\infty} \int_{-\pi}^{\pi} \int_0^{\infty} \rho_e(r, z) \exp(i q_r r \cos \psi) \cdot \exp(i q_z z) r dr d\psi dz \quad (3.14)$$

The polar integral can be analytically solved with a zero-order Bessel-function,

$$J_0(q_r r) = \frac{1}{2\pi} \int_{-\pi}^{\pi} \exp(i q_r r \cos \psi) d\psi$$

simplifying $F(\mathbf{q})$ to:

$$F(\mathbf{q}) = 2\pi \int_{-\infty}^{\infty} \exp(i q_z z) dz \int_0^{\infty} \rho_e(r, z) J_0(q_r r) r dr \quad (3.15)$$

This work uses exclusively the hard cylinder model shown in Fig. 3.4a with radius R , length L , and a constant difference in its electronic density $\Delta\rho_e$. The electronic density distribution $\rho_e(r, z)$ of the hard cylinder model is:

$$\rho_e(r, z) = \begin{cases} \Delta\rho_e & \text{for : } r \leq R \text{ and } |z| \leq L/2 \\ 0 & \text{otherwise} \end{cases}, \quad (3.16)$$

The longitudinal integral can then be analytically computed to:

$$\int_{-\infty}^{\infty} \rho_e(r, z) \exp(i q_z z) dz = \int_{-L/2}^{L/2} \rho_e(r) \exp(i q_z z) dz = \Delta\rho_e \frac{\sin(q_z L/2)}{q_z/2} \quad (3.17)$$

When Eq. (3.17) is substituted into Eq. (3.15), the following expression is obtained:

$$F(\mathbf{q}) = L \frac{\sin(q_z L/2)}{q_z L/2} 2\pi \int_0^R \Delta\rho_e \cdot J_0(q_r r) r dr \quad (3.18)$$

To evaluate the remaining radial integral, the following identity is used, with $J_1(x)$ as the first-order Bessel function:

$$R \cdot J_1(q_r R)/q_r = \int_0^R J_0(q_r r) r dr \quad (3.19)$$

This results in:

$$F(\mathbf{q}) = 2\pi R^2 L \Delta\rho_e \frac{\sin(q_z L)}{q_z L} \frac{J_1(q_r R)}{q_r R} \quad (3.20)$$

At small angles, q_z is small, hence the approximation

$$\lim_{q_z \rightarrow 0} \sin(q_z L/2) / (q_z L/2) = 1$$

is justified. The scattering amplitude then finally has the form [12, 15]:

$$F(q_r) = 2\pi R^2 L \Delta\rho_e \frac{J_1(q_r R)}{q_r R} \quad (3.21)$$

For the purpose of simplification, q_r is simply referred to as q -vector for the remainder of this work with:

$$q := q_r = \sqrt{q_x^2 + q_y^2} \quad (3.22)$$

Scattering Intensities

The SAXS measurements in the present work typically average over more than 1 million tracks. Although these tracks all possess nearly identical radii, a polydispersity parameter was introduced to take small variations between the individual tracks as well as radial changes along the length of individual tracks into account. For this purpose, the intensity was convoluted with a Gaussian distribution with standard deviation σ_R . Furthermore, it is assumed that not all tracks are perfectly aligned under an angle α to the incident X-ray beam. Hence, a small angular distribution is also used through a Gaussian distribution with σ_α . The total scattering intensity $I(q)$ can be expressed with the following formula:

$$I(q) = I_0 \frac{1}{\sqrt{2\pi\sigma_R^2}} \frac{1}{\sqrt{2\pi\sigma_\alpha^2}} \int \int |F(q, R, L)|^2 \exp\left[-\frac{\alpha^2}{2\sigma_\alpha^2}\right] \exp\left[-\frac{R - \tilde{r}^2}{2\sigma_R^2}\right] d\alpha d\tilde{r} + I_b \quad (3.23)$$

This formula can be used for non-linear least squares fitting to the experimental patterns in this work. The fitting parameters resulting from this expression are listed in Table 3.1. It is noted that the intensity $I_0 = I(q \rightarrow 0)$ superposes with the transmitted primary (non-scattered) beam and thus is not accessible by the measurement of the SAXS detector. In fact, for low values of q , the scattered photons are blocked out by a beam-stop to prevent damage of the detector from the very intense primary beam.

To increase the speed of the fitting algorithm, the polydispersity integrals for radius and angle are typically only computed for $\pm 3\sigma_R$ and $\pm 3\sigma_\alpha$, respectively. The track length is not fitted but derived from the sample thickness or ion track length estimate using SRIM [18], whatever is shorter. From the parameters that can be directly obtained from the fit of the SAXS patterns, the difference in relative density $\Delta\rho$ between track and host matrix can be calculated. Most ion tracks in this work consist of amorphous zones that only differ from the crystalline host structure they are embedded in by a small difference in density. To calculate the relative density

Table 3.1 Fitting parameters of the hard cylinder model used in the present work

Symbol	Description:
I_0	Scattering intensity at $q \rightarrow 0$
R	Ion track radius
σ_R	Radius polydispersity
σ_α	Tilt angle polydispersity
I_b	Background adjustment
L	Track length (fixed value)

difference, an accurate calibration of the scattering intensity is required (compare Sect. 4.4.2 for details on the calibration). From Eq. (3.20) the scattering amplitude $F(q)$ at $q \rightarrow 0$ can be derived⁴ as:

$$F(q \rightarrow 0) = \pi R^2 L \Delta \rho_e \quad (3.24)$$

Combining this expression with the definition of intensity for a track density N from Eq. (3.23) leads to:

$$I_0 = I(q \rightarrow 0) = N |F(q \rightarrow 0)|^2 = N |\Delta \rho_e|^2 (\pi R^2 L)^2 = N |\Delta \rho_e|^2 V^2 \quad (3.25)$$

with the individual track volume $V = \pi R^2 L$ known from the parameters the fit provides. As the intensity depends on the *square* of the electronic density difference, no conclusion can be made from SAXS whether the particle is over- or under-dense compared to its host matrix. The equation assumes a formation efficiency of 100%, thus every single ion results into the formation of an ion track, which is reasonable for the present work.

To get a reliable value for the track length parameter L , ideally samples with a thickness below the estimated ion range are used. For swift heavy ions in the GeV-regime, this corresponds to $L \lesssim 100 \mu\text{m}$. Otherwise the distance between the sample surface and the point of the stopping power falling below the track formation threshold is used instead. Although this value can be calculated by SRIM [18], this method leads to larger uncertainties in L as the error of the SRIM values are often around 10%. Therefore, the majority of samples used in the present work were sufficiently thin and only when irradiation was carried out using 100–200 MeV ions, the estimated ion range had to be used to estimate L .

To relate the change in the electronic scattering length density $\Delta \rho_e$ [cm^{-2}] with the mass density ρ [$\text{g}\cdot\text{cm}^{-3}$], $\Delta \rho_e$ requires normalisation to the total electronic density ρ_{e0} . This can be calculated, provided the exact stoichiometric composition is known. Assuming the density is reduced by the same amount of anions and cations escaping from the structure and the stoichiometry remains unchanged, the relative mass density $\Delta \rho$ [no units] is calculated via:

$$\Delta \rho = \Delta \rho_e / \rho_{e0} = I_0 \cdot N^{-1} (\rho_{e0} \pi R^2 L)^{-2} \quad (3.26)$$

3.3.2 Intersection Between the Ewald Sphere and Ion Tracks

The scattering pattern seen on a 2D-detector screen resembles the intersection of the Ewald sphere with the reciprocal representation of the scattering objects, similar as discussed for the description of XRD in Sect. 3.2.

⁴using $\lim_{x \rightarrow 0} J_1(x)/x = 0.5$ and $\lim_{x \rightarrow 0} \sin(x)/x = 1$.

Figure 3.5a shows a schematic for the scattering of the incident X-ray \mathbf{k}_i and the elastic scattered beam \mathbf{k}_0 . The small angles and short wavelengths of SAXS experiments result in an Ewald sphere (blue) with a radius that is large compared to the size of the reciprocal object. As the cylinders in reciprocal space only span across a small region of the surface of the Ewald sphere, its curvature can be approximated by a straight wavefront for most nano-sized angles (small angle approximation). The ion tracks resemble long, narrow cylinders in real space, hence, in reciprocal space they assume the shape of a thin disk with a radial oscillating pattern. The oscillations between maxima follow the shape of a Bessel function as in Eq. (3.20) with spacings $\Delta q = 2\pi/R$ and a decrease in intensity. If the main axis of the cylinders is in alignment with the direction of the X-ray beam \mathbf{k}_i ($\gamma = 0$), the reciprocal cylinder disk intersects with the Ewald sphere tangential. The Ewald sphere does not overlap with the entire width of the disk, due to its small thickness.

For a cylinder tilted by an angle γ away from the direction of the X-ray beam, the reciprocal cylinder disk responds with a rotation in q -space as well. For an angle α on the detector plane between q_x and q_y and without using the small angle approximation for the scattering angle 2θ , the \mathbf{q} -vector transforms to [12]:

$$q_x = |\mathbf{q}| \cdot (\cos \alpha \cos \gamma \cos \theta + \sin \gamma \sin \theta) \quad (3.27)$$

$$q_y = |\mathbf{q}| \cdot (-\sin \alpha \cos \theta) \quad (3.28)$$

$$q_z = |\mathbf{q}| \cdot (\cos \alpha \sin \gamma \cos \theta - \cos \gamma \sin \theta) \quad (3.29)$$

Figure 3.5b shows the upper section of the reciprocal cylinder to tilt into the Ewald sphere and the lower section further away from the sphere surface. Due to the finite thickness of the reciprocal cylinder disk, its middle section still intersects with the surface of the Ewald sphere. These areas are indicated by the red dashed line and are of curved character due to the curvature of the Ewald sphere. The curvature is reduced for higher increased tilt angles γ or X-rays with larger \mathbf{k}_i (higher energies). The intersection points that make up a typical detector image resemble a highly anisotropic pattern of the shape of a streak.

3.3.3 Experimental SAXS Detector Images

Figure 3.6a1 shows an experimental detector image of aligned ion tracks that represents the interaction between the cylindrical geometry and the Ewald sphere for 11 keV X-rays.

The experimental detector images in Fig. 3.6a2, a3 are showing such streaks for angles $\gamma = 5^\circ$ and $\gamma = 10^\circ$, respectively. Since the geometry remains unchanged, the patterns all show similarly spaced oscillations. For small values of γ , the streaks are slightly bent and their intensity is covering a larger area. For larger angles, the streaks become straight and their intensity is narrow and more distinctive. This can be understood from Fig. 3.5b, as the higher angle decreases the area of inter-

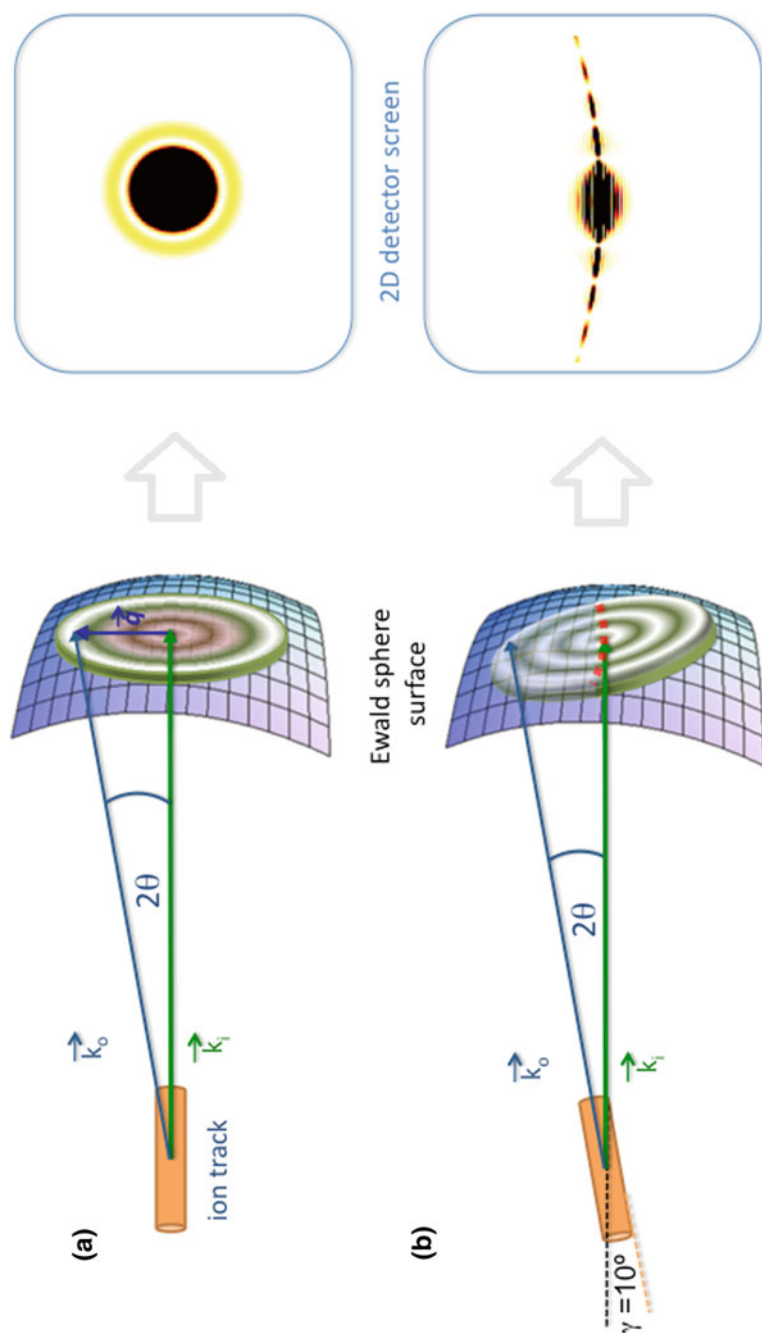


Fig. 3.5 **a** The incident \mathbf{k}_i and scattered \mathbf{k}_o beams are shown for an arbitrary \mathbf{q} -vector (navy blue arrow) on the surface of the Ewald sphere (purple, only partially shown), where it intersects with the disk-shaped reciprocal cylinder (green). The intersection area between Ewald sphere and reciprocal cylinder (transparent red) result in the isotropic SAXS pattern measured by the 2D-detector. **b** For the angle $\gamma = 10^\circ$ between X-ray beam and cylinder axis, the upper part of the reciprocal cylinder tilts into the Ewald sphere, while its lower part tilts away from the surface of the Ewald sphere. The remaining intersection points between tilted reciprocal cylinder disk and the Ewald sphere form a banded streak pattern (red dashed line) when measured by a 2D-detector

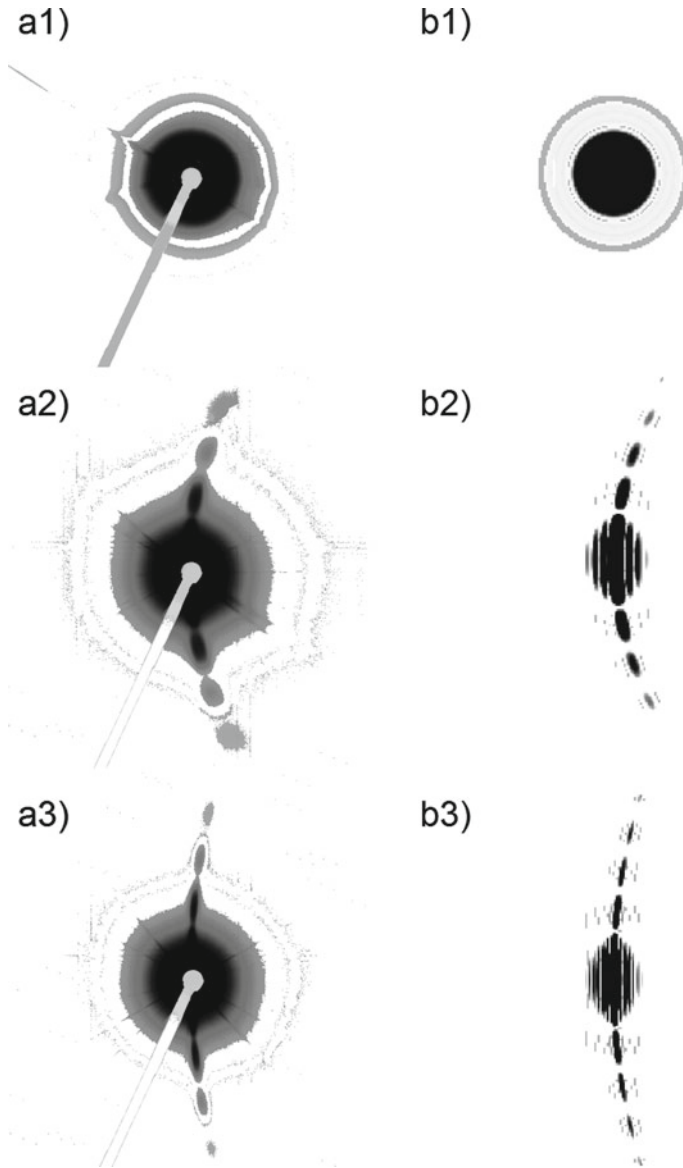


Fig. 3.6 a1–a3 Experimental detector images of ion tracks in quartz and b1–b3 analytically calculated ion tracks. Patterns are shown for angles γ between incident X-ray beam and track direction of 0° (top row), 5° (centre row), and 10° (bottom row). Darker shades correspond to high scattering intensities and vice versa

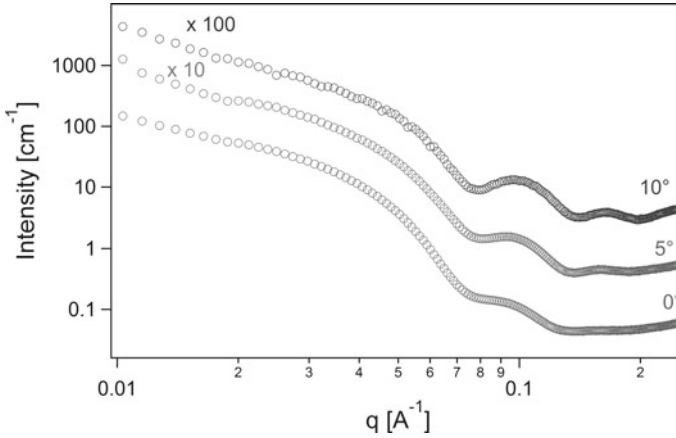


Fig. 3.7 Experimental SAXS patterns for angles γ between incident X-rays and ion track direction of 0° (top circles), 5° (centre circles), and 10° (bottom circles). The SAXS patterns were obtained by isolating the “streak” in the 2D-SAXS images from Fig. 3.6a1–a3. Patterns are offset to enhance visibility

section between the reciprocal cylinder disk and the surface of the Ewald sphere. Figure 3.7 shows experimental the SAXS intensities along the streaks as a function of $q = |\mathbf{q}|$ for the three different values of γ shown in Figure 3.6a1–a3. Only two oscillations are visible as the patterns level out to a background intensity of approximately 0.1 cm^{-1} .

Using the analytical Bessel-function formula from Eq. (3.23), an ab-initio calculation of the SAXS images can be performed. Figure 3.6b1–b3 show calculated SAXS detector images for ion tracks in alignment with X-ray beam $\gamma = 0^\circ$ as well as with a tilt of 5 and 10° at an X-ray energy of 11 keV. The calculations assumed a cylindrical geometry with a radius of 5 nm and a length of $1 \mu\text{m}$. The experimental patterns show a very comparable bending angle and oscillations as reproduced by the calculations. The shorter length was chosen to reduce the computational requirements. For longer track lengths, the oscillations would show similar spacings and angles, but would appear much thinner.

The general shape of the SAXS pattern is governed by an oscillating function that is decreasing in intensity, following Eq. (3.23). The SAXS images under tilted geometry show a streak with more visible oscillations than its aligned counterpart. With an increase of the angle γ between the main axis of the ion track and the X-ray beam direction, the streaks also become more straight. The strong intensity oscillations indicate a sharp density transition between the track and the surrounding matrix.

It is further noted that SAXS averages over $> 10^7$ tracks for a typical measurements in this work, carried out with a beam-size diameter $\varnothing \approx 200 \mu\text{m}$ on samples irradiated with ion fluences of $1 \times 10^{11} \text{ cm}^{-2}$. However, the mono-energetic ion irradiation normal to the surface produces almost identical, well-separated, and parallel ion

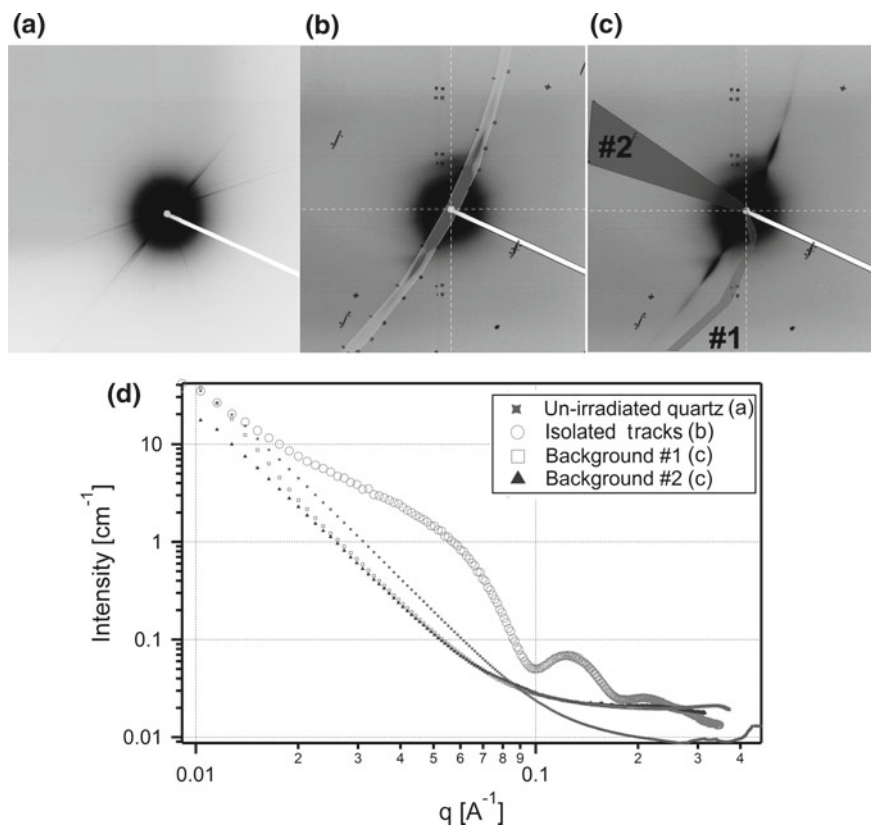


Fig. 3.8 SAXS detector images for **a** non-irradiated quartz sample, **b** ion irradiated quartz sample with a mask around the streak, **c** ion irradiated quartz sample with two different masks for background subtraction; Darker colours correspond to high scattering intensities. **d** The 1D SAXS patterns corresponding to the masked areas in the images **a–c**

tracks. Hence, the information from the SAXS analysis can be related to the of “individual” track structure.

To subtract the background the pattern of a non-irradiated sample can be used. Alternatively a region on the tilted irradiated sample can be used, as the radial component of the track scattering is contracted in the thin oscillating streaks. Typically, the latter technique was employed in this work as it provides better results due to identical sample thickness and composition as well as subtracting out potential shadowing effects that would otherwise remain in the difference image.

Figure 3.8 shows different SAXS detector images for quartz. The SAXS image of a quartz sample without ion tracks (a) mainly consists of an isotropic scattering around the origin. The thin straight lines through the centre are a result of parasitic scattering within the sample and can also be observed in some quartz samples with ion tracks. For the image of a tilted ion track in quartz (b) a characteristic anisotropic

streak is visible. Only the streak is isolated (shaded area), allowing to transform the 2D SAXS image into a 1D-pattern. To subtract the background two different methods are discussed (c). Method #1 follows the area of the streak closely and provides the most accurate background in case of large variations of the background scattering. Method #2 is chosen perpendicular to the streak.

Figure 3.8d displays 1D-patterns for each background together with the isolated scattering pattern for the ion tracks (open circles). The pattern from the non-irradiated sample (solid stars) provides an acceptable method for background subtraction. However, at higher q , where the intensity falls rapidly, the pattern is significantly lower than the ion track data. This is a result of the lower background scattering in this particular non-irradiated sample and leads to less pronounced peaks after this background is subtracted. The other two backgrounds were taken from the irradiated sample and give a significant better agreement at high q . Additionally, they also remove potential isotropic components within the sample. Such effects can result from isotropic features, i.e. nano-sized voids that display ring-shaped oscillations at a distinct q -value.

In summary, a direct comparison of the different methods for background subtraction does not show different results for the track parameters, but mainly increase the agreement with the fitting function. For a small number of samples, anisotropic shadowing effects required a scaling of the background between 0.8 and 1.1 to match the intensity at high q -values.

References

1. W.C. Röntgen, Ueber eine neue Art von Strahlen. Sonderabdruck aus den Sitzungsberichten der Würzburger Physik.-medic. Gesellschaft **1895**, 1–11 (1895)
2. W. Demtröder, *Experimentalphysik 2: Elektrizität und Optik* (Springer, Berlin, 2005)
3. D. Attwood, *Soft X-rays and Extreme Ultraviolet Radiation: Principles and Applications* (Cambridge University Press, Cambridge, 2007)
4. J.H. Lambert, *Photometria sive de mensura et gradibus luminis, colorum et umbrae [Photometry, or, On the measure and gradations of light, colors, and shade]* (Eberhardt Klett, 1760)
5. A. Beer, Bestimmung der Absorption des rothen Lichts in farbigen Flüssigkeiten. *Annalen der Physik und Chemie* **86**, 78–88 (1852)
6. O. Glatter, O. Kratky, *Small Angle X-ray Scattering* (Academic Press, Cambridge, 1982)
7. W.H. Bragg, W.L. Bragg, The reflection of X-rays by crystals. *Proc. R. Soc. Lond. A: Math. Phys. Eng. Sci.* **88**(605), 428–438 (1913)
8. D. Albrecht, P. Armbruster, R. Spohr, M. Roth, Small angle neutron scattering from oriented latent nuclear tracks. *Radiat. Eff.* **65**(1–4), 145–148 (1982)
9. L.A. Feigin, D.I. Svergun, *Structure Analysis by Small-Angle X-ray and Neutron Scattering* (Plenum Press, New York, 1987)
10. A. Guinier, G. Fournet, *Small-Angle Scattering of X-rays, Structure of Matter Series* (Wiley, New Jersey, 1955)
11. D.S. Sivia, *Elementary Scattering Theory: For X-ray and Neutron Users* (Oxford University Press, Oxford, 2011)
12. M. Engel, B. Stühn, J.J. Schneider, T. Cornelius, M. Naumann, Small-angle X-ray scattering (SAXS) off parallel, cylindrical, well-defined nanopores: from random pore distribution to highly ordered samples. *Appl. Phys. A* **97**(1), 99–108 (2009)

13. Y. Eyal, S.A. Saleh, Structure model and small-angle scattering cross sections of latent ion tracks in dielectric solids. *J. Appl. Cryst.* **40**, 71 (2007)
14. P. Kluth, C.S. Schnohr, O.H. Pakarinen, F. Djurabekova, D.J. Sprouster, R. Giulian, M.C. Ridgway, A.P. Byrne, C. Trautmann, D.J. Cookson, K. Nordlund, M. Toulemonde, Fine structure in swift heavy ion tracks in amorphous SiO₂. *Phys. Rev. Lett.* **101**, 175503–175506 (2008)
15. B. Afra, M. Lang, M.D. Rodriguez, J. Zhang, R. Giulian, N. Kirby, R.C. Ewing, C. Trautmann, M. Toulemonde, P. Kluth, Annealing kinetics of latent particle tracks in Durango apatite. *Phys. Rev. B* **83**, 064116 (2011)
16. D. Schauries, B. Afra, T. Bierschenk, M. Lang, M.D. Rodriguez, C. Trautmann, W. Li, R.C. Ewing, P. Kluth, The shape of ion tracks in natural apatite. *Nucl. Instrum. Method Phys. Res. B* **326**, 117–120 (2014). (17th International Conference on Radiation Effects in Insulators (REI))
17. T. Bierschenk, R. Giulian, B. Afra, M.D. Rodriguez, D. Schauries, S. Mudie, O.H. Pakarinen, F. Djurabekova, K. Nordlund, O. Osmani, N. Medvedev, B. Rethfeld, M.C. Ridgway, P. Kluth, Latent ion tracks in amorphous silicon. *Phys. Rev. B* **88**, 174111 (2013)
18. J.F. Ziegler, J.P. Biersack, U. Littmark, *The Stopping and Range of Ions in Matter* (Pergamon, New York, 1985)

Chapter 4

Experimental Methods



This chapter describes the experimental techniques used for the present work. These range from the handling of the samples in the lab to the application of large-scale facilities for ion acceleration and X-ray and neutron characterisation.

Section 4.1 discusses the preparation of the samples, including the separation of the natural specimen from the rock and their thickness reduction through polishing.

Section 4.2 discusses the set-up and handling of diamond anvil cells (DAC) to expose the samples to an environment of high pressure. The section also describes the capability of heating of the DACs used in this thesis as well as the used pressure calibration method.

Section 4.3 discusses the experimental aspects of the sample irradiation with swift heavy ions. The three different ion accelerators used are compared: Irradiation up to 185 MeV Au was carried out at the Australian National University in Canberra; ions of higher energies were created at either The Universal Linear Accelerator or the Heavy Ion Synchrotron, both located in Darmstadt, Germany.

Section 4.4 discusses the set-up of the Australian Synchrotron in Melbourne, Australia. The focus are small angle X-ray scattering (SAXS) experiments, the primary characterisation technique for ion tracks in this work. This includes the calibration of q -range and scattering intensity as well as the handling of annealing stage and DAC holder.

Section 4.5 briefly shows the generation of neutrons on two different types of neutron sources that were used for the small angle neutron scattering (SANS) experiments in the present work, at the Australian Nuclear Science and Technology Organisation (ANSTO) in Sydney, Australia and at Oak Ridge National Laboratory (ORNL), Tennessee.

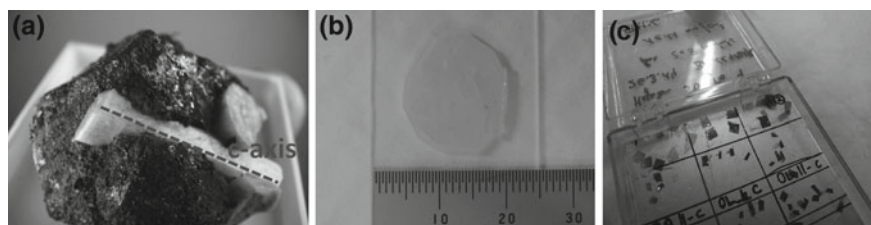


Fig. 4.1 **a** Apatite crystal from Dashkesan (Azerbaijan) embedded in a Co-Fe rock before cutting with its hexagonal structure and *c*-axis clearly visible. **b** Apatite from Durango (Mexico) after it was sliced perpendicular to the *c*-axis to approximately 1 mm in thickness and 15 mm in diameter using the diamond saw. **c** A variety of apatite samples, polished down to $\sim 50\ \mu\text{m}$ thickness, after ion irradiation

4.1 Sample Preparation Techniques

Natural Mineralogical Samples

The sample preparation progress starts with separating the apatite crystal from the rock. For example, the Dashkesan-apatite sample shown in Fig. 4.1a, was surrounded with Co-Fe ore. The hexagonal shape of the apatite single-crystal and its *c*-axis can easily be identified. By using a diamond saw the apatite crystal was cut out of the other minerals within the rock. This required the specimen to be mounted on a glass slide using crystal bond at a temperature of approximately 100°C . Once the apatite crystal was isolated, small layers of approximately 1 mm thickness and 15 mm in diameter were cut from the mineral in two orientations, parallel and perpendicular to the *c*-axis as shown in Fig. 4.1b. The layers were further cut into smaller, individual samples of $\sim 0.2\ \text{cm}^2$ to prevent breaking or crack formation of the fragile material during the polishing process. For polishing, the thin samples were mounted on a polishing tripod using epoxy glue. A rotating disk polishing machine with diamond polishing paper of 15 and $5\ \mu\text{m}$ grain size was used under constant water flow to reduce the sample thickness to between 30 and $200\ \mu\text{m}$. Upon reaching its final thickness, the surface was polished again by using $1\ \mu\text{m}$ diamond paper, removing the larger scratches that occurred during the rough polishing process. Following this, the epoxy glue was removed using acetone for a duration of $\sim 2\text{--}5\ \text{h}$. Finally, the thinned samples were mounted on an aluminium plate for ion radiation, as shown in Fig. 4.1c.

In this work, only two different natural samples from Durango, Mexico and Dashkesan, Azerbaijan were investigated. The different compositions of the two single crystals was determined with microprobe analysis [1, 2]. They show the following halogen composition:

- Durango apatite 3.4 wt% F and 0.4 wt% Cl
- Dashkesan apatite 3.5 wt% F and 0.5 wt% Cl

Synthetic Wafers

The synthetic quartz for this work was purchased as crystalline wafers with thicknesses of 0.5 mm as x -, y - and z -cuts, as well as 0.050 mm for z -cuts only. The cut direction is a technical term for the surface normals along the $[11\bar{2}0]$ -direction (x -cut), $[10\bar{1}0]$ -direction (y -cut) or $[0001]$ -direction (z -cut). The thin wafers did not require any polishing and were directly characterised using SAXS after ion irradiation. The thick quartz wafers were polished to reduce their thicknesses after ion irradiation from the backside to a final thickness of approximately 70–90 μm . This reduces parasitic scattering from the non-irradiated section of the samples, reducing noise levels in the resulting SAXS patterns. The same rotating disk polishing method as described in the previous section was used. Typically a diamond paper of 30 μm grain size was used for polishing the sample down to 0.15 mm, followed by the use of 15 μm grain size. Scratches were removed by using 1 μm grain size paper.

4.2 High-Pressure Diamond Anvil Cells

To expose the samples to high pressures, of similar or higher magnitude as deep within the earth's crust, Diamond Anvil Cells (DAC) were used. For fission tracks, depth levels up to 5000 m are relevant, where typically pressures up to 0.2 GPa are encountered. However, DACs are even capable of reaching far higher pressures, ~ 1 –100 GPa, comparable with much deeper levels within the earth or those present during shock waves. With pressure P defined as force F per area A , i.e.

$$P = \frac{F}{A}, \quad (4.1)$$

pressures in excess of several GPa can only be achieved for reasonable forces when the area is limited to a small region.

Figure 4.2 (bottom) illustrates the device with pictures of an opened and closed DAC. These cells consist of a metallic frame with the key features visible being the diamond anvils, the heater wires, and the screws on the outside. The diamond anvils and their seats are shown schematically in Fig. 4.2 (top). The main components are the two diamonds of a few millimetre in size, fixed onto their tungsten carbide seats. Unlike in the traditional diamond cut, their top end is cut in the shape of a flat anvil with a hexadecagonal surface, called cutlet, of 400 μm diameter. The diamonds are fixed on the seats using Zircar Al-CEM cement that was let dried at 110 $^{\circ}\text{C}$ for 1 h. The cement is used instead of glue for this set-up as the DAC is capable of heating up to 400 $^{\circ}\text{C}$, which would melt the glue. The non-metallic seats are also manufactured to be resistant to creep when heated up. To ensure both diamond surfaces are perfectly parallel to each other, a high level of cleanness and precision is required. The seats also contain a circular opening to allow X-rays to penetrate the cell for in situ measurements.

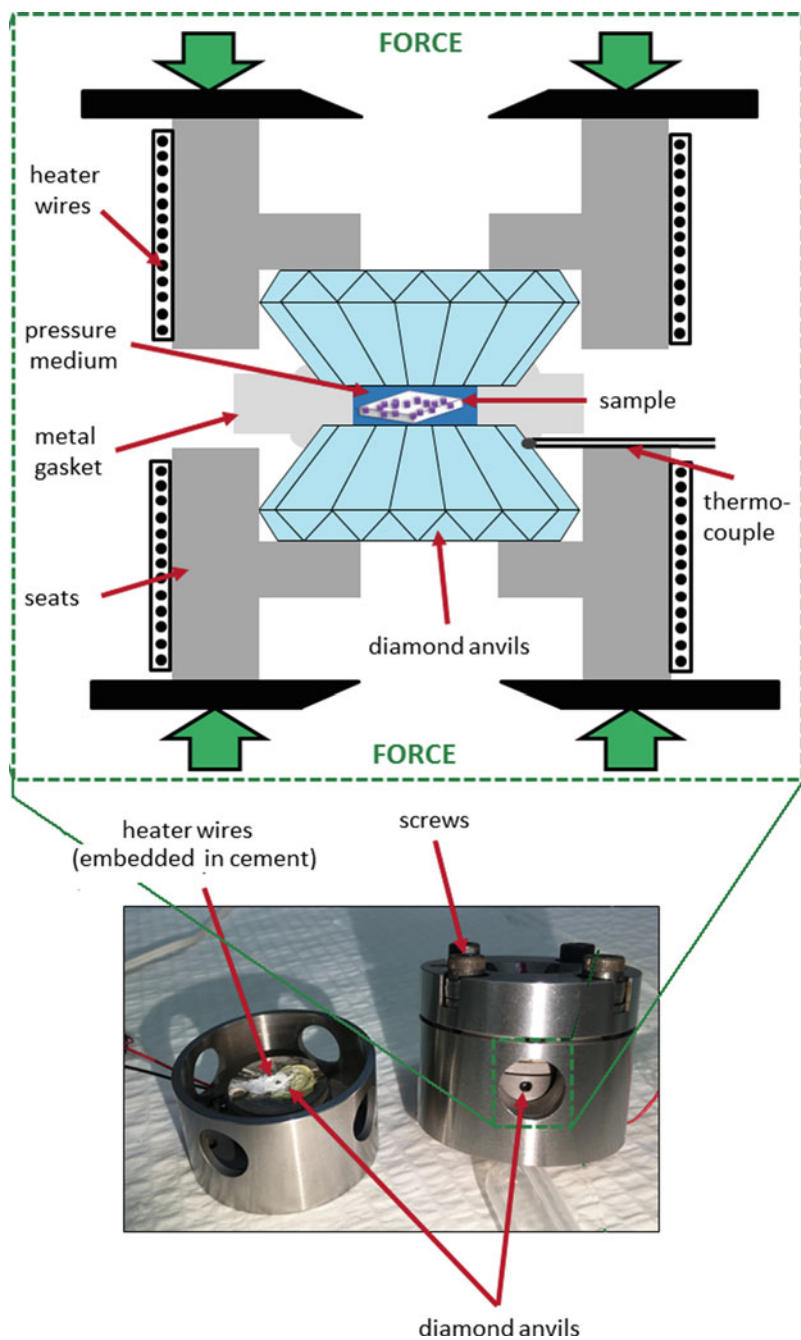


Fig. 4.2 (Top) Schematic of the main components surrounding the diamond seats. (Bottom) Picture of an opened and closed DAC with resistance heating capability

A metal gasket is placed between the two diamonds. A small hole in its centre is used as the pressure volume and can hold samples of dimensions less than $\sim 200\ \mu\text{m}$ in diameter and $50\ \mu\text{m}$ in thickness. The pressure volume is filled with a pressure medium to maintain a true hydrostatic environment and to prevent the closure of the hole upon the application of pressure. Such medium can either be a liquid, solid, or gas. Gaseous media which turn into liquid under pressure have the advantage of maintaining the best hydrostatic pressure-environment, but liquids are easier to handle. In the present work, a mixture of 80% methanol and 20% ethanol was used. Such liquids have the downside of only being applicable for a certain pressure range, as they start to solidify at pressures that are too high (10 GPa for the ethanol/methanol mixture used in the present work [3]). Thus for extremely high pressures, solids are the more appropriate choice. When the gasket is fully filled with a powder instead of a (crystalline) sample, no pressure medium is required to prevent the closure of the gasket hole, although this does not provide hydrostatic pressure conditions. The pressure is applied through force by slowly tightening the four screws and reducing the distance between the two diamond tips. To ensure a parallel alignment of the diamonds, pairs of screws on opposite sides are tightened simultaneously.

The DAC is heated with a metallic coil embedded within a cement disk. It is placed around each diamond to allow temperatures up to approximately 500°C . An S-type thermocouple from Omega Engineering, was attached to one of the diamonds using Zircar cement. Its temperature reading might be below the real temperature of the sample, although this error is expected to be small, due to the good heat conductivity of the diamond and steel gasket [4].

Gasket Indentation

For every DAC set-up, it is crucial to create a new metal gasket capable of holding the sample. This is achieved by putting a suitable gasket in between the two diamonds. Typically steel or rhenium gaskets of approximately $250\ \mu\text{m}$ in thickness are used. Once the screws of the DAC are tightened, the diamonds indent the gasket by approximately $100\ \mu\text{m}$ from each side, so that they are only separated by approximately $50\ \mu\text{m}$ of gasket material. The deformation of the gasket leads to an increased thickness in the gasket around the indent, which can be used as a reference for the remaining thickness of the indentation. The diameter of the indentation is equal with the cutlet size of $400\ \mu\text{m}$.

Figure 4.3 shows optical microscopy images of gaskets before indentation (a) and after less than $70\ \mu\text{m}$ separation between the two diamonds (b) Figure 4.3c shows the gasket with the diamonds removed after a circular-shaped hole was drilled in the remaining layer of the gasket with an easyLab Boehler microDriller using a tungsten carbon drilling tip of $200\ \mu\text{m}$ in diameter. Finally, the gasket is put back in place on the same position as the indenting took place.

It is noted that the indentation process is crucial to achieve the best performance of the cells. Therefore, for best results the hole should be drilled around the centre of the indentation. Non-uniform or unclean indentation results in lower achievable pressure values. It can also make the pressure medium leak outside, resulting in self-closing of the hole.

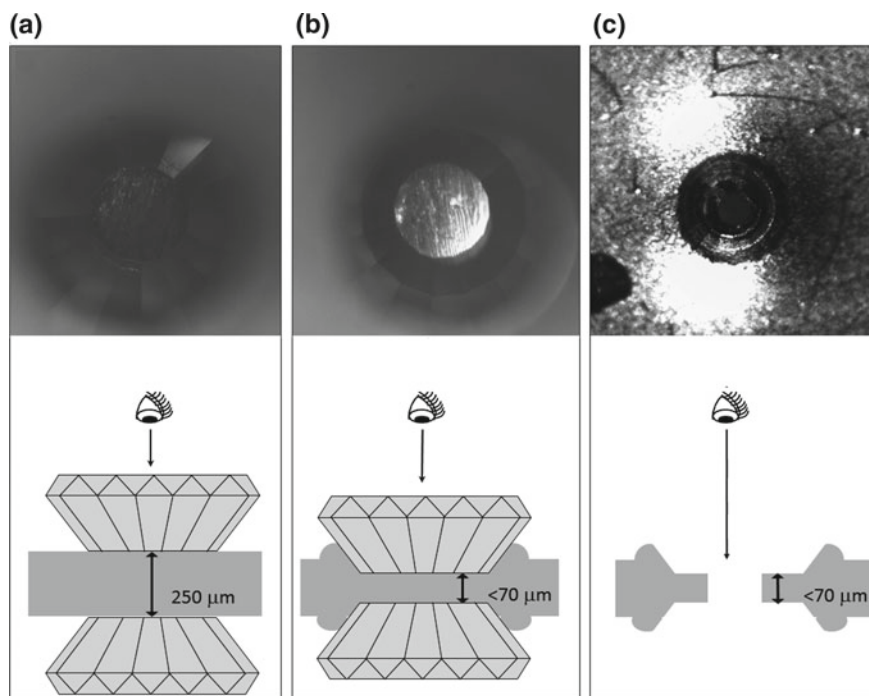


Fig. 4.3 Schematic illustration for the indentation of the gasket in a DAC and corresponding microscope images. **a** Initially the gasket has a thickness of $250\ \mu\text{m}$. **b** After less than $70\ \mu\text{m}$ thickness the indentation results in dark and circular-shaped region in the microscope view (top, centre). **c** Gasket after indenting with removed diamond anvils

Pressure Calibration

The pressure within the cell can be measured using a range of different techniques. They either rely on a known pressure-dependence of the studied material, for example lattice constants, or the addition of a calibrant with a pressure-dependent property. The former method typically requires the use of X-ray diffraction as explained in detail in Sect. 7.2.3. For most of the experiments in this work, however, the widely used ruby fluorescence technique [5] was used.¹ This utilises the pressure-dependence of the fluorescence signal from a ruby crystal ($\text{Cr}:\text{Al}_2\text{O}_3$).

For this purpose a small ruby crystal is inserted into the pressure chamber and exposed to light of a laser with 532 nm wavelength. This leads to a fluorescence spectrum² that is filtered from the bright green laser light and analysed with a spectrometer. It shows two peaks corresponding to the R-line with the main peak at 694.3 nm in

¹Other gems that can be added for calibration of very high pressures or temperatures are Sm:YAG [6] or Sm:SrB₄O₇ [7].

²For the generation of fluorescence light, the incident laser first levels the electrons into higher, excited states. Afterwards the electrons drop to the lower R-state via non-radiative relaxations.

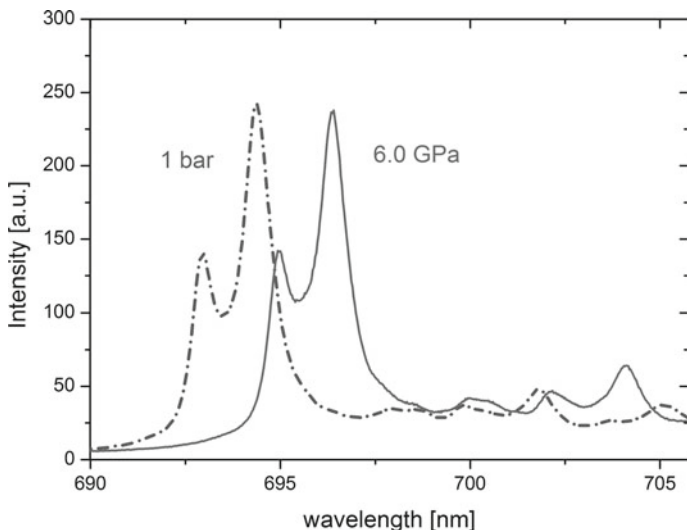


Fig. 4.4 Fluorescence spectrum of a ruby within a DAC without application of pressure (dashed line) and under 6.0 GPa hydrostatic pressure (solid line)

the absence of pressure. Once the sample volume is exposed to elevated pressures, both lines show a shift towards higher wavelengths. The relationship between ruby fluorescence and pressure was initially described by Mao et al. [5] and subsequently improved by Dewaele et al. [8]. Figure 4.4 shows typical fluorescence spectra at ambient pressure (dashed line) and at a pressure of 6.0 GPa (solid line). For temperatures below 100 °C, the pressure P can be calculated from the initial peak wavelength λ_0 and that under pressure λ_p by:

$$P = A/B \left(\left(\lambda_p / \lambda_0 \right)^B - 1 \right) \quad (4.2)$$

with the experimental fitting constants $A = 1920$ GPa and $B = 9.61$. For the pressures in this work that are typically below 10 GPa, the formula can be linearised to:

$$P[\text{GPa}] = A/\lambda_0 \cdot (\lambda_p - \lambda_0) \approx 2.76 \text{ nm}^{-1} \cdot (\lambda_p - \lambda_0) \quad (4.3)$$

Ruby fluorescence on a well resolved peak can measure the pressure with an accuracy to approximately 0.1–0.3 GPa for DACs at room temperature. Main factors that influence the uncertainty are the peak width and the level of hydrostatic pressure. When the cell is heated up, however, the pressure is commonly known to decrease. This is due to the thermal expansion of the tungsten carbide seats [4] and results in uncertainties of pressure up to 50%.

However this state is not stable and the electrons fall back to their initial states under emission of photons of particular wavelengths, resulting in the observed spectrum.

4.3 Swift Heavy Ion Irradiation

The ion tracks in this work were all generated by using swift heavy ion (SHI) irradiation in high energy ion accelerators. They allow us the creation of tracks with full control over ion species and energy, environmental parameters (temperature, pressure) and fluence. The tracks are thus created under nearly identical conditions with almost no variation between them, i.e. mono-disperse and parallel to each other.

Ions of similar energies allow the creation of tracks with a very distinct distribution of their radii and lengths. This approach is superior to natural induced tracks from spontaneous fission, where the tracks are oriented in random directions. When accessing the properties of track annealing, freshly induced tracks possess the advantage of not having experienced a partial recrystallisation and size reduction.

For the SHI-irradiation in this work, three different ion accelerators were used. Ions with an energy range of up to 185 MeV were produced at the Heavy Ion Accelerator Facility (HIAF) at the Australian National University (ANU) in Canberra. Ions of higher energies up to 2.3 GeV were obtained by using the Universal Linear Accelerator (UNIversal Linear ACcelerator) at the Helmholtz Centre for Heavy Ion Research (GSI) in Darmstadt, Germany. While the ANU facility only creates tracks in apatite and quartz of approximately 10 μm in length, the GSI accelerators are capable of producing tracks of approximately 100 μm in length. Finally, to irradiate samples while under pressure within a Diamond Anvil Cell, ions with energies capable of penetrating through more than 2 mm of diamond before hitting the sample with sufficient energy are required. This was achieved by using the SIS (Schwerionen-synchrotron, German for “heavy ion synchrotron”) at GSI with Au ions of 37.2 GeV energy.

4.3.1 ANU Heavy Ion Accelerator Facility

The largest accelerator within the ANU Heavy Ion Accelerator Facility (HIAF) is the 14UD (14 unit double) pelletron accelerator [9], which is essentially a tandem version of a Van de Graaff generator [10]. It was built during the early 1970s and produced its first beam in 1974. Figure 4.5 shows a schematics of the main components of the machine.

Negative ions are initially generated by a Multi Cathode Source of Negative Ions by Caesium Sputtering (MC-SNICS), developed by NEC Corp. These feed a high resolution injector system and a comprehensive pulsing system. The pulser boasts a programmable chopper which produces intervals of beam as short as 50 ps with repetition rates from sub-microseconds to multi-milliseconds. The ions are pre-accelerated to 150 keV. An injection magnet acts as a mass discriminator and a magnetic triplet quadrupole lens focuses the emerging beam. Additional slits can be used to further define the shape of the beam before they enter the accelerator tank.

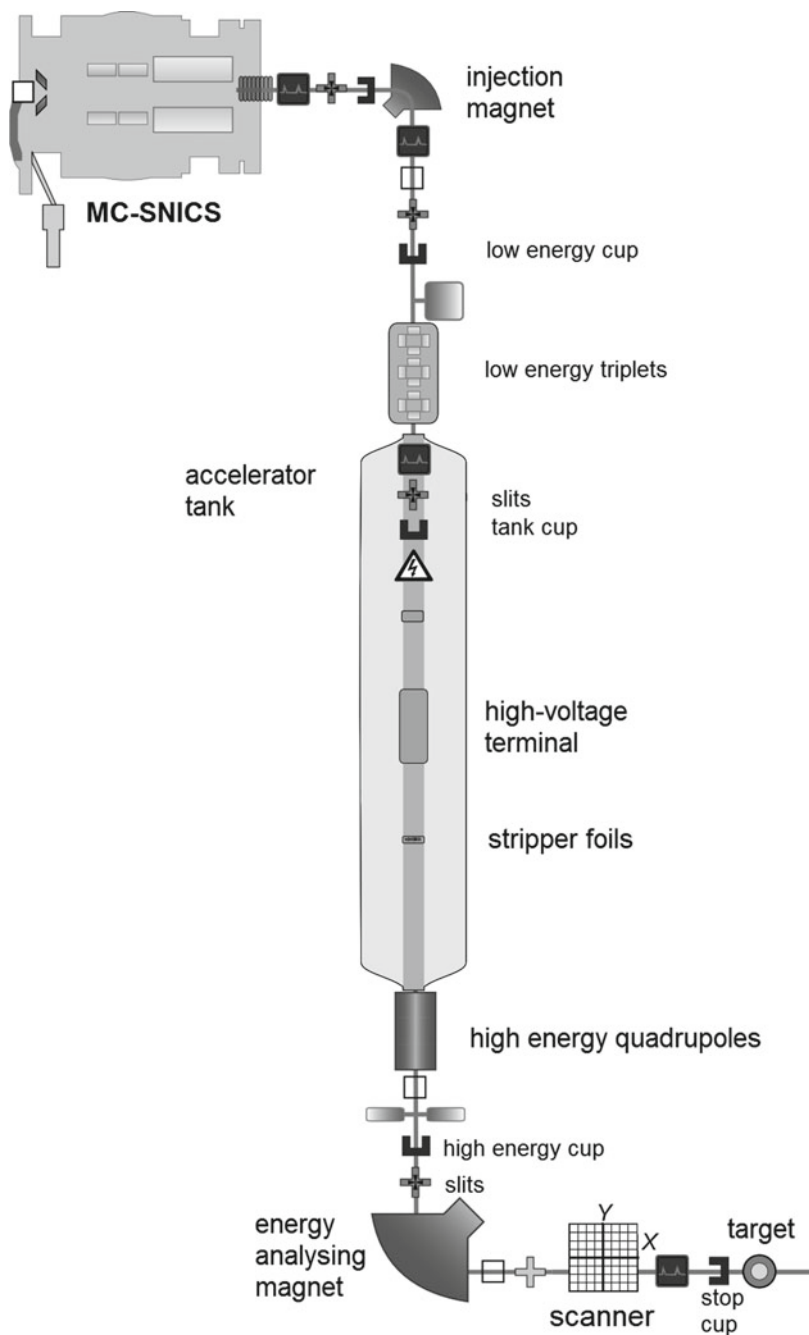


Fig. 4.5 Schematic overview of the ANU Heavy Ion Accelerator (modified screenshot of the control screen, an elaborative description can be found in the text)

The ion beam pulses are then compressed to less than 1 ns in width and injected into the 14UD terminal. Within the terminal a large voltage of up to $V = 13.2$ MV is used to accelerate these negatively-charged ions of charge q to energies $E = q \cdot V$. The charge is acquired through three inductive charging chains of nylon and stainless steel pellets. Each of the chains is 20 m long and moves at speeds in excess of 50 km/h. To prevent unwanted electric discharges, the tank is filled with pressurised sulphur hexafluoride gas (SF_6).

Within the middle of the voltage terminal, the negatively charged ions pass a carbon foil (or alternatively a gas stripper), stripping a significant amount of electrons off, resulting in a spectrum of positively charged ions. After this flip in polarity, the ions are accelerated even further along the second half of the tank until they pass the analysing magnet. The magnet selects the desired charge states (i.e. $13+$ for Au ions with 185 MeV) from the spectrum of differently positively charged ions, although the current component from the other charge state gets lost. From here, the ion beam passes another set of slits and hits the irradiation target at beamline 0. To ensure a homogenous irradiation of the entire sample size, an x-y raster scanner moves the beam over an area of $3 \text{ mm} \times 6 \text{ mm}$ with a sine-pattern. The integrated ion current, respectively the accumulated charge is measured on the sample holder. Its total integrated charge is used to estimate the irradiation fluence. The beam can be directed further into a wide range of other beamlines for a variety of experiments [11]. A range of Faraday cups (compare Fig. 4.5) can be inserted into the pathway of the beam to measure the current at certain points. To maximise the length of the ion tracks, Au ions with an energy of 185 MeV or 0.9 MeV/u were typically used. Their velocity corresponds to $\sim 4\%$ of the speed of light. The ion irradiation was carried out to a fluence of $5 \times 10^{10} \text{ cm}^{-2}$ with an ion flux of $\sim 10^8 \text{ cm}^{-2} \text{ s}^{-1}$.

4.3.2 GSI UNILAC

To accelerate ions to energies up to a several GeV, the GSI UNILAC shown in Fig. 4.6 was used. Its 120 m long tube allows the irradiation with a wide range of ions, which can be produced by different ion sources. In contrast to the inductive charging chains used in HIAF, the UNILAC uses a series of multi-staged radio frequency power amplifiers, leading to a higher, non-linear ion acceleration. Consequently, the ions can reach final energies around 11.4 MeV/u. After passing through three degrading Al-foils, each $1 \mu\text{m}$ in thickness, it is reduced to 11.1 MeV/u or 15% the speed of light. These Al-foils are used as a secondary-electron transmission monitor to measure and calibrate the ion flux. Additional Al-foils of thicknesses between 16 and $64 \mu\text{m}$ can be used to reduce the energy on the samples. In contrast to the ANU HIAF, the irradiation is carried out with a defocused beam, capable of simultaneously irradiating an area of approximately $5 \text{ cm} \times 5 \text{ cm}$.

In this work, irradiations were carried out at the M-branch with 8.4 MeV/u (1.7 GeV for ^{197}Au) and 11.1 MeV/u (2.2 GeV for ^{197}Au , 2.3 GeV for ^{209}Bi) with an ion flux of approximately $2 \times 10^8 \text{ cm}^{-2} \text{ s}^{-1}$. The irradiation fluences

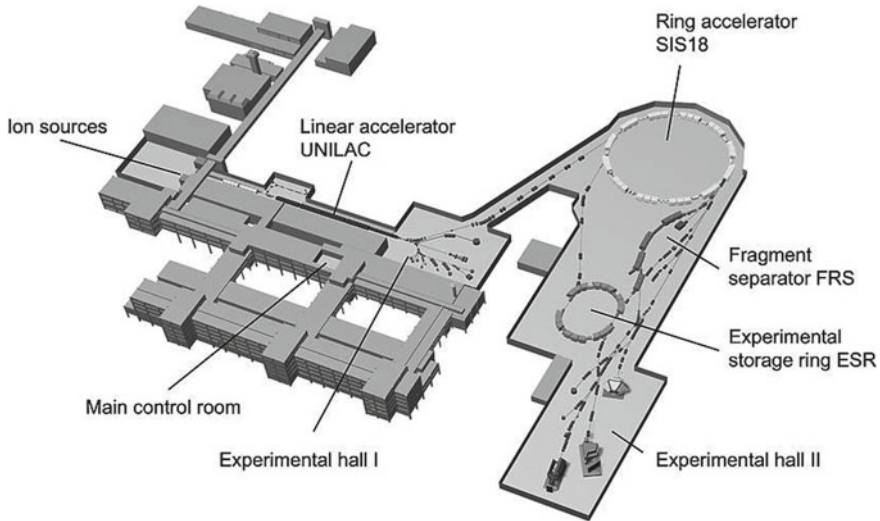


Fig. 4.6 Schematic overview of the UNILAC and SIS18 accelerator facilities at GSI in Darmstadt, Germany [Image courtesy: GSI Darmstadt]

$F = \text{flux} \times \text{time}$ were typically chosen to obtain a high track density, but still maintain individual tracks without significant track overlap (compare Sect. 5.2.1). This was typically achieved at approximately $1 \times 10^{11} \text{ cm}^{-2}$ within a time t of several minutes. We assume that each ion leads to the formation of an ion track, therefore the fluence is equal to the number of ion tracks per area N .

The tracks created by this accelerator were used for most experiments in this work as to their length of nearly 10 times above those generated in HIAF. The resulting high scattering volume leads to a better signal to noise ratio during track characterisation [12]. In addition, tracks generated with these high energies show a greater uniformity along their length resulting in more pronounced SAXS patterns and a well-defined track radius.

4.3.3 GSI SIS 18

The ions from the UNILAC can be further accelerated by injecting them into the SIS-18 ring as shown in Fig. 4.6. With its circumference of 216 m, this synchrotron device accelerates the charged ions in a near-circular path. This is achieved through the use of combined electric and magnetic fields, similar to an electron synchrotron (compare Sect. 4.4). This allows us to increase the ion energy from initially several MeV/u to relativistic energies of up to 2 GeV/u or 90% the speed of light.

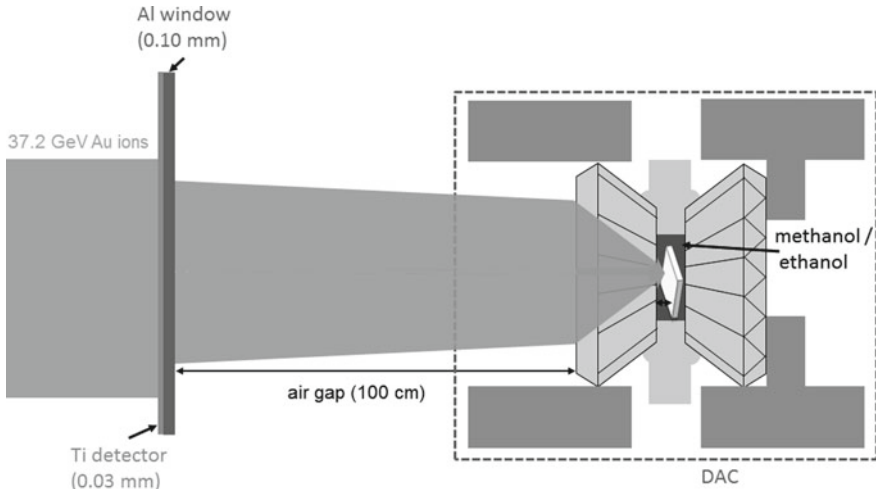


Fig. 4.7 Schematic overview of the irradiation of a diamond anvil cell (DAC) at the SIS18 accelerator with 37.2 GeV Au ions

Irradiation of Diamond Anvil Cells

The ions produced by the SIS can be used to irradiate samples within a diamond anvil cell (DAC) as they possess sufficient energy to penetrate several millimetres of diamond and still retain enough energy to create ion tracks over the entire sample length. The energy loss of the ion along its penetration through the diamond can be calculated by SRIM-2008 [13]. Figure 4.7 shows a schematic of the DAC-irradiation after M. Lang. A more detailed overview is given in his PhD thesis [14].

The irradiation was carried out with ^{197}Au ions of 189 MeV/u, which corresponds to an initial energy of 37.2 GeV. An ion fluence of $1 \times 10^{11} \text{ cm}^{-2}$ was used with a flux of $2 \times 10^8 \text{ cm}^{-2} \text{ s}^{-1}$. The ion beam first passes through a beam current monitor consisting of three titanium foils (total thickness 0.03 mm) and loses approximately 0.3 GeV. It then penetrates through an aluminium window (thickness 0.10 mm) where an additional 0.6 GeV gets lost. Subsequently, the ion beam still has to pass an air gap of 100 cm until it reaches the entrance of the DAC, which reduces the ion energy further by 2.8 GeV. Finally, the ions penetrate the diamond of approximately 2.145 mm thickness, which leaves an ion energy of ~ 6.8 GeV when the beam reaches the sample. The energy lost within the $20 \mu\text{m}$ of the methanol/ethanol pressure medium is less than 0.1 GeV and is therefore negligible.

The remaining energy is more than sufficient to form an ion track of several hundred micrometres length. In fact, it is above what is typically used for ion track formation at the UNILAC in the absence of pressure and further away from the Bragg peak in quartz. Because 6.8 GeV Au ions have energies above the Bragg peak, they only possess an energy loss between 16 and 17 nm/keV within $50 \mu\text{m}$ of quartz. Thus, ions of such energies still allow the formation of ion tracks of slightly smaller but still comparable sizes as for ~ 2 GeV Au. The high ion energy upon reaching the

sample also allows room for experimental errors during the irradiation such as a tilt between direction of the beam and diamond length and an underestimation of the diamond thickness that can lead to increased absorption.

The high energy ions typically excite the electrons of any present metallic material, such as the steel component of the DAC, resulting in a radioactivity of the irradiation target. This requires the sample to be kept onsite for a period of several weeks until they can be safely handled outside of the facility.

4.4 Synchrotron-Based Small Angle X-Ray Scattering

For all SAXS measurements in this work, synchrotron radiation was employed due to their high brilliance and high photon flux. This is required to obtain a sufficiently strong SAXS signal that can be used to calculate the track size with sub-nanometre precision.

This section explains the fundamentals of the Australian Synchrotron, where all SAXS experiments were performed. In particular the SAXS/WAXS beamline is introduced and how the set-up at this beamline was tailored to the specific needs of the different experimental questions in this work.

4.4.1 *The Australian Synchrotron*

An electron synchrotron is a circular-shaped particle accelerator that uses synchronised magnetic and electric fields to bring electrons on a circular motion with relativistic velocities (>99.99% speed of light). Since all synchrotron-related X-ray radiation measurements for this work were carried out at the Australian Synchrotron in Melbourne, the functionality of a synchrotron shall be explained on the basis of this accelerator (Fig. 4.8).

The electrons originate from a tungsten cathode by thermal emission, the so-called electron gun (label 1) and enter a Linear Accelerator (LINAC). The LINAC (label 2) utilises a 3 GHz radio frequency (RF) cavity to accelerate the electrons to an energy of 100 MeV.

The electrons then enter the booster synchrotron (label 3) with its 130 m circumference for pre-acceleration. A linear accelerator powerful enough to bring electrons to the final energy of 3 GeV would be substantially longer (e.g. Stanford Linear Accelerator Center [15]). Inside the booster synchrotron, another RF cavity with 500 MHz brings the electrons to their final energy. The electrons are kept on a circular path through dipole magnets, which slightly bend the electron beam, hence they are called bending magnets (BM). Afterward they are injected into the storage ring (label 4). It has a circumference of 216 m and uses a total of 28 BMs. Each of them changes the direction of the velocity of the relativistic electrons by a few degrees. This acceleration by the BM results in the generation of X-rays, the so-called syn-

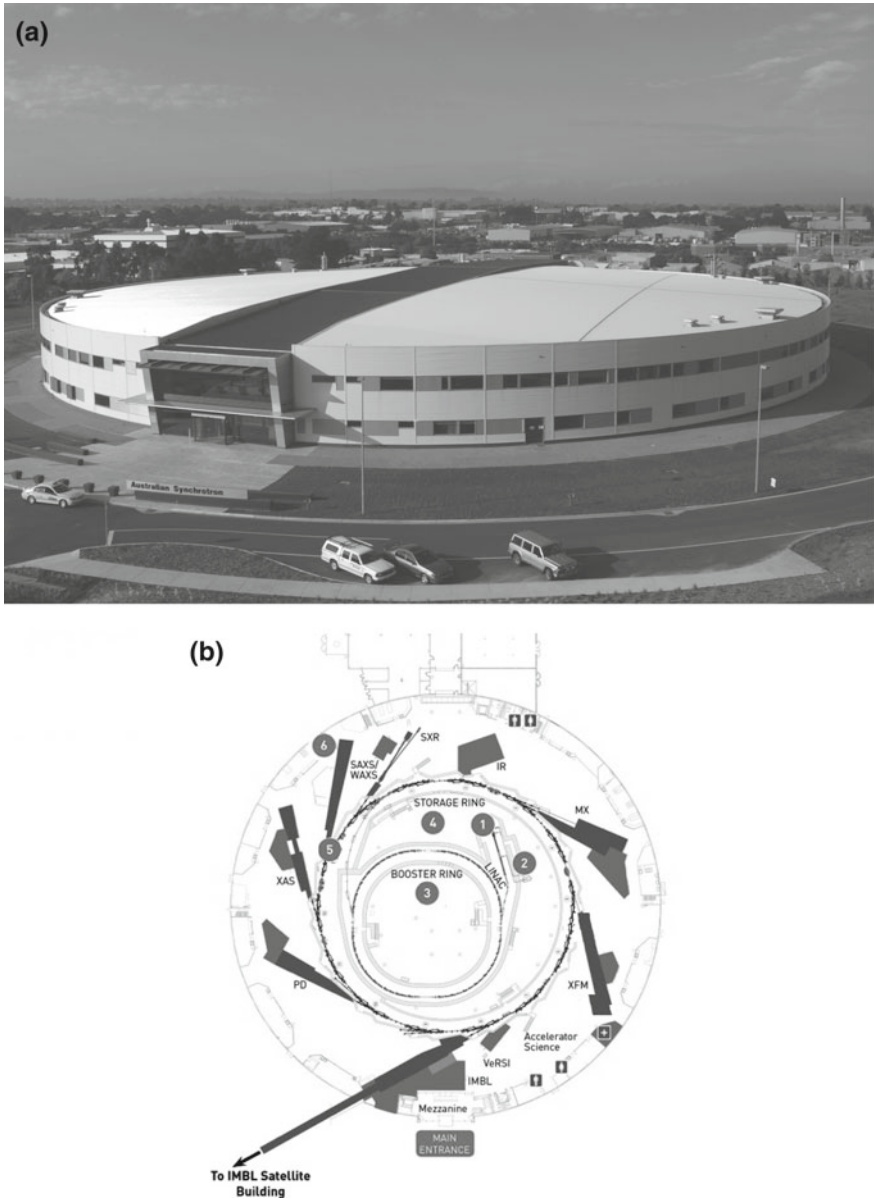


Fig. 4.8 **a** Aerial view of the Australian Synchrotron in Clayton, Victoria. **b** Illustration of the main components of a synchrotron: (1) electron gun, (2) LINAC, (3) booster ring, (4) storage ring, (5) insertion device, (6) end-station [Image courtesy: Australian Synchrotron]

chrotron radiation or Bremsstrahlung, consisting of high intensity X-ray radiation (the physical explanation for these emissions were discussed in Chap. 3). The ring current of the electron beam is typically kept at 200 mA (i.e. 10^{18} electrons), with losses in the storage ring compensated continuously by new electron injections every few minutes (the so-called top-up mode). The entire synchrotron building is temperature-controlled within $1\text{ }^\circ\text{C}$ precision (the accelerator tunnel even within $\pm 0.5\text{ }^\circ\text{C}$) to minimise thermal drifting effects and preventing beam instabilities.

The key performance of the synchrotron X-ray beam is measured by its brilliance (or brightness) and is defined as

$$B = \text{photons}/(\text{seconds} \times \text{mrad}^2 \times \text{mm}^2 \times 0.1\% \text{ BW}), \quad (4.4)$$

which is the amount of photons per time, angular divergence, beam cross-section area and within a bandwidth of 0.1% of the central wavelength [17]. Figure 4.9a shows a comparison for the brilliance and photon energy by a variety of different X-ray sources. It is evident that X-ray produced by BM are several orders of magnitudes above that over conventional, lab-based X-ray sources. They also provide a larger flexibility, as they covers a range of photon energies between 300 eV and $\gtrsim 20$ keV.

Figure 4.9b1 shows an illustration of a BM and the resulting X-rays (cone). In addition, quadrupole magnets of different gradients are used to compensate the mutual

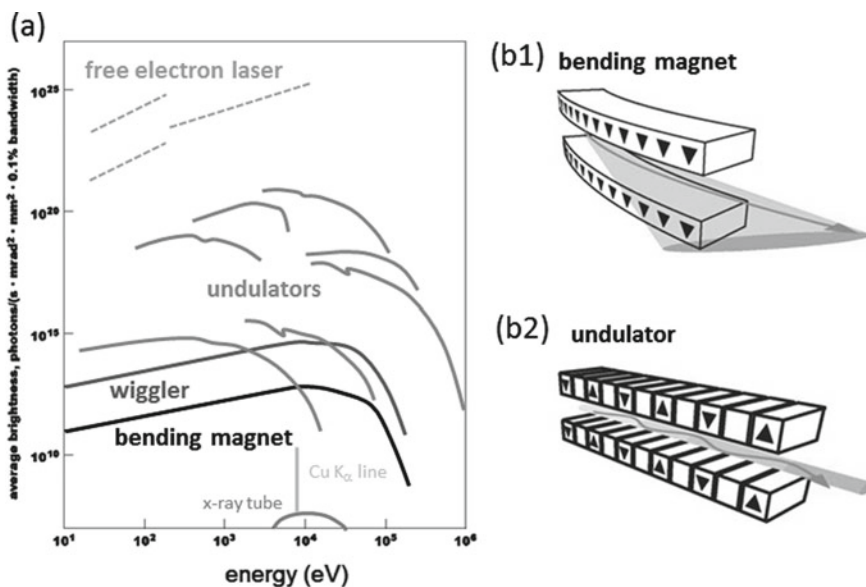


Fig. 4.9 **a** Overview for the brilliance and photon energy of lab-based and synchrotron-powered X-rays sources. Higher brilliances can also be achieved by free electron lasers [16]. **b** Schematic illustration showing the change of the electron trajectory (orange arrow) and X-ray generation (cone) for a bending magnet (top) and undulator (bottom) [Image courtesy: Australian Synchrotron]

repulsion of the electrons, which is induced by the Coulomb force. As this keeps the electron beam-size focused, they are also called magnetic lenses. In addition to these linear corrections, additional sextupole and octupole magnets are used for higher order corrections.

At the Australian Synchrotron, as a third-generation synchrotron, the BMs are not the only source of X-rays. To generate X-rays of even higher brilliance, several insertion devices (ID) are incorporated into straight sections of the storage ring (label 5). For the measurements in this work only X-rays from undulators were used. Figure 4.9b2 shows an illustration of such an undulator ID with two planar arrays of magnets of alternating polarity. These magnets cause a Lorentz force acting on the electrons that leads to a periodic oscillation of their momentum and consequently the generation of synchrotron radiation. For the periodic alignment of the permanent magnets, these X-rays experience constructive interference and form beam of very high brilliance, superseding X-rays from BM by a couple of additional orders of magnitudes. After leaving the insertion device, the beam follows a straight path towards the end-station or beamline (label 6).

A third types of devices to generate X-rays at the Australian Synchrotron is wiggler (not shown). In this insertion device, a comparable set-up to the undulator (just without constructive interference) is used to produce X-rays of higher energies, but less brilliance.

Together with the BMs, the two types of IDs cover a large spectrum between low-energetic photons (terahertz and infrared radiation) up to X-ray photons with a maximum of 31 keV (hard X-rays).

4.4.2 The SAXS/WAXS Beamline

At the Australian Synchrotron, the small and wide angle X-ray scattering (SAXS/WAXS) beamline can resolve shapes and sizes of structures as large as ~ 400 nm and down to sizes of 1 nm. With SAXS as the primary experimental technique in this work, this section will mainly focus on this technique and only briefly discuss the WAXS capabilities of this beamline.

A schematic overview is shown in Fig. 4.10. The SAXS/WAXS beamline is located at insertion device IVU 22 of the storage ring. This undulator produces X-rays with energies between 5 and 21 keV at a flux of 10^{12} – 10^{13} photons/s. After entering the beamline, the photons pass through a range of different X-ray optics, before they finally reach the sample and photon detector. A radiation shutter allows sealing off the remainder of the beamline from X-ray exposure, so it can safely be accessed for work. From there, the X-rays pass into the first hutch (“optics hutch”). A beamline hutch is a lead-covered enclosures that prevent radiation to escape. After passing a set of white beam slits the X-ray spectrum hits a flat double-crystal Si(111) monochromator. Here only photons of a certain wavelength are selected with a peak width resolution of 0.1 eV. For SAXS experiments on thin samples typically an energy of 11–12 keV is selected as the insertion device shows its highest brilliance in this

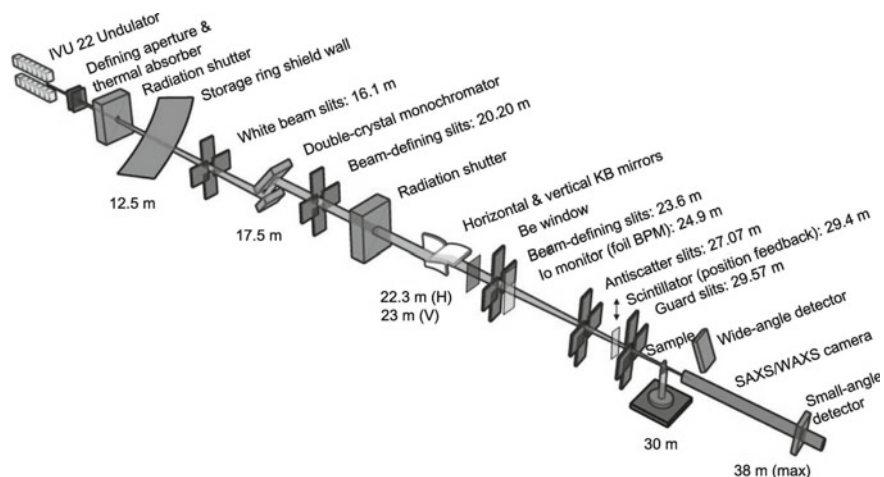


Fig. 4.10 Setup of the SAXS/WAXS beamline at the Australian Synchrotron for transmission geometry measurements under ambient conditions [Image courtesy: N. Kirby [18]]

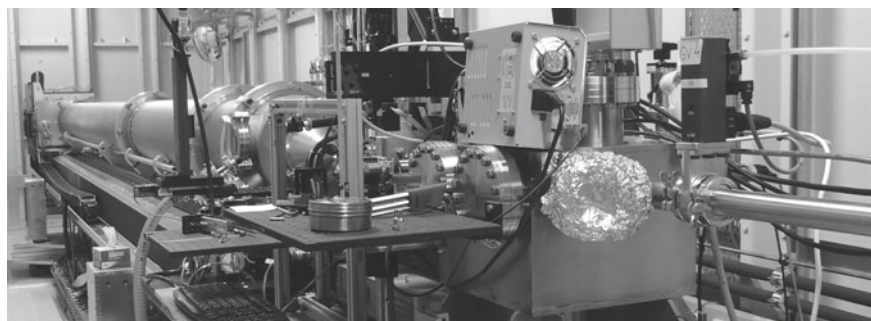


Fig. 4.11 Photograph of the experimental hutch of the SAXS/WAXS beamline. The detector is positioned on the far left end. The sample holder is within the centre (partially covered). The X-ray is coming through the tube from the right hand side

energy range ($\sim 2 \times 10^{13}$ photons/s), but any energy between 5 and 21 keV can be selected. Subsequently, the X-rays reach the second hutch (“experimental hutch”), the photograph in Fig. 4.11 is showing its main components.

In this hutch the now monochromatic X-rays pass a pair of Kirkpatrick–Baez (KB) mirrors with ultra-high quality elliptically curved surfaces for achromatic and versatile focusing (right-hand-side in Fig. 4.11). Finally, the X-ray beam leaves the vacuum of the mirrors and storage ring by passing through a 100 μm -thick Beryllium window. The last components that the X-ray beam passes before hitting the sample, are an intensity-calibration foil and a series of slits. Those are typically open enough so that the unaltered beam of 220 $\mu\text{m} \times 100 \mu\text{m}$ (FWHM) can pass through. For

applications where smaller beam-sizes are required, these slits allow narrowing down the beam to a minimum of approximately $50\ \mu\text{m} \times 50\ \mu\text{m}$.

The sample is positioned on a goniometer allowing lateral and angular adjustment of the sample with respect to the X-ray beam.³ Other set-ups for thermal annealing or high pressure as discussed at the end of this subsection.

SAXS Camera and Detector

After the X-rays pass through the sample, they enter the camera through a 200 nm thin silicon nitride window. To prevent the sample holder from accidentally touching this window, the samples are positioned approximately 3 cm away. The air scattering on the additional path length is generally of negligible size compared with the scattering intensities of the samples. The camera consists of an evacuated tube with a pressure below 0.005 mbar, in order to minimise interaction between the scattered photons and the air. For transmission SAXS, most of the X-ray beam penetrates the thin sample without scattering and only experiences a reduction in intensity, as described by the Lambert–Beer equation (3.2). This component carries no useful information about the sample structure and to prevent damage on the detector, it is fully blocked out by a beam-stop.

The scattered components of the beam, however, are collected by a photon counting detector, positioned at the end of the camera. The vacuum tube allows us to position the detector at a range of different positions between 600 and 7200 mm away from the sample, which results in a maximal angular range between 8° and 0.6° , respectively. For the SAXS measurements, the images were taken with a Pilatus-1M photon counting detector from Dectris (Switzerland). This detector consists of a two-dimensional array of pn-diodes and has more than 1 millions pixels over an area of $170\ \text{mm} \times 180\ \text{mm}$. As the maximum amount of pixels for such a photon detector are limited, the Pilatus 1M consists of 10 single modules, arranged in a 2×5 array. The vertical and horizontal gaps in-between single modules lead to dark areas, where no photons can be detected. However, this can be corrected for by taking a series of three images at different lateral detector positions and combining them to eliminate the gaps in the resulting image. As a result, the exposure time also triples in addition to the time required to move the detector, preventing this method to be used for the characterisation of fast changing objects.

Calibration of q -Range

Figure 4.12 shows the general SAXS set-up with the primary beam hitting the centre of the detector and the scattered beam showing a deflection by 2θ . The scattering angle is measured by the detector as pixels away from the primary beam. Thus, a calibration of each pixel with its corresponding \mathbf{q} -value is required for the analysis of the measured scattering images. The detector-sample distance L (camera length) and lateral detector coordinates \mathbf{d} are correlated via the trigonometric relation:

³To prevent accidental collision between sample and beamline components the movements of all parameters are limited by the software. Also no adjustment of the sample in the direction of the beam is possible as this would change its distance to the detector.

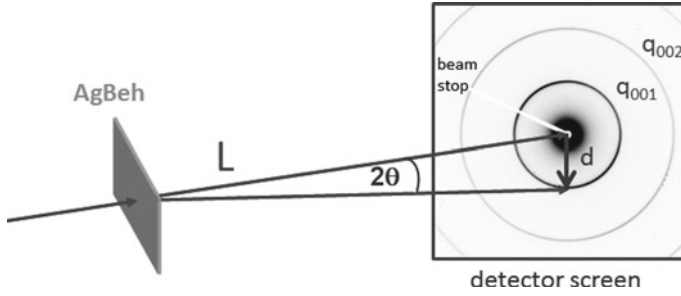


Fig. 4.12 Set-up of the SAXS measurements and detector screen image of a silver behenate (AgBeh) reference film. The well-defined rings with known q -values are used to calculate L and thus calibrate the q -range of detector screen

$$\frac{d}{L} = \tan(2\theta) \approx \sin(2\theta) \quad (4.5)$$

Using $q = 4\pi \sin(2\theta)/\lambda$ this gives the following relation between scattering vector q and d :

$$q = \frac{4\pi}{\lambda} \times \frac{d}{L} \quad (4.6)$$

This shows that a precise measurement of L is required for the calibration. In particular, when comparing values from different set-ups the uncertainty has to be as small as possible, rendering a direct measurement of the detector-sample distance unpractical. Instead, a silver behenate ($\text{AgC}_{22}\text{H}_{43}\text{O}_2$, short AgBeh) standard is used that possesses a large number of well-defined isotropic peaks in the low angle range at multiples of $q_{001} = 0.1076 \text{ \AA}^{-1}$, $q_{002} = 0.2152 \text{ \AA}^{-1}$, etc. These tabulated peaks can be correlated with each measured d to obtain L via Eq. (4.6) for a given q -range. Higher X-ray energies can be used to obtain more peaks.

Calibration of Scattering Intensity

The intensity of the scattering is typically expressed through the scattering coefficient μ_s which is measured in cm^{-1} . The scattering coefficient is defined as the cross-sectional area per unit volume. To calibrate the scattering intensity of the detector, a reference sample of known scattering strength is required. A material suitable for this purpose requires a very constant scattering over a wide q -range.

A commonly used material for calibration is water, as a large number of SAXS experiments are conducted in aqueous solution. However, its weak X-ray scattering cross-section requires long exposure times. During the last decade, glassy carbon has been established as one of the most suitable materials [19]. A collaboration between the group of I. Ilavsky at the USAXS beamline at the APS (Advanced Photon Source) and the NIST (National Institute of Standards) has developed an officially certified glassy carbonate standard. It is available for purchase as NIST Standard Reference

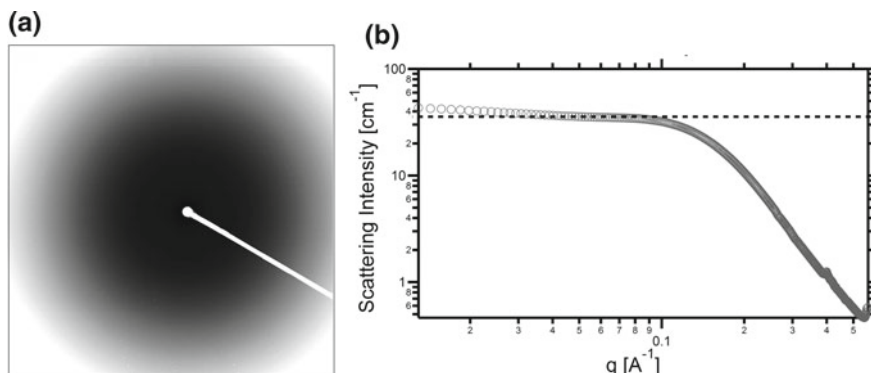


Fig. 4.13 SAXS intensity of a glassy carbon reference with the **a** detector image showing a radial symmetrically scattering image and **b** scattering intensity as a function of q . The SAXS pattern on glassy carbon possesses constant scattering behaviour (dashed line) over a wide q -range with an intensity of 35 cm^{-1}

Material 3600 [20]. Glassy carbon can be used for the q -range $0.008\text{--}0.25 \text{ \AA}^{-1}$ which is sufficient for the present work. A thorough description of requirements on scattering reference materials and the workings of glassy carbon is available in Ref. [20].

Figure 4.13 shows an example of the scattering image and scattering pattern from glassy carbon on a calibrated set-up. The calibration is performed by taking images with different exposure durations (1, 2, 5, and 10 s). As the amount of photons is linearly dependent on the expose time, this can decrease the amount of uncertainty in the measurements. The scattering intensity is also proportional to the interaction volume, requiring a precise knowledge of the thickness of the glassy carbon sample needs. In the present work, typically samples with a thickness of 1 mm were used. For the measurements on the mineral samples, the scattering pattern of each individual samples is then normalised to their respective thickness.

Finally, the absolute calibration of intensity is only necessary when the density of the objects is of interest. For a sole characterisation of the radial particle size, an accurate calibration of the q -range is sufficient. In this work, SAXS patterns used only for the size determination are sometimes shown with its scattering intensity in arbitrary units (a.u.).

In situ Annealing Furnace

The Linkam TS-1500 annealing stage allows samples of around 1 cm^2 in size to be heated to temperatures up to 1500°C , while being simultaneously penetrated by the X-ray beam during in situ transmission geometry SAXS. The set-up is shown in Fig. 4.14. The furnace is controlled by an external PID temperature controlling unit working together with a thermocouple placed close to the sample.⁴ The PID

⁴The temperature was calibrated using an external temperature sensor with a precision of $\sim 5^\circ\text{C}$.

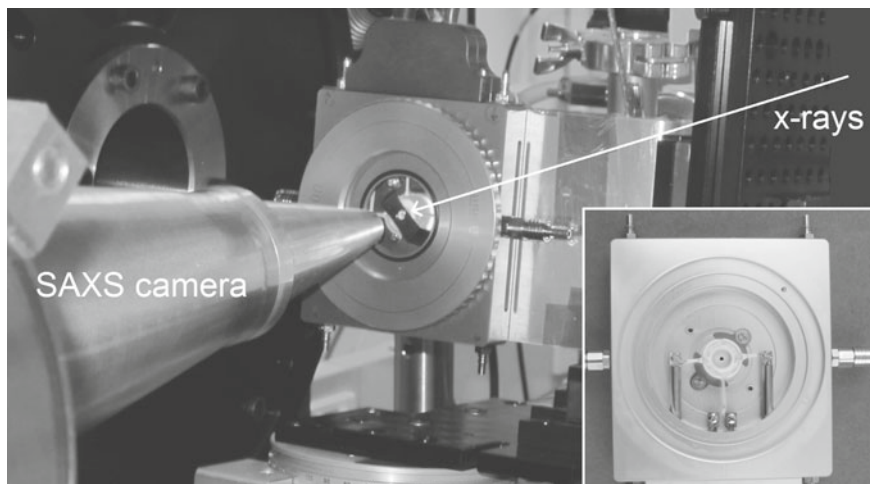


Fig. 4.14 The Linkam TS-1500 stage mounted for in situ measurements at the SAXS/WAXS beamline. The inset shows the opened heating element and sample holder

control can be programmed to execute a series of different temperatures. In this work, changes in temperature were typically performed with a rate of $130^{\circ}\text{C}/\text{min}$.

In general, the TS-1500 also supports annealing under different atmospheres by sealing the annealing volume with a glass window and floating it with a range of gases. However, the glass window was removed due to its low transparency for X-rays and all annealing was carried out under ambient air atmosphere.

Diamond Anvil Cell (DAC) Set-Up

To perform in situ annealing experiments of ion tracks under pressure a set of heatable DACs was used. Details about the handling and components of DACs were discussed in Sect. 4.2. For these measurements, the DAC was placed in a specifically designed holder that allows the sample to be exposed to the X-ray beam, as shown in Fig. 4.15. The scattered component of the X-rays in transmission geometry can still be imaged by the detector up to an exit angle of 30° , being more than sufficient for all SAXS set-ups. The heating coils were controlled by a Lambda ZUP20-10 DC power supply capable of up to 10 A at 12 V that was positioned outside of the beamline hutch. The thermocouple was read out by an E6C PID controller from RS company. To protect the diamonds from the effects of temperature, the sample holder was purged with Argon gas during heating.

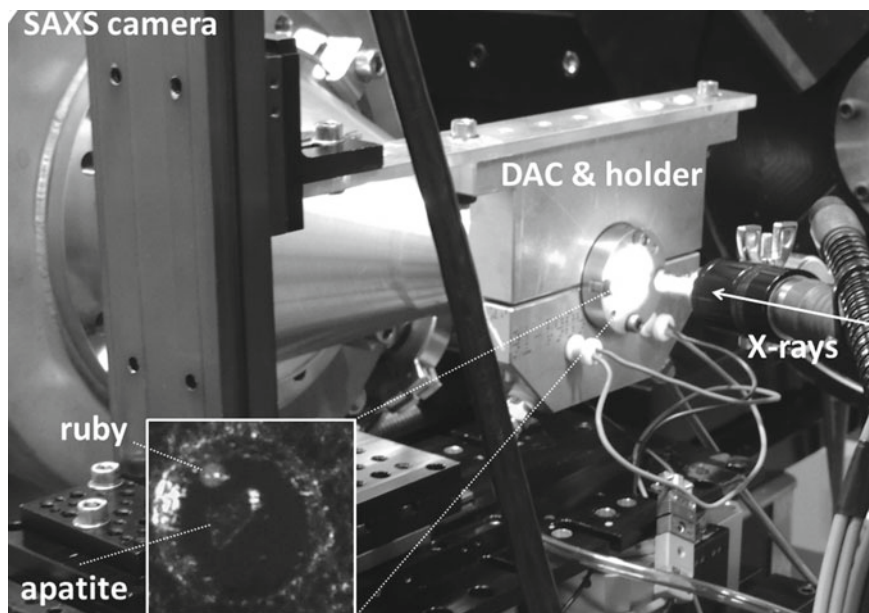


Fig. 4.15 Setup of the heatable DAC at the SAXS/WAXS beamline at the Australian Synchrotron. The inset shows a microscopy image of the gasket hole ($200\ \mu\text{m}$ \O) with a small apatite sample and ruby inside

4.5 Neutron Sources

The SAXS measurements in this work are accompanied by small angle neutron scattering (SANS) experiments on a few samples, carried out at two different facilities. SANS underlies the same principles as SAXS and allows a precise characterisation of the ion track radii by using a neutron instead of X-ray beam. Neutrons differ in element sensitivity to X-rays and allow us to gain some information on the stoichiometric composition of the ion tracks. In the context of this work, complementary SAXS and SANS allows a more complete structure characterisation of ion tracks. The relatively low flux of neutrons ($\sim 10^7\text{--}10^8\text{cm}^{-2}\text{s}^{-1}$) over a larger beam-spot size ($\sim 1\text{cm}^2$) in comparison to those of photons at synchrotron facilities, requires significantly longer exposure times. For the samples in the present work, with only $\sim 1\text{cm}^2$ cross-section and a relevant thickness of $<100\ \mu\text{m}$, the SANS data acquisition took around 8 h per sample.

4.5.1 Open Pool Australian Lightwater (OPAL) at ANSTO

The Open Pool Australian Lightwater nuclear reactor at the Bragg Institute at the Australian Nuclear Science and Technology Organisation (ANSTO) in Sydney is a

typical purpose-built 20 MW research reactor that produces neutrons for scientific and commercial applications [21]. It uses the same principle of induced fission as a nuclear power plant. By irradiating a ^{235}U nucleus with a neutron, it splits into two lighter fission fragments and per fission event produces 2–3 free neutrons and releases a kinetic energy of about 200 MeV. Figure 4.16a shows a schematic illustration of the main components of OPAL. While the focus in a nuclear power plant is to harvest this energy, a neutron source creates far less power, as its sole purpose is the creation of a steady flux of neutrons.⁵

For the scattering experiments requiring neutrons of large wavelength (i.e. lower energies, so-called cold neutrons) the neutron beam is extracted from the reactor and moderated (slowed down) by passing through liquid deuterium. They are then directed towards the end-user instruments along the beamline. The SANS experiments were carried out at the so-called QUOKKA instrument. It allows a variety of different camera-sample positions to cover a q -range between 0.004 and 0.7 \AA^{-1} with a flux of $\sim 4 \times 10^7 \text{ cm}^{-2} \text{ s}^{-1}$.

4.5.2 Spallation Neutron Source (SNS) at ORNL

In contrast to a nuclear reactor, a spallation source uses accelerator-based technology to accelerate negatively charged hydrogen atoms (H^-). They are then brought to an energy of 2.5 MeV when leaving the ion source. Subsequently, the H^- ions are injected into a LINAC, accelerating them up to 1000 MeV using rf-cavities. Finally, the ion beam is injected in a nearly-circular accelerator, the Proton Accumulator Ring. By passing into the ring through a stripper foil, the H^- ions lose both of their electrons, resulting in the formation of protons. By accumulating protons over approximately 1200 turns, they are simultaneously released within $\sim 1 \mu\text{s}$ in order to hit a liquid mercury target. This process triggers a spallation, creating 20–30 neutrons for each Hg atom, with a frequency of 60 Hz. Finally, this pulsed neutron beam is delivered to different neutron instruments within the target hall such as the EQ-SANS facility used in this work.

While the high energy of such pulses allows a range of short-time experiments, for the SANS experiments only the amount of neutrons over the entire exposure duration of several hours is important. With an integrated flux around $\sim 10^8 \text{ cm}^{-2} \text{ s}^{-1}$, the signal quality and exposure times at the EQ-SANS are comparable to the SANS beamline at a neutron reactor such as OPAL. Further details on the operation of the SNS can be found in Refs. [23, 24].

⁵Neutrons can be utilised for scattering experiments as in the present work, but are also used to irradiate materials to amend their properties (e.g. silicon neutron transmutation doping to change single silicon atoms into phosphorous [22]) or creating new isotopes (e.g. Molybdenum-99 or Iodine-99 with applications for nuclear medicine [21]).

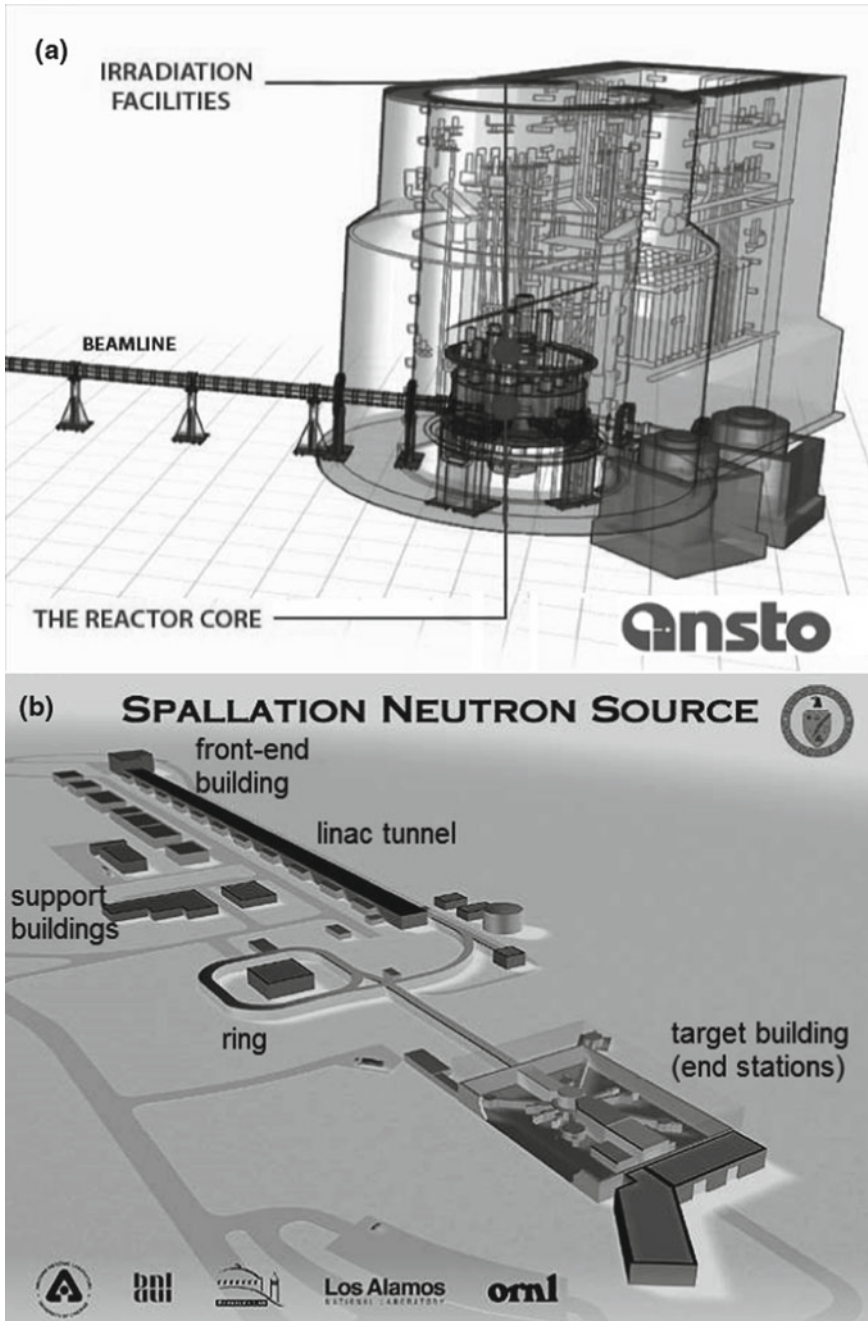


Fig. 4.16 Schematic representation of **a** the Open Pool Australian Lightwater reactor at ANSTO [Image courtesy: ANSTO, official media release image] and **b** the Spallation Neutron Source at ORNL [Image courtesy: ORNL, public domain image]

References

1. L.-K. Sha, B.W. Chappell, Apatite chemical composition, determined by electron microprobe and laser-ablation inductively coupled plasma mass spectrometry, as a probe into granite petrogenesis. *Geochim. Cosmochim. Acta* **63**(22), 3861–3881 (1999)
2. N.G. Ware, Combined energy-dispersive-wavelength-dispersive quantitative electron microprobe analysis. *X-ray Spectrom.* **20**(2), 73–79 (1991)
3. A. Jayaraman, Diamond anvil cell and high-pressure physical investigations. *Rev. Mod. Phys.* **55**, 65–108 (1983)
4. H. Keppler, D.J. Forst, *Introduction to Minerals Under Extreme Conditions in Mineral Behaviour at Extreme Conditions*, vol. 7 (University Press, Heidelberg, 2005)
5. H.K. Mao, J. Xu, P.M. Bell, Calibration of the ruby pressure gauge to 800 kbar under quasi-hydrostatic conditions. *J. Geophys. Res. Solid Earth* **91**(B5), 4673–4676 (1986)
6. N.J. Hess, D. Schiferl, Comparison of the pressure-induced frequency shift of Sm:YAG to the ruby and nitrogen vibron pressure scales from 6 to 820 K and 0 to 25 GPa and suggestions for use as a high temperature pressure calibrant. *J. Appl. Phys.* **71**(5), 2082–2086 (1992)
7. F. Datchi, R. LeToullec, P. Loubeyre, Improved calibration of the SrB4O7:Sm²⁺ optical pressure gauge: advantages at very high pressures and high temperatures. *J. Appl. Phys.* **81**(8), 3333–3339 (1997)
8. Agnès Dewaele, Marc Torrent, Paul Loubeyre, Mohamed Mezouar, Compression curves of transition metals in the Mbar range: experiments and projector augmented-wave calculations. *Phys. Rev. B* **78**, 104102 (2008)
9. T.R. Ophel, J.S. Harrison, J.O. Newton, R.H. Spear, E.W. Titterton, D.C. Weisser, The 14UD pelletron accelerator at the Australian National University. *Nucl. Instrum. Methods* **122**, 227–234 (1974)
10. R.J. Van de Graaff, K.T. Compton, L.C. Van Atta, The electrostatic production of high voltage for nuclear investigations. *Phys. Rev.* **43**, 149–157 (1933)
11. Website heavy ion accelerator facility (<http://physics.anu.edu.au/nuclear/hiaf.php>)
12. B. Afra, M.D. Rodriguez, C. Trautmann, O.H. Pakarinen, F. Djurabekova, K. Nordlund, T. Bierschenk, R. Giuliani, M.C. Ridgway, G. Rizza, N. Kirby, M. Toulemonde, P. Kluth, Saxs investigations of the morphology of swift heavy ion tracks in alpha-quartz. *J. Phys. Condens. Matter* **25**(4), 045006 (2013)
13. J.F. Ziegler, J.P. Biersack, U. Littmark, *The Stopping and Range of Ions in Matter* (Pergamon, New York, 1985)
14. M. Lang, *The Effect of Pressure on Ion Track Formation in Minerals*. Ph.D. thesis, Heidelberg University (2004)
15. Website stanford linear accelerator center (<http://www.slac.stanford.edu/>)
16. C.A. Brau, Free-electron lasers. *Proc. 2nd Int. Symp. Adv. Nucl. Energy Res.* **2**, 778 (1990)
17. D.M. Mills, J.R. Helliwell, Å. Kvik, T. Ohta, I.A. Robinson, A. Authier, Report of the working group on synchrotron radiation nomenclature - brightness, spectral brightness or brilliance? *J. Synchrotron Radiat.* **12**(3), 385 (2005)
18. N.M. Kirby, S.T. Mudie, A.M. Hawley, D.J. Cookson, H.D.T. Mertens, N. Cowieson, V. Samardzic-Boban, A low-background-intensity focusing small-angle X-ray scattering undulator beamline. *J. Appl. Crystallogr.* **46**(6), 1670–1680 (2013)
19. F. Zhang, J. Ilavsky, G.G. Long, J.P.G. Quintana, A.J. Allen, P. Jemian, Glassy carbon as an absolute intensity calibration standard for small-angle scattering. *Metall. Mater. Trans. A* **41**(5), 1151–1158 (2010)
20. A.J. Allen, F. Zhang, R.J. Kline, W.F. Guthrie, J. Ilavsky, Nist standard reference material 3600: absolute intensity calibration standard for small-angle X-ray scattering. *J. Appl. Cryst.* **50**, 462–474 (2017)
21. <http://www.ansto.gov.au/aboutansto/opal/capabilities/index.htm>
22. <http://www.ansto.gov.au/businessservices/siliconirradiationservices/>
23. <http://neutrons2.ornl.gov/facilities/sns/works.shtml>

24. T.E. Mason, T.A. Gabriel, R.K. Crawford, K.W. Herwig, F. Klose, J.F. Ankner, The spallation neutron source: a powerful tool for materials research, in *XX International Linac Conference, Monterey, California*, FR203:1043 (2000)

Chapter 5

Ion Track Formation Under Ambient Conditions



This chapter presents the experimental results on the influence of the parameters of the ion irradiation on the resulting ion tracks as well as the physical parameters of the irradiated materials. The results contribute towards the further understanding of the fundamental processes of ion track formation. With the primary focus of this work on ion tracks in minerals and an increased understanding of fission tracks, the materials investigated were natural apatite and quartz. Apatite is among the most common materials used for fission track dating [1], while quartz has a simple and well-understood structure, allowing to run a series of simulations on track formation under different conditions [2].

First, results from a characterisation of ion tracks in apatite and quartz by means of SAXS and SANS are shown. Secondly, the influence of ion fluence, mass, energy, and energy loss is investigated using SAXS. These results are also necessary to choose the ideal irradiation parameters to analyse the effects of temperature and pressure on tracks in the remaining chapters. Finally, the effects of material parameters on the resulting track size are discussed. This includes an anisotropy for the track radius along different crystallographic orientations in non-cubic materials. The results are compared with the quantitative simulations of track formation.

5.1 Track Characterisation with SAXS and SANS

Natural apatite from Dashkesan, AZ was irradiated with 2.3 GeV Bi ions and synthetic quartz was irradiated with 2.2 GeV Au ions, both at a fluence of $1 \times 10^{11} \text{ cm}^{-2}$ at the UNILAC at GSI in Darmstadt, Germany. Figure 5.1 shows images of the tracks in apatite measured with SAXS (a) and SANS (b) and similar images of the tracks in quartz measured with SAXS (c) and SANS (d). The ion tracks were tilted by 5° with respect to the X-ray or neutron beam. This results in the anisotropic “streak” features in the detector images. To measure the background, an non-irradiated sample was imaged (compare Sect. 3.3.3). The oscillating intensities extracted from the streaks are shown as a function of q in Fig. 5.2 for SAXS (a) and SANS (b).

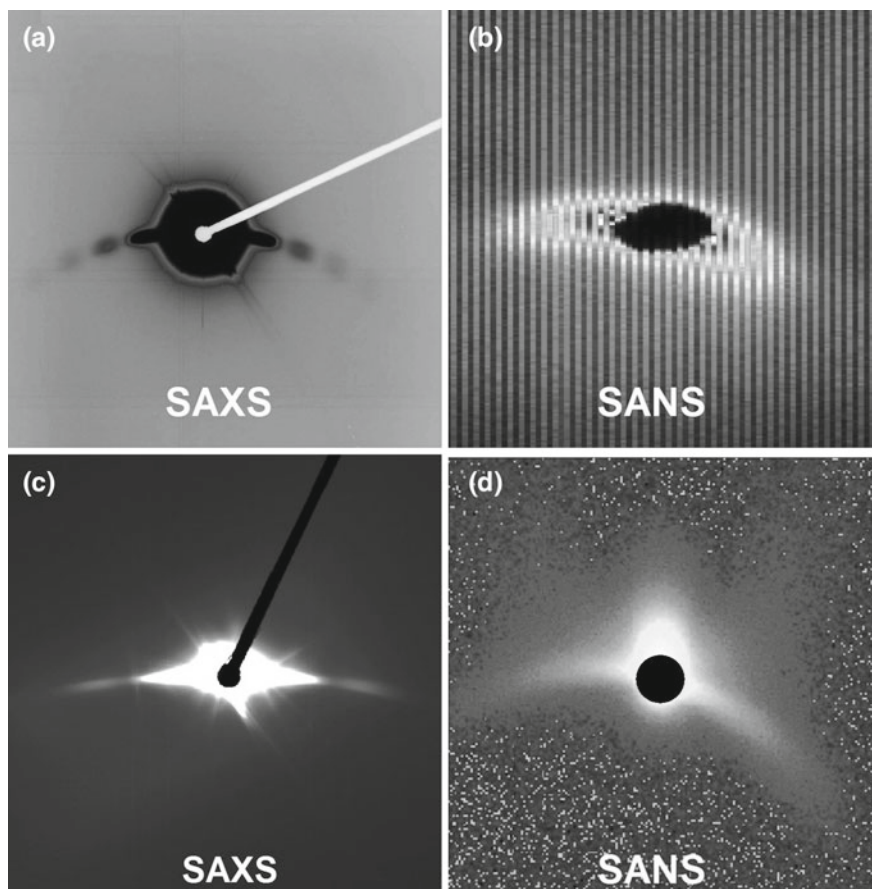


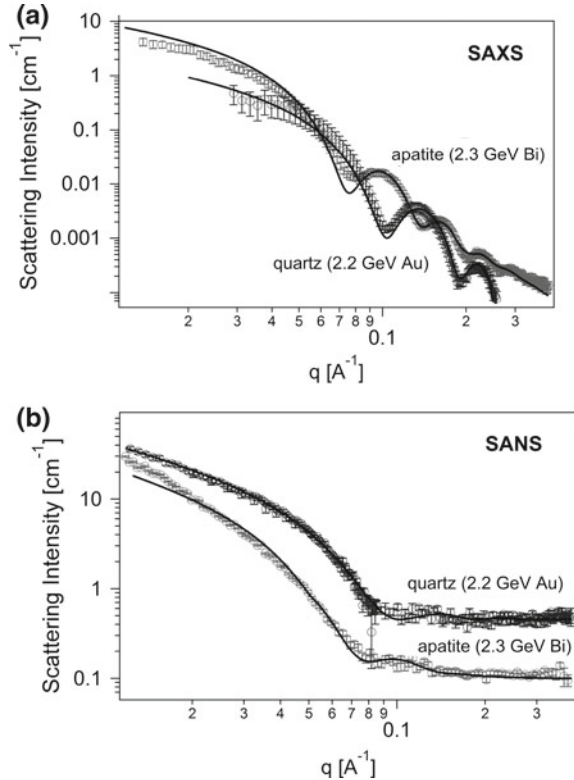
Fig. 5.1 [upper row] Detector images for ion tracks in apatite, characterised by **a** SAXS and **b** SANS. [bottom row] Detector images for ion tracks in quartz, characterised by **c** SAXS and **d** SANS

The SAXS patterns were obtained at the Australian Synchrotron with 11 keV X-ray with exposure times of approximately 5 s.¹ After background subtraction, the patterns were fitted by using a hard cylinder, resulting in an excellent agreement with the data. Only at very low q the intensities are slightly below the fitted values. This deviation is mostly attributed to the difficulty in isolating the streak from the background in close proximity to the beam-stop.

The fits reveal cylinder radii of 5.19 ± 0.05 nm (0.5 nm polydispersity) for apatite and 3.8 ± 0.1 nm (0.4 nm polydispersity) for quartz. The scattering intensity I_0 at $q \rightarrow 0$ from the fits were 18 and 10 cm^{-1} for apatite and quartz, respectively. This

¹Each image has been created from three separate images to eliminate the detector gaps, therefore the total exposure time was around 15 s.

Fig. 5.2 Comparison of q -patterns for **a** SAXS and **b** SANS from ion tracks in apatite (black circles) and quartz (grey circles). A hard cylinder model was used to fit the results (solid lines)



value can be directly correlated with the track number density N , radius R , length L and the change in electronic density $\Delta\rho_e$ between track and undamaged material via:

$$I_0(\text{SAXS}) = I(q \rightarrow 0) = N |\Delta\rho_e R^2 L|^2 \quad (5.1)$$

As shown in Sect. 3.3.1, when all parameters, but $\Delta\rho_e$ are known, the electronic density difference can be estimated. Here, a value of $\Delta\rho_e = 2.3 \times 10^9$ and $\Delta\rho_e = 3.0 \times 10^9 \text{ cm}^{-2}$ and a relative (mass) density change of $0.8 \pm 0.3\%$ and $1.0 \pm 0.3\%$ was found for apatite and quartz, respectively. The relative density change was calculated by dividing the electronic density change by the total electronic density change of $2.7 \times 10^{11} \text{ cm}^{-2}$ for apatite and $2.3 \times 10^{11} \text{ cm}^{-2}$ for quartz. These values were estimated by linear combination of the single-element coefficients by using the IRENA software [3].

The same samples were measured with small angle neutron scattering (SANS). Tracks in quartz were measured at the QUOKKA beamline at the Bragg Institute in Sydney, Australia. Tracks in apatite were measured at the EQ-SANS beamline at the SNS at Oak Ridge National Laboratory in the USA. The resulting SANS patterns

Table 5.1 Track properties measured by SAXS/SANS for ion tracks in apatite and quartz

Apatite	SAXS	SANS
Radius	5.19 ± 0.05 nm	5.0 ± 0.5 nm
Radius polydispersity	0.5 ± 0.1 nm	0.7 ± 0.2 nm
Density change	$0.8 \pm 0.3\%$	$0.7 \pm 0.3\%$
Quartz	SAXS	SANS
Radius	3.8 ± 0.1 nm	4.0 ± 0.7 nm
Radius polydispersity	0.4 ± 0.1 nm	0.4 ± 0.1 nm
Density change	$1.0 \pm 0.3\%$	$0.9 \pm 0.5\%$

were obtained with exposure times of ~ 8 h each to ensure a sufficient high neutron count at higher q -ranges. At QUOKKA, neutrons with a wavelength of 4.9 \AA were used. Two measurements were carried out at different sample-detector distances of 2 and 8 m in order to cover a q -range between 0.01 and 0.3 \AA^{-1} . At EQ-SANS (BL-6) neutrons of wavelength 2 \AA were used. A single camera length of 2.5 m was used to cover the entire q -range between 0.02 and 0.7 \AA^{-1} .

In direct comparison with SAXS, the background of SANS measurements is much larger; this allows only the first oscillation to be visible and usable for analysis and modelling. The same hard cylinder model used to fit the SAXS patterns was applied to the SANS patterns. This has allowed to derive the track radius and scattering intensity. A track radius of 5.0 ± 0.5 nm (0.7 nm polydispersity) and 4.0 ± 0.7 (0.4 nm polydispersity) was found for apatite and quartz, respectively. The intensities I_0 after normalisation to their respective track lengths were 42 and 35 cm^{-1} . This allows the nuclear density change $\Delta\rho_n$ to be calculated with a very similar formula:

$$I_0(\text{SANS}) = N |\Delta\rho_n R^2 L|^2 \quad (5.2)$$

The SANS-measured values for the change in nuclear density $\Delta\rho_n$ were 2.7×10^8 and $3.8 \times 10^8 \text{ cm}^{-2}$ and the relative density change $\Delta\rho$ were $0.9 \pm 0.5\%$ for quartz and $0.7 \pm 0.3\%$ for apatite. These values were obtained by normalising the density change with respect to the total nuclear density of 4.3×10^{10} and $4.2 \times 10^{11} \text{ cm}^{-2}$ for the known compositions of apatite and quartz, respectively.

All results from the fits for SAXS and SANS are summarised in Table 5.1. For apatite and quartz they show fairly similar track radii measured by SAXS and SANS within their respective uncertainties. For both techniques, a track radius of 5 nm for apatite and radius of 4 nm for quartz was measured, with approximately 10% polydispersity each. This is of particular interest, as both techniques have different element sensitivity: X-ray scattering scales with the electron density of the target atoms such that scattering from heavy elements such as Si, Ca and P dominates; neutron scattering is element-dependent and more sensitive to lighter elements such as O [4]. The combined measurements indicate that the ion track damage is of similar extent for the cation (heavy-element) and for the anion (oxygen) sub-lattices. Also the

relative reduction in density is approximately 1% for tracks in each material, whether its determined with SAXS or SANS. As the relative density change has to be identical and the total electronic/nuclear density was obtained by using the composition of the unchanged material, it is assumed that no major change in stoichiometry from the composition of the undamaged material has occurred.

For the relative change in density observed for apatite ($0.8 \pm 0.3\%$) and quartz ($1.0 \pm 0.5\%$), it cannot be derived solely from SAXS-measurements whether the change correlates to an increase or decrease in the track density. This is related to the fact that SAXS and SANS only measure the scattering intensity $I \propto |F(\Delta\rho)|^2$, instead of the scattering amplitude $F(\Delta\rho)$, directly. However, the mechanisms typically used to explain the track formation, suggest that an underdense and amorphous track is the most likely explanation for the change in density. In particular for quartz, the densities of crystalline α -quartz and amorphous SiO_2 have been investigated thoroughly. While crystalline α -quartz has a density of 2.65 g/cm^3 , amorphous SiO_2 typically has 2.20 g/cm^3 , which is 17% lower. This shows that the reduction in track density by 1% for the ion tracks is still far away from the low density of genuine amorphous quartz and, rather, an amorphous phase under extremely high pressure within the crystalline matrix [5].

5.2 Effects of Ion Irradiation Parameters on Tracks

5.2.1 Ion Fluence Effects

The ion irradiation fluence is defined as the product of the ion flux (ions per time per area) multiplied with the irradiation time (compare Sect. 4.3). For low fluences each ion creates an individual track, such that the fluence is equivalent to the number of tracks per area. For higher fluences tracks cannot be treated as individual, well-separated objects anymore and the effect of track overlap becomes important.

Here, ion tracks created as a function of ion fluence were investigated. The irradiation was carried out on apatite at the GSI UNILAC with 2.2 GeV Au ions at a flux of $2 \times 10^8 \text{ cm}^{-2} \text{ s}^{-1}$. These parameters were kept constant for the whole irradiation series and only the irradiation time was varied. Samples with fluences between 5×10^{10} and $1 \times 10^{12} \text{ cm}^{-2}$ were prepared, covering between 3 and 52% of the sample surface with ion tracks.

Figure 5.3a shows SAXS patterns of samples irradiated with different fluences. The oscillating SAXS patterns show a very similar shape for all fluences, yet a clear shift of the first minima towards lower q -values with increasing fluence is apparent. Each pattern was fitted with the hard cylinder model and the obtained radii are displayed in Fig. 5.3b. One can see the radius for ion tracks at the employed range of fluences to be either around 4.8 nm (lower fluences, i.e. $\lesssim 1 \times 10^{11} \text{ cm}^{-2}$) or around 5.1 nm (higher fluences, $\gtrsim 5 \times 10^{11} \text{ cm}^{-2}$). This shows an increase in track radius with irradiation fluences of approximately 6% for an increase in fluence between the

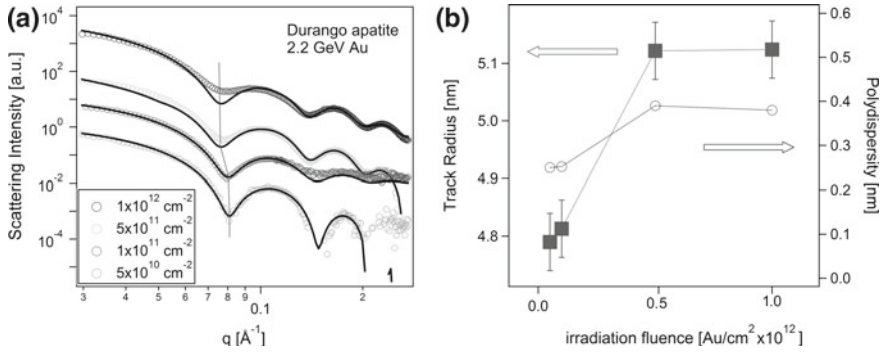


Fig. 5.3 **a** SAXS patterns for ion tracks in apatite created by different ion fluences. A hard cylinder model was used to fit the results (solid lines). Patterns are offset for clarity. **b** Track radii (left axis) and polydispersities (right axis) for each fit from **a** as function of irradiation fluence

regime of lower and higher fluences. The errors from the SAXS measurements were typically around 0.05 nm for tracks in apatite. This demonstrates an increase of the irradiation fluence results in larger track radii R , clearly above the uncertainty of SAXS. A hike in the polydispersity of the tracks for higher fluences was observed as well. While low fluence tracks only showed 0.25 nm radius polydispersity (5%), the high fluence tracks showed 0.40 nm (8%). The density difference between host material and ion track is of comparable values ($\lesssim 1\%$) for irradiation with all four fluences.

To allow a comparison between the effects of different fluences on the irradiated surface, the relative area A_{cov} , covered by tracks with radius R and areal track density N , can be calculated via [6]:

$$A_{\text{cov}} = 1 - \exp[-\pi R^2 N] \quad (5.3)$$

Figure 5.4 shows statistical distributions of tracks for the four different fluences. The schematic was created by randomly distributing circular-shaped tracks with a radius of 5 nm, similar to the experimental findings. For the low fluences in this work, the coverage is below 10% and all tracks appear well-separated. For the high fluence regime, however, track overlap becomes very common when more than a quarter of the total area is covered by tracks. The statistical track overlap can be calculated by summarising the total area of all tracks, $A_{\text{tracks}} = N \times \pi R^2$ and subtracting A_{cov} , showing a negligible statistical overlap area for low fluences $5-10 \times 10^{10} \text{ cm}^{-2}$ (0.1 and 0.3% respectively) and a more significant one for the higher fluences $5-10 \times 10^{11} \text{ cm}^{-2}$ (7 and 24% respectively). It is noted that all scattering patterns were fitted by using the hard cylinder model assuming a circular shape of each track. From Fig. 5.4 it becomes evident that this assumption is reaching its limits for higher fluences due to the significant overlap ratio and non-circular character. Therefore, the increase in track radius of less than 10% is attributed to the larger track area

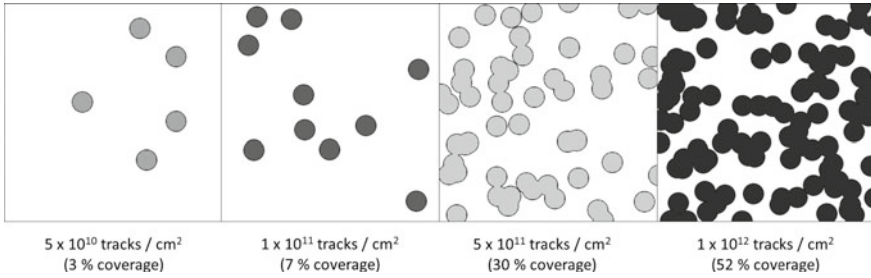


Fig. 5.4 Statistical track coverage for fluences between $5 \times 10^{10} \text{ cm}^{-2}$ to $1 \times 10^{12} \text{ cm}^{-2}$. Each square represents an area of $100 \times 100 \text{ nm}^2$ with a track radius of 5 nm

of overlapping tracks. The increased track radius polydispersity results from non-circular shaped track geometry at higher fluences. Despite this change in cross-section, the large amount of tracks measured by SAXS still allows an excellent agreement between cylinder model and experimental data.

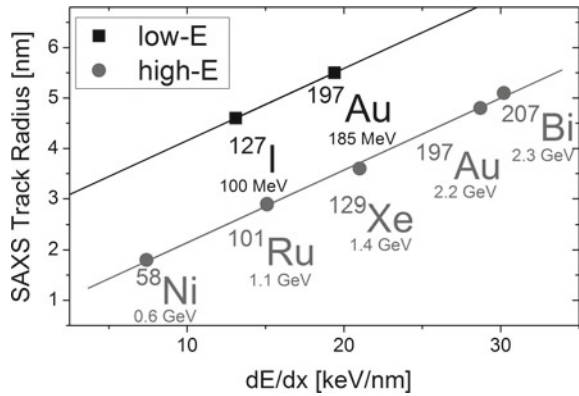
These results show that all irradiation for apatite around or below $1 \times 10^{11} \text{ cm}^{-2}$ can be considered to result in well-separated tracks. Ion irradiation at higher fluences, on the other hand, leads to track overlap and consequently a less well-defined radius. Therefore for the majority of experiments in this work, the low fluence regime ($5\text{--}10 \times 10^{10} \text{ cm}^{-2}$) was used.

5.2.2 Ion Energy and Energy Loss

At the GSI UNILAC, the samples were typically irradiated with ions of 11.1 MeV per nucleon (MeV/u). By changing the type of ion and, consequently, its mass, a range of different irradiation energies can be achieved. Afra et al. [7] have reported on SAXS-measured average track radii as a function of average energy loss for irradiation with ^{58}Ni , ^{101}Ru , ^{129}Xe , and ^{197}Au ions, as shown in Fig. 5.5. Similar irradiations using ^{207}Bi ions are also shown, representing an energy range between 0.6 and 2.3 GeV (high-E). These were complemented by low-E irradiations at the ANU HIAF with 0.8–0.9 MeV/u. The ions ^{127}I and ^{197}Au were used [8], resulting in absolute energies of 100 and 185 MeV (low-E), respectively.

Using SRIM calculations for the different ions and energies, the average energy loss dE/dx values for each ion type can be estimated. As SAXS provides a measure of the average volume-weighted track radius over the sample depth, the energy loss was also averaged with respect to the change in energy loss along the ion trajectory. This was straight-forward for all 11.1 MeV/u irradiated samples, as they were kept much thinner (30–40 μm) than the total track length of 72–90 μm such that the variation of the electronic energy loss did not exceed 5%. As this variation is small, the track volume weighted average energy loss corresponding to the radius measured by SAXS can be approximated by the average of the electronic dE/dx over the entire

Fig. 5.5 The dependence of track radius on average energy loss dE/dx for ion tracks in apatite created by irradiation with low-E (0.8–0.9 MeV/u, squares) and high-E (11.1 MeV/u, circles, after Afra et al. [7]) ions



sample thickness. In contrast, tracks produced by low energy ions are much shorter (10–14 μm) and deviate significantly from cylindrical tracks, as demonstrated by TEM measurements [9]. For ions with energies below the Bragg peak (i.e. 185 MeV Au), the energy loss strongly varies along the ion path before the projectile comes to rest. Here, the average energy loss is taken from the depth where the track has equal volume parts, when approximated as cone-shape.

The track radii shown in Fig. 5.5 display a linear correlation with the average energy loss. For a given energy loss, the radii of tracks produced by low energy ions are nearly 2 nm larger than those by high energy ions. This difference is attributed to the velocity effect (compare Sect. 2.2) which is based on the effect that higher ion velocities result in larger electron cascades. The deposited energy is then spread out into a larger volume resulting in a lower deposited radial energy density. Hence, the radial distance away from the trajectory where the energy loss exceeds the track formation threshold is higher for low-E ions. This effect explains the smaller track radii at higher beam velocities with comparable energy loss [10, 11].

5.3 Effects of the Crystallographic Direction on Tracks

In addition to the parameters controlling the ion beam, the properties of the target material (i.e. quartz, apatite) also have an influence on the ion tracks. This section discusses ion tracks along different axes within the single-crystalline lattice of quartz and apatite.

For quartz, the different crystallographic directions possess different properties when used for electronic applications.

For apatite, it is well established that the annealing rate for fission tracks differs with the angle to the c-axis. Those tracks oriented parallel to the c-axis show the slowest annealing rate compared to those with an angle to the c-axis [19]. For

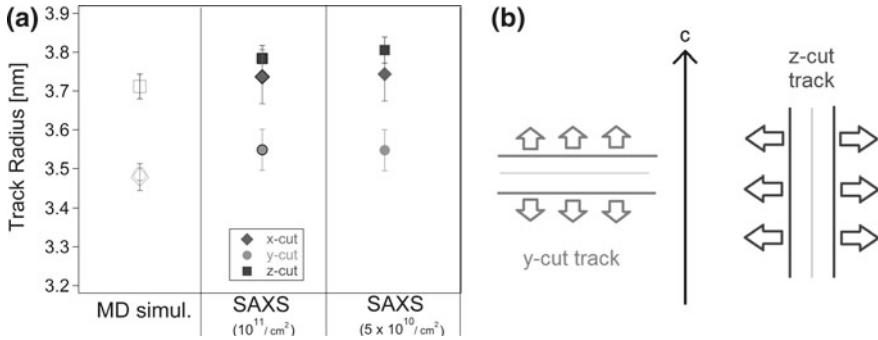


Fig. 5.6 **a** Ion track radii of tracks quartz along different orientations. Values are measured by SAXS (solid symbols) and calculated with MD simulations (open symbols). **b** Schematic illustration of ion tracks perpendicular (left) and parallel (right) to the *c*-axis. The thermal conductivity is shown in radial orientation to the ion trajectory (arrows)

comparison between different studies, it is therefore common practice to limit fission track analysis to tracks parallel to the *c*-axis.

5.3.1 Quartz

Synthetic quartz of different crystallographic cuts was irradiated with 2.2 GeV Au ions of fluences between 0.5 and $1 \times 10^{11} \text{ cm}^{-2}$. The radius of the ion tracks was measured by SAXS on at least four different samples for each crystallographic orientation.²

Figure 5.6a shows the measured track radii for tracks along all three different quartz cuts. For the batch irradiated at $1 \times 10^{11} \text{ cm}^{-2}$ average track radii of $3.69 \pm 0.07 \text{ nm}$ (*x*-cut), $3.54 \pm 0.04 \text{ nm}$ (*y*-cut) and $3.76 \pm 0.04 \text{ nm}$ (*z*-cut) were measured. For the second set of samples, irradiated at $1 \times 10^{11} \text{ cm}^{-2}$, nearly identical values were obtained: $3.74 \pm 0.07 \text{ nm}$ (*x*-cut), $3.55 \pm 0.04 \text{ nm}$ (*y*-cut) and $3.78 \pm 0.04 \text{ nm}$ (*z*-cut). This demonstrates a good reproducibility of the irradiation process and the SAXS-measured radii. The radii of the ion tracks in *y*-direction were typically 6 % smaller than in the *z*-direction. Accompanying MD simulations were provided by the group of Kai Nordlund at the University of Helsinki in Finland [2]. They show ion track radii in quartz of $3.48 \pm 0.03 \text{ nm}$ (*x*-cut), $3.49 \pm 0.02 \text{ nm}$ (*y*-cut) and $3.71 \pm 0.03 \text{ nm}$ (*z*-cut) as displayed by the open symbols in Fig. 5.6a. For the ion tracks in *y*-cut and *z*-cut quartz, the simulated radii correlate well with the absolute experimental values. Track radii from both, MD and SAXS, show a difference of 6% between those in *y*- and *z*-cut quartz.

²The characterisation of several parts of the irradiated samples in independent SAXS acquisitions provides a better reproducibility and lower uncertainties.

The difference in the track radii between the track directions in the MD simulations is attributed to the anisotropy in the crystal structure, as indicated by Fig. 5.6b. Due to the hexagonal structure of quartz, the lattice constants a and c are not identical ($c > a$) and consequently also the thermal conductivity calculated by MD differs with ~ 1.8 W/mK along the x - as well as the y -direction and ~ 2.5 W/mK in z -direction. As the thermal conductivity is critical for the size of the ion tracks (compare Sect. 2.2), these crystallographic differences are the origin of the discrepancy in the MD simulations. In the present case, a track along the z -direction experiences a thermal conductivity of only 1.8 W/mK along its radial component. In contrast, an ion track perpendicular to the z -direction experiences a thermal conductivity of 1.8 and 2.5 W/mK in along its radial component. As a lower thermal conductivity allows a larger extend of the damage this can be partially explain the difference in track sizes. Furthermore, a track along the y -direction should show an anisotropic cross-section, rather than a circular one, which is confirmed experimentally in Sect. 5.5.

When accessing the results of the MD simulations, the radius for the x -cut is identical to that of y -cut quartz. In fact, the x -cut is closer to the y -cut from a crystallographic aspect, which is explaining these results. However, when comparing these simulations with the experimental values, the radius of tracks along the x -cut is much closer to that of the z -cut. Indeed, the x -cut has previously reported to be unique as the only cut in which etched ion tracks display different shapes in twinned crystal planes [12]. This suggests that other non-crystallographic effects may be responsible for the larger tracks in x -cut than y -cut quartz.

5.3.2 Apatite

In most natural apatite single-crystals of larger size, the c -axis can be easily identified due to their hexagonal structure (compare Fig. 4.1a in Sect. 4.1). This allows us to cut thin samples of apatite that are oriented either parallel or perpendicular to the c -axis. As a result, tracks aligned in these two directions can be produced to compare the effect of the lattice anisotropy on the track radius. The irradiation was performed with 2.3 GeV Bi ions at 1×10^{11} cm⁻².

Figure 5.7a shows the SAXS patterns for ion tracks in apatite from two different geographic locations, apatite from Durango, Mexico (circles) and Dashkesan, Azerbaijan (triangles). The corresponding track radii are shown in Fig. 5.7b. The radius is clearly larger for tracks oriented $\parallel c$ -axis, in a similar manner, as it was demonstrated for quartz. Depending on the geographic origin of the mineral specimen, the difference was between 7% (Durango) and 2% (Dashkesan). The former apatite has an F/Cl ratio of 8:1, while Dashkesan apatite only has an F/Cl ratio of 6.8:1.

This can be compared with MD simulations by Rabone et al. that shown a dramatic effect of the mineral composition on the size anisotropy [13]. Their calculations show track radii approximately 4% larger along the $\parallel c$ -direction in pure F-apatite (comparable to Durango apatite) and even 10% larger in F-OH apatite. This track radius anisotropy reduces with increasing Cl-composition (as in Dashkesan apatite)

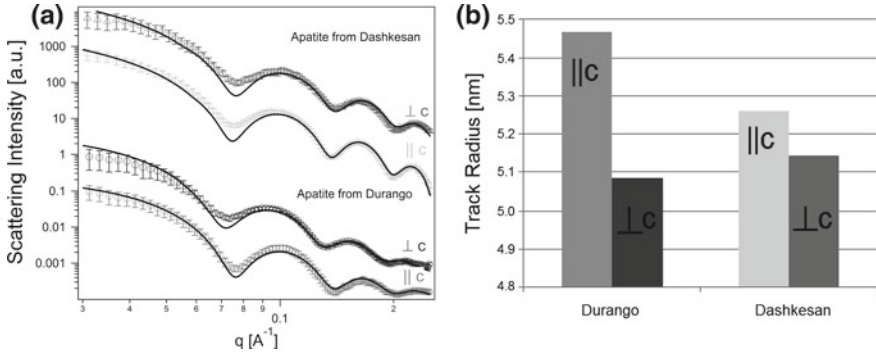


Fig. 5.7 **a** SAXS patterns for ion tracks parallel ($\parallel c$) and perpendicular to the c -axis ($\perp c$) in apatite from Durango, Mexico (circles) and Dashkesan, Azerbaijan (triangles). A hard cylinder model was used to fit the results (solid lines). Patterns are offset for clarity. **b** The corresponding track radii from the fits for all 4 samples show an anisotropy for track sizes in both types of apatite

and even reverses for pure Cl-apatite. The slightly higher Cl-concentration is most likely responsible for the less pronounced effect of anisotropy. Our measurements verify these simulation results.

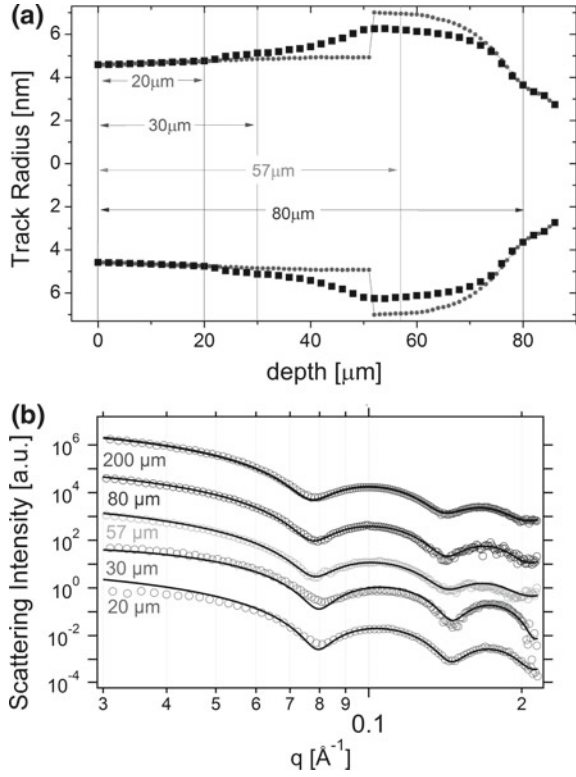
With the thermal conductivity as the most important parameter for the radial size of ion tracks, the present results suggest a higher thermal conductivity along the c -axis than perpendicular, similar to quartz. The present results also agree with TEM measurements on 2.2 GeV Au ion-irradiated apatite from Durango [14]. The present results are of smaller magnitude, but display a similar trend as a previous TEM investigation on Durango apatite irradiated with fission products of induced ^{238}U fission [15].

5.4 The Shape of Ion Tracks in Apatite

The shape of chemically etched tracks has been studied extensively as summarised by Wagner and Van den Haute [16]. They have characterised the appearance of tracks after etching with respect to applications in fission track dating. In this section, the combination of SRIM-2008 calculations and SAXS measurements is used to estimate the shape of an ion track [17].

It was previously shown (compare Sect. 5.2.2) how the track radius depends on the energy loss of the ion, which is gradually changing as the energy decreases with the ion penetrating through the crystal. This has already led to the conclusion, that ion irradiation with energies above the Bragg-peak should demonstrate its larger cross-section in their middle, where dE/dx is at its maximum [18]. However, the absolute track radius is not solely determined by the dE/dx , but also by the ion velocity. In fact, *lower* velocities yielded *larger* radii, as a result of the velocity effect.

Fig. 5.8 **a** Illustration of the longitudinal profile of ion tracks in apatite based on calculations of the energy loss for low and high energies (small squares) and interpolation of the track shape (large black squares). The double-arrows show different sample thicknesses used for characterisation with SAXS. **b** SAXS patterns of ion tracks in apatite of different thicknesses. A hard cylinder model was used to fit the results (solid lines). Patterns are offset for clarity



To reconstruct the full shape of the an ion track, the track radius in the high-energy (above the Bragg-peak, energy > 800 MeV) and low-energy sections (below the Bragg peak, energy < 800 MeV) of the ion trajectory were deduced from the two data sets in Sect. 5.2.2 (Fig. 5.5). This was achieved by separately interpolating the respective radius-versus- dE/dx curves, as they show a linear relationship in the energy ranges studied. The energy of the Bragg-peak (800 MeV) was chosen to allow an unbiased transition between the energy range where the velocity effect is negligible and where it is clearly visible. Using SRIM, the energy loss of an 2.2 GeV Au ion was calculated as it penetrates through the apatite crystal. The energy loss remains above the track formation threshold until passing a distance of ~ 80 μm . The energy of the ion at any position can be correlated with the experimentally observed track radii from Fig. 5.5. These track radii were measured on very thin samples (~ 30 – 40 μm), hence they relate directly to the ion energies of the incident swift heavy ions as their energy losses are nearly constant over such lengths.

The shape of the ion track in Fig. 5.8a (circles) within the high-velocity regime (section 0–52 μm) displays almost cylindrical geometry, while in the low-velocity regime (section 52–85 μm) the radius is initially 30% larger than on the surface and then decreases rapidly towards the track end to approximately half the size. To connect

Table 5.2 Radius R for ion tracks in apatite of different thicknesses, calculated using the simulated shape of an ion track and measured experimentally by SAXS. The maximum length of an ion track from 2.2 GeV Au ions in apatite is $\sim 80 \mu\text{m}$

Thickness [μm]	Calculated R [nm]	SAXS track R [nm]	R polydispersity [nm]
20	4.7	4.81	0.26
30	4.8	4.87	0.31
57	5.2	5.03	0.38
80	5.3	5.01	0.48
200	5.2	5.04	0.37

the two velocity regimes, the radius curve was smoothed by linear interpolation (squares) illustrating the cigar-like track shape.

As previously demonstrated, SAXS provides a measure of the average track radii in apatite with very high precision. Figure 5.8b shows the SAXS intensity for ion tracks in apatite samples of different thicknesses irradiated with 2.2 GeV Au ions at $5 \times 10^{10} \text{cm}^{-2}$. The sample thicknesses are marked by vertical lines in Fig. 5.8a and indicate the parts of the track that are contained in the sample. For the thin samples (20, 30 μm) average track radii of 4.81 and $4.87 \pm 0.05 \text{nm}$ were measured. The thicker samples (57, 80 and 200 μm) show a radius between 5.01 and $5.04 \pm 0.05 \text{nm}$, an increase of 3–4% over the thin samples. The polydispersity for the average radii increases from $0.25 \pm 0.05 \text{nm}$ for thin to $0.48 \pm 0.05 \text{nm}$ for thick samples, reflecting the larger variations in the track cross-sections in the thicker samples as they contain longer sections of the tracks.

The fitting parameters are listed in Table 5.2 together with the estimates of the calculated average track radii R_{ave} from Fig. 5.5. These values were calculated by integrating the radius R_{ave} over the respective sample thickness L via:

$$\pi R_{ave}^2 L = V_{ave} = \pi \int_0^L R^2(z) dz \quad (5.4)$$

The calculated results show comparable radii for the thin samples, although their absolute value is slightly underestimated. They correctly predict an increase towards thicker samples due to the largest cross-section being present around a depth of $55 \pm 5 \mu\text{m}$.

It is noted, that the samples originate from three different ion irradiation experiments over the course of several years. This demonstrates the reproducibility and consistency of the observed track formation as well as the reliability of the SAXS measurements.

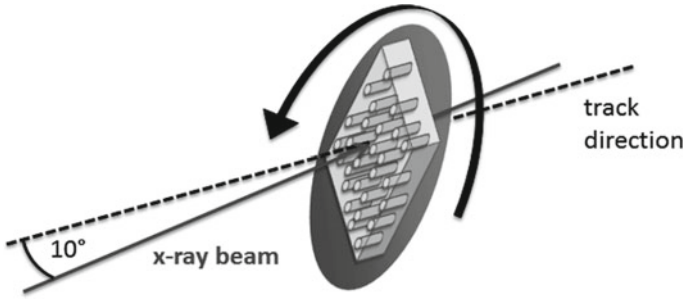


Fig. 5.9 Experimental set-up to study the non-circularity of the track cross-section by tilting the sample around the track axis (black dashed line)

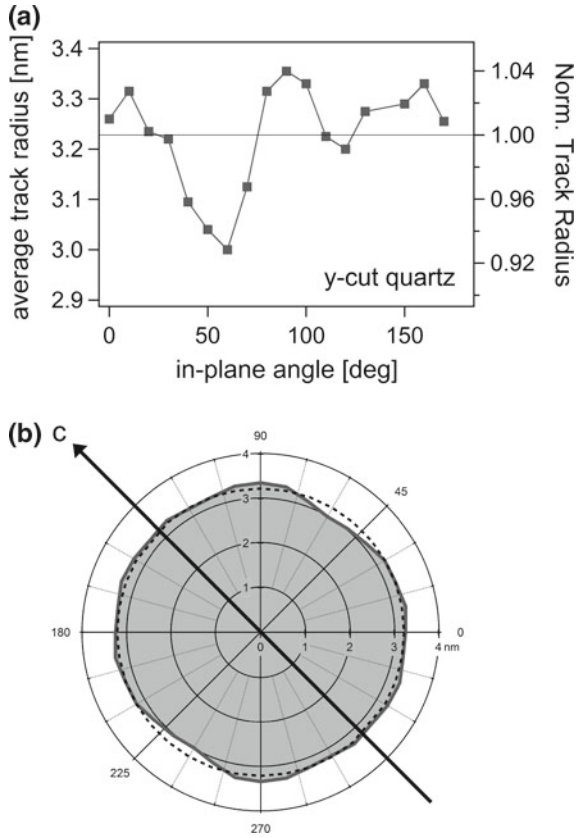
5.5 The Cross-Section of Ion Tracks in Quartz

For all results discussed in this work, it is assumed that the ion track cross-section displays a perfect circular shape. The use of SAXS also allows us to verify this hypothesis by characterising a tilted sample under different in-plane angles. For this experiment, the sample was aligned so that the ion tracks pointed in the same direction as the beam. Afterwards the sample was tilted by 10° as shown in Fig. 5.9. In this geometry, SAXS measures the track radius parallel to the tilt axis. A series of SAXS measurements was then taken by rotating the sample around the track axis between 0 and 180° in steps of 10° . This is equivalent to measuring the track radius around a 180° segment of the track cross-section and allows its reconstruction. Each SAXS images showed the well-known anisotropic scattering pattern and the signal from each streak was independently isolated and fitted with a hard cylinder. The radii, averaged from both streaks, are shown in Fig. 5.10 for tracks in quartz together with the normalised radius for each pattern with respect to the average radius (right axis). The position of 0° was arbitrarily chosen.

Ion tracks in *y*-cut quartz show a distinct minimum (at around 60°) over the half-period, that is stretching from 0 to 180° . Furthermore, the data shows two additional, much less pronounced, minima around 60° before and after the main one. However, as their values are extremely close to the average track radius, they only have negligible effects on the overall shape of the tracks. Figure 5.10b shows the estimated cross-section of a track along *y*-cut quartz. The elliptical-shaped cross-section is drawn by discretely plotting the experimental SAXS track radii obtained in 10° steps. Intermediate values were obtained by linear interpolation and values for angles between 180 to 360° assuming periodicity. For comparison, the average track radius was computed by drawing a circle with the average track radii. The track shows an elliptical shape with a numerical eccentricity of 0.4 .

This elliptical cross-section can be explained in the framework of track formation through the anisotropy of the thermal conductivity of quartz. As the track is pointing along the crystal's *y*-direction, its cross-section consists of the *x*-direction, as the

Fig. 5.10 **a** SAXS-measured radius (left axis) for ion tracks under different angles in quartz [tracks created along y -axis]. The normalised track radii (right axis) are computed with respect to the average track radius. **b** Estimated shape of the track cross-section (filled shape) and a circular pattern, based on the average track radius (dashed line)



other in-plane direction, and the z -direction. Those components of the heat transfer pointing in the z -direction are known to have a higher thermal conductivity (compare Sect. 5.3) and are therefore expected to show less spread of damage than along the x -direction.

In conclusion, these results show the cross-section of ion tracks in y -cut quartz. Tracks in this material show a deviation from a perfect circle with tendency to a more elliptical shape. Based on these results, further investigations would be of great benefit: If the same experiment would be performed on z -cut quartz, a more circular shape would be expected, due to the higher symmetry of the radial thermal conductivity.

5.6 Summary

In this chapter, the correlation between the ion irradiation parameters and the structure of the resulting ion tracks was shown. Depending on the energy, two different regimes were identified, low-E (below the Bragg peak) and high-E (above the Bragg peak). Within each regime the track radius showed a linear dependence with the energy loss in a certain range. However, comparing similar energy losses between low and high ion energies, the track radii were nearly 2 nm larger for lower energies. This is explained with the higher radial energy density distribution for low-E as a result of the velocity effect. The crystallographic direction was also shown to influence the size of the ion tracks with the track radii in quartz and apatite differing between axes by around 2–7%. As a primary factor of this size anisotropy, the different radial thermal conductivities were identified. Finally, deviations of ion track shapes from cylinders were investigated. A slightly elliptical cross-section was found for ion tracks in y-cut quartz and a variation of the cross-section along the track length was estimated for tracks in apatite.

Comparing the results of SAXS and SANS measurements on ion tracks in quartz and apatite, similar values were found for the track radii and density differences between track and host matrix. This indicates a uniform damage profile among the cation and anion sub-lattice. All ion tracks measured by SAXS and SANS were modelled with the same hard cylinder model.³ The use of this model can only give an average value for the radius, unless additional parameters are introduced to take a non-circular shape or length-dependent change in radius into account. However, the deviations from cylindrical shapes are small such that the investigations in the upcoming chapters will use this simplified model. This is further justified by the primarily focus of this work on the understanding on the influences of external parameters (e.g. temperature, pressure) on the relative change of the tracks size. For this purpose, the average track sizes yields acceptable results.

References

1. F. Lisker, B. Ventura, U.A. Glasmacher, Apatite thermochronology in modern geology. *Geol. Soc. Lond. Spec. Publ.* **324**(1), 1–23 (2009)
2. A.A. Leino, S.L. Daraszewicz, O.H. Pakarinen, K. Nordlund, F. Djurabekova, Atomistic two-temperature modelling of ion track formation in silicon dioxide. *Europhys. Lett.* **110**(1), 16004 (2015)
3. J. Ilavsky, P.R. Jemian, Irena: tool suite for modeling and analysis of small-angle scattering. *J. Appl. Crystallogr.* **42**(2), 347–353 (2009)

³The only deviations from a set of perfectly aligned homogenous cylinders taken into account are the Gaussian distributed radius polydispersity and a Gaussian distributed tilt of the tracks to each other.

4. D. Albrecht, P. Armbruster, R. Spohr, M. Roth, Small angle neutron scattering from oriented latent nuclear tracks. *Radiat. Eff.* **65**(1–4), 145–148 (1982)
5. B. Afra, K. Nordlund, M.D. Rodriguez, T. Bierschenk, C. Trautmann, S. Mudie, P. Kluth, Thermal response of nanoscale cylindrical inclusions of amorphous silica embedded in α -quartz. *Phys. Rev. B* **90**, 224108 (2014)
6. P. Kluth, O.H. Pakarinen, F. Djurabekova, R. Giulian, M.C. Ridgway, A.P. Byrne, K. Nordlund, Nanoscale density fluctuations in swift heavy ion irradiated amorphous SiO₂. *J. Appl. Phys.* **110**(12), 123520 (2011)
7. B. Afra, M. Lang, M.D. Rodriguez, J. Zhang, R. Giulian, N. Kirby, R.C. Ewing, C. Trautmann, M. Toulemonde, P. Kluth, Annealing kinetics of latent particle tracks in Durango apatite. *Phys. Rev. B* **83**, 064116 (2011)
8. D. Schauries, M. Lang, O.H. Pakarinen, S. Botis, B. Afra, M.D. Rodriguez, F. Djurabekova, K. Nordlund, D. Severin, M. Bender, W.X. Li, C. Trautmann, R.C. Ewing, N. Kirby, P. Kluth, Temperature dependence of ion track formation in quartz and apatite. *J. Appl. Crystallogr.* **46**(6), 1558–1563 (2013)
9. W. Li, M. Lang, A.J.W. Geladow, M.V. Zdrovets, R.C. Ewing, Thermal annealing of unetched fission tracks in apatite. *Earth Planet. Sci. Lett.* **321**, 121–127 (2012)
10. S. Klaumünzer, Ion tracks in quartz and vitreous silica. *Nucl. Instrum. Methods Phys. Res. B* **225**, 136–153 (2004)
11. W. Li, L. Wang, M. Lang, C. Trautmann, R.C. Ewing, Thermal annealing mechanisms of latent fission tracks: apatite versus zircon. *Earth Planet. Sci. Lett.* **302**(1–2), 227–235 (2011)
12. T. Sawamura, S. Baba, H. Yamazaki, Effect of twinning caused by thermal annealing on etched tracks in synthetic quartz. *Jpn. J. Appl. Phys.* **30**(No. 2A), L212–L214 (1991)
13. J.A.L. Rabone, A. Carter, A.J. Hurford, N.H. de Leeuw, Modelling the formation of fission tracks in apatite minerals using molecular dynamics simulations. *Phys. Chem. Miner.* **35**(10), 583–596 (2008)
14. W. Li, P. Kluth, D. Schauries, M.D. Rodriguez, M. Lang, F. Zhang, M. Zdrovets, C. Trautmann, R.C. Ewing, Effect of orientation on ion track formation in apatite and zircon. *Am. Miner.* **99**(5–6), 1127–1132 (2014)
15. T.A. Paul, P.G. Fitzgerald, Transmission electron microscopic investigation of fission tracks in fluorapatite. *Am. Miner.* **77**, 336–344 (1992)
16. G.A. Wagner, P. Van den Haute, *Fission-Track Dating* (Kluwer Academic Publishers, Dordrecht, 1992)
17. B. Afra, T. Bierschenk, M. Lang, M.D. Rodriguez, C. Trautmann, W. Li, R.C. Ewing, P. Kluth, The shape of ion tracks in natural apatite. *Nucl. Instrum. Methods Phys. Res. B* **326**, 117–120 (2014). (17th International Conference on Radiation Effects in Insulators (REI))
18. Beam Interact, J. Olivares, A. Garcia-Navarro, A. Mendez, F. Agullo-Lopez, G. Garcia, A. Garcia-Cabanes, M. Carrascosa, Novel optical waveguides by in-depth controlled electronic damage with swift ions. *Nucl. Instrum. Methods Phys. Res. Sect. B. Mater. Atoms* **257**, 765–770 (2007)
19. R.A. Donelick, M.K. Roden, J.D. Mooers, B.S. Carpenter, D.S. Miller, Etchable length reduction of induced fission tracks in apatite at room temperature: crystallographic orientation effects and initial mean lengths. *Int. J. Radiat. Appl. Instrum. Part D. Nucl. Tracks Radiat. Meas.* **17**(3), 261–265 (1990)

Chapter 6

Track Formation Under Temperature and Pressure



This chapter discusses the influence of two external ion irradiation parameters on ion track formation: temperature and pressure. In natural environments where fission tracks are generated, both parameters can be significantly elevated compared with ambient conditions. This particularly applies to fission tracks formed several thousand metres below the earth's surface, which are relevant for oil and gas exploration [1]. The majority of irradiation experiments that simulate fission tracks, however, are conducted under ambient conditions for practical reasons. Lang et al. have investigated track formation under high temperature (250 °C) and in the presence of elevated pressure (0.75 GPa), by irradiating zircon within a heatable high-pressure cell [2]. The track sizes were measured with TEM and indicate a small, positive correlation between track cross-section and a simultaneous increase in temperature and pressure during track formation. The present work systematically investigates the influences of temperature and pressure independently in quartz and apatite. The results are explained by using existing models for track formation.

6.1 Temperature-Dependence of Ion Track Formation

Natural fission tracks in apatite and zircon can typically be observed up to a maximum temperature of 120–150 °C and 250 °C, respectively, their so-called closure temperature [3–5]. These temperatures correspond to depth levels down to 5–8 km. When fission tracks are formed at these depths, the track creation process also occurs in the presence of elevated temperatures. However, when artificial fission tracks are created for lab-based experiments, the tracks are generally formed at room-temperature, thus making the assumption that the effects of temperature during the track formation on the resulting tracks are negligible. This could potentially affect geo-thermochronological data derived from the fission tracks. If tracks were longer if created under elevated temperatures, this would underestimate the track shrinkage effects and consequently underestimate fission track ages.

In the field of materials science, only a few investigations regarding the effects of the irradiation temperature on ion track formation have been carried out. In 1991, the effect of different irradiation temperatures on latent ion tracks was studied in magnetic insulators such as $(\text{Ba}, \text{Sr})\text{Fe}_{12}\text{O}_{19}$ and $\text{Y}_3\text{Fe}_5\text{O}_{12}$ [6]. The results did not show a clear dependence of the irradiation temperature on the ion track dimensions. This may be a result of the experimental technique used, as Mössbauer spectroscopy could not measure the track cross-sections with an uncertainty below 20%. However, for ion irradiation with lower energies ($dE/dx < 10 \text{ keV/nm}$), where only discontinuous damage fragments are formed, an increase of their cross-section was observed for elevated substrate temperatures. The same issue was addressed again in 2001, using lab-based SAXS for different irradiation temperatures on LiF [7]. Although an increase of the track size for high temperatures was observed again, it could not be confirmed within the uncertainty of the size-measurement.

The present work shows track formation under elevated temperatures in apatite and quartz. The use of synchrotron-based SAXS leads to reduced uncertainties and a larger amount of samples has increased the statistical significance. This has clearly confirmed the positive correlation between irradiation temperature and track size [8]. The effect of the formation temperature on track sizes in apatite was investigated in the context of fission track dating.

For quartz, the simple and well-understood structure has allowed simulations of track formation using theoretical models. From these simulations, performed using the thermal spike model and molecular dynamics simulations, quantitative parameters such as the track radius can be investigated for different formation temperatures. This enables us to gain an understanding of the mechanisms responsible for the effects of temperature on track formation.

6.1.1 Apatite

Durango apatite was chosen for irradiation at a range of different temperatures at the UNILAC at GSI in Darmstadt, Germany. The irradiation was carried out with 2.2 GeV Au ions at a fluence of $5 \times 10^{10} \text{ cm}^{-2}$ (compare Sect. 4.3). The temperature of the samples was controlled to values between RT and 360 °C by a furnace. For comparison, a set of reference samples was also irradiated at RT and, subsequently, placed in the furnace. These samples were covered to prevent an additional exposure to the ion beam. During the irradiation, these samples underwent an identical heating cycle as those irradiated at the elevated temperature. The purpose of these reference samples was to assess the influence of the heating cycle on existing tracks, to isolate the sole effects of the substrate temperature during irradiation on the size of the tracks. An additional set of apatite samples was irradiated with 1.7 GeV Xe ions at liquid helium (24 K) and RT to also study track formation in the cryogenic temperature regime.

Figure 6.1a shows SAXS detector images of tracks formed at RT (a1) and 360 °C (a2). The similarity of the oscillating patterns in both images indicates no structural

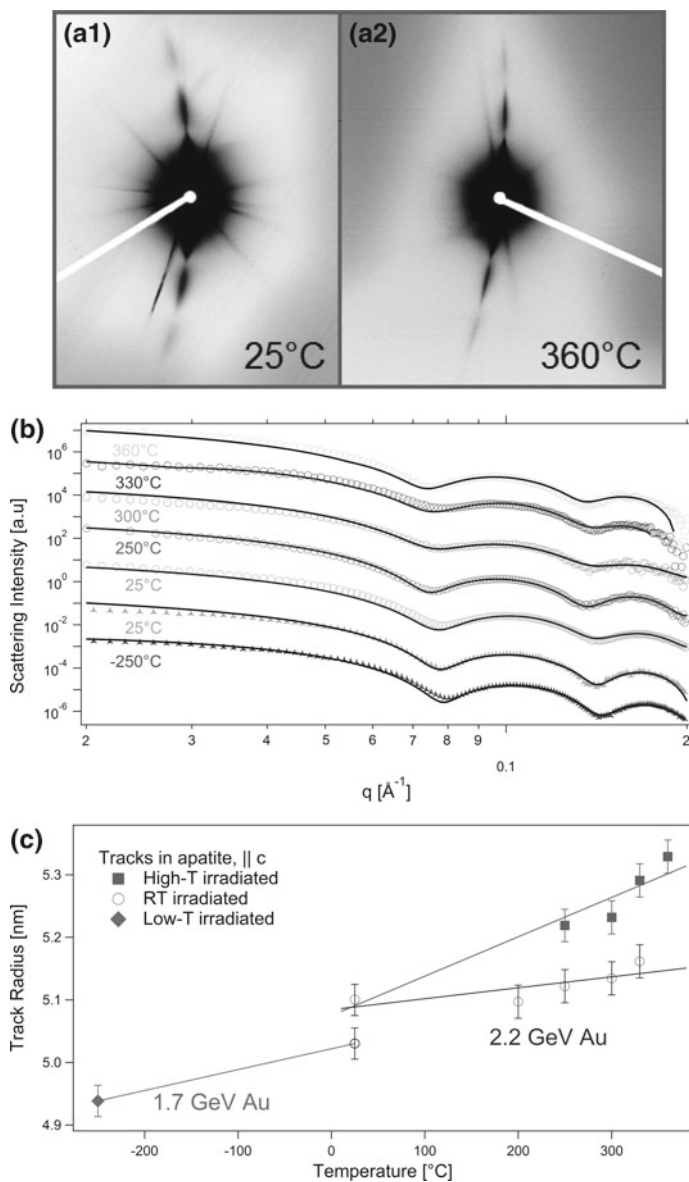


Fig. 6.1 **a1, a2** SAXS detector images of ion tracks in apatite irradiated at RT and 360 $^{\circ}\text{C}$. Darker colours correspond to high scattering intensities. **b** SAXS intensities as a function of q for apatite irradiated with 2.2 GeV (open circles) and 1.7 GeV (solid triangles) Au ions. A hard cylinder model was used to fit the results (solid lines). Patterns are offset for clarity. **c** Corresponding ion track radii as a function of irradiation temperature for high temperature (solid squares) and -250°C (solid diamonds). For reference purposes, a set of RT-irradiated samples underwent the same annealing cycle as the high-T irradiated samples (open circles). A linear regression fit was applied between radius and temperature (lines)

difference between the two different irradiation temperatures. Figure 6.1b shows the SAXS intensities as a function of q for all irradiation temperatures. The SAXS patterns display a small shift of the intensity minima towards lower q values with increasing irradiation temperature. For SAXS measurements on cylindrical objects, the spacings $\Delta q = q_n - q_{n-1}$ between the minima can be derived from the scattering amplitude (or form factor). As it can be derived from Eq. (3.21) in Sect. 3.3.1, these minima Δq correspond to the zeros of the Bessel function $J_1(R \cdot q) = 0$. Hence, Δq is inversely proportional to the size of the scattering objects, and its shortening is a clear indication of an increase in track radius.

The best results in fitting the SAXS patterns were obtained by using a cylinder model as discussed in Sect. 3.3.3. A variation in track radius was modelled by convoluting R with a normal distribution with standard deviation σ_R . This polydispersity in the track radius was typically found to be within the range of 0.4–0.6 nm (8–11% of R) and corresponds approximately to the variation in track radius over the length of the track. The fits for each SAXS curve are shown as solid lines in Fig. 6.1b. The track radii deduced from the fitting procedure are shown in Fig. 6.1c. For tracks in apatite irradiated at RT a radius of 5.1 nm was observed, which is in good agreement with TEM measurements [9, 10]. Tracks produced at elevated irradiation temperatures increase approximately linearly in radius with a rate of 0.06 ± 0.01 nm per 100°C . The apatite samples irradiated at -250°C and RT show the effects of irradiation at cryogenic temperature. They also show a positive correlation between track size and temperature, with an increase at a rate of 0.03 nm per 100°C . The absolute radii of these two samples cannot be compared directly with the high-T series, as they were irradiated with slightly lower ion energy.

Figure 6.1c also shows the track radii of the reference samples (open circles). They underwent the same heating cycle as the primary samples. The total time for the temperature ramping and heated up stage, the irradiation, and subsequently, the cooling process accumulates to less than 15 min. Together with the relatively moderate temperatures in comparison to their recrystallisation temperature, it is reasonable to expect no significant reduction in the overall track size of recrystallisation. In fact, the radii of the tracks in all reference samples have actually increased slightly during the thermal annealing. However, their size has only increased with a rate that is three to four times less than the samples irradiated under elevated temperatures. The physical origin of this effect is likely related to a shortening in track length from the defect annealing and recrystallization processes at the track boundaries. As shown in Sect. 5.4, tracks in apatite have a smaller radii towards their end, where the ion projectile has stopped as a result of lower energy losses. Upon thermal annealing, this end typically recrystallises first [10]. As SAXS measures averages over the entire track length, an initial damage recovery at the track end, i.e. where the track radius is small, leads to an increase in the average track radius measured by SAXS.

6.1.2 Quartz

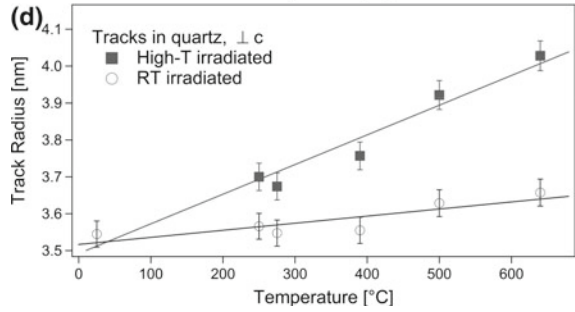
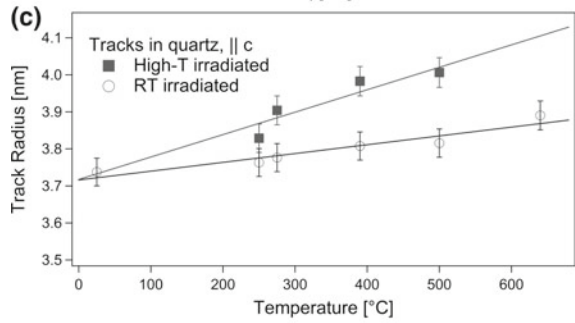
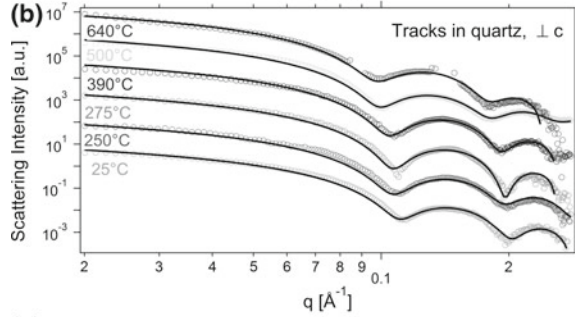
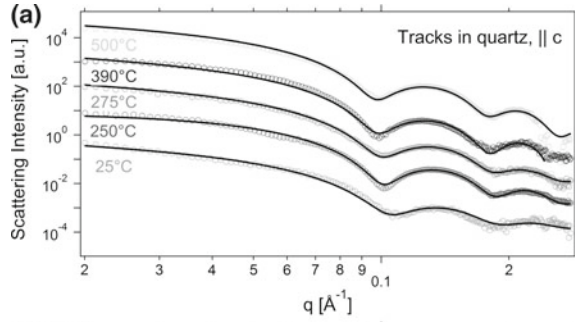
Natural quartz samples were irradiated in a similar setup as apatite with 2.2 GeV Au ions at a fluence of $5 \times 10^{10} \text{ cm}^{-2}$. Tracks in quartz possess a higher recrystallisation temperature than apatite, therefore higher temperatures up to 640 °C could be employed without the danger of annealing the tracks during creation. Prior to irradiation, the quartz samples were polished and cut with the surface normal \parallel c -axis (z -cut) or \perp c -axis (x - or y -cut). The corresponding SAXS patterns for the tracks are shown in Fig. 6.2a and b, respectively. The SAXS patterns were again fitted using the hard cylinder model and the resulting track radii are shown in Fig. 6.2c and d. The radius polydispersity obtained from the fits was typically around 0.2–0.4 nm (5–10% of R). Tracks in quartz show typical radii of 3.5–3.7 nm when created at RT, which is of similar magnitude to TEM measurements at comparable stopping powers [11]. Additionally, the tracks \parallel c in quartz show a 5% larger radius than those \perp c . The origin of this difference is attributed to the anisotropy of the thermal conductivities of quartz along different crystallographic directions as has been discussed in Sect. 5.3.

With increasing temperature, the ion tracks show a linear increase in radius of $0.08 \pm 0.02 \text{ nm}$ per 100 °C for tracks \perp c -axis and $0.06 \pm 0.02 \text{ nm}$ per 100 °C for tracks \parallel c -axis. These values are of comparable magnitude to tracks in apatite. The annealing of RT irradiated quartz reference samples also leads to an increase in the track radius at a rate of $0.02 \pm 0.01 \text{ nm}$ per 100 °C. This is a factor of three to four below the growth rate observed for high-T irradiations. The effect may be attributed to a heat-induced irreversible expansion of the ion tracks [12]. The increase of the track radius is linear over the entire temperature range tested, although above 573 °C, α -quartz undergoes a reversible phase transition into β -quartz with a change of the crystal structure from trigonal into hexagonal. The temperature effect on the track size appears to be unaltered by the phase transition. Regardless of the irradiation temperature, a density change of $\Delta\rho = 1.0 \pm 0.4\%$ was found using the procedure described in Sect. 3.3.3.

6.1.3 Simulations and Discussion

The physical origin for the increase in track radius can be understood within the limits of the inelastic thermal spike model (iTS) [13]. The model explains track formation through a melting-process of atoms along the ion trajectory. Hence, the energy required to form a track mainly depends on the difference between melting energy E_m and the internal energy E_i of the atoms. The internal energy changes with irradiation temperature T_0 , consequently irradiation at elevated temperatures reduces the amount of energy required for the melting process as shown schematically in Fig. 6.3. If the energy difference is reduced, this increases the volume where the deposited ion energy exceeds the melting temperature of the host material. As a consequence,

Fig. 6.2 SAXS scattering intensities for **a** ion tracks $\parallel c$ and **b** $\perp c$ in quartz for different irradiation temperatures (open circles). A hard cylinder model was used to fit the results (solid lines). SAXS patterns are offset for clarity. Radius obtained from the SAXS patterns for **c** tracks $\parallel c$ and **d** $\perp c$ for high-T (filled squares) and RT (open circles) irradiated samples. The corresponding reference samples underwent the same heat cycle (open circles). A linear regression fit was applied between radius and temperature (lines)



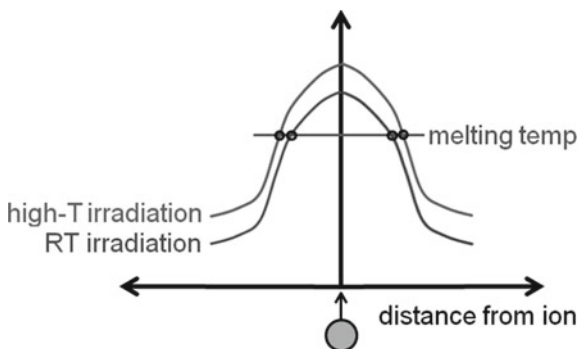


Fig. 6.3 Schematic explanation for the larger track radii at ion irradiation high temperatures (high-T) in comparison to room-temperature (RT)

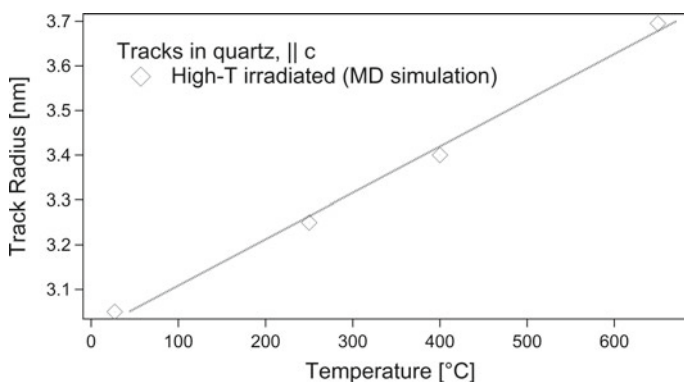


Fig. 6.4 MD simulations (open diamonds) for ion tracks in quartz at different temperatures. A linear regression fit was applied between radius and temperature (line)

an increase occurs for the radial distance around the ion trajectory where the energy loss is high enough for ion track formation to occur, yielding larger track radii. For irradiation at sub-zero degree temperatures, the same physical explanation can be applied to the observed reduction in track size. The magnitude of the effect is lower due to the reduced heat capacity of solids at cryogenic temperatures. Calculations using the iTS model by Marcel Toulemonde from the CIMAP Laboratory in Caen, show an increase of $0.07 \text{ nm}/100^\circ\text{C}$ for the radius of tracks in quartz [8]. This provides an excellent match to the experimental values of $0.06 \pm 0.02 \text{ nm}/100^\circ\text{C}$ for tracks $\parallel c$ and $0.08 \pm 0.02 \text{ nm}/100^\circ\text{C}$ for tracks $\perp c$.

Figure 6.4 shows the results of the MD simulations for tracks in quartz, performed by the group of Kai Nordlund at the University of Helsinki in Finland [8]. The values display a linear trend of the track radius with a relative increase of $0.10 \text{ nm}/100^\circ\text{C}$, which is also consistent with the experimental results. Despite the good agreement between MD and SAXS on the relative effects of temperature during irradiation,

the absolute track radii differ by 0.7 nm. Such an offset is commonly observed in results from the atomic potential used for SiO_2 , which may not fully describe this complex phenomenon. It is potentially affected by the melting point, thermal expansion and elastic properties of the potential, at least. Also the uncertainties in the energy deposition might affect the track size as a function of temperature.

Overall, the MD simulations as well as iTS calculations for ion track formation in quartz confirm the experimental observations by showing a larger track cross-section when they are formed at elevated temperatures. In fact, the calculated increase in radius is of comparable magnitude between the experimental results and those from iTS-calculations and MD simulations.

In other materials, such as crystals exhibiting a strong ionic binding character like LiF [7], a linear increase in damage cross-section was also observed (0.04 nm/100 °C). This is of particular interest, as ion tracks in LiF are not amorphous, but rather consist of discontinuous arrays of point-defect clusters [14]. This shows that the increase in damage radius with elevated temperature during formation is not only limited to amorphisable materials such as apatite and quartz, but of a more general character for damage created by swift heavy-ion irradiation. In contrast to the present observation of a constant density change, the density range in LiF decreases with increasing temperature, indicating that while the damage cross-section increases, the damage morphology (possibly point-defect density) decreases. This might be a result of competing processes of dynamic annealing and defect production. For quartz, no measurements of the radius as a function of irradiation temperature are available for comparison [15].

For ion irradiation with low-energy ions in the keV to low MeV range (nuclear range of stopping power), elevated temperatures generally lead to lower defect concentrations, displaying the exact opposite of the findings of this work for high MeV to GeV [16, 17]. This is attributed to the thermally induced dynamic defect recovery, so-called dynamic annealing. The present case shows that for the regime of electronic stopping power this negative correlation between temperature and damage sizes is not visible. However, it is possible that if the irradiation was to be conducted at higher temperatures, the effects of dynamic annealing would be visible and the obtained tracks would again be smaller in size.

In Sect. 7.2.2 the thermal stability of these tracks upon expose to high temperatures is compared with tracks created under ambient conditions.

6.2 Ion Irradiation Under Pressure

In this section, the effects of irradiation of quartz under pressure are systematically investigated up to pressures of 4.4 GPa by combining ion irradiation in diamond anvil cells (DAC) and subsequent SAXS characterisation. The experimental results are compared with simulations using the iTS model and MD.

To date, the influence of pressure on the formation of ion tracks has only been studied to a limited extent. Lang et al. have demonstrated a small increase in size

for tracks in zircon when irradiation is carried out at elevated temperature and pressure (250 °C and 0.75 GPa) using TEM [2]. Additional results by Lang show that quartz, when irradiated at a pressure of 5.1 GPa, shows ion tracks with an unusually large radius of 7.5 nm as measured by TEM [18]. Despite the larger uncertainty of ion tracks measured by TEM, this radius is significantly larger than expected under ambient conditions. For comparison, typical track radii observed by TEM for comparable energy losses are just around 5 nm [11, 19]. However, the lack of a reference sample, irradiated at ambient pressure with similar energy has prevented definitive conclusions about the effects of pressure on tracks in quartz from this single data point. Nevertheless, these results indicate a positive correlation between pressure and the track radii in quartz.

At this stage, no theoretical work has been published on the effects of elevated pressure on the formation of ion tracks in insulators.

6.2.1 Track Formation in Quartz Within Diamond Anvil Cells

To address this question experimentally, quartz was irradiated under pressure and subsequently characterised using SAXS while still under pressure and again after the release of the pressure. For this purpose a set of four DACs was used. Each cell was loaded with a small piece of synthetic quartz of 50 μm thickness and about 0.02 mm^2 in size. The two diamonds used had a thickness of about 2.15 mm each. Details about the set-up of DACs can be found in Sect. 4.2. The DACs were set to pressures of 2.0, 3.9, 4.4 and 9.6 GPa with uncertainties of about ± 0.3 GPa. As reference, an additional quartz piece of similar size was placed on the anvil of a single diamond to obtain tracks formed under ambient conditions (1 bar) with similar ion energies. Table 6.1 shows a summary of the conditions of each DAC.

The DACs were irradiated with 37.2 GeV Au ions at the GSI Heavy Ion Synchrotron (SIS) as outlined in Sect. 4.3.3. While penetrating the diamond, the electronic energy loss of the ions was calculated to be ~ 10 keV/nm using SRIM-2008 [20]. When reaching the quartz sample, the initial ion energy has dropped to approximately 6.8 GeV. With only 50 μm thickness of the quartz sample within the DAC, this energy is more than sufficient to penetration the entire sample while the energy loss was estimated to be ~ 16 keV/nm at the surface and rising to 17 keV/nm towards the end. An irradiation fluence of $5 \times 10^{10} \text{ cm}^{-2}$ was used to prevent potential overlap effects in case the track radius increases significantly from their size at ambient conditions.

After irradiation, the ion tracks were characterised with SAXS while the quartz samples were still within the DACs and remained under the same pressure as during irradiation. The DACs were aligned with approximately 5° tilt to the incident X-ray beam. Figure 6.5 shows the SAXS detector images for the 1 bar reference sample (a) and those irradiated at 2.0 (b), 3.9 GPa (c), and 4.4 GPa (d). After the pressure of the 2.0 GPa cell (b) was released, the SAXS image shown in (e) was measured.

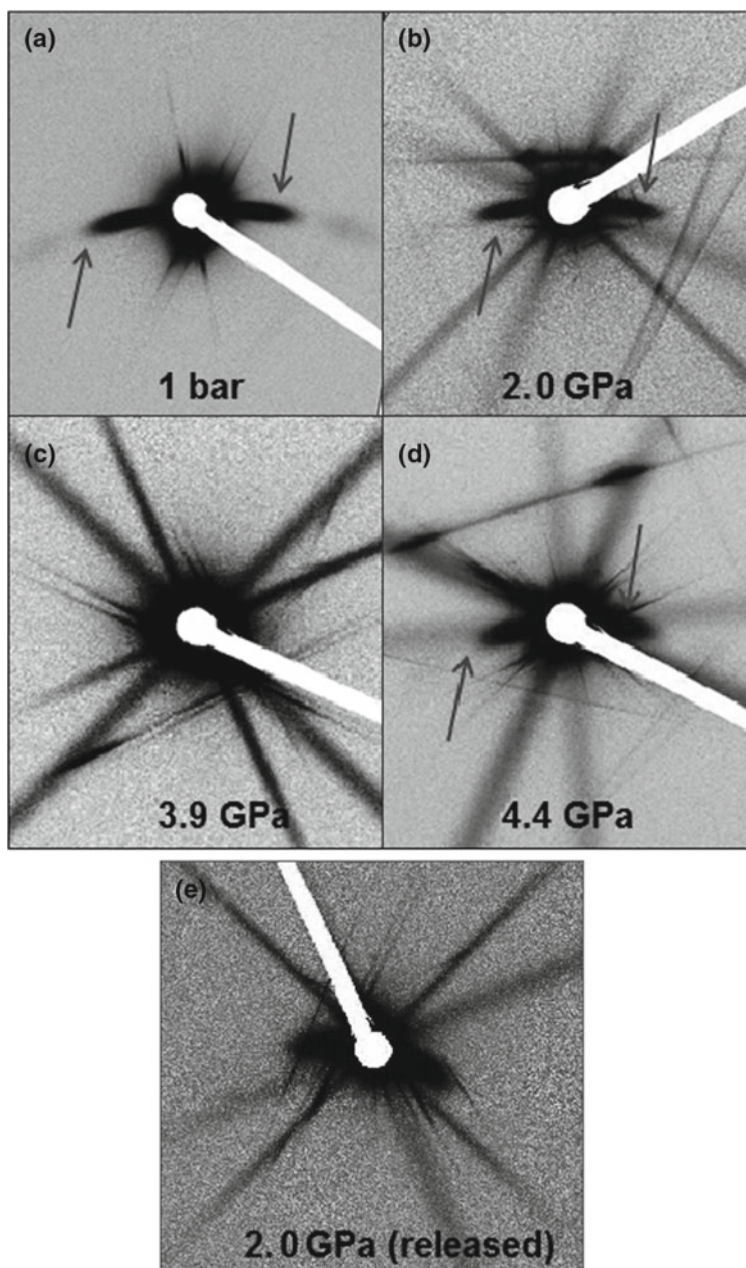


Fig. 6.5 SAXS detector images for ion tracks in quartz, imaged while still under pressure and tilted by 5° to the incident X-ray beam. The samples were irradiated at **a** 1 bar, **b** 2.0 GPa, **c** 3.9 GPa, and **d** 4.4 GPa. **e** The 2.0 GPa cell after the release of pressure. The arrows indicate the streaks resulting from the ion tracks. The parasitic streaks in **b–d** are a result of scattering on the diamond of the DAC. The absence of curved streaks for the 3.9 GPa sample in **c** indicates no ion tracks were found. Darker colours correspond to high scattering intensities

Table 6.1 Data sheet for the DACs used for irradiation under pressure. The pressure P was measured using ruby fluorescence

Cell id	P [GPa]	Diamond thickness [mm]
Ref.	0.0001	2.240 ± 0.001
DAC3	2.0 ± 0.3	2.144 ± 0.001
DAC2	3.9 ± 0.3	2.145 ± 0.001
DAC4	4.4 ± 0.3	2.147 ± 0.001
DAC1	9.6 ± 0.3	2.147 ± 0.001

No SAXS signals resulting from ion tracks were found for the cells pressurised at 3.9 GPa (c) and at 9.6 GPa (SAXS image not shown, but similar to c). This is despite the X-ray beam having a comparable spot size to the entire sample chamber within the DAC. The only X-ray scattering that was observed originates from the diamond. It remains unclear why only two of the four quartz samples have displayed ion tracks in the present SAXS measurements. Their pressure values were in-between those cells showing clear evidence of ion tracks, meaning that enhanced pressure itself to inhibit track formation is very unlikely to cause this behaviour. Similarly, the SAXS set-up allows a very precise alignment of the X-ray beam and the obtained images clearly show that the quartz sample was hit correctly. This leaves the process of irradiation at the SIS accelerator as the most likely source of error for the failure in track formation. Critical for the formation of tracks are the proper alignment of the beam as well as sufficient ion energy to penetrate through the first diamond to reach the sample. The thickness of the diamonds was measured with approximately $4 \mu\text{m}$ precision and even a small angle leading to a longer path throughout the diamond cannot fully explain a total absorption of the initial ion energy. This leaves a misalignment of the sample with the ion beam as the most likely reason for not observing ion tracks with SAXS in these two cells.

The SAXS measurements show no indication that ion tracks have been formed in diamonds as a result of the irradiation. This is in agreement with previous experimental investigations on the formation of tracks in diamonds, which have not observed continuous ion tracks [21]. Simulations using MD, however, have suggested that for energy losses above 10.5 keV/nm amorphous tracks could at least temporarily form in diamond. The lack of experimental observations is attributed to the inefficient electron-phonon coupling [22].

Figure 6.6a shows the isolated SAXS patterns for the streaks of quartz irradiated under 1 bar, 2.0 and 4.4 GPa and of the 2.0 GPa sample after the release of pressure. All samples were imaged in different DACs and show a different extend of overlap with the parasitic scattering with the diamond. Thus the patterns appear to differ in shape at higher q -values. However, this might not necessary be an indication of a different track structure. All SAXS patterns show a clearly visible first oscillation and could be fitted by using the same hard cylinder model, as previously used for quartz irradiated under ambient conditions. The resulting track radii are shown in Fig. 6.6b.

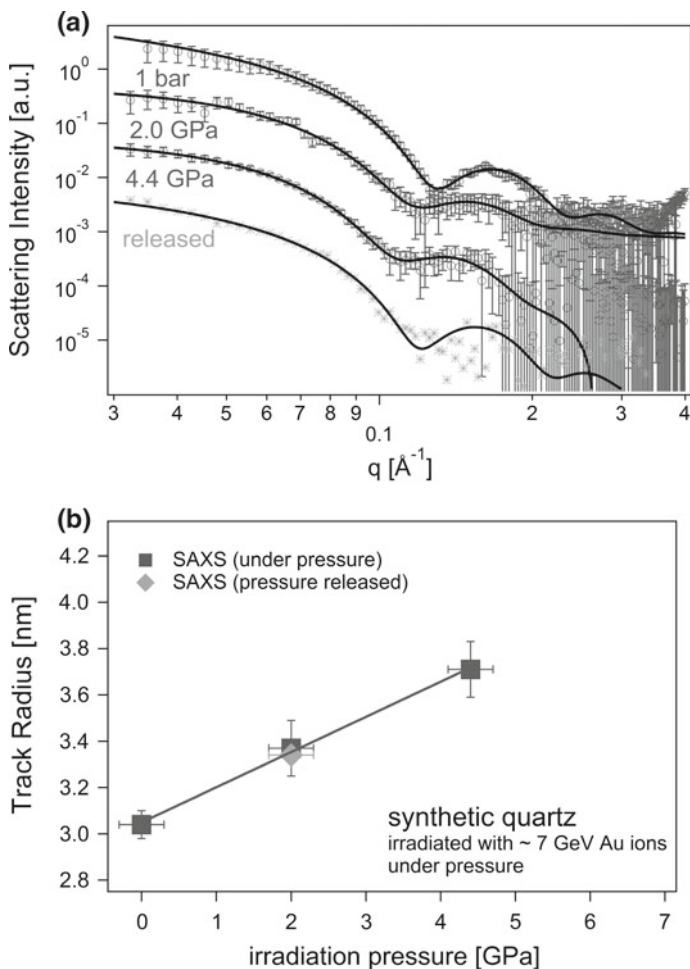


Fig. 6.6 **a** SAXS patterns for ion tracks in quartz in DACs, tilted by 5° , irradiated under pressures at 1 bar (top circles), 2.0 GPa (centre circles), and 4.4 GPa (bottom circles) and after release of the 2.0 GPa cell (crosses). A hard cylinder model was used to fit the results (solid lines). Patterns are offset for clarity. **b** Track radii derived from the SAXS patterns in **a** as a function of pressure during ion irradiation. A linear regression was applied between radius and irradiation pressure (line)

They clearly indicate a positive correlation between pressure and the average track radius. The increase of the radius, as a consequence of the increased pressure, is of the order of 0.15 nm/GPa or approximately an increase in size by 22% between irradiation at 1 bar and 4.4 GPa (Table 6.1).

To test whether the effect of the pressure on the tracks was permanent, the pressure in the DAC was released and the samples measured again. The corresponding SAXS pattern for the 2.0 GPa cell is shown in Figs. 6.5e and 6.6b (solid diamond). The tracks irradiated at 2.0 GPa have shown the same radius within the uncertainty after

pressure release. It is noted that the 4.4 GPa sample did not show any streaks or signs of ion tracks after the pressure release. The X-ray spot was observed to clearly hit the sample, as some scattering originating from non-track related defects in the crystalline quartz structure was observed. A possible explanation could be that the sudden unloading of the DAC and rapid reduction of pressure from 4.4 GPa down to ambient conditions led to a recrystallisation of the tracks. For the 2.0 GPa sample, this quenching process might have been less strong, thus the track fully survived the pressure release. In fact, the SAXS signal for the 2.0 GPa sample appears to be weaker in comparison with the measurement under pressure. This might indicate a partial recrystallisation mechanism could take place here as well. However, the low amount of samples does not allow a further investigation within this work. It is noted that if the experiment was repeated, a slow release of pressure might therefore be advisable for the DACs to determine whether this causes the disappearance of the ion tracks.

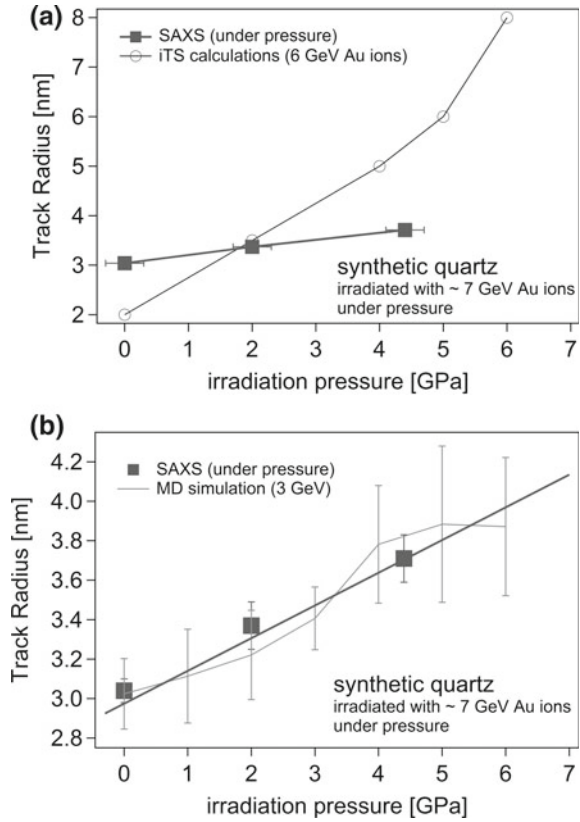
It is noted that the SAXS patterns not only differ by the measured average track radius, but also in polydispersity, background and intensity. This is more attributed to the use of DAC, leading to a range of discrepancies between each sample. This includes different sample sizes, measurements under different angles, and different X-ray attenuation due to the use of different diamonds and X-ray angles. Thus parameters beyond the track radius, requiring the absolute scattering intensity (i. e. density difference), cannot be derived from these SAXS patterns. The success of the hard cylinder model on fitting the SAXS patterns, however, suggests a rather similar structure for tracks created under pressure in comparison with ambient conditions.

6.2.2 *Thermal Spike Calculations for Elevated Pressure*

The experimental SAXS results have clearly demonstrated an increase in the track radius when quartz was irradiated under elevated pressure. The similarity of the track radii before and after the release of the pressure shows that the radial increase is a permanent effect, which is resulting directly from the higher pressure conditions during the formation of the ion tracks. These results can be compared with inelastic thermal spike (iTS) calculations, which were carried out by Marcel Toulemonde [23].

In Sect. 6.1, the same model was used to simulate the size of tracks as a function of temperature. The model uses the difference between the initial energy E_i and the melting energy E_m , which is the energy required to reach the melting temperature plus the energy for the phase transition from solid to liquid. When elevated pressure levels are taken into account, E_i increases due to an additional term $-PdV$ with $dV < 0$. This increase amounts to 0.08 eV/at per GPa, based on calculations taking into account the volume change, as shown by Yamanaka et al. [24]. At the same time elevated pressure is known to increase the melting temperature of SiO_2 , as evident from the phase diagram of quartz at its equilibrium state shown in Sect. 1.3.1. This leads to an increase of E_m by ~ 0.03 eV/at per GPa for pressures less than 7 GPa [25]. The overall change in the total energy now required for ion track formation under pressure is:

Fig. 6.7 Ion track radii for high-pressure irradiated quartz from the experimental SAXS patterns in Fig. 6.6 (full squares) together with theoretical results (open circles) from **a** iTS calculations and **b** MD simulations. A linear regression fit was applied between experimental radii and irradiation pressure (solid lines)



$$d(E_m - E_i)/dP = -0.05\text{eV/at per GPa} \quad (6.1)$$

Using $d(E_m - E_i)/dP < 0$, the increase in track radius can be explained in a similar way as for elevated temperatures in Sect. 6.1. The reduced energy required for track formation at elevated pressures leads to more available energy as compared with ambient conditions. This excess in energy is deposited in radial direction and consequently leads to an increase in radius for the (cylindrical) region in which the deposited energy is above the track formation threshold.

Figure 6.7a shows the experimentally obtained SAXS results (solid squares) together with the iTS calculations for comparable conditions to the irradiation (36 MeV/u and 13 keV/nm) [26]. Both, the iTS model and the experimental results show an increase as a function of pressure although they strongly differ in the rate of increase. The experimental rate of 0.15 nm/GPa is significantly lower than the calculated rate of ~0.8 nm/GPa. Given the simplifications of the iTS, the discrepancy is most likely a result of an overestimation of the pressure-related effects from the model. This overestimation is likely a result of the assumptions about the melting phase transition from solid to liquid made by the iTS model. While the iTS model

takes the parameters at the equilibrium into account, the effects of swift heavy ions in solids are, in fact, far away from equilibrium. Hence, the calculated values may not necessarily fully reproduce the effects of pressure on the track radius in a quantitative way.

6.2.3 *Molecular Dynamics Simulations*

MD simulations have also been used to study track formation under pressure by the group of Kai Nordlund [8, 27]. Figure 6.7b shows the experimental track radii together with MD simulations for track formation at a range of different pressure values up to 6 GPa using the TT-MD code. The parameters are similar to Ref. [11, 28]. The initial pressure in the simulation cells is created with a Berendsen thermostat [29] in a 50 ps relaxation run. During the simulation, no pressure control is applied. The overall agreement between the increase in radius, as reported by the TT-MD model and the SAXS measurements, is remarkably good.

6.3 Summary

In this chapter, it was demonstrated how the radii of amorphous tracks formed in crystalline apatite and natural quartz, shows a positive correlation with the temperature during formation (1–2% per 100 °C). The effect has appeared in a range of insulators, and is not only limited to phosphate minerals and simple oxides, but has also been observed in ferrite and metallic garnets [6], as well as ionic-bonded crystals [7].

In a similar manner, a positive correlation between track radius and pressure during track formation was shown. For synthetic quartz, pressure has shown a relatively large influence on the ion track radius ($\gtrsim 5\%$ per 1 GPa). As only one material system was investigated at only a small range of pressures, it would be interesting to carry out similar experiments using a wider range of materials and pressures.

The results on temperature- and pressure-dependence were both compared to molecular dynamics (MD) simulations, showing a good agreement in both cases. The results were also explained by thermodynamical considerations showing a reduction in the energy required to reach the melting point. Calculations with the iTS model for swift heavy ion irradiation under pressure have identified two competing pressure-dependent terms: Firstly, the amount of energy required to reach the melting temperature, which decreases with pressure. Secondly, the energy required for the melting process of the material, which increases with pressure. As the first term is dominating over the second, increased pressure leads to an overall decrease of the energy required for track formation and consequently an increase in track size. The iTS calculations have overestimated the magnitude of this effect. This is likely a

result of these calculations at the equilibrium state not taking all aspects of the phase transition into account, as these processes occur far from the equilibrium state.

Simulations using MD, however, have provided a good quantitative agreement with the experimental results. This can be attributed to the far more accurate approach MD uses, as it calculates the atomistic response to the swift heavy ions under pressure and does not assume equilibrium conditions.

References

1. Ch. Augustine, J.W. Tester, B. Anderson, S. Petty, B. Livesay, A comparison of geothermal with oil and gas well drilling costs, in *Proceedings, Thirty-First Workshop on Geothermal Reservoir Engineering* (2006)
2. M. Lang, J. Lian, F. Zhang, B.W.H. Hendriks, Ch. Trautmann, R. Neumann, R.C. Ewing, Fission tracks simulated by swift heavy ions at crustal pressures and temperatures. *Earth Planet. Sci. Lett.* **274**, 355–358 (2008)
3. F. Lisker, B. Ventura, U.A. Glasmacher, Apatite thermochronology in modern geology. *Geol. Soc. Lond. Spec. Publ.* **324**(1), 1–23 (2009)
4. G.A. Wagner, P. Van den Haute, *Fission-Track Dating* (Kluwer Academic Publishers, 1992)
5. H. Martin, Dodson, Closure temperature in cooling geochronological and petrological systems. *Contrib. Mineral. Petrol.* **40**(3), 259–274 (1973)
6. C. Houpert, F. Studer, H. Pascard, J. YunFan, M. Toulemonde, Influence of the substrate temperature on the latent track damage cross section in magnetic insulators. *Nucl. Tracks Radiat. Meas.* **19**, 85 (1991)
7. K. Schwartz, A. Benyagoub, M. Toulemonde, Ch. Trautmann, Effect of temperature on track formation by energetic heavy ions in lithium fluoride. *Radiat. Eff. Defects Solids* **155**(1–4), 127–131 (2001)
8. D. Schauries, M. Lang, O.H. Pakarinen, S. Botis, B. Afra, M.D. Rodriguez, F. Djurabekova, K. Nordlund, D. Severin, M. Bender, W.X. Li, C. Trautmann, R.C. Ewing, N. Kirby, P. Kluth, Temperature dependence of ion track formation in quartz and apatite. *J. Appl. Crystallogr.* **46**(6), 1558–1563 (2013)
9. B. Afra, M. Lang, M.D. Rodriguez, J. Zhang, R. Giulian, N. Kirby, R.C. Ewing, C. Trautmann, M. Toulemonde, P. Kluth, Annealing kinetics of latent particle tracks in Durango apatite. *Phys. Rev. B* **83**, 064116 (2011)
10. W. Li, M. Lang, A.J.W. Geladow, M.V. Zdorovets, R.C. Ewing, Thermal annealing of unetched fission tracks in apatite. *Earth Planet. Sci. Lett.* **321**, 121–127 (2012)
11. B. Afra, M.D. Rodriguez, C. Trautmann, O.H. Pakarinen, F. Djurabekova, K. Nordlund, T. Bierschenk, R. Giulian, M.C. Ridgway, G. Rizza, N. Kirby, M. Toulemonde, P. Kluth, Saxs investigations of the morphology of swift heavy ion tracks in alpha-quartz. *J. Phys.: Condens. Matter* **25**(4), 045006 (2013)
12. B. Afra, M. Lang, T. Bierschenk, M.D. Rodriguez, W.J. Weber, C. Trautmann, R.C. Ewing, N. Kirby, P. Kluth, Annealing behaviour of ion tracks in olivine, apatite and britholite. *Nucl. Instrum. Meth. Phys. Res. B* **326**, 126 (2014)
13. M. Toulemonde, W. Assmann, C. Dufour, A. Meftah, C. Trautmann, Nanometric transformation of the matter by short and intense electronic excitation: experimental data versus inelastic thermal spike model. *Nucl. Instrum. Methods Phys. Res. Sect. B: Beam Interact. Mater. Atoms*, **277**, 28 (2012). (Basic Research on Ionic-Covalent Materials for Nuclear Applications)
14. Ch. Trautmann, M. Toulemonde, K. Schwartz, J.M. Costantini, A. Müller, Damage structure in the ionic crystal LiF irradiated with swift heavy ions. *Nucl. Instrum. Meth. Phys. Res. B* **164–165**, 365–376 (2000)

15. S. Klaumünzer, Ion tracks in quartz and vitreous silica. *Nucl. Instrum. Meth. Phys. Res. B* **225**, 136–153 (2004)
16. Sankar Dhar, Wolfgang Bolse, Klaus-Peter Lieb, Ion-beam induced amorphization and dynamic epitaxial recrystallization in alpha-quartz. *J. Appl. Phys.* **85**(6), 3120–3123 (1999)
17. W. Jiang, Y. Zhang, W.J. Weber, Temperature dependence of disorder accumulation and amorphization in Au-ion-irradiated 6H-SiC. *Phys. Rev. B* **70**, 165208 (2004)
18. M. Lang, *The effect of Pressure on Ion Track Formation in Minerals*. Ph.D. thesis, Heidelberg University (2004)
19. A. Meftah, F. Brisard, J.M. Costantini, E. Dooryhee, M. Hage-Ali, M. Hervieu, J.P. Stoquert, F. Studer, M. Toulemonde, Track formation in SiO₂ quartz and the thermal-spike mechanism. *Phys. Rev. B* **49**, 12457–12463 (1994)
20. J.F. Ziegler, J.P. Biersack, U. Littmark, *The Stopping and Range of Ions in Matter* (Pergamon, New York, 1985)
21. M. Lang, U.A. Glasmacher, R. Neumann, D. Schardt, C. Trautmann, G.A. Wagner, Energy loss of 50-GeV uranium ions in natural diamond. *Appl. Phys. A* **80**(4), 691–694 (2005)
22. D. Schwen, E.M. Bringa, Atomistic simulations of swift ion tracks in diamond and graphite. *Nucl. Instrum. Methods Phys. Res. Sect. B: Beam Interact. Mater. Atoms* **256**(1), 187–192 (2007)
23. M. Toulemonde, *iTS Calculations of Track Formation with Pressure in Quartz* (Unpublished)
24. T. Yamanaka, T. Fukuda, J. Mimaki, Bonding character of SiO₂ stishovite under high pressures up to 30 GPa. *Phys. Chem. Miner.* **29**(9), 633–641 (2002)
25. G. Shen, N. Sata, N. Taberlet, M. Newville, M.L. Rivers, S.R. Sutton, Melting studies of indium: determination of the structure and density of melts at high pressures and high temperatures. *J. Phys.: Condens. Matter* **14**(44), 10533 (2002)
26. M. Toulemonde, Experimental results and model calculations for electronic sputtering of vitreous SiO₂ compared to crystalline SiO₂, in *Radiation Effects in Insulators* (2015)
27. K. Nordlund, *MD Simulations on the Formation of Ion Tracks Under Pressure in Quartz*
28. A.A. Leino, S.L. Daraszewicz, O.H. Pakarinen, K. Nordlund, F. Djurabekova, Atomistic two-temperature modelling of ion track formation in silicon dioxide. *Europhys. Lett.* **110**(1), 16004 (2015)
29. H.J.C. Berendsen, J.P.M. Postma, W.F. van Gunsteren, A. DiNola, J.R. Haak, Molecular dynamics with coupling to an external bath. *J. Chem. Phys.* **81**(8), 3684–3690 (1984)

Chapter 7

Thermal Annealing of Ion Tracks



At ambient temperatures, ion tracks in minerals are known to be stable and fairly constant in size. Even over geological timescales, in the range of hundreds of million years, only small reductions in length occur [1]. This changes dramatically when the tracks are exposed to elevated temperatures, leading to a recrystallisation of the damaged structure and a shrinkage in track size (i.e. length and radius). This process is extremely temperature-dependent, with a full recovery and disappearance of all tracks at 170–200 °C over geological timescales of 10^6 years [2]. When annealed at 350–400 °C, however, a duration of less than 1 h is sufficient to fully erase all tracks [3]. This is a result of the rate of recrystallization being typically associated with an exponential dependence of the diffusion rate of the displaced atoms incorporated in the ion tracks on temperature.

Fission track thermochronology correlates the length distribution with the temperature to reveal the thermal history (assuming the values are not affected by pressure). For this purpose, a detailed understanding of the effects of temperature on the shrinkage of the tracks is necessary. This not only requires a collection of natural samples with well-known history, but also a range of lab-based annealing experiments over short timescales. The latter experiments typically involve freshly induced tracks from an external source (e.g. from a nuclear isotope or an ion accelerator) that have never been subjected to thermal annealing before [1]. The annealing of these tracks under controlled conditions, typically between several days up to a few months, yields the distribution in tracks lengths and consequently the shrinkage rates. These values can then be extrapolated to geological timescales (see Sect. 1.2.3 for a comparison of different models). Less understood than temperature, are the effects of pressure on the annealing rate of ion tracks. In fact, a range of contradicting claims report annealing rates for fission tracks in apatite that are either increased [4], or rates that are reduced [5, 6], as well as annealing rates that display no measurable influences at elevated pressures [2, 7, 8].

This chapter starts with an investigation of thermal annealing of apatite and quartz in a series of experiments under ambient pressure conducted over timescales below 1

hr. All characterisation of the ion tracks in this chapter is carried out using SAXS. This allows high-precision measurement of the track directly, while the relative change in length can be estimated indirectly through the scattering intensity and the volume of the tracks. For quartz, annealing of ion tracks along the three main axes is compared. For apatite, only ion tracks parallel to the *c*-axis were investigated, as this direction is the preferential orientation used for fission track analysis. To investigate the effects of simultaneous exposure of temperature and pressure on tracks under controlled conditions, thermal annealing was conducted for ion tracks in apatite by using heatable diamond anvil cells (DACs). Continuous measurements of the track sizes with in situ SAXS were used to investigate whether elevated pressures influence the track annealing process. In order to translate these findings to fission track annealing, the effects of pressure gained from these results were subsequently extrapolated down to geologically relevant pressures.

The key goal of these experiments is to investigate the annealing mechanism of latent ion tracks in quartz and apatite. Using SAXS, the reduction in radius and length can be monitored on the latent tracks during the annealing process using in situ measurements. This is fundamentally different to previous track annealing studies, altering the structure of the tracks via chemical etching and subsequently imaging them with optical microscopy. The advantage of characterising latent tracks is a direct access to the annealing kinetics without the influence of the etching kinetics. The aim of these experiments is to complement the wealth of previous investigations on etched tracks and verify their results. This includes the reduction of radius and length at a range of different annealing temperatures and for tracks along different crystallographic orientations. Another major aspect the present experiments address is the effect of elevated pressure during track annealing.

The annealing was carried out in two different ways: isochronal and isothermal annealing. For isochronal annealing, the samples were heated for a series of steps at different temperatures, all for a constant period time. The track size was either monitored ex situ when the sample was cooled down to RT, or in situ at the respective annealing temperature. For isothermal annealing, the samples were heated to a specific temperature, which was often determined by previous isochronal annealing over a larger range of temperatures and the track size was characterised continuously in situ [9].

In all annealing experiments within this work, freshly induced ion tracks were used. Those tracks were created under well-controlled conditions with detailed knowledge of all relevant parameters. Even more importantly, unlike spontaneous fission tracks, those tracks have not been exposed to higher temperatures prior to annealing, ensuring no annealing history has rendered those tracks more resistant [8].

7.1 Ion Tracks in Quartz

Ion tracks were created in synthetic quartz of well-defined cuts along the x , y and z -direction by irradiation with 2.2 GeV Au ions at fluences of $5\text{--}10 \times 10^{10} \text{ cm}^{-2}$ at the UNILAC at GSI in Darmstadt, Germany. Irradiation was carried out perpendicular to the surface of each respective cut. The samples were polished down to thicknesses between 60 and 80 μm , which is below the estimated track length of 95 μm . Hence, all track length correspond to the sample thicknesses.

During the annealing process, an in situ SAXS image was taken every minute, with the patterns shown in Fig. 7.5 corresponding to the end of each annealing step. The samples were heated using the Linkam TS-1500 annealing stage, which is described in detail in Sect. 4.4.2.

7.1.1 Isochronal Annealing

For isochronal annealing, the samples were exposed to a range of temperatures to study the recrystallisation mechanism of the amorphous tracks that form under the given irradiation conditions back to the initial crystalline structure, similar to their surrounding host matrix. Due to the high thermal stability of ion tracks in quartz, the first annealing temperatures were chosen at 400 and 600 $^{\circ}\text{C}$ and then increased in steps of typically 20 $^{\circ}\text{C}$ for durations of 20 min until the track signature in the SAXS images disappeared.

Figures 7.5 and 7.1 show the in situ SAXS patterns in two- and one-dimensional q -space, respectively, at different stages of the ion track annealing. The oscillations can be seen to stretch to higher q with increasing temperatures, indicating a gradual decrease in the track radius. For x -cut, the streaks in the SAXS patterns vanished almost instantly upon reaching 640 $^{\circ}\text{C}$. In the case of y - and z -cut, on the other hand, the ion tracks remained present up to a temperature of 1040 $^{\circ}\text{C}$. The 1D patterns in Fig. 7.1 were obtained by extracting the scattering of the “streak” from each image in Fig. 7.5.

Reduction of the Ion Track Radius

The track radii obtained at the end of each temperature step from the respective fits are shown in Fig. 7.2a. For ion tracks in y - and z -cut quartz, no significant reduction of the ion track size was observed until a temperature of around 800 $^{\circ}\text{C}$ was reached. When compared with annealing studies on quartz utilising chemical etching, these results show a very similar behaviour. For a range of different ion track orientations, Sandhu et al. has demonstrated a reduction in length for etched ion tracks starting at 700 $^{\circ}\text{C}$ and showing a significant reduction at 950 $^{\circ}\text{C}$ [10]. The ion track retention, the ratio between the registration efficiency of annealed and un-annealed etched samples, were studied by Sawamura et al. in x -, y - and z -cuts, using similar techniques [11]. In agreement with the findings of this work, they reported x -cuts showing an ion track retention of less than half of that for y/z -cuts at 550 $^{\circ}\text{C}$. Ion tracks in x -cut quartz have

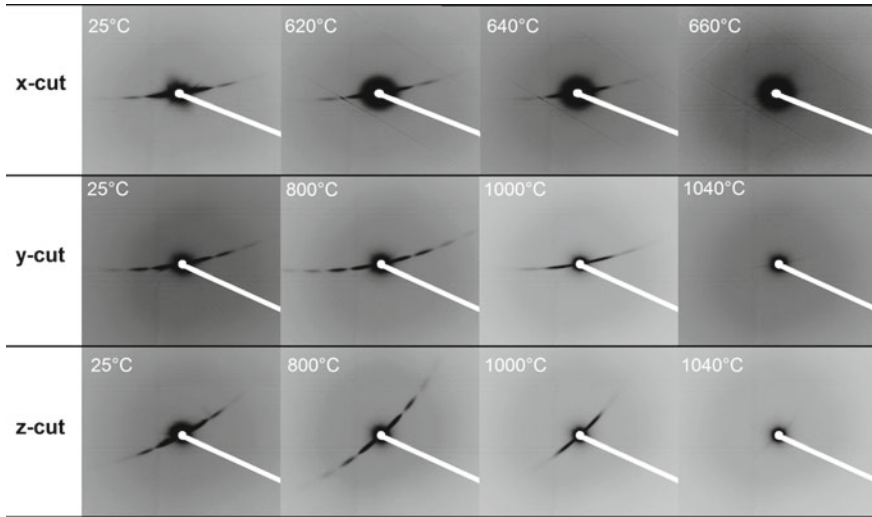


Fig. 7.1 Detector images for in situ SAXS showing ion tracks in quartz at different temperatures after successive annealing for 20 min at each temperature. Darker colours correspond to high scattering intensities. [top row: tracks along x -cut direction, centre row: tracks along y -cut direction, bottom row: tracks along z -cut direction]

previously demonstrated unique behaviour compared to other orientations showing different etching rates in twinned areas [12].

The recrystallization process is typically explained by thermally induced diffusion of the displaced atoms, i.e. a recombination of interstitial atoms with lattice vacancies [13, 14]. Particularly when studied in a geological context, the cylindrical nature of the ion tracks normally leads to the assumption that ion track recrystallization depends mainly on the diffusion perpendicular to the ion track direction [13, 15, 16]. For O-atoms in c -SiO₂, the diffusion constant D is indeed higher for parallel than for perpendicular orientation to the quartz c -axis [17]. In addition, the activation energy for diffusion is lower in the parallel direction to the c -axis, compared to perpendicular (1.5 vs. 2.1 eV). The anisotropy of the diffusion rates of displaced oxygen atoms in ion tracks within z -cut quartz suggests recrystallization would take longer and require higher temperatures than in x -cut, in accordance with what is observed in the present study. However, radioactive tracing studies for Si atoms in c -SiO₂, show very similar diffusion constants in all directions, suggesting the diffusion of the Si cations cannot explain a difference in the annealing behaviour for different orientations [18]. Yet as the diffusion of Si-atoms in c -SiO₂ is significantly lower than that of O-atoms, the diffusion of silicon represents a bottleneck for ion diffusion [19]. Furthermore, the anisotropy of the diffusion cannot explain the similarity of the ion track recrystallization in y - and z -cut, opposed to the x -cut. This indicates that diffusion is not the sole contributor responsible for ion track recrystallization and yet unknown effects might play a similarly important role. The present work shows agreement with previous experiments on etched ion track recrystallization, however,

the underlying cause for the difference in directional recrystallization, particularly between ion tracks in x - and y -direction, remains elusive.

Figure 7.2b shows the evolution of the scattering intensity at different annealing temperatures from an extrapolation of the fitting curves to $q \rightarrow 0$, where the intensity is saturating to I_0 . Up to 400°C the scattering intensity remains almost constant, but between 400 and 600°C all three cuts show a significant drop in intensity. The scattering intensity for the ion track density N can be expressed as (compare Sect. 3.3.3):

$$I_0(R, L, \Delta\rho) = I(q \rightarrow 0) = N (\Delta\rho \cdot \rho_e)^2 (\pi R^2 L)^2 \quad (7.1)$$

As the ion track radius R was shown to remain mostly unchanged within this temperature range, and similar results have been reported for the ion track length L [10], the rapid drop in intensity is mainly attributed to a change in the relative density difference $\Delta\rho$ between ion track and host material with electronic density ρ_e . The origin of the decrease can be attributed to the phase transition of α -quartz into β -quartz at 573°C that is accompanied with a reduction in the density of the host material. While the density of the amorphous ion track should remain constant, the density of the surrounding matrix material decreases by 5%, from 2.65 to 2.53 g/cm³ (Refs. [3, 20]).

Using the absolute scattering intensity, the reduction in density of the ion tracks compared to the matrix can be estimated to be approximately $1.0 \pm 0.3\%$ (Sect. 3.3.1). Assuming the amorphous ion track is not affected by the phase transition of the crystalline material, its absolute density would remain unchanged while the surrounding host matrix material shows a reduction in density exceeding the initial $\Delta\rho$. Consequently, this suggests a change of the ion track density difference from underdense to overdense. From Eq. (7.1) it can be derived that the SAXS intensity only depends on the absolute square of the density change. Therefore, the change from under- to overdense has no substantial effect on the scattering pattern.

However, the present findings show a reduction of the intensity by about a factor of 2–3 as a result of the phase transition. Using Eq. (7.1), this implies a new $\Delta\rho$ around 0.6–0.7%. With the reduction of the host matrix by 5%, this opens the question on the accuracy of the present $\Delta\rho$. A more suitable value for $\Delta\rho$ would be $\sim 3\%$. In that case, the density misfit would be $\sim 2\%$, fully explaining the reduction of the density of the matrix by 5%. An error in the calculation of $\Delta\rho$ by a factor of 3, however, would yield a scattering intensity 9 times as large as evident from Eq. (7.1) (the values for R and L are well-known with an uncertainty below a few percent). This seems not realistic, even when the typically large uncertainties in determining I_0 are considered. To verify the present approach, it would be advisable to carry out further testing and to measure $\Delta\rho$ on a number of ion tracks with well-known density difference and geometry (e.g. etched tracks of cylindrical shape).

For temperatures beyond the α to β -quartz phase transition, a much slower decrease of the intensity is observed, mainly due to the reduction in ion track volume with the decrease in ion track radius and length. For the remainder of the anneal-

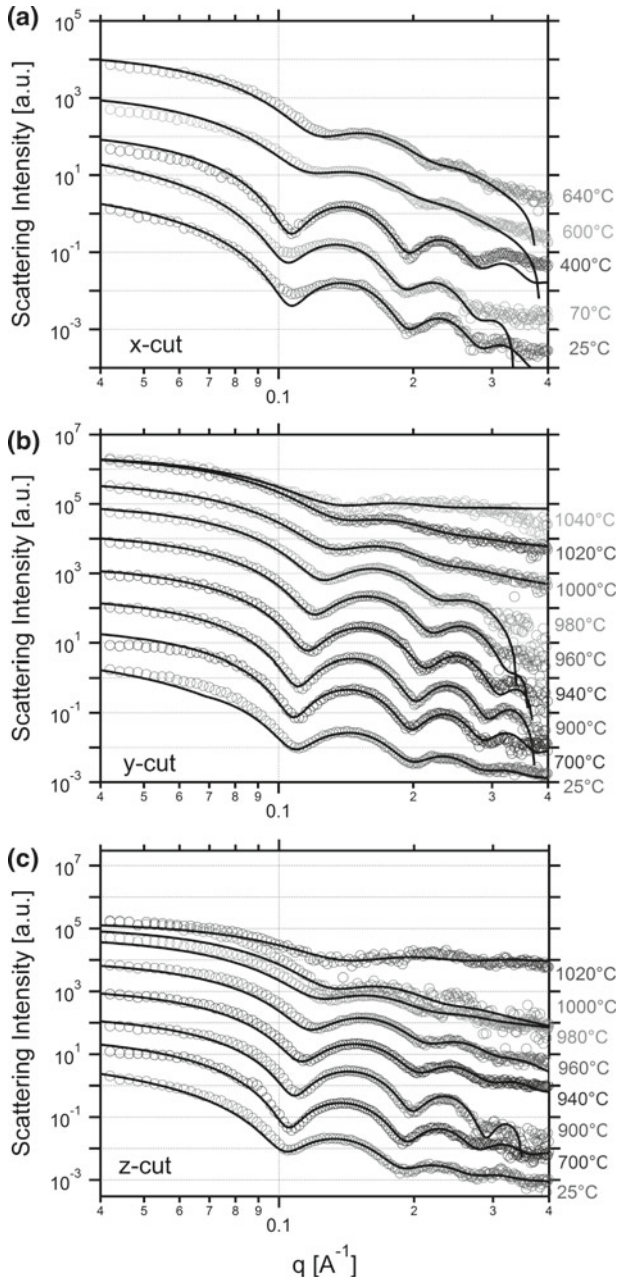


Fig. 7.2 In situ SAXS q -patterns for ion tracks in quartz of **a** x -cut, **b** y -cut, and **c** z -cut at RT and after annealing at different temperatures (open circles). A hard cylinder model was used to fit the results (solid lines). Patterns are offset for clarity

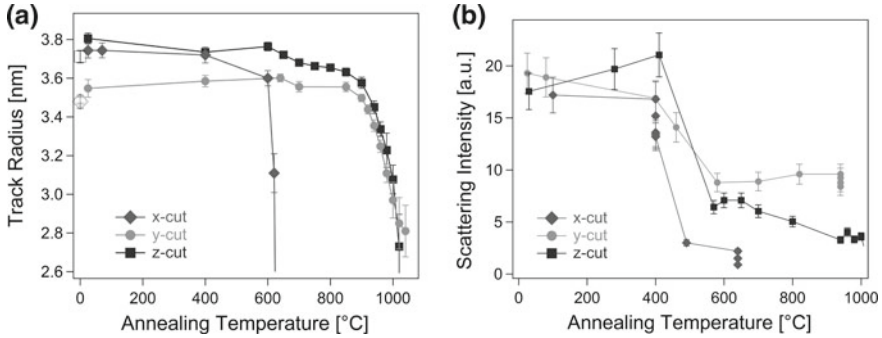


Fig. 7.3 **a** Ion track radii and **b** SAXS intensity I_0 as a function of temperature for isochronal in situ annealing. Ion tracks in quartz along x -direction (diamonds), y -direction (circles), and z -direction (squares) as shown. The track radii remain approximately constant for low temperatures and show a rapid reduction at higher temperatures. The SAXS intensity shows a strong drop around 550°C as result of the quartz $\alpha \rightarrow \beta$ transition

ing process β -quartz remains the dominating structure, as the 870°C transition into α -tridymite only occurs in natural quartz possessing certain impurities and is not present in synthetic quartz [21].

Reduction of the Ion Track Length

The SAXS patterns contain more information than just the track radius. It is also possible to use Eq. (7.1) to calculate the (relative) track length during annealing [22]. This requires knowledge of the time-dependent SAXS intensity $I_0(t)$, the radius $R(t)$ and the density difference $\Delta\rho$.

The former two quantities can be directly accessed from the data on track annealing during in situ SAXS. Figure 7.3 shows results for the (a) y -cut ($\perp c$) and (b) z -cut ($\parallel c$) from Fig. 7.2, with the normalised ion track cross-section $A = R^2\pi$, and normalised intensity I_0 . The track radii were normalised with respect to the intensity at 650°C , allowing a comparison of both cuts despite different absolute values in scattering intensity. This temperature point was chosen as the track cross-section was still close to its initial size, but the host matrix had undergone the phase transition from α to the β -quartz at 573°C . This is critical for the calibration of the density difference $\Delta\rho$ between the amorphous (under-dense) ion track and its host material. During the annealing process the track cross-section remains fairly constant for moderate temperatures and only starts to show a reduction for tracks along both orientations in the temperature range $800\text{--}1000^\circ\text{C}$.

The density difference $\Delta\rho$, the third and final parameter that connects track length with SAXS intensity, is assumed to be constant over time. This assumption is necessary as the present SAXS measurements do not allow us to probe $L(t)$ and $\Delta\rho(t)$ independently, but only their product $L(t) \cdot \Delta\rho(t)$, as evident from Eq. (7.1). However, $\Delta\rho(t) = \text{const.}$ is supported by findings that underdense amorphous tracks (as in the present work) recrystallise by a recombination of their defects along the track surface [23]. Hence, for radial reductions in track size, the average density difference only changes along the interface between its cylinder surface and the surrounding matrix material.

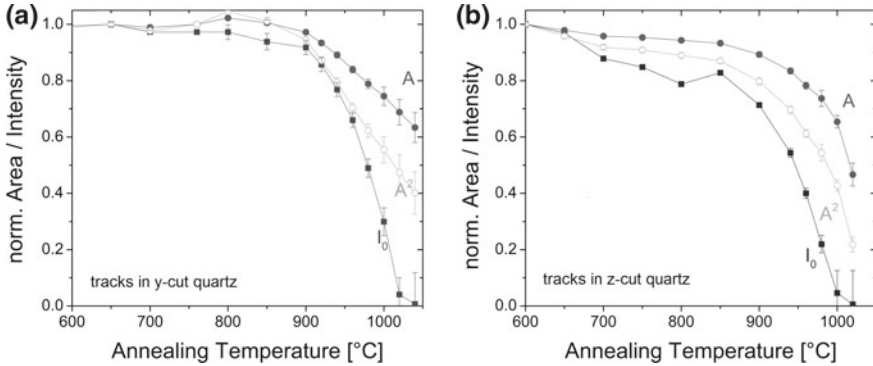


Fig. 7.4 Ion track cross-section area for in situ thermal annealing for ion tracks in quartz of **a** y-cut and **b** z-cut. The area of the track cross-section A (full circles), its square A^2 (open circles), and the SAXS intensity I_0 (solid squares) are shown

Figure 7.4 shows a comparison of the normalised track radius $R(t)$ and relative track length $L(t)$ calculated based on the assumption that the density change is constant over time. Up to temperatures of 940°C , no significant change in track length was observed. Above 940°C , however, track lengths start to decrease rapidly. Upon reaching 1010°C they dropped down to approximately 30% of their initial value. This is significantly faster than the shrinkage of the respective track radii within the same temperature range, which are only showing a reduction to approximately 80% of their initial values. Finally, at temperatures of approximately $1020\text{--}1040^\circ\text{C}$, the intensities are approaching zero for both orientations, indicating complete recrystallization of the ion tracks is imminent (compare Fig. 7.5). Similar to the track radius discussed earlier in this section, for tracks along y- and z-direction, the orientation of the tracks within the crystal structure does not show any significant influence on the reduction of the track length. In fact, tracks in z-cut quartz show a similar curve as in y-cut quartz, but shifted to lower temperatures by approximately 20°C . Although this deviation is above the uncertainty of the furnace temperature, it is potentially possible that other experimental conditions (e.g. slightly different thickness, non-identical annealing cycle) are responsible for this difference.

These results agree with previous results of track annealing by Aframian, who did not detect any annealing anisotropy when studying track shrinkage up to 950°C by using chemical etching [24]. In contrast, Sandhu et al. reported a slower track length reduction in track parallel to the c -axis than in tracks oriented perpendicular to the c -axis. At 950°C they have reported a typical track reduction to 50% for the former, but a length contraction down to only 20% for the latter [10]. Both experiments, however, differ from the present results not only through their use of chemical etching, but were also conducted with lower ion irradiation energy and in natural quartz.

In conclusion, these results indicate that the reduction of the track radii and lengths during thermal annealing in synthetic, crystalline quartz is comparable for tracks in y- and z-cut quartz. This leads to the assumption that different alignments of the

track with respect to the c -axis of quartz, can yield similar annealing rates, as shown on tracks parallel (z -cut) and perpendicular (y -cut) to the c -axis (assuming a constant density difference). However, this stands in direct contrast to the total disappearance of the tracks in x -cut quartz (also perpendicular to the c -axis) between 620 and 660 °C. It is suggested that the phase transition from α to the β -quartz (573 °C) might have an impact on track annealing for x -cut tracks, while y -cut tracks remain unaffected. This could be the reason why these two quartz cuts, although in both cases tracks are oriented perpendicular to the c -axis, show a very different annealing behaviour and recrystallise at different annealing temperatures.

7.1.2 Isothermal Annealing

The previous subsection has demonstrated a strong resilience of ion tracks in quartz when annealed at moderate temperatures. Only when a sufficiently high temperature is reached, an appreciable reduction of the ion track size was observed. The temperatures for isothermal annealing were chosen based on the values obtained in the previous subsection, such that the ion tracks displayed a significant amount of recrystallization within a duration of approximately 30 min. For the quartz x -cut samples, this range is 600–640 °C, while a range between 940–980 °C was used for the y - and z -cut samples. Figure 7.6 shows the ion track recrystallization in quartz of x - (a), y - (b) and z -cuts (c) as a function of annealing time for different temperatures. The respective annealing temperatures after ramping are reached at the point of $t = 0$ of the time axis (vertical black line). Ion tracks in all orientations show a rather fast reduction in ion track size for the highest temperature (triangles), while slightly lower temperatures exhibit much slower ion track recovery (circles, squares). These annealing experiments were conducted by using fresh, un-annealed samples for each temperature. This differs from the previously used methodology as it avoids potential cumulative annealing effects, which could result from the successive increases in temperatures. Nevertheless, previous results on track annealing in apatite indicate that such cumulative annealing effects can be neglected [25, 26].

By applying the laws of diffusion to the recrystallisation of the amorphous tracks, an activation energy E_a of the process can be extracted. The diffusion constant according to Fick's law typically shows a Boltzmann distribution:

$$D(T) = D_0 \exp\left(-\frac{E_a}{k_B T}\right) \quad (7.2)$$

It is further assumed that the change in radius is linear on a logarithmic scale, which is typically not true for *extrapolations* from laboratory timescales to geological timescales of millions of years (compare Sect. 1.2.3). For the *interpolations* in this work, however, such an approximation is generally sufficient [27–31]. Using Eq. 1.6 for the Arrhenius model, the activation energy can be found by varying one of two parameters that dictate the change of defect concentration: the annealing temperature

T or the annealing duration t . For isochronal annealing of tracks in apatite with $t = \text{const}$, the activation energy E_a of the recrystallization process is calculated by:

$$\ln \left[1 - \frac{r}{r_0} \right] = C - \frac{E_a}{k_B T} + n \cdot \ln(t) \quad (7.3)$$

Here r/r_0 is a suitable normalised parameter to describe the track fading via its change in defect concentration [13, 32]. Since the number of defects is proportional to the volume of the ion track and therefore the square of the track radius R^2 , the track normalised radius R/R_0 can be used as a parameter describing the track size reduction. For constant annealing temperature T , Eq. (7.3) allows a calculation of the activation energy by either keeping the radius $R(t)$ constant (horizontal lines in Fig. 7.6) or the annealing time t constant (vertical lines in Fig. 7.6).

$$\ln \left[1 - \frac{R}{R_0} \right] = C_1 - \frac{E_a}{k_B T} \implies E_a = - \frac{\partial \ln \left[1 - \frac{R}{R_0} \right]}{\partial [1/(k_B T)]} \quad t = \text{const.} \quad (7.4)$$

$$n \cdot \ln(t) = C_2 + \frac{E_a}{k_B T} \implies E_a = n \frac{\partial [\ln(t)]}{\partial [1/(k_B T)]} \quad R = \text{const.} \quad (7.5)$$

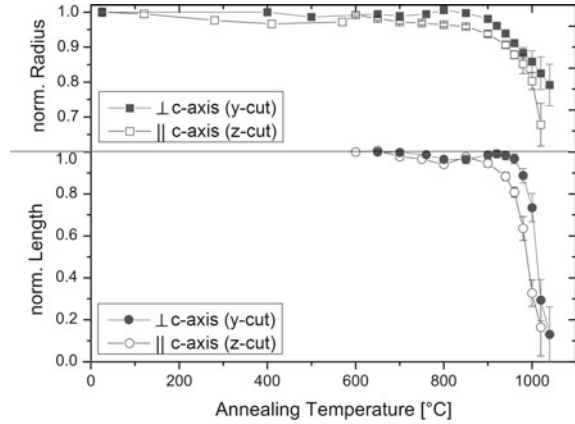
Figure 7.6d–f show the corresponding Arrhenius plots, with the slope of the linear fits resembling the respective E_a values for $t = \text{const.}$ (open symbols) and $R = \text{const.}$ (full symbols).

For the vertical cross-cut method from Eq. (7.4), a range of annealing times was chosen and the corresponding annealing radii were determined for the different temperatures. For tracks in x -cut quartz sample, the tracks did disappear relatively quickly, despite the lower temperatures. This prevents an analysis with the vertical cross-cut method due to the low amount of data points along the time axis. For tracks in y - and z -cut quartz samples, $g(R) = |\ln [1 - R/R_0]|$ is shown as a function of reciprocal temperature in Fig. 7.6e–f, using linear regression to calculate the slope. The activation energy can directly be derived from the slope to E_a of 5.5 ± 0.3 eV (y -cut) and 5.2 ± 0.5 eV (z -cut).

For the horizontal cross-cut method from Eq. 7.5, a range of reduced track radii was chosen and the corresponding annealing times were determined for the different temperature. For tracks in all three quartz cuts, $\ln [t_i]$ is shown as a function of reciprocal temperature in Fig. 7.6d–f, using linear regression to calculate the slope. To derive E_a for the track recrystallisation, a knowledge of the value of n in Eq. 7.5 is required. Here, $n = 1$ is estimated, as the short annealing times in this experiment should allow the use of a simpler track annealing model [28]. The calculations for the E_a of recrystallisation of tracks in quartz show: 3.6 ± 0.7 eV for the x -cut, 6.3 ± 0.5 eV for the y -cut and 5.6 ± 0.7 eV for the z -cut. These values are just within the uncertainty of the horizontal cross-cut method, thus justifying the assumption $n = 1$.

The E_a of the recrystallisation from both methods only shows small differences between tracks in y - and z -cut quartz. For tracks in x -cut quartz, however, signif-

Fig. 7.5 Normalised track radius (squares) and track length (circles) measured by in situ SAXS with isochronal annealing for ion tracks in quartz of y-cut (solid symbols) and z-cut (open symbols)



icantly lower values for E_a were found. This reduced activation energy for recrystallisation in x -cut direction is in agreement with the present results on isochronal annealing shown in Sect. 7.1.1. Although the direct mechanism for this behaviour is not identified in the present work, it can be speculated that effects by the phase transition from α to β -quartz might contribute to the faster recrystallisation of tracks in a particular crystalline direction.

The present results can be compared to recrystallization experiments of thin amorphous films (solid-phase epitaxy). Their significantly larger amorphous area allows an easier characterisation in comparison to nano-sized ion tracks. The activation energies might differ slightly, as their geometry differs from ion tracks by possessing a flat recrystallization front, instead of cylindrically shaped one. Using Rutherford backscattering (RBS), Gasiorek et al. have found an activation energy of 3.6 eV in z -cut silica under ambient atmosphere, that was previously amorphised via low energy (175 keV) Rb ions [33]. For amorphous SiO_2 , Wagstaff and Richards reported 3.3 eV in H_2O -vapour atmosphere, but 5.8 eV when crystallisation occurred in vacuum [34]. The latter suggests a strong dependence of the (re)crystallisation process on impurities and defects within the host crystal. For example water molecules can be trapped within natural quartz [35] and can consequently lead to a similar decrease in the activation energies of the crystallisation as they occur under water-vapour atmosphere.

The synthetic quartz used in the present study is largely free of such impurities, showing no hydroxyl inclusions within the detection limit of Fourier transform infrared spectroscopy measurements. This suggests the source of the higher activation energies in the present work might be the high purity and lower defect concentration of synthetic quartz in comparison with natural quartz and their very different recrystallisation rates [19]. This is supported by further investigation on natural quartz, which have reported activation energies that were consistently lower, e.g. 3.5 eV [36] (no specific cut mentioned), 3.8 eV [24] (no specific cut mentioned), and 2.1 eV [10] (random cut).

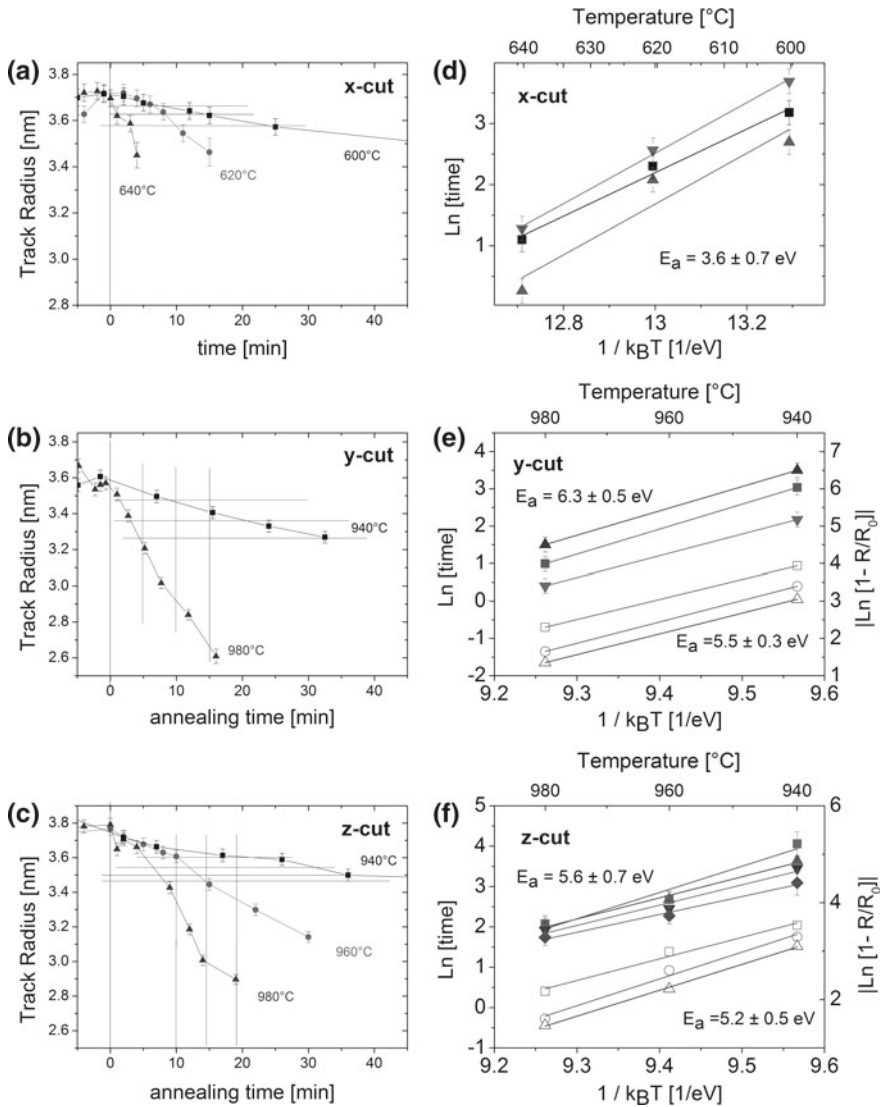
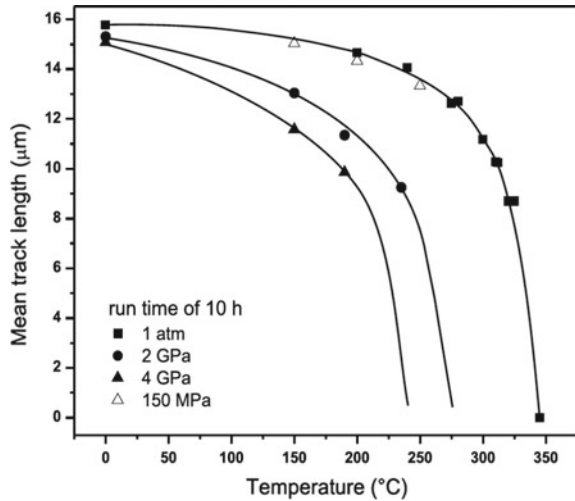


Fig. 7.6 Ion track radius over time for different annealing temperatures for tracks in **a** x-cut, **b** y-cut, and **c** z-cut quartz (full symbols). Negative times denote the annealing during the temperature ramping period. **d-f** Arrhenius plots from horizontal (solid symbols, left axis) and vertical (open symbols, right axis) cross-cuts with constant annealing time. Linear fits were used to calculate E_a (lines)

Fig. 7.7 Mean length of etched apatite tracks as a function of annealing temperature at 1 atm, 2 and 4 GPa (solid symbols). The curve at 150 MPa (open triangles) was extrapolated from the higher pressure data. [Image courtesy: Schmidt et al. [4]]



7.2 Ion Tracks in Apatite and the Effects of Pressure

The minerals apatite, zircon and olivine are routinely used for fission track thermochronology due to their high abundance of radioactive uranium impurities [1]. These minerals differ from each other by their closure temperature T_C , which is the geological term for the temperature where all fission tracks are fully erased when annealed for geological timescales of ~ 1 million years (compare Sect. 1.2.3). The value of T_C for fission tracks in apatite is among the lowest and ranges between 90 and 150 °C, depending on the apatite composition [37–40]. This makes apatite the ideal system for applications in low-temperature thermochronology, which measures the timing and the rate at which rocks cool.

When apatite samples with fission tracks from deeper depths within the earth are investigated, the tracks will have been exposed to elevated temperatures in the presence of elevated pressures. The geothermal gradients are typically in the range of 30 °C/km and 30 MPa/km [41]. The low closure temperature of fission tracks in apatite, thus only makes pressures up to 150 MPa (0.15 GPa) of interest for fission track analysis in this material. For apatite grains from depths of >5 km, the natural thermal annealing processes will have erased all tracks [1, 39]. It is noted that these depths are still accessible via fission track analysis with minerals of higher closure temperature, such as zircon.

The current literature shows only a limited amount of thermal annealing studies of ion tracks where pressure was taken into account. In the context of fission track dating, those are mainly focused on the change in etched track lengths, rather than the latent track radius. Early work by Fleischer et al. has shown no effect of pressure up to 8 GPa on annealing rates of fission tracks in zircon and olivine [42], which was independently confirmed for zircon by more recent work [43]. For apatite in

particular, Naeser and Faul have demonstrated no effects of pressure on the fission track annealing behaviour around typical geological pressures for fission tracks in apatite of ~ 0.2 GPa [2]. However, more recent investigations by Wendt and Vidal have indicated that pressures between 0.1 and 0.3 GPa may indeed have a *stabilising* effect on track annealing [5, 6], although the authors received criticism for their methodology and its contradiction to that of previous investigations [8].

The most recent study by Schmidt et al. reported *enhanced* annealing rates at higher pressures [4] as shown in Fig. 7.7. These tracks were annealed at 1 atm (0.0001 GPa) and 2–4 GPa over the duration of 10 hrs. Subsequently, the tracks were enlarged through chemical etching with 5 M HNO₃ for 20 s. The mean track length was measured using optical microscopy on up to 400 individual tracks. Their findings demonstrate that tracks annealed under pressures of 2 and 4 GPa display a reduction in length by approximately one third at ~ 210 and 190°C respectively (solid circles & triangles), while 310°C was required for similar effects in the absence of pressure (squares). Despite the clear accelerating effect of pressure on track annealing, their results were consistent with earlier findings. When extrapolated down to geologically relevant values ≤ 0.15 GPa, the effect of pressure became significantly smaller and insignificant for apatite fission track analysis [4, 8] (open symbols).

The use of DACs in the present work, represents a novel approach by allowing in situ characterisation of latent track annealing under pressure. DACs also allow us to expose minerals to higher pressures than those occurring for natural fission tracks. This may further accelerate the pressure effects for annealing at laboratory time scales and allow a more accurate measurement. Subsequently the effects can be extrapolated to lower pressure to assess their relevance for geological applications. The approach is similar to the investigation of temperature-related effects during track formation in this work (compare Sect. 6.1) and has been used for previous investigations of pressure on ion track annealing by Schmidt et al. [4].

The aim of this section is to investigate ion track annealing under similar higher pressure conditions (~ 1 – 2 GPa) by using heatable DACs, while simultaneously measuring the ion tracks with in situ SAXS. This is fundamentally different to conventional optical imaging, as SAXS does not require the prior chemically etching of the tracks. Thus, once a sample at a fixed annealing time was characterised with the optical microscope, the tracks have been dissolved and cannot be annealed further. SAXS, on the other hand, is capable of delivering a precise measurement of the track radius (and length) during the entire duration of the annealing process on a single sample.

7.2.1 Isothermal Annealing Under Ambient Pressure

First, a range of control measurements are carried out to study the annealing kinetics of ion tracks in apatite under ambient pressure. For this purpose, small samples were cut from an apatite single-crystal along a random orientation. Hence, the direction of the tracks with respect to the apatite *c*-axis is unknown, but is consistent between

samples. The samples were mechanically polished to thicknesses around $50 \mu\text{m}$. Irradiation was performed with 2.2 GeV Au ions at the UNILAC at GSI in Darmstadt, Germany. The apatite mineral was extracted from a rock from Durango, Mexico, and consequently had a dominating F-concentration as discussed in detail in Sects. 1.2.3 and 4.1. The sample preparation and in situ SAXS measurements were performed by Afra et al. [44].

The characterisation of the tracks during isothermal annealing was performed in a similar manner as for quartz (see Sect. 7.1.2). This allows us to probe the recrystallisation of the ion tracks as a function of annealing time t at constant temperature T .

Reduction of the Ion Track Radius

Figure 7.8a shows the track radii from the in situ SAXS measurements as a function of time for four different annealing temperatures (320, 345, 365 and 390 °C) as a function of time. Negative times denote the annealing during the temperature ramping period. Only a small, but measurable reduction in track radius was observed for annealing at 320 °C. For the higher two temperatures, 365 and 390 °C, the tracks showed a rapid reduction in radii. After 10 min of annealing at each respective temperature, a measurable reduction in track radius is observed for all temperatures. For 365 and 390 °C, the radius is reduced by 14 and 24%, respectively. After a total of 15 min the tracks have vanished beyond the resolution of SAXS.

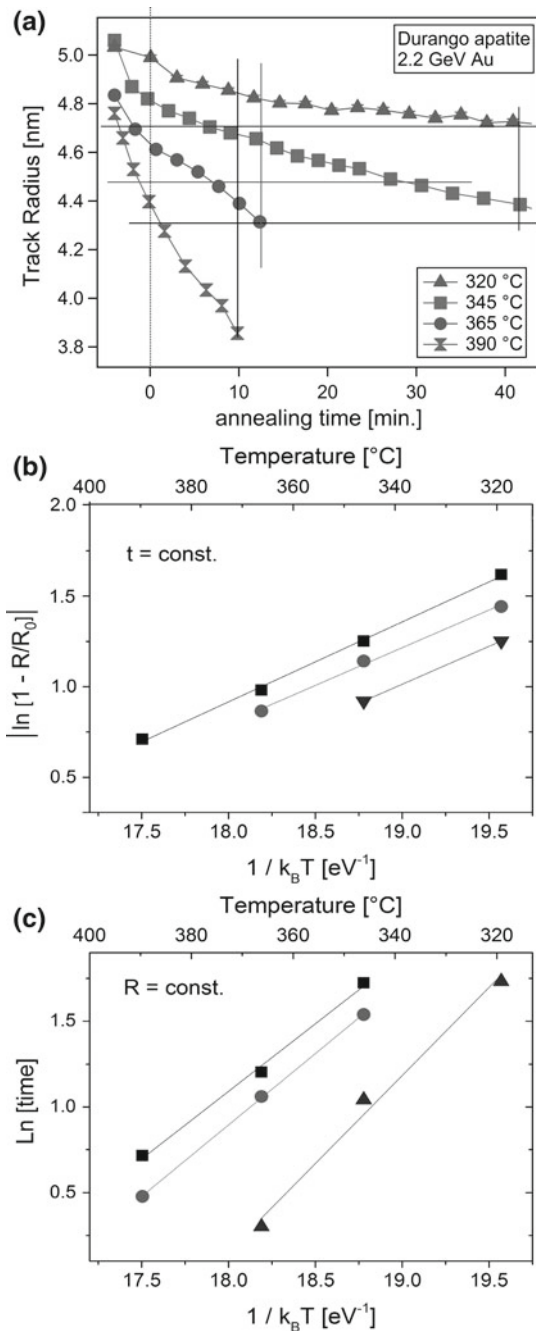
Similar as in Sect. 7.1.2, the track radii and annealing times are displayed in an Arrhenius plot to assess the activation energy E_a of the track recrystallisation. It is noted that for the annealing curves at high temperatures, only a limited number of data points is available, as those tracks have disappeared within 10–20 min after reaching temperatures $\geq 365 \text{ }^\circ\text{C}$.

Figure 7.8b shows the method of vertical cross-cuts with $t_i = \text{const.}$ (compare Eq. (7.4)), displaying $g(R) = |\ln[1 - R/R_0]|$ for different values of t_i as a function of inverse temperature $1/(k_B T)$. A fit with linear regression was used to interpolate the data. Its slope gives direct access to the activation energy with a value of $0.42 \pm 0.04 \text{ eV}$. This value does appear significantly too low, as it is not in agreement with E_a typically observed for annealing of ion tracks in Durango apatite when measured with SAXS. Depending on the orientation between track and crystal lattice, values between $0.72 \pm 0.04 \text{ eV}$ [45] and $0.90 \pm 0.17 \text{ eV}$ [46] were found in previous work using ex situ SAXS.

Figure 7.8c shows the method of horizontal cross-cuts with $R_i = \text{const.}$ (compare Eq. (7.5)) displaying annealing times $\ln[t_i]$ for different values of R as a function of inverse temperature $1/(k_B T)$. A fit with linear regression was used to interpolate the data. The lack of knowledge for the constant n prevents the direct derivation of E_a through the slope of the fit. However, for isothermal annealing with short timescales, a simpler model with $n = 1$ has been used successfully to interpolate track annealing rates in apatite [31, 47]. With this assumption, values for E_a of approximately $0.9 \pm 0.3 \text{ eV}$ were found.

The different values for E_a resulting from vertical and horizontal cross-cuts come from same annealing experiment. Thus, this discrepancy raises questions about the use of the vertical cross-cut method to calculate activation energies for ion tracks

Fig. 7.8 Results from in situ SAXS on isothermal annealing of ion tracks in apatite at different temperatures. **a** Track radius as a function of time for temperatures between 320 °C and 390 °C. **b** Arrhenius plots from vertical cross-cuts with *constant annealing time*. **c** Arrhenius plots from horizontal cross-cuts with *constant track radius*. Linear fits were used to calculate E_a (lines)



in apatite. A potential source of error for this approach is the rapid shrinkage and disappearance of the tracks annealed at 365 – 390 °C. Thus the activation energy is predominantly calculated from a single isothermal annealing curve at only two temperatures, 320 – 345 °C.

Track annealing in the literature is typically conducted by using optical microscopy on chemically etched tracks after ex situ annealing. Virk has reported an E_a between 0.71 and 0.74 eV for ion tracks in apatite created under comparable conditions as in the present work [47]. Sandhu et al. have reported values between 0.57 and 0.71 eV, depending on the crystalline orientation of the track [48]. These activation energies match the values of ex situ SAXS (0.72 ± 0.04 eV [45] and 0.90 ± 0.17 eV [46]) as well as the present findings from in situ SAXS from the horizontal cross-cut method ($R = \text{const.}$). The increased uncertainty of the present findings is potentially a result of the low number of samples that were annealed. However, the values derived from in situ SAXS do match the previously measured values, thus demonstrating the validity of this technique to study activation energies for track annealing. The differences in E_a can be reduced further, by using a more complex annealing model with $n \neq 1$. Since the present work has only measured $n \cdot E_a = 0.9 \pm 0.3$ eV, an accurate value of n is then required. Under the assumption that the activation energy derived from the ex situ SAXS experiments by Afra et al. is the same as in the current experiment [45], a value of $n = 1.25$ was derived, which is not uncommon to be measured for ion tracks in minerals of similar mass density as apatite, i.e. $n = 1.2$ in Bronzite [49].

It is noted that all previous studies rely on the use of optical microscopy on etched tracks to derive the activation energy from the reduction in the track length [16, 39, 50–52]. Thus no information on E_a from in situ measurements of track radii in apatite other than our previous work is available [45, 46]. Other than SAXS, only transmission electron microscopy (TEM) offers an alternative to measure the radius on latent tracks in situ during annealing [23, 53].

Reduction of the Ion Track Length

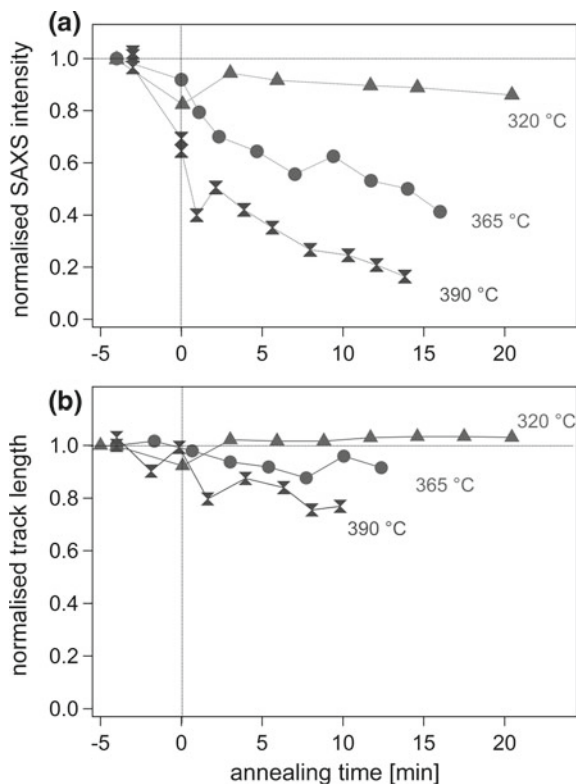
By using the absolute SAXS intensity at $q \rightarrow 0$ and the track radius, it is also possible to estimate the relative change in track length in a similar fashion as in Sect. 7.1.2. The normalised SAXS intensities I_0 are shown in Fig. 7.9a. The results show a larger difference for the effects between those temperatures. While at 320 °C only a small change of I_0 is observed, tracks annealing at the higher temperatures disappear within the duration of ~20 min. The resulting relative lengths were calculated using the relation:

$$I_0 = I_0(R, L, \Delta\rho) = N (\Delta\rho \cdot \rho_e)^2 (\pi R^2 L)^2 \quad (7.6)$$

with the known values for $I_0(t)$ and $R(t)$, and by assuming $\Delta\rho \cong 1\% = \text{const.}$, as previously discussed for ion tracks in synthetic quartz. Figure 7.9b shows the relative lengths for track annealing at 320, 365 and 390 °C. For the lowest annealing temperature the present findings show no measurable decrease in track length (solid triangles).

For annealing at 365 and 390 °C, a small reduction in the track length is observed, with 10 min annealing leading to a relative decrease in track length of 10 and 25%,

Fig. 7.9 **a** The relative SAXS intensity I_0 and **b** the relative track length from in situ SAXS on isothermal annealing of ion tracks in apatite under ambient pressure as a function of annealing time. Annealing at temperatures of 320 °C (triangles), 365 °C (circles), and 390 °C (bi-triangles) is shown



respectively. These relative size reduction is of similar magnitude as measured for the track radius at similar temperatures (14% for 365 °C and 24% for 390 °C after 10 min). However, the shrinkage of the length depends on the absolute length of $L \sim 50 \mu\text{m}$. Thus the absolute contraction rates are 0.7 nm (365 °C) and 1.2 nm (390 °C) for the track radii and $5 \mu\text{m}$ (365 °C) and $10 \mu\text{m}$ (390 °C), which is a difference of about 4 orders of magnitude.

The fast recrystallisation for higher temperatures leaves only a small number of data points after more than 10 min of annealing. Thus, the relative uncertainties of these recrystallisation rates are potentially larger and in the range of 20–35%. Thus, effects that could lead to an anisotropy in recrystallisation (i.e. anisotropic diffusion within the apatite crystal lattice) are beyond the resolution of these measurements.

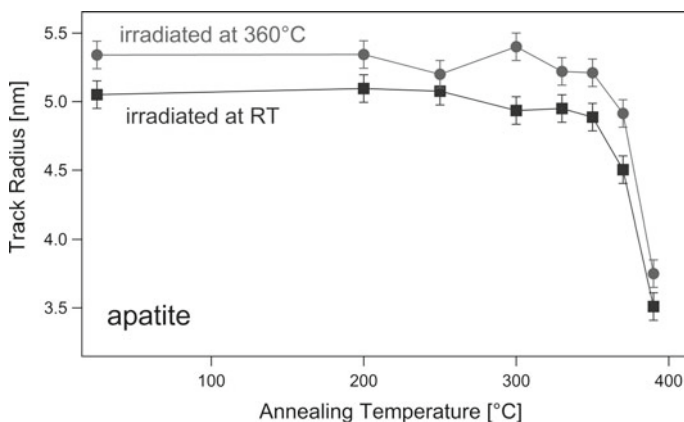


Fig. 7.10 Thermal annealing behaviour of ion tracks in apatite created at ambient conditions (squares) and at a temperature of 360 °C (circles). Both samples were successively annealed for 20 min at each temperature step. The track radius was measured with SAXS after each step

7.2.2 Thermal Stability of Ion Tracks Formed at Elevated Temperatures

In Sect. 6.1, the formation of tracks was studied under a range of different temperatures. This has demonstrated an increased ion track radius for track formation at elevated temperatures and reduced track radius for sub-zero temperatures. Consequently it was evaluated whether this size offset remains once tracks are again exposed to elevated temperatures and their radius shrinks as a result of recrystallisation. For this purpose, two apatite samples were chosen, one was irradiated at 360 °C, the highest temperature of the series, and the other sample at RT, as a reference. They were then simultaneously annealed at a range of temperatures for a time interval of 20 min and their track radius was measured with SAXS after each annealing step on the cooled sample at RT.

The respective track radii are shown in Fig. 7.10. The tracks initially show a difference in radius of approximately 0.3 nm between the tracks formed at RT and 360 °C. Upon annealing both samples show a similar decrease in track radius with no significant variation in the difference of the track radii. This shows that the size increase for the track cross-section remains present at post-formation annealing.

In a context of fission track annealing, this indicates that tracks formed at elevated temperatures possess larger radii than those created under ambient conditions. These results show that this difference is preserved even after thermal annealing. The similar annealing behaviour allows the conclusion that the nature of the damage in apatite is the same for irradiation at room-temperature and elevated temperatures. However, it remains open whether this also affects the fission track length, which is the key parameter used for fission track dating.

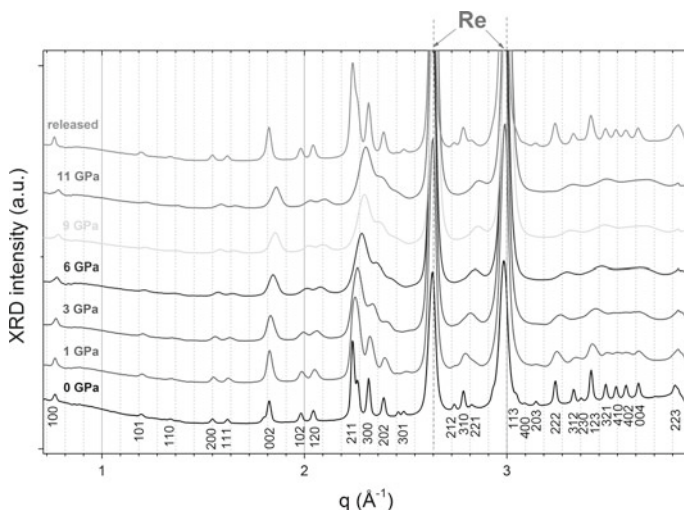


Fig. 7.11 X-ray powder diffraction patterns of apatite in a DAC as a function of q . Patterns are shown for pressures between ambient pressure (~ 0 GPa) and 11 GPa, as well as after the release of the pressure. All reflexes are labelled by their respective Miller indices. Patterns are offset for clarity. The peak from the Rhenium-gasket of the DAC (indicated by Re) is not related to the lattice of apatite

7.2.3 Effect of Pressure on Non-irradiated Apatite and Pre-existing Tracks

To identify possible pressure-related effects that are not related to annealing, the structure of crystalline apatite was characterised for elevated pressures and the radius of existing tracks was measured for the relevant pressure used for annealing in this work.

In order to access the bulk structural properties of apatite at various pressures, X-ray diffraction (XRD) was carried out at the powder diffraction (PD) beamline at the Australian Synchrotron in Melbourne. Apatite crystals from Durango, Mexico were crushed into a powder and loaded into a single DAC. Section 4.2 discusses the experimental basics for the use of DACs. Here, the entire sample volume within the gasket was filled with the crushed apatite crystals, making the use of a pressure medium redundant. It is noted that the apatite powder with the DAC might have had a pressure gradient in comparison to ideal hydrostatic conditions.

Figure 7.11 shows the XRD patterns of apatite as a function of the q -vector.¹ The patterns were taken with pressures successively increased from 10^{-4} GPa (ambient pressure, 1 bar) to a total of 11 GPa. Each diffraction peak is labelled with its respec-

¹Although diffraction patterns typically are displayed as a function of 2θ , this work shows them as a function of $q = 4\pi \sin(\theta)/\lambda$ to eliminate the energy-dependence and to remain consistent with SAXS.

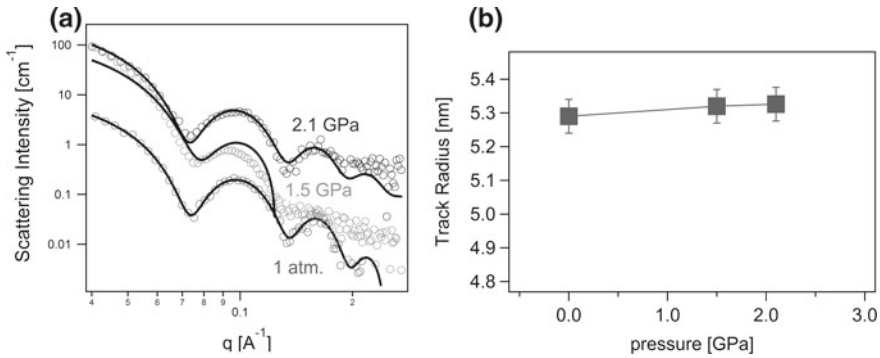


Fig. 7.12 **a** SAXS patterns (open circles) and **b** track radii (solid squares) for ion tracks in apatite as a function of pressure at ambient temperatures. No measurable change in radius was observed between ambient pressure and 2 GPa. The 1 atm. value was taken outside a DAC

tive Miller index of the corresponding lattice plane. It is noted that the two large dominating peaks around 2.6 and 3 Å⁻¹ originate from the Rhenium-gasket (Re) used for this DAC and thus are not related to the structure of apatite.

The XRD patterns show a gradual broadening of the peaks and a shift towards larger q -values with increasing pressure, which is attributed to pressure-induced strain on the crystal lattice. However, all peaks remain present and therefore the possibility of a phase change for pressures lower than 11 GPa is eliminated.² After release of the pressure (top curve), the XRD patterns assume their initial shape. This indicates that the pressure-induced strain effects are fully reversible. Other investigations using infrared and Raman spectroscopy also found no phase change up to values of 25 and 23 GPa, respectively [55].

In addition to investigating the effects of pressure on the thermal annealing of ion tracks, the influence of pressure on the stability of ion tracks without annealing was investigated. A previous study on the effects of shock waves has reported an effect of the exposure to pressure shock waves between 1 and 10 GPa on ion tracks. A gradual reduction of the amount of visible tracks by approximately 10% for each GPa pressure increase was shown [56]. Figure 7.12 shows the radius for ion tracks at different pressures, as measured by SAXS. For pressure values up to 2 GPa, the radius seems to be unaffected.

A recent SAXS investigation of ion tracks in apatite under pressure has reported similar results [57]. For pressures up to 10 GPa, no change in radius was observed. However, a relatively strong decrease in the scattering intensity I_0 was observed with increasing pressure. The SAXS intensity is directly proportional to the density difference between track and host matrix $\Delta\rho$, and the track volume V :

²All pressures were obtained by ruby fluorescence. An analysis of the shift of the (210), (310), and (002) peaks at 11 GPa yields similar values as attributed to only 8 GPa by Matsukage et al. [54]. Although this value is different from 11 GPa, this discrepancy has no effect on the conclusions of the following work, as only pressures up to 1–2 GPa are discussed.

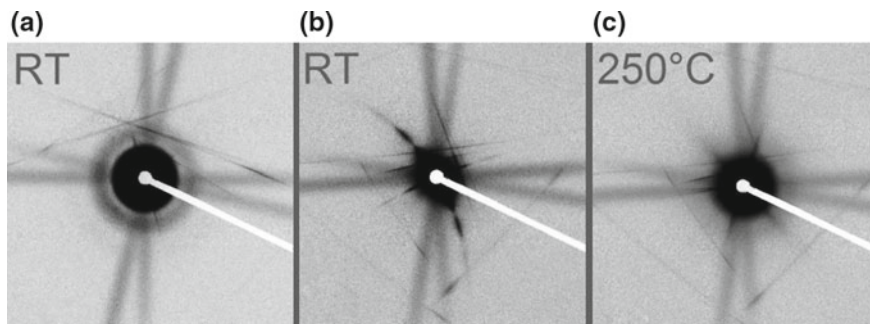


Fig. 7.13 SAXS patterns for ion tracks in apatite within a heatable DAC. **a** Aligned tracks at ambient temperature before annealing. **b** Tracks tilted by 5° with respect to the incident X-ray beam at ambient temperature before annealing. **c** Tracks tilted by 5° with respect to the incident X-ray beam after 5 min annealing at 250°C . Darker colours correspond to high scattering intensities

$$I_0 \propto (\Delta\rho \cdot V)^2 \quad (7.7)$$

Thus the decrease in I_0 can be attributed to a higher compressibility of the amorphous material in the ion tracks as compared to the crystalline matrix. Since $\Delta\rho$ is only within the order of $\sim 1\%$ (compare Sect. 5.1) it can undergo major changes with negligible effects on the volume, i.e. even an decrease of $\Delta\rho$ by 1% only leads to a 0.4% change in V . This is within the uncertainty of the radius measurement of SAXS. Thus, we cannot see the change in the track radius due to the increased compression of the tracks. Once the pressure was fully released, the tracks assumed their initial density difference again. This demonstrates the reversibility of this process and a completely elastic behaviour of the system under pressure.

Ion tracks under pressure in apatite were also investigated with XRD by Schowink et al. [58]. They have proposed a reduction in the lattice strain from the ion track volume mismatch as a result of increasing pressure. This explanation is consistent with the observed decrease in $\Delta\rho$; it further supports the reversibility of this effect when the pressure is released.

7.2.4 *In situ* Annealing Using Diamond Anvil Cells

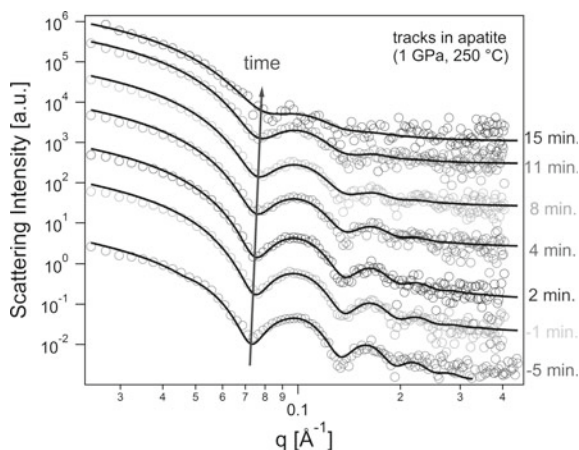
Ion tracks in Durango apatite were annealed under pressure using heatable DACs and characterised by in situ SAXS. The apatite was cut parallel to the c -axis and polished to a thickness of $65\ \mu\text{m}$. The thin samples were subsequently irradiated with 2.3 GeV Bi ions at a fluence of $1 \times 10^{11}/\text{cm}^2$ at the UNILAC at GSI, in Darmstadt Germany. The irradiation direction was kept parallel to the c -axis of the crystal, as tracks in this directions are routinely used for fission track analysis [59].

Figure 7.13 shows the SAXS detector images of ion tracks within a DAC under pressure. Each image was taken with an exposure time of 20 sec to allow for enough scattering contrast when using DACs. The samples within the DACs were brought to a pressure of 2.0 GPa as measured by the ruby fluorescence. In Fig. 7.13a the ion tracks are aligned in the direction of the incident X-ray beam leading to a circular pattern. The image was taken at RT and 2.0 GPa. The linear streaks through the centre of the image arise from interaction between the X-rays and the diamonds in the DAC. Figure 7.13b shows the same sample with a small tilt of 5° between the X-ray beam and ion track direction. Tilting allows a positioning of the streaks of the tracks in a direction that is not affected by the artefacts from the diamonds. It also makes the measurement less sensitive to small changes in sample alignment, during the heating process than the aligned and symmetric pattern. Figure 7.13c shows the same set-up after annealing at 250°C for a duration of 5 min. A clear weakening of the streak intensity from the tracks can be observed. This is a direct result of the partial recrystallisation of the amorphous ion tracks. After annealing the cell was allowed to cool down to RT and the pressure was measured again. This revealed a significant drop from 2 GPa to approximately 1 GPa. This change in pressure can be attributed to thermal expansion. As the expansion of the metal components (i.e. screws) is far higher than for the diamonds, the force acting on the diamond is decreased and consequently leading to a lower pressure. Miletich has reported on the reduction in pressure at comparable temperatures than used for apatite in the present subsection. For calcite, the pressure has dropped from 3.6 to 2.1 GPa when exceeding a temperature of 140°C [60]. The measured drop in the present work by approximately 50% is in agreement with typical DAC experiments without cell cooling. Hence, it is sensible to assume that the pressure during thermal annealing was closer to 1 GPa than the initial 2 GPa. In future work, the drop in pressure could be reduced by actively cooling the metal frame around the diamond anvils to reduce thermal expansion.

The SAXS patterns of the time series for annealing under pressure are shown in Fig. 7.14 as a function of q . To study the decrease in track length, the SAXS intensity was extracted from each pattern. The intensity is a suitable measure of the general track fading respective to damage recovery as it is proportional to the square root of track area, track length and density change, as shown in Eq. (7.1). Figure 7.15 compares (a) the track radii R , (b) SAXS intensity I_0 , and (c) track length L from in situ SAXS from the samples annealed under ~ 1 GPa pressure (solid squares) together with the samples annealed at ambient pressure (crosses) from Sect. 7.2.1. The annealing curves under pressure result from two different annealing series (grey and black), albeit under identical conditions. The difference in their behaviour is mainly attributed to the variation in the temperature control of the heatable DAC. The uncertainty of the SAXS results extracted from the measured patterns is assumed to be negligible until the SAXS intensity has dropped significantly.

The annealing results under high pressure are compared with those under ambient pressure from Sect. 7.2.1. The apatite samples only differ in the type of ion used for the irradiation. For the pressurised samples, $2.3\text{ GeV }^{209}\text{Bi}$ ions were used. For the samples annealed under ambient pressures, $2.2\text{ GeV }^{197}\text{Au}$ ions were used. These

Fig. 7.14 SAXS patterns of ion tracks in apatite within a DAC at ~ 1 GPa during annealing as a function of time (open circles). Negative times denote the annealing during the temperature ramping period. Patterns are offset for clarity with shifts to the top correlating to longer annealing times (grey arrow)



very similar energy losses of the two ion types only lead to a small difference in the track radii, as it was demonstrated in Sect. 5.2.2. The pressurised samples were annealed using the heatable DACs, the ambient pressure samples with the Linkam TS-1500 furnace.

Reduction of the Ion Track Radius

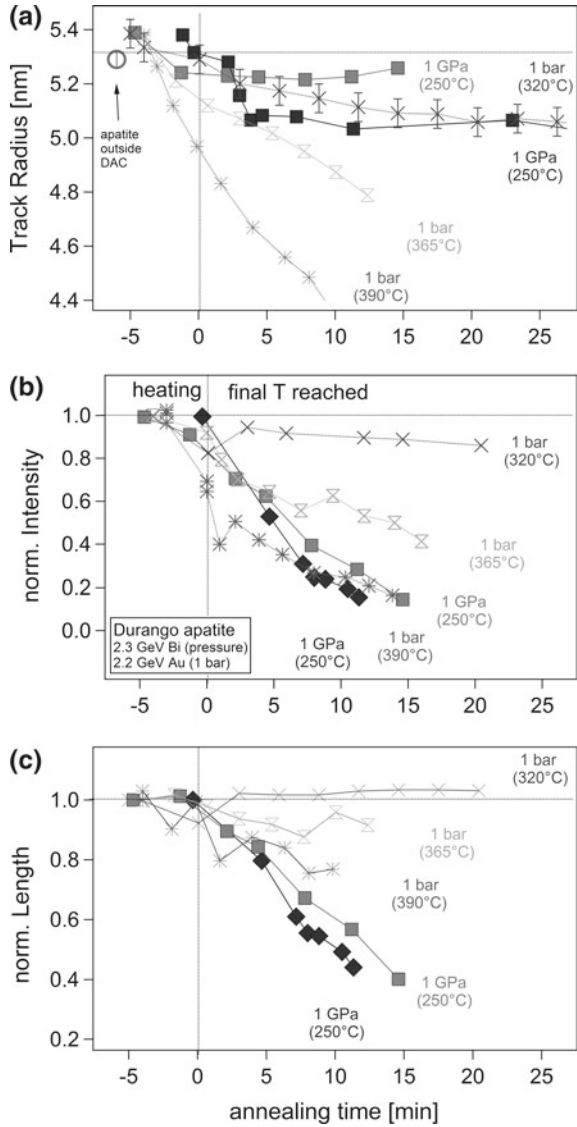
The samples under high pressure display a fast decrease in track radius (Fig. 7.15a) within a few minutes after the annealing was started. The decrease in the range of 0.2–0.4 nm (4–8%) of the initial radius is similar to that at 320 °C at ambient pressure. Upon reaching this value, the ion track radius appears to remain almost constant and unchanged for a period of 15–30 min.

The SAXS intensity, however, continues to decrease gradually. This behaviour is very different to the annealing at ambient pressure, where the tracks show a gradual decrease in radius and SAXS intensity. Despite no further reduction in radius, the measured SAXS intensity from the tracks was observed to decrease until the scattering signal had eventually disappeared. This suggests that track recrystallisation might undergo a different pathway when tracks are exposed to high pressures.

Reduction of the Ion Track Length

Figure 7.15b shows the decrease in I_0 for tracks annealed at ambient pressure for constant temperatures of 320, 365 and 390 °C. When the annealing is performed under hydrostatic pressure of 1 GPa, I_0 decreases significantly despite the lower temperature of 250 °C. Based on the two high-pressure annealing curves, the decrease in intensity at 250 °C at 1 GPa is similar to that at 390 °C at ambient pressures. This shows a temperature difference of 140 °C or approximately 14 °C/0.1 GPa. It is acknowledged that the experiments were conducted using different equipment (Linkam annealing stage for 1 bar, heatable DACs for 1 GPa). Both used resistive heating and had a thermocouple positioned very closely to the sample, minimising any discrepancy in temperature between each other below 10 °C. In fact, the present findings show similar annealing at of the two annealing experiments that are more 14

Fig. 7.15 Annealing of ion tracks in apatite under pressure (1 GPa, solid squares) and under ambient atmosphere (1bar, crosses). Evolution over time of **a** the track radius, **b** normalised SAXS intensity, and **c** normalised length. Negative times denote the annealing during the temperature ramping period



times greater than this uncertainty. Thus the difference can clearly not be attributed to the use of different annealing set-ups.

At high pressures, the effects of thermal annealing on the track radius and length seem to differ substantially from those at ambient pressure. For pressures around 1 GPa, even lower temperatures such as 250 °C seem to lead to a significant reduction in track length for ion tracks parallel to the *c*-axis. At the same time, only small reductions in the track radius was observed. It remains unclear why elevated pressure

appears to influence the thermal annealing of the track length to a much stronger extent than its radius. To address this questions, additional investigations are required at a variety of pressures and temperatures, as well as tracks oriented along different crystallographic directions.

To explain the effects of pressure within the diffusion model [28], the argument in the Boltzmann equation has to be amended, similar to Wendt et al. [5]. The pressure P can be incorporated into the Boltzmann equation by reducing the activation energy E_a with the subtraction of a pressure term:

$$D(T, P) = D_0 \exp\left(-\frac{E_a - P \cdot \Delta V}{k_B T}\right) \quad (7.8)$$

with D_0 as the pre-exponential constant, as described by Fick's first law of diffusion. The activation volume ΔV is the difference between the initial amorphous region and the recrystallised volume. Equation (7.8) indicates increased atomic diffusion rates at elevated pressure. Therefore, using the diffusion model for track recrystallisation, the increased annealing rate of tracks under hydrostatic pressure would indeed be expected.

7.2.5 Discussion and Extrapolation to Geologically Relevant Pressures

Figure 7.16 shows an Arrhenius plot of the annealing time required to reach 90% of the initial track length as a function of reciprocal temperature (the temperature itself is shown on the top axis). The values are extracted from the relative track length from Fig. 7.15c. They represent the duration until the length was reduced to 90% of its initial value for annealing with 365 and 390 °C at 1 bar and 250 °C at ~1 GPa. The comparison between ion tracks annealed under pressure and 250 °C shows a similar reduction in track length to annealing at ambient pressure and significantly higher temperatures (~380 °C).

However, the effect becomes significantly smaller when extrapolated to the upper limit of geologically relevant values (150 MPa), similar to Schmidt et al. as shown in Fig. 7.7 [4]. In fact, they have found the extrapolated annealing rate in a similar range as the annealing curve in the absence of pressure. For the present findings, extrapolation from 1 GPa to 150 MPa also reveals that the influence of pressure is small at geological relevant pressures. Assuming a linear dependence of the track annealing on the reciprocal temperature [4]:

$$1/T_{150\text{MPa}}[K] = 1/T_2[K] + (1/T_1[K] - 1/T_2[K]) \times (0.15\text{GPa}/1\text{GPa}) \quad (7.9)$$

where $T_2 = 380^\circ\text{C}$ and $T_1 = 250^\circ\text{C}$ are the annealing temperatures at ambient pressure and 1 GPa, respectively. This demonstrates thermal annealing at 150 MPa would

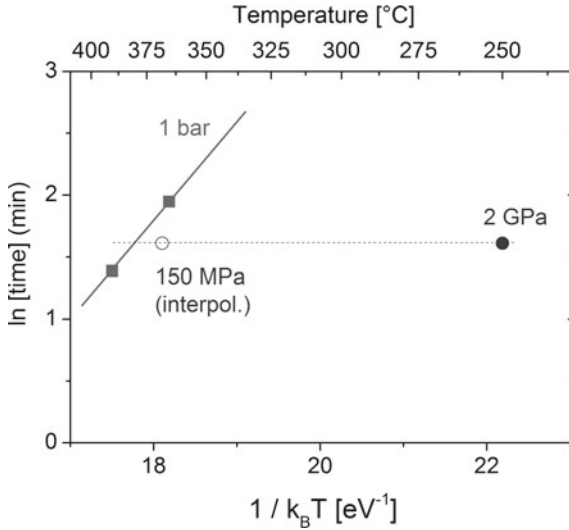


Fig. 7.16 Arrhenius plot of the annealing time required to reach 90% of the initial track length as a function of (reciprocal) temperature in apatite. The solid squares show the annealing times to reach 90% track length at temperatures of 390 and 365 °C at ambient pressure. Annealing at 1 GPa (solid circle) shows a similar annealing rate at only 250 °C. The effects of pressure are extrapolated to lower pressures (open circle), making the influence of geologically relevant pressures close to insignificant

require 357 °C to obtain a similar annealing as 380 °C at 1 bar or 250 °C at 1 GPa. Consequently, a pressure of 150 MPa corresponds to a decrease in annealing by 23 °C, although this value only applied to short timescales (≤ 1 h) and far higher temperatures ($\gg 150$ °C) than geologically relevant.

A pressure of 150 MPa is the maximum pressure relevant for fission tracks in apatite, as at higher depths the temperatures under normal circumstances exceed the closure temperature. Although this value might be relevant for fission track results taken at 5 km, it has no relevance for most of the apatite samples used for fission track dating that are taken from a much lower depth. Therefore, these results imply that the majority of apatite-based thermochronology does not have to be revised, as claimed by previous studies [5].

Donelick et al. have conducted experiments studying the length reduction over the course of 24 h at 250 and 302 °C [7, 61]. Regardless of pressure (1 bar, 0.05 and 0.10 GPa), they found a reduction by 10 and 30%, respectively. The present results, extrapolated to 24 h would only lead to an insignificant change in annealing temperature at elevated pressures. This explains why in these results no influence of pressure has been observed.

7.3 Summary

The recrystallisation of ion tracks has been investigated for apatite and quartz using *in situ* SAXS. In agreement with previous investigations, the tracks did not change significantly over timescales of 1 h below a certain material-dependent temperature. Above this temperature point, the track radius showed a significant reduction, together with a rapid drop in the SAXS scattering intensity until no indication of tracks could be observed. In direct comparison with annealing experiments carried out using chemical etching and optical microscopy, the tracks were observed to disappear at higher temperatures. This demonstrates the higher sensitivity when investigating latent tracks in comparison with etched tracks. The size reduction was explained by the triggering of diffusion that moves the atoms back into ordered lattice positions.

When ion tracks in apatite were annealed in the presence of high pressure, a faster recovery rate than under ambient pressure was observed. Over the duration of 15 min, an annealing temperature of 250 °C with a pressure of 1 GPa has shown a similar recrystallisation rate for the track length as for 380 °C at ambient pressures. This is a significant effect and the first time ion track sizes were characterised *in situ* during annealing under high pressure. The results have allowed a calculation of the recrystallisation rate and explanation of the trend qualitatively using the diffusion model. The decrease in radius was less affected by the high pressure. After an initial drop by 4–6%, it remained constant over the course of 15–30 min, although the intensity of the SAXS signal has shown a substantial reduction to less than 10% of its initial value.

When put into a geological context, the results have no significant influence on the field of apatite fission track analysis, as the effects are negligibly small at pressures relevant for these tracks. This makes the results consistent with the majority of previous investigations, reporting an insignificant increase in the annealing rate for fission tracks from high depth [2, 4, 42, 56]. The results also clearly rule out the claims of stabilising effects of pressure [5]. The results were also discussed using empirical descriptions, predominantly in the framework of atomic diffusion as the key mechanism behind ion track recrystallisation.

The use of SAXS allowed a precise characterisation of the track radius under the assumption that the ion tracks are roughly cylindrical-shaped and display a uniform radial shrinkage. Both assumption are considered to be reasonable and valid for tracks induced by swift heavy ions of 2.2–2.3 GeV. For the characterisation of the ion track length, however, an additional assumptions were made, by assuming a constant density difference $\Delta\rho$. As ion track length and density cannot be verified independently by the means employed in this work, the validity of this assumption cannot be fully confirmed. Potentially, the value for the average $\Delta\rho$ of the track also reduces and thus the estimation for the length reduction might be stronger than stated. It is noted that such a behaviour would not affect the conclusions drawn in this work: In Sect. 7.1.1, the length reduction of ion tracks in quartz is compared to measure a potential anisotropy between tracks along different crystalline orientations. The track

radius R and the product of length and density difference $L \cdot \Delta\rho$ did not show such an effect. It is reasonable to assume that each of the two factors also does not show any anisotropic behaviour, as they would be to be contrary to each other. Secondly, it was concluded that the reduction in track length when annealed under pressure is of similar magnitude as for annealing under ambient pressure. If in fact $\Delta\rho$ would also decrease for annealing under pressure or ambient atmosphere, the reduction in L would be overestimated. However, the general rate of decrease would still be within similar magnitude between the different pressures, still allowing the conclusion that geological pressure values only have negligible influence on the annealing rate of ion tracks.

References

1. G.A. Wagner, P. Van den Haute, *Fission-Track Dating* (Kluwer Academic Publishers, Dordrecht, 1992)
2. C.W. Naeser, H. Faul, Fission track annealing in apatite and sphene. *J. Geophys. Res.* **74**(2), 705–710 (1969)
3. B. Afra, M. Lang, T. Bierschenk, M.D. Rodriguez, W.J. Weber, C. Trautmann, R.C. Ewing, N. Kirby, P. Kluth, Annealing behaviour of ion tracks in olivine, apatite and britholite. *Nucl. Instrum. Meth. Phys. Res. B* **326**, 126 (2014)
4. J.S. Schmidt, M.L.M.V. Lelarge, R.V. Conceicao, N.M. Balzaretto, Experimental evidence regarding the pressure dependence of fission track annealing in apatite. *Earth Planet. Sci. Lett.* **390**, 1–7 (2014)
5. A.S. Wendt, O. Vidal, L.T. Chadderton, Experimental evidence for the pressure dependence of fission track annealing in apatite. *Earth Planet. Sci. Lett.* **201**, 593–607 (2002)
6. O. Vidal, A.S. Wendt, L.T. Chadderton, Further discussion on the pressure dependence of fission track annealing in apatite: reply to the critical comment of Kohn, et al., *Earth Planet. Sci. Lett.* **215**(1–2), 307–316 (2003)
7. R. Donelick, K. Farley, P. O’ Sullivan, P. Asimow, Experimental evidence concerning the pressure dependence of He diffusion and fission-track annealing kinetics in apatite. *On track: Newsl. Int. Fission-track Commun.* **13**(2), 19–21 (2003)
8. B.P. Kohn, D.X. Belton, R.W. Brown, A.J.W. Gleadow, P.F. Green, J.F. Lovering, Comment on: Experimental evidence for the pressure dependence of fission track annealing in apatite by A.S. Wendt, et al., *Earth Planet. Sci. Lett.* **201** (2002) 593. *Earth Planet. Sci. Lett.* **215**, 299–306 (2003)
9. D. Schauries, A.A. Leino, B. Afra, M.D. Rodriguez, F. Djurabekova, K. Nordlund, N. Kirby, C. Trautmann, P. Kluth, Orientation dependent annealing kinetics of ion tracks in c-SiO₂. *J. Appl. Phys.* **118**, 224305 (2015)
10. A.S. Sandhu, S. Singh, H.S. Virk, Anisotropic etching and annealing of fission tracks in quartz. *Mineralogical J.* **14**(1), 1–11 (1988)
11. T. Sawamura, S. Baba, M. Narita, Anisotropic annealing of fission fragments in synthetic quartz. *Radiat. Meas.* **30**(4), 453–459 (1999)
12. T. Sawamura, S. Baba, H. Yamazaki, Effect of twinning caused by thermal annealing on etched tracks in synthetic quartz. *Jpn. J. Appl. Phys.* **30**(No. 2A), L212–L214 (1991)
13. S.A. Durrani, R.K. Bull, *Solid State Nuclear Track Detection* (Pergamon Press, Oxford, 1987)
14. A.J.W. Gleadow, D.X. Belton, B.P. Kohn, R.W. Brown, Fission track dating of phosphate minerals and the thermochronology of apatite. *Rev. Mineral. Geochem.* **48**(1), 579 (2002)
15. I.G. Berzina Ya.E. Geguzin, I.V. Vorob’eva, Thermal stability of uranium fission fragment tracks in muscovite single crystals (effect of anisotropy). *Soviet Phys. Solid St.* **10**, 1431–1434 (1968)

16. P.F. Green, S.A. Durrani, Annealing studies of tracks in crystals. *Nucl. Track Detect.* **1**(1), 33–39 (1977)
17. John B. Brady, *Diffusion Data for Silicate Minerals, Glasses, and Liquids* (American Geophysical Union, 1995)
18. D.J. Cherniak, Diffusion in quartz, melilite, dilivsyrovskite and mullite. *Rev. Mineral. Geochem.* **72**, 735–756 (2010)
19. M.L.F. Nascimento, E.D. Zanotto, Mechanisms and dynamics of crystal growth, viscous flow, and self-diffusion in silica glass. *Phys. Rev. B* **73**, 024209 (2006)
20. Website quartz, <http://www.quartzpage.de/>
21. P.J. Heaney, Structure and chemistry of the low-pressure silica polymorphs. *Rev. Mineral.* **29**, 1–40 (1994)
22. D. Schauries, B. Afra, M.D. Rodriguez, C. Trautmann, A. Hawley, P. Kluth, Ion track annealing in quartz investigated by small angle X-ray scattering. *Nucl. Instrum. Methods Phys. Res. Sect. B. Mater. Atoms* **365**, 380–383 (2015)
23. W. Li, L. Wang, M. Lang, Ch. Trautmann, R.C. Ewing, Thermal annealing mechanisms of latent fission tracks: apatite vs. zircon. *Earth Planet. Sci. Lett.* **302**(1–2), 227–235 (2011)
24. A. Aframian, Track retaining properties of quartz for high temperature in-core neutron fluence measurements. *Radiat. Effects* **33**(2), 95–100 (1977)
25. B. Afra, K. Nordlund, M.D. Rodriguez, T. Bierschenk, C. Trautmann, S. Mudie, P. Kluth, Thermal response of nanoscale cylindrical inclusions of amorphous silica embedded in α -quartz. *Phys. Rev. B* **90**, 224108 (2014)
26. J. Burchart, J. Galazka-Friedman, J. Kral, Experimental artifacts in fission-track annealing curves. *Nucl. Tracks* **5**, 113–120 (1981)
27. P.F. Green, I.R. Duddy, A.J.W. Gleadow, P.R. Tingate, G.M. Laslett, Fission-track annealing in apatite: Track length measurements and the form of the Arrhenius plot. *Nucl. Tracks Radiat. Meas.* (1982), **10**(3), 323–328 (1985)
28. G.M. Laslett, P.F. Green, I.R. Duddy, A.J.W. Gleadow, Thermal annealing of fission tracks in apatite. a quantitative analysis. *Chem. Geol.: Isot. Geosci. Sect.* **65**(1), 1–13 (1987)
29. H.S. Virk, Single-activation-energy model of radiation damage in solid-state nuclear-track detectors. *Curr. Sci.* **61**, 386–390 (1991)
30. R.A. Ketcham, R.A. Donelick, W.D. Carlson, Variability of apatite fission-track annealing kinetics; III, Extrapolation to geological time scales. *Am. Mineral.* **84**(9), 1235–1255 (1999)
31. R.A. Ketcham, A. Carter, R.A. Donelick, J. Barbarand, A.J. Hurford, Improved modeling of fission-track annealing in apatite. *Am. Mineral.* **92**(5–6), 799–810 (2007)
32. A.C. Damask, G.J. Dienes, *Point Defects in Metals* (Gordon and Breach Science, Philadelphia, 1963)
33. S. Gasiorek, S. Dhar, K.P. Lieb, Epitaxial recrystallization of Rb-irradiated α -quartz during thermal annealing in air. *Nucl. Instrum. Meth. Phys. Res. B* **193**, 283–287 (2002)
34. F.E. Wagstaff, K.J. Richards, Kinetics of Crystallization of Stoichiometric SiO₂ Glass in H₂O Atmospheres. *J. Am. Ceramic Soc.* **49**, 118–121 (1966)
35. P.M. Ihlen Axel Müller, J. Egil Wanvik, *Quartz: Deposits, Mineralogy and Analytics* (Springer Geology, 2012)
36. W. Primak, H. Szymanski, Radiation damage in vitreous silica: annealing of the density changes. *Phys. Rev.* **101**, 1268–1271 (1956)
37. A.J.W. Gleadow, I.R. Duddy, A natural long-term track annealing experiment for apatite. *Nucl. Tracks* **5**, 169–174 (1981)
38. P.F. Green, Comparison of zeta calibration baselines for fission-track dating of apatite, zircon and sphene. *Chem. Geol.: Isot. Geosci. Sect.* **58**(1), 1–22 (1985)
39. P.F. Green, I.R. Duddy, A.J.W. Gleadow, P.R. Tingate, G.M. Laslett, Thermal annealing of fission tracks in apatite: 1. A qualitative description. *Chem. Geol.: Isot. Geosci. Sect.* **59**, 237–253 (1986). Calibration of the Phanerozoic Time Scale
40. J. Barbarand, A. Carter, I. Wood, T. Hurford, Compositional and structural control of fission-track annealing in apatite. *Chem. Geol.* **198**, 107–137 (2003)
41. Beno Gutenberg, *Physics of the Earth's Interior* (Academic Press, New York, 1959)

42. R.L. Fleischer, P.B. Price, R.M. Walker, Effects of temperature, pressure, and ionization of the formation and stability of fission tracks in minerals and glasses. *J. Geophys. Res.* **70**(6), 1497–1502 (1965)
43. M.R. Brix, B. Stoeckhert, E. Seidel, T. Theye, S.N. Thomson, M. Koester, Thermobarometric data from a fossil zircon partial annealing zone in high pressure-low temperature rocks of eastern and central Crete, Greece. *Tectonophysics* **349**, 309–326 (2002). *Low Temperature Thermochronology: From Tectonics to Landscape Evolution*
44. B. Afra. In situ annealing of ion tracks in apatite (unpublished) (2014)
45. B. Afra, M. Lang, M.D. Rodriguez, J. Zhang, R. Giuliani, N. Kirby, R.C. Ewing, C. Trautmann, M. Toulemonde, P. Kluth, Annealing kinetics of latent particle tracks in Durango apatite. *Phys. Rev. B* **83**, 064116 (2011)
46. A. Nadzri, D. Schauries, P. Mota-Santiago, S. Muradoglu, C. Trautmann, A. J. W. Gleadow, A. Hawley, and P. Kluth. Composition dependent thermal annealing behaviour of ion tracks in apatite. *Nuclear Instruments and Methods in Physics Research Section B: Beam Interactions with Materials and Atoms*, 379:211 – 214, 2016. 18th International Conference on Radiation Effects in Insulators (REI-18) Dates: 26th to 31st October, (2015)
47. H.S. Virk, Modgil-Virk formulation of single activation energy model of radiation damage annealing in SSNTDs: a critical appraisal. *Solid State Phenomena* **239**, 215–242 (2015)
48. A.S. Sandhu, S. Singh, H.S. Virk, Activation energy of track annealing in minerals as a function of interatomic spacing. *Int. J. Radiat. Appl. Instrum. Part D. Nucl. Tracks Radiat. Meas.* **15**(1–4), 235–238 (1988). Special Volume Solid State Nuclear Track Detectors
49. S.K. Modgil, H.S. Virk, Annealing of fission fragment tracks in inorganic solids. *Nucl. Instrum. Methods Phys. Res. Sect. B: Beam Interact. with Mater. Atoms* **12**(2), 212–218 (1985)
50. A. Raymond, Donelick, Crystallographic orientation dependence of mean etchable fission track length in apatite; an empirical model and experimental observations. *Am. Mineral.* **76**(1–2), 83–91 (1991)
51. R.A. Donelick, M.K. Roden, J.D. Mooers, B.S. Carpenter, D.S. Miller, Etchable length reduction of induced fission tracks in apatite at room temperature: crystallographic orientation effects and initial mean lengths. *Int. J. Radiat. Appl. Instrum. Part D. Nucl. Tracks Radiat. Meas.* **17**(3), 261–265 (1990)
52. S. Watt, P.F. Green, S.A. Durrani, Special volume: Solid state nuclear track detectors studies of annealing anisotropy of fission tracks in mineral apatite using track-in-track (tint) length measurements. *Nucl. Tracks Radiat. Meas.* (1982) **8**(1), 371–375 (1984)
53. W. Li, P. Kluth, D. Schauries, M.D. Rodriguez, M. Lang, F. Zhang, M. Zdorovets, Ch. Trautmann, R.C. Ewing, Effect of orientation on ion track formation in apatite and zircon. *Am. Mineral.* **99**(5–6), 1127–1132 (2014)
54. K.N. Matsukage, S. Ono, T. Kawamoto, T. Kikegawa, The compressibility of a natural apatite. *Phys. Chem. Miner.* **31**(9), 580–584 (2004)
55. Q. Williams, E. Knittle, Infrared and raman spectra of $\text{Ca}_5(\text{PO}_4)_3\text{F}_2$ -fluorapatite at high pressures: compression-induced changes in phosphate site and Davydov splittings. *J. Phys. Chem. Solids* **57**(4), 417–422 (1996)
56. R.L. Fleischer, R.T. Woods, H.R. Hart, P.B. Price, N.M. Short, Effect of shock on fission track dating of apatite and sphene crystals from the Hardhat and Sedan underground nuclear explosions. *J. Geophys. Res.* **79**(2), 339–342 (1974)
57. P. Kluth, M. Lang, M.D. Rodriguez, D. Schauries, B. Haberll, J. Bradby, B. Schuster, B. Afra, R. Miletich, C. Trautmann, N. Kirby, R.C. Ewing, Influence of high-pressure on the formation and stability of simulated fission tracks in Durango apatite. in preparation, n.a.:n.a., (2016)
58. P. Schouwink, R. Miletich, A. Ullrich, U.A. Glasmacher, Ch. Trautmann, R. Neumann, B.P. Kohn, Ion tracks in apatite at high pressures: the effect of crystallographic track orientation on the elastic properties of fluorapatite under hydrostatic compression. *Phys. Chem. Miner.* **37**(6), 371–387 (2009)
59. J. Barbarand, T. Hurford, A. Carter, Variation in apatite fission-track length measurement: Implications for thermal history modelling. *Chem. Geol.* **198**, 00423 (2003)

60. H. Keppler, D.J. Forst, *Introduction to Minerals Under Extreme Conditions in Mineral Behaviour at Extreme Conditions*, vol. 7 (University Press, Heidelberg, Germany, 2005)
61. R. Donelick, K. Farley, P. Asimow P. O'Sullivan, Experimental evidence concerning the pressure dependence of He diffusion and fission-track annealing kinetics in apatite. *Geochimica et Cosmochimica Acta*, **67**, Supplement 82 (2003)

Chapter 8

Summary and Outlook



This work has investigated the effects of the irradiation and material parameters as well as the influence of different temperatures and pressures on the formation and recrystallisation process of ion tracks.

The ion tracks were created by irradiating single-crystalline apatite and quartz with swift heavy ions, resulting in amorphous cylindrical inclusions in the materials with high aspect ratios. The irradiations were performed at the UNILAC and SIS accelerators in Darmstadt, Germany using ~ 2 GeV Au/Bi ions as well as 37 GeV Au, respectively. Lower energy ion irradiation was conducted at the HIAF in Canberra, Australia using 100 MeV I and 185 MeV Au ions. The majority of irradiation were carried out at fluences around $1 \times 10^{11} \text{ cm}^{-2}$, such that less than 10% of the total material volume was transformed into ion tracks. The observed tracks were found to be well-separated with minimal overlap and diameters between 7 and 11 nm.

The ion tracks were characterised by using SAXS at the Australian Synchrotron in Melbourne, Australia. The characterisation by SAXS was chosen due to its high precision and ability to measure the tracks in their latent state without empirical etching or laborious sample preparation required for imaging techniques such as optical or electron microscopy, respectively. The oscillating SAXS patterns were fitted using mathematical models incorporating information about the track size and shape. A cylindrical structure with constant density, a length of approximately $100 \mu\text{m}$, and typically 7–11 nm in diameter was characterised the tracks appropriately and is consistent with the formation of amorphous tracks in the crystalline matrices. The radial size was convoluted with a normal distributed variation of $\sim 10\%$ of its value.

In **Chap. 5** it is shown that the direction of the tracks with respect to their non-cubic crystal lattice plays a measurable role on the radial size of the resulting tracks. This effect was attributed to the anisotropy of the thermal properties of the crystals. For both materials, quartz and apatite, ion tracks aligned parallel to the *c*-axis were observed to show larger track radii. In addition, possible variations from the ideal cylindrical shape were investigated: A slightly elliptical cross-section was found for ion tracks in quartz. For ion tracks in apatite, the length profile was investigated and a cigar-shaped structure was observed.

In **Chap. 6**, the effects of temperature and pressure on track formation were investigated. One irradiation series was carried out with a set of samples irradiated while placed within a furnace at temperatures up to 640 °C. To form ion tracks under pressure, quartz samples were irradiated within diamond anvil cells (DACs). These cells allow small samples to be exposed to pressures up to tens of GPa. For this purpose, the cells were irradiated with 37.2 GeV Au ions at the SIS in Darmstadt, Germany. Such high energy ions are capable of penetrating the >2 mm thick diamond anvils and create ion tracks in the quartz samples under pressure.

The investigation with SAXS has revealed a clear positive correlation between the track size and the temperature as well as pressure during their formation with rates of approximately 0.08 nm/100 °C and 0.15 nm/GPa, respectively. Comparable values were obtained by using simulations of track formation in quartz at different temperatures and pressures, using the thermal spike model and molecular dynamics calculations. This positive correlation of the track radius with temperature during ion irradiation is in contrast to dynamic annealing for ion irradiation in the keV range, where elevated temperatures generally lead to a reduction in ion induced damage.

In **Chap. 7**, the effects of temperature on existing tracks were studied in quartz and apatite. In contrast to the effects of elevated temperature during track formation, track annealing is well-known to reduce the radial size and length of ion tracks due to recrystallisation effects. An anisotropy of the track recrystallisation rate was found in quartz, showing a dependence on the orientation of the tracks along the crystalline directions. Using heatable DACs, the track annealing in apatite was studied while the sample experienced high pressure. This was motivated by previous controversial investigations on the influence of pressure on track recrystallisation, reporting either a negative, slightly positive or no measurable correlation. The present results have confirmed a small positive correlation on annealing at high-pressures by obtaining comparable annealing rates with 1 GPa and 250 °C in comparison with 380 °C under ambient pressure. However, in the context of fission tracks, these results are negligible when extrapolated to geological relevant pressures (~0.1 GPa).

8.1 Future Directions

While this work has contributed to the understanding of the effects of temperature and pressure on ion track formation and stability, it has also opened up possibilities for interesting further investigations:

8.1.1 Effects of Pressure on the Recrystallisation of Tracks

To further study the effects of pressure on track annealing, the DAC annealing experiments should be complemented with measurements at a range of different temperatures below 250 °C at longer annealing times. These results would allow us to

calculate the activation energy for track recrystallisation in a similar way as shown for ambient pressure in this work. Such a more quantitative analysis would also strengthen the findings of this work that high pressures increase the rate of track annealing in apatite.

Another direction would be investigating ion track annealing under pressure in other materials. Ion tracks in zircon possess a higher closure temperatures up to 200–300 °C. Such tracks require higher temperatures to recrystallise and potentially their thermal annealing shows a different dependence on pressure. Quartz crystals, on the other hand, have no direct application for fission track thermochronology, but tracks in quartz exhibit even higher stability to thermal annealing. In addition, the structure and track annealing kinetics are well-studied for quartz. Hence, including quartz in future investigations could contribute to establish a more theoretical framework to explain track recrystallisation under pressure.

8.1.2 Generalisation of the Effects of Pressure During Track Formation

Ion irradiation under pressure has demonstrated a linear trend for the track radius in quartz. Preliminary results on track formation in apatite show a more complicated dependence for tracks. A challenge for experiments and theoretical models in the future will be to explain whether there is a general behaviour or whether pressure can have very different effects on ion track formation in different host materials. Materials that would be good candidates for irradiation under pressure are zircon (ZrSiO_4) or LiF.

The main challenge with these experiments is the access to suitable facilities. If irradiation is performed with ions penetrating through the diamonds of a DAC, only a limited facilities world-wide offer the required energy, e.g. SIS in Darmstadt, Germany used in the present work. This limits the amount of samples that can be irradiated under pressure to only a few per year.

8.1.3 Small Angle Neutron Scattering

For the characterisation of ion tracks, additional work could be done using neutron-based small angle scattering. This technique has shown to provide much higher noise levels and thus requires expose times of several hours, making it no alternative to SAXS for size characterisation. However, to probe the composition of ion tracks, the combination of SAXS with SANS does provide additional insights as both techniques have different sensitivity to the elements of the target. This promises additional information about the damage of the anion-sublattice, that consists of light elements for

most materials and is, therefore, barely taken into account by X-ray characterisation techniques.

8.1.4 SAXS Modelling of Tracks with Non-uniform Depth Profiles

The majority of SAXS measurements in the present work has been used to evaluate the average track radius. For the high-energy ions used in this work, this is a very good approximation due to the homogeneity of the track along its length of tens of micrometres. For tracks created by ions with energies below 1 GeV, which show significantly more complicated shapes, it would be interesting to expand the work conducted in Sect. 5.4 and measure the track radii along the individual slices of the track. Due to experimental constraints when slicing irradiated minerals, a suitable candidate for such investigations would be multiple layers of a polymer that are stacked for the irradiation. Layered crystals such as mica would be another suitable choice.

8.1.5 Simulations of Track Recrystallisation

On the simulation side, it would be a promising approach to study the effects of temperature, pressure, and lattice anisotropy on ion tracks and investigate how the tracks shrink and recover. The long timescales at which recrystallisation occurs, prevent calculations by Molecular Dynamics, but other techniques such as Kinetic Monte Carlo simulations would be suitable.

Such simulations could explain the results observed in the work on the recrystallisation of tracks. This interplay between experimental results and theory has a great potential to significantly increase the understanding of the stability of ion tracks as well as other radiation damage in materials.

Curriculum Vitae

Author Biography



Daniel Schauries, Ph.D.

Nationality: German-Australian

Email: schauries@gmx.de

Education

Australian National University, Canberra (Aug 2012–July 2016)

Doctor of Philosophy (Ph.D.) in Physics, supervised by Prof. Dr. Patrick Kluth

University of Duisburg-Essen, Germany (Oct 2006–May 2012)

German Diploma in Physics, Thesis supervised by Prof. Dr. Andreas Ney

Loughborough University, UK (Sep 2009–Jun 2010)

ERASMUS Scholarship (Study Abroad)

Conferences Contributions

18th International Conference on Radiation Effects in Insulators (REI)

Jaipur, India (Oct 2015)

Talk: In situ SAXS characterization of ion track annealing under high pressure

International School on Ions Beams in Material Science

Jaipur, India (Oct 2015)

Talk: Ion tracks in solids studied by small angle X-ray and neutron scattering

9th International Symposium on Swift Heavy Ions in Matter (SHIM)

Darmstadt, Germany (May 2015)

Talk: SAXS and SANS characterisation of ion tracks in polymers

79th Spring Meeting der Deutschen Physikalischen Gesellschaft (DPG)

Berlin, Germany (Mar 2015)

Talk: Effects of heavy-ion irradiation in solids studied by SAXS and SANS

9th European Winterschool on Neutron and Synchrotron Radiation (NESY)

Altaussee, Austria (Mar 2015)

Talk: Ion Tracks in Minerals studied by SAXS/SANS

Best Young Researcher Presentation

AIP-2014 Australian Institute of Physics Congress

Canberra, Australia (Dec 2014)

Talk: Effects of heavy-ion irradiation in minerals studied by SAXS

Australian Synchrotron User Meeting

Melbourne Australia (Nov 2014)

Talk: SAXS and SANS characterisation of ion irradiation in polymers

MRS Spring Meeting and Exhibit

San Francisco, USA (Apr 2014)

Talk: Ion tracks in minerals and the role of temperature studied by SAXS

Best Young Researcher Talk Award and MRS Graduate Award (Silver)

Australian Synchrotron User Meeting

Melbourne Australia (Nov 2013)

Talk: SAXS-based analysis of ion tracks in minerals and the role of temperature

7th Asia-Oceania Forum for Synchrotron Radiation Research

Himeji, Japan (Sep 2013)

Poster: Temperature dependent formation of ion tracks studied using SAXS

17th International Conference on Radiation Effects in Insulators (REI)

Helsinki, Finland (Jul 2013),

Poster: Temperature dependent formation of ion tracks studied using SAXS

Australian Synchrotron User Meeting

Melbourne, Australia (Nov 2012)

Poster: Temperature dependent formation of ion tracks studied using SAXS

Best Poster Award

Publications

Composition Dependent Thermal Annealing Behaviour of Ion Tracks in Apatite

A. Nadzri, **D. Schauries**, P. Mota-Santiago, S. Muradoglu, A. Hawley, C. Trautmann, P. Kluth

Nucl. Instrum. Meth. Phys. Res. B 379 (2015) 211.

Orientation Dependent Annealing Kinetics of Ion Tracks on Synthetic Quartz

D. Schauries, B. Afra, A. A. Leino, M. D. Rodriguez, F. Djurabekova, K. Nordlund, N. Kirby, C. Trautmann, P. Kluth

J. Appl. Phys. 118 (2015) 224305.

SAXS Study on the Morphology of Etched and Un-etched Ion Tracks

A. Nadzri, **D. Schauries**, B. Afra, M. D. Rodriguez, P. Mota-Santiago, S. Muradoglu, A. Hawley and P. Kluth,

European Journal of Physics, Web of Conferences 91 (2015) 00009.

Ion Track Annealing in Quartz Investigated by Small Angle X-ray Scattering

D. Schauries, B. Afra, M. D. Rodriguez, C. Trautmann, A. Hawley, and P. Kluth

Nucl. Instr. Meth. Phys. Res. B 365 (2015) 380.

The Shape of Ion Tracks in Natural Apatite

D. Schauries, B. Afra, T. Bierschenk, M. Lang, M. Rodriguez, C. Trautmann, W. Li, R.C. Ewing, P. Kluth

Nucl. Instr. Meth. Phys. Res. B 326 (2014) 117.

Effect of Orientation on Ion Track Formation in Apatite and Zircon

W.X. Li, P. Kluth, **D. Schauries**, M.D. Rodriguez, M. Lang, F. Zhang, M. Zdorovets, C. Trautmann, R. C. Ewing

American Mineralogist 99 (2014) 1127.

Temperature Dependence of Ion Track Formation in Quartz and Apatite

D. Schauries, M. Lang, O. H. Pakarinen, S. Botis, B. Afra, M. D. Rodriguez, F. Djurabekova, K. Nordlund, D. Severin, M. Bender, W.X. Li, C. Trautmann, R. C. Ewing, N. Kirby and P. Kluth.

J. Appl. Crystallogr. 46 (2013) 1558.

The following publications are based on work conducted during the Ph.D. candidature, but are not directly related to the primary project:

Highly Selective Ionic Transport Through Subnanometer Pores in Polymer Films

Q. Wen, D. Yan, F. Liu, M. Wang, Y. Ling, P. Wang, P. Kluth, **D. Schauries**, Ch. Trautmann, P. Apel, W. Guo, G. Xiao, J. Liu, J. Xue, Y. Wang

Adv. Functional Materials 26 (2016) 5796.

Orientation Dependence of Swift Heavy Ion Track Formation in Potassium Titanyl Phosphate

Y.-J. Ma, P. Mota Santiago, M. D. Rodriguez, F. Kremer, **D. Schauries**, B. Afra, T. Bierschenk, D. J. Llewellyn, F. Lu, M. C. Ridgway, P. Kluth
J. Materials Research 31 (2016) 2329.

Size Characterization and Thermal Annealing of Latent Ion Tracks in PET and PTFE

D. Schauries, M.D. Rodriguez, B. Afra, T. Bierschenk, C. Trautmann, S. Mudie, P. Kluth
Nucl. Instr. Meth. Phys. Res. B 365 (2015) 573.

Characterization of Ion Track Morphology Formed by Swift Heavy Ion Irradiation in Silicon Oxynitride Films

P. Mota-Santiago, **D. Schauries**, A. Nadzri, K. Vora, M.C. Ridgway, P. Kluth
European Journal of Physics, Web of Conferences 91 (2015) 00008.

SAXS and TEM Investigation of Ion Tracks in Nd-Doped Y-Al-Garnet

M.D. Rodriguez, W.X Li, F. Chen, C. Trautmann, T. Bierschenk, B. Afra, **D. Schauries**, R.C. Ewing, S.T. Mudie, P. Kluth
Nucl. Instr. Meth. Phys. Res. B 326 (2014) 150.

Latent Ion Tracks in Amorphous Silicon

T. Bierschenk, R. Giulian, B. Afra, M.D. Rodriguez, **D. Schauries**, S. Mudie, O.H. Pakarinen, F. Djurabekova, K. Nordlund, O. Osmani, N. Medvedev, B. Rethfeld, M.C. Ridgway, P. Kluth
Phys. Rev. B 88 (2013) 174111.